



HAL
open science

Superhydrophobic thermoplastics obtained by simple texturing processes

Guillaume Espy

► **To cite this version:**

Guillaume Espy. Superhydrophobic thermoplastics obtained by simple texturing processes. Materials. Université de Lyon, 2021. English. NNT : 2021LYSEI027 . tel-04709906

HAL Id: tel-04709906

<https://theses.hal.science/tel-04709906v1>

Submitted on 26 Sep 2024

HAL is a multi-disciplinary open access archive for the deposit and dissemination of scientific research documents, whether they are published or not. The documents may come from teaching and research institutions in France or abroad, or from public or private research centers.

L'archive ouverte pluridisciplinaire **HAL**, est destinée au dépôt et à la diffusion de documents scientifiques de niveau recherche, publiés ou non, émanant des établissements d'enseignement et de recherche français ou étrangers, des laboratoires publics ou privés.



N°d'ordre NNT : 2021LYSEI027

THESE de DOCTORAT DE L'UNIVERSITE DE LYON
opérée au sein de
l'INSA de Lyon

Ecole Doctorale N° 34
Matériaux de Lyon

Spécialité/ discipline de doctorat :
Science des Matériaux

Soutenue le 12/05/2021, par :
Guillaume ESPY

**Superhydrophobic thermoplastics
obtained by simple texturing processes**

**Thermoplastiques superhydrophobes
obtenus par des procédés de
texturation simples**

Devant le jury composé de :

ROUCOULES Vincent, Professeur des Universités, Université de Haute Alsace,
BILLON Laurent, Professeur des Universités, UPPA,
GROHENS Yves, Professeur des Universités, Université Bretagne Sud,
GOURGON Cécile, Chargée de Recherche CNRS, Université Grenoble Alpes,
DUCHET-RUMEAU Jannick, Professeur des Universités, INSA Lyon,
GERARD Jean-François, Professeur des Universités, INSA Lyon,
LIVI Sébastien, Maître de conférences, INSA Lyon,
LHOST Olivier, Docteur, Total,

Président
Rapporteur
Rapporteur
Examinatrice
Directrice de thèse
co-Directeur de thèse
co-Encadrant
Encadrant industriel

SUMMARY

Plastics are nowadays mainly produced for the packaging industry, with a very limited lifetime of less than a year. The mass production of such objects generates an important volume of waste, which need to be recycled at the maximum in order to reduce both the volume of final wastes and the need of fossil-based resources needed for their production. By integrating to plastic packaging superhydrophobic materials, mimicking the "lotus effect", their soiling by the content they protect might be avoided, favorizing their recycling while offering to the consumer the full amount of the product he bought. To reach such properties on materials with a low added-value, simple texturing ways of hydrophobic thermoplastics such as high-density polyethylene (HDPE) and polypropylene (PP) have been studied. After a review of the ways presented in the scientific literature to reach superhydrophobicity, an understanding of the wetting mechanism has been conducted, thanks to a modeling of a Cassie-Baxter's interface. Using guidelines established thanks to this model, simple texturing ways have been studied: texturing using fillers, from immiscible polymer blends, foaming using supercritical CO₂, or foaming in extrusion. Despite generating textured surfaces, none of these approaches led to superhydrophobicity. However, exposing thermoplastics to a solvent at a high temperature permitted to generate rough superhydrophobic surfaces. This process has been developed and its mechanisms studied in order to have at the end an in-line polyolefin film texturing process by an exposition to low-toxicity and low-volatility solvents.

RESUME

Les matières plastiques sont aujourd'hui majoritairement produites pour l'industrie de l'emballage, avec un temps de vie très court, inférieur à une année. La production de masse de tels objets génère de nombreux déchets, qui se doivent d'être recyclés au maximum pour réduire à la fois le volume de déchets finaux et la quantité de ressources fossiles nécessaire à leur production. En intégrant aux emballages plastiques des matériaux aux propriétés superhydrophobes, mimant « l'effet lotus », leur souillage par le contenu qu'ils protègent pourrait être évité, favorisant leur recyclage et offrant au consommateur l'accès à l'intégralité du produit qu'il a acheté. Pour arriver à de telles propriétés sur des matériaux à faible valeur ajoutée, des voies de texturation simples de thermoplastiques hydrophobes comme le polyéthylène haute densité (HDPE) ou le polypropylène (PP) ont été étudiées. Après une étude des moyens présentés dans la littérature scientifique permettant d'accéder à la superhydrophobie, une compréhension des mécanismes de mouillage a été réalisée, grâce à une modélisation de la stabilité d'une interface de type Cassie-Baxter. Grâce aux lignes-guide établies à l'aide de ce modèle, des voies simples de texturation ont été étudiées : texturation par ajout de charge, par réalisation de mélanges de polymères immiscibles, par moussage par voie CO₂ supercritique, ou par moussage en extrusion. Malgré la génération de surfaces texturées, aucune de ces approches n'a permis d'atteindre la superhydrophobie. En revanche, l'exposition de thermoplastiques à des solvants à haute température a permis de générer des surfaces texturées superhydrophobes. Ce procédé a été développé et ses mécanismes étudiés afin de fournir *in fine* un procédé de texturation en ligne de films de polyoléfines par exposition à des solvants peu toxiques et peu volatils.

REMERCIEMENTS

Je souhaiterais commencer par remercier les membres du jury chargés d'évaluer mes travaux de thèse, en particulier Messieurs Laurent Billon et Yves Grohens, en leur qualité de rapporteurs, ainsi que Madame Cécile Gourgon et Monsieur Vincent Roucoules, examinateurs. Merci à eux pour leur temps consacré à la lecture de ce manuscrit, mais aussi pour les discussions intéressantes qui ont suivi la défense de cette thèse.

Je remercie également le Groupe Total et l'ANRT pour le financement de ce projet de recherche.

Merci à mes encadrants académiques, Jannick Duchet-Rumeau, Jean-François Gérard et Sébastien Livi, pour leur accompagnement pendant ces trois années de thèse. Je leur suis reconnaissant de la confiance qu'ils m'ont accordé sur ce projet, des conseils qu'ils m'ont prodigués, et de leur bienveillance.

Merci à Olivier Lhost, qui a suivi de près ces travaux de recherche pour le Groupe Total, pour toutes les discussions enrichissantes que nous avons pu avoir, ainsi que pour son accueil et son enthousiasme. Je remercie également Yves Trolez pour son intérêt envers ces travaux.

Mes remerciements vont aussi envers tous les membres du laboratoire Ingénierie des Matériaux Polymères, pour leur accueil et pour toutes les discussions, techniques ou non. Tous les membres du laboratoire, permanents ou de passage, contribuent à faire de cette structure un environnement de travail agréable et stimulant. Merci en particulier à Isa et Mallou pour leur aide précieuse au secrétariat, et pour leur gentillesse. Merci aux personnes qui ont pu m'appuyer directement dans mes travaux de recherche, en particulier Pierre Alcouffe et Benjamin Fornacciarri pour la microscopie, et Guilhem, Vivien, Laura, Raph et Ahmed dans le quotidien du laboratoire.

Je remercie également tous les doctorants, post-doctorants, ingénieurs de recherche, ou stagiaires, pour les bons moments passés ensemble au laboratoire, mais aussi en dehors, que ce soit à l'occasion de grands week-ends, ou plus simplement autour « d'une » bière en fin de journée. Merci à tous mes co-bureaux successifs, Amélie, Emilie et Mickael qui m'ont accueilli à l'IMP, Emma, Marc, Jérémy, et David dans nos bureaux successifs, ainsi que toutes les plantes qui nous accompagnaient (RIP Willy et Scarlett). Merci aussi à Laetitia, Ricardo, et Asja pour les cafés et les débats enflammés du midi. Merci à mon dernier co-bureau David (bis) pour l'art de la rhétorique et le goût de la polémique. Merci aussi à Amélie, Valentina, Adrien et Victor pour avoir ouvert leur bureau à mes pauses caféinées, et pour leur bonne humeur rayonnante ! Merci à Mélissa pour avoir accepté si souvent de m'entendre râler, et pour son amitié. Merci aussi à Amel pour les joutes verbales, merci à Xavier pour les logos, merci à Liuyin pour son énergie, merci à Martin pour sa bonne humeur, merci au Liban pour Raymond, merci à Hubert et Anatole pour leur **imp**étuosité ... et merci à tous les autres aussi !

Je terminerai en remerciant mes amis et ma famille pour leur soutien pendant cette thèse, mais aussi bien avant, et je l'espère encore longtemps après.

GENERAL SUMMARY

General introduction	2
Chapter 1 – Bibliographic Study	6
I. Surface tension and wettability	8
I.1. Surface tension: Basic features	8
I.2. Static wetting of a liquid on a smooth solid surface	9
I.3. Dynamic wetting: Moving a liquid on a smooth solid surface	10
I.4. Conclusion	11
II. Wettability of a rough surface: to superhydrophobicity and beyond	12
II.1. Complete wetting	12
II.2. Partial wetting	13
II.3. Complete or partial wetting: Definition of superhydrophobicity	14
II.4. Cassie-Baxter’s interface stability	15
II.5. Conclusion	18
III. How to obtain superhydrophobic or even superomniphobic surfaces?	19
III.1. Reduction of surface energy	19
III.2. Processed textures	21
III.3. Isotropic textures	25
III.3.a. Texturation followed by surface tension lowering	25
III.3.b. Use of hydrophobic particles	28
III.3.c. “Self-texturation” of polymers	35
III.4. Conclusion	43
IV. Chapter conclusion	44
V. References	46
Chapter 2 – Designing superhydrophobic surfaces	52
I. Literature Review	54
I.1. Wenzel’s and Cassie-Baxter’s wetting regimes balance	54
I.2. Effect of asperities size	55
I.3. Role of multi-scale roughness	56
I.4. Re-entrant asperities	58
I.5. Conclusion: Definition of an ideal superhydrophobic surface	59
II. Modeling superhydrophobicity as easily as possible	60
II.1. Model definition	60
II.2. Application to model surfaces	62
II.3. Conclusion	67
III. Confronting the model to the reality	68
III.1. Patterned and isotropic surfaces	68
III.2. Critical pressure prediction	69
III.3. Conclusion	71
IV. Chapter conclusion	72
V. References	73
Chapter 3 – Exploring simple texturing methods to reach superhydrophobicity	76
I. Review of relevant routes to produce textured surfaces	79
I.1. Texturing using particles	79
I.1.a. Particles deposition on the surface	79
I.1.b. Particles dispersed in the bulk	80
I.2. Porous membranes and foams	81

I.2.a.	Removing a phase of an immiscible polymer blend	81
I.2.b.	Foaming a thermoplastic using supercritical CO ₂	81
I.2.c.	Using blend interfaces to enhance foam nucleation	83
I.3.	Conclusion	84
II.	Materials and methods	85
II.1.	Materials	85
II.2.	Processing techniques	86
II.2.a.	Processing polymer blends	86
II.2.b.	Sc-CO ₂ foaming	87
II.2.c.	Blown-film extrusion	88
II.3.	Characterization methods	88
II.3.a.	Scanning Electron Microscopy	88
II.3.b.	Surface roughness measurements	89
II.3.c.	Wettability measurements	89
III.	Texturing from fillers	90
III.1.	Classical fillers	90
III.2.	Glass microspheres	92
III.3.	Organic particles	94
III.3.a.	PTFE microparticles	94
III.3.b.	UHMWPE particles	94
III.4.	Conclusion	96
IV.	Immiscible polymer blends	97
IV.1.	Polyethylene / polyethyleneoxide immiscible blend	97
IV.2.	Filled PE/PEO immiscible blend filled based on hydrophilic silica	99
IV.3.	Filled HDPE/PEO immiscible blend based on hydrophobic silica	100
IV.4.	Filled HDPE/PEO immiscible blends based on PTFE microparticles	101
IV.5.	Conclusion	103
V.	Batch foaming using supercritical carbon dioxide	104
v.1.	Foaming HDPE and PP with Sc-CO ₂	104
V.1.a.	Influence of the foaming temperature	104
V.1.b.	Influence of the depressurization rate	107
V.1.c.	Influence of fillers as nucleating agents	108
V.2.	Foaming immiscible polymer blends	112
V.2.a.	Polypropylene / polystyrene immiscible blend	112
V.2.b.	Polypropylene / polyethylene immiscible blend	114
V.3.	Conclusion	116
VI.	Continuous foaming process (extrusion)	117
VI.1.	Blowing agents	117
VI.2.	Extrusion of polyethylene foams	120
VI.2.a.	Influence of the CBA loading	120
VI.2.b.	Influence of the CBA compound	122
VI.2.c.	Influence of the nucleating agents	123
VI.2.d.	Extruding a HDPE foam with a high matrix viscosity	124
VI.3.	Conclusion	126
VII.	Chapter conclusion	127
VIII.	References	129
Chapter 4 – Thermoplastic texturing by solvent-induced reorganization		132
I.	Texturing a polymer by a solvent exposure	135
I.1.	Texturing HDPE surfaces with xylene	135
I.1.a.	Immersing HDPE in hot xylene	135
I.1.b.	Multiple baths immersion of HDPE in xylene	136

I.1.c.	Final process for texturing HDPE surfaces	138
I.2.	Applying the developed process to various polyethylene grades and polypropylene	139
I.2.a.	Influence of HDPE grade	139
I.2.b.	Impact of the polymer nature: texturing PP	140
I.2.c.	Influence of the presence of fillers in HDPE	142
I.3.	Resulting wettability	143
I.3.a.	Wettability predictions	143
I.3.b.	Water wettability	145
I.3.c.	Textured surface wetting by low surface tension liquids	146
I.4.	Conclusion	148
II.	Use of less-toxic solvents for surface texturing	149
II.1.	Solvents selection	149
II.2.	Processing HDPE and resulting surface textures	150
II.2.a.	Dipentene	150
II.2.b.	α -pinene	151
II.2.c.	Decane	151
II.2.d.	Paraffin wax	152
II.2.e.	Olive oil	153
II.2.f.	Summary of the texturing conditions and resulting wettability	155
II.3.	Application to PP and resulting surface textures	156
II.3.a.	Dipentene	156
II.3.b.	α -pinene	157
II.3.c.	Decane	158
II.3.d.	Olive oil	159
II.3.e.	Summary of the texturing conditions and resulting wettability	159
II.4.	Towards simplification for scale-up	161
II.4.a.	One-bath texturing of HDPE films	161
II.4.b.	One-bath texturing of PP films	164
II.4.c.	Continuous texturing proof-of-concept	167
II.5.	Conclusion	170
III.	Understanding the texturing mechanisms	171
III.1.	Texturing from crystallization/precipitation	171
III.1.a.	Expected mechanisms	171
III.1.b.	Investigating the solvent-assisted crystallization of HDPE and PP	173
III.1.c.	Investigating the crystallization-induced precipitation	175
III.2.	Influence of solvent nature and temperature	178
III.2.a.	Crystallization temperature and surface morphology	178
III.2.b.	Polymer/solvent solubility considerations	179
III.3.	Conclusion	181
IV.	Chapter conclusion	182
V.	References	184
	<i>General conclusion and perspectives</i>	186
	<i>Annexes</i>	190
I.	Tables of Figures	191
I.1.	Figures	191
I.2.	Tables	201

GENERAL INTRODUCTION

The production of polymer resins, which are usually called “plastics” even if they are thermoplastics, thermosets or elastomers, keep growing almost exponentially since the discovery of Bakelite in the early 20th century, as illustrated by Figure 1 that depicts the yearly global plastics production from 1950 to 2015. However, it was after world war II that the worldly plastic production and consumption started to really rise, with their use in consumer goods for their lightness, cheapness and aesthetic qualities. But the main use of plastics is for packaging, with about 45% in weight of all plastics produced in 2015 dedicated to this sector¹ (Figure 2). And the main drawback of plastics used for packaging is that they are single-use objects, with an average lifetime of half a year between their production and they wasting. If these materials are very useful for preventing food spoiling or contamination during its transport and distribution, their mass production and spread consumption rise difficulties for their life end.

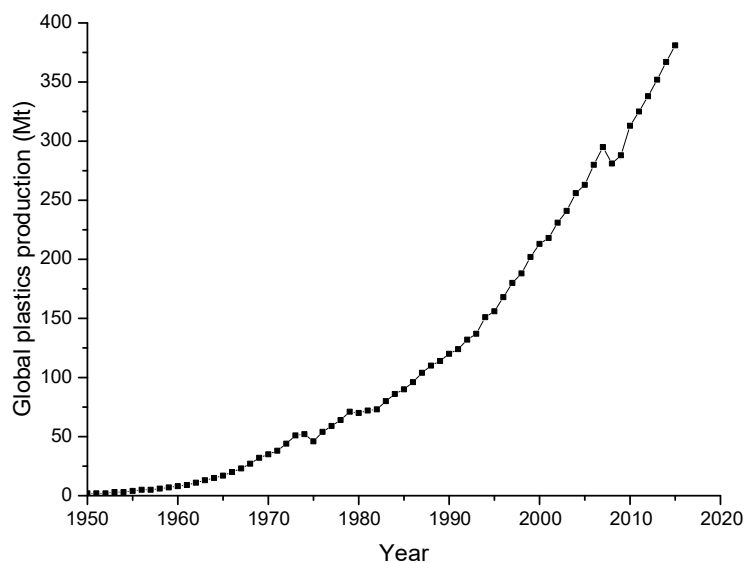


Figure 1 – Global plastic production per year from 1950 to 2015, in megatons, based on data from Geyer *et al.*².

Geyer *et al.*¹ estimated that between 1950 and 2015, 8'300Mt of plastics have been produced as polymer resins, fibers or additives. They estimated that in 2015, 2'500Mt was still in-use, 4'900Mt have been simply discarded, 800Mt have been incinerated and only 600Mt have been recycled at least once (The total of these values exceeds 8'300Mt as 500Mt of recycled plastics have then be recycled again, incinerated or discarded). The discarded plastics finish their life in landfills or even in the rivers and then in the oceans. The incineration of plastic wastes produces energy, and keep the wastes out of the environment, and can be seen as a way of valorizing “second-hand” petrol. But recycling goes further in the revalorization process with the reuse of plastic objects, polymer resins or monomers, thus limiting the need of fossil fuels for the global plastic production. If petrol-based production will always be necessary in a growing production as nowadays experienced, the incorporation of more and more recycled materials and feedstocks will reduce the amount of discarded wastes while limiting the exposition of the plastic industry to petrol. In the same time, consumers of rich countries have more and more expectations on the plastics packaging they use, with a pressure to benefit from recycled products in a spirit of waste reduction. For all these reasons, the players of the plastic industry as well as their clients that transform these plastics into packagings for their products are looking for more sustainable materials, that would be easily recyclable. When looking at the distribution of the polymers used in the packaging industry (Figure 2), only four types of polymers constitute 92% in weight of the total: low-density polyethylene (LDPE) and linear low-density polyethylene (LLDPE), polyethyleneterephthalate (PET), high-density polyethylene (HDPE) and polypropylene (PP).

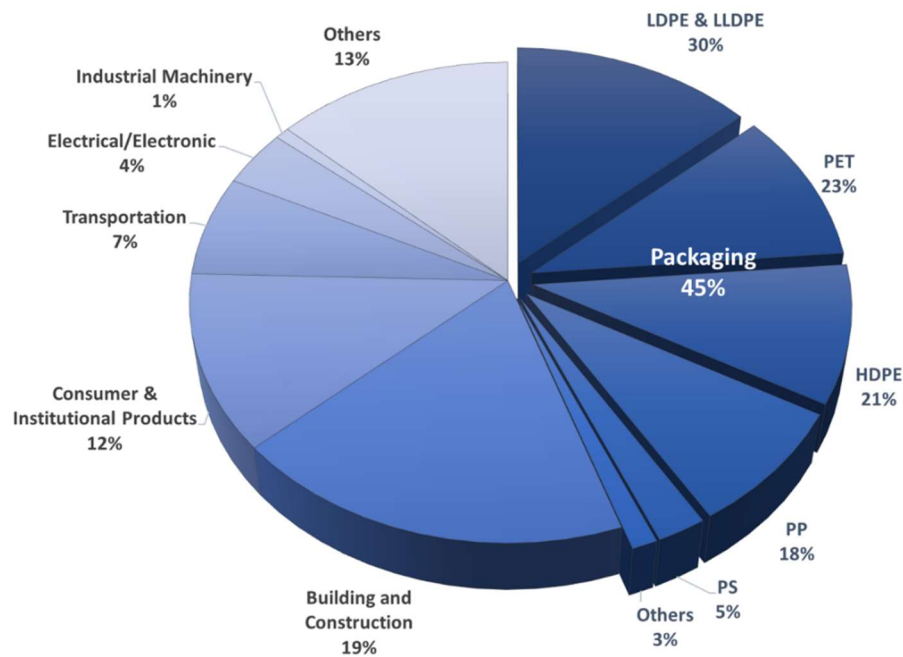


Figure 2 – Shares of total polymer resin production depending on their use, with a detail of the polymer resins nature used in the packaging industry in 2015, based on data from Geyer et al.².

For recycling plastic packaging products, they have to be cleaned from the product they were protecting, that could soil it. Developing new materials that could repel the product that it contains, like lotus leaves repel water (Figure 3a), will make easier the recycling of plastic packaging by reducing their soiling. Moreover, with such materials the content loss due to product stuck in the packaging would be reduced, for the greater benefit of the consumer. The “lotus effect” is called superhydrophobicity, and is characterized by a very low adhesion of liquid water on a given surface. The lotus leaves are rough surfaces, as illustrated by Figure 3b which is a SEM observation of such leaf, and most artificial superhydrophobic surfaces involve both intrinsic hydrophobicity and roughness, mimicking the lotus leaf.

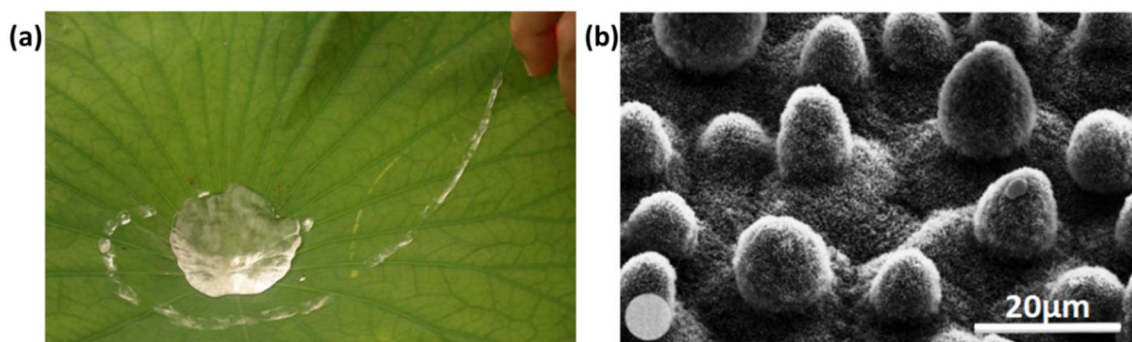


Figure 3 – The « Lotus effect »: the superhydrophobicity of the lotus leaves, (a) illustrated by a photography, (b) with the corresponding surface roughness observed by SEM. (b) is reprinted from³, Copyright 1997 Springer.

In addition to this anti-fouling property, superhydrophobicity is also useful for self-cleaning surfaces, oil-water separation, drag reduction for ships, anti-corrosion, etc. Thanks to all these interesting properties, superhydrophobicity is a largely studied topic with a growing interest in the last decade, as shown by the major increase of yearly published articles since 2005 to nowadays (Figure 4). Still, all mechanisms behind superhydrophobicity are not yet fully understood, and new ways to obtain surfaces with such properties are regularly getting reported.

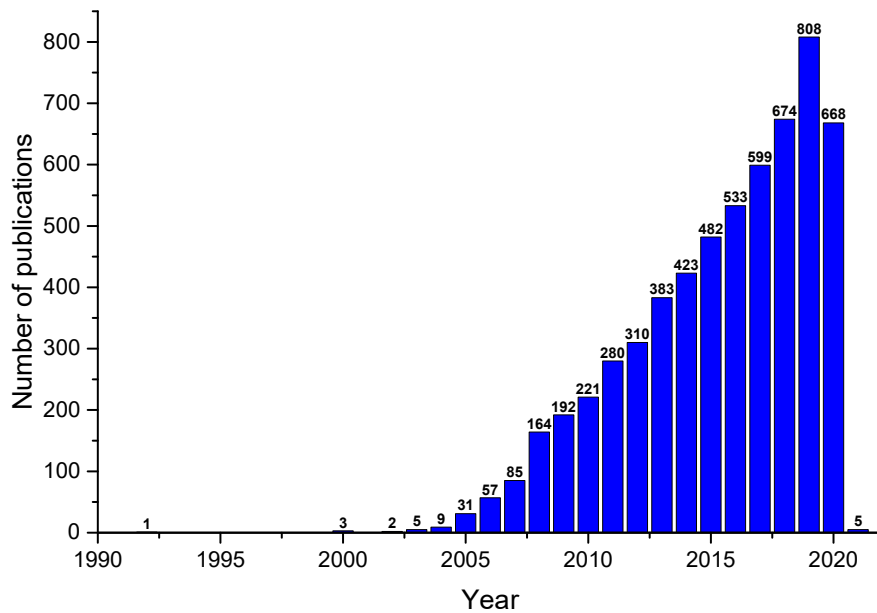


Figure 4 – Number of publications per year on the topic “superhydrophobicity”, based on Web of Science database analysis realized on December 2020.

The goal of the current research project, sponsored by the Total company, is to find easy ways of producing superhydrophobic thermoplastics surfaces for a use as packaging materials. This goal will be pursued by seeking a texturing of hydrophobic thermoplastics such as polyethylene and polypropylene, ideally without changing the materials transformation processes. As Total is a polymer resins manufacturer, it does not have all the liberty of changing processes in their client’s factories. The solution that will be searched need to acknowledge this particularity, by developing solutions coming from the materials, and suitable to typical transformation processes. The polymers of interest are mainly HDPE and PP, as they are the most used resins for the aimed packaging applications, in particular bottles for cosmetics. Because of the will to adapt such materials to contents such as cosmetics or food, the developed material should be suitable for food-contact. Moreover, product end-life might be taken into account when developing solutions. All these reasons led to the strategy of testing commercial grades of HDPE or PP resins from the Total company using new and simple ways.

In the first chapter of this thesis manuscript, an introduction on superhydrophobicity will be done, followed by a quick review of some existing ways of turning a surface superhydrophobic. In the second chapter, the question of how a surface need to be textured to be superhydrophobic will be tried to be answered, through a review of existing models and the development of a simple geometrical model. Using the guidelines offered by the model developed in the second chapter, the third chapter will describe the prospection of new ways of texturing a thermoplastic surface seeking superhydrophobicity, and the last chapter will describe a successful texturing process using various solvents through precipitation and crystallization of polymers.

References

1. Geyer, R., Jambeck, J. R. & Law, K. L. Production, use, and fate of all plastics ever made. *Sci. Adv.* **3**, 25–29 (2017).
2. Geyer, R., Jambeck, J. R. & Law, K. L. Production, use, and fate of all plastics ever made. *Sci. Adv.* **3**, 19–24 (2017).
3. Barthlott, W. & Neinhuis, C. Purity of the sacred lotus, or escape from contamination in biological surfaces. *Planta* **202**, 1–8 (1997).

CHAPTER 1 – BIBLIOGRAPHIC STUDY

Bibliographic study

I.	Surface tension and wettability	8
I.1.	Surface tension: Basic features	8
I.2.	Static wetting of a liquid on a smooth solid surface	9
I.3.	Dynamic wetting: Moving a liquid on a smooth solid surface	10
I.4.	Conclusion	11
II.	Wettability of a rough surface: to superhydrophobicity and beyond	12
II.1.	Complete wetting	12
II.2.	Partial wetting	13
II.3.	Complete or partial wetting: Definition of superhydrophobicity	14
II.4.	Cassie-Baxter's interface stability	15
II.5.	Conclusion	18
III.	How to obtain superhydrophobic or even superomniphobic surfaces?	19
III.1.	Reduction of surface energy	19
III.2.	Processed textures	21
III.3.	Isotropic textures	25
III.3.a.	Texturation followed by surface tension lowering	25
III.3.b.	Use of hydrophobic particles	28
III.3.c.	"Self-texturation" of polymers	35
III.3.c.i.	Precipitation/crystallization of polymers from solutions	35
III.3.c.ii.	Original processes	41
III.4.	Conclusion	43
IV.	Chapter conclusion	44
V.	References	46

In this first chapter, superhydrophobicity origin will be discussed for a better understanding, before answering the following question in the second chapter: How to effectively design a superhydrophobic surface? The fundamental wettability principles will be discussed in this chapter, and different approaches to obtain superhydrophobic surfaces will be reviewed. Three major way of designing superhydrophobic surfaces will be detailed: Reducing the surface energy, producing tailored texture, or producing isotropic textures. This review will help understanding the needed properties for a stable superhydrophobic surface, thus helping in defining design guidelines.

I. Surface tension and wettability

I.1. Surface tension: Basic features

Before discussing wettability, it is crucial to clearly define surface tension and surface energy. Atoms and molecules at the surface of a substance have less neighbors than the ones in the bulk to share energy with, through metallic, ionic, or covalent bonds (Figure 5a). This lack of neighbors leads to a different force balance between surface and bulk atoms or molecules. The surface energy will thus be higher for atoms with a large inter-atoms or inter-molecules energy. That is why ceramics (as a material or as a passivation layer of some metals) with ionic bounds, and metals with metallic bounds, have higher surface energy than polymers which involves Van Der Waals interactions. For example, surface energy values goes from 1,240mJ/m² for silicon and 230mJ/m² for calcium carbonate to 36,1mJ/m² for polyethylene and up to 22,5mJ/m² for polytetrafluoroethylene^{1,2}.

According to the Owens-Wendt theory³, the surface energy can be divided into a dispersive and a non-dispersive parts. The dispersive part corresponds to London instantaneous dipoles interactions, and the non-dispersive part, corresponds to permanent dipoles interactions and hydrogen bonding (Keesom, Debye and H-bonds interactions). For example, water has a surface energy of 72,8mJ/m² composed of a dispersive part of 21,8mJ/m² and a non-dispersive part of 50,0mJ/m², while diiodomethane has a surface energy of 50,8mJ/m² composed of a dispersive part of 49,5mJ/m² and a non-dispersive part as low as 1,3mJ/m².³

As nature always tends to lower the energy of a system, the surface energy must be consequently minimized. To pursue this objective, a substance has to maximize its average number of neighbors per unit, through lowering surface atoms or molecules (which have few neighbors) and increasing bulk ones (which have maximum neighbors). For solids, no active strategy exists to lower their surface energy, but higher reactivity of surface atoms might lead to chemical modifications. As gas have very few neighbors and no defined surface, their surface energy is often considered neglectable when comparing to liquids and solids. On the opposite, fluids can change their shape and lower their volume on surface ratio, thus reducing their surface energy. That is why a liquid will self-organize into a perfect sphere in absence of external constraint, because of the lowest surface on volume ratio of such a shape.

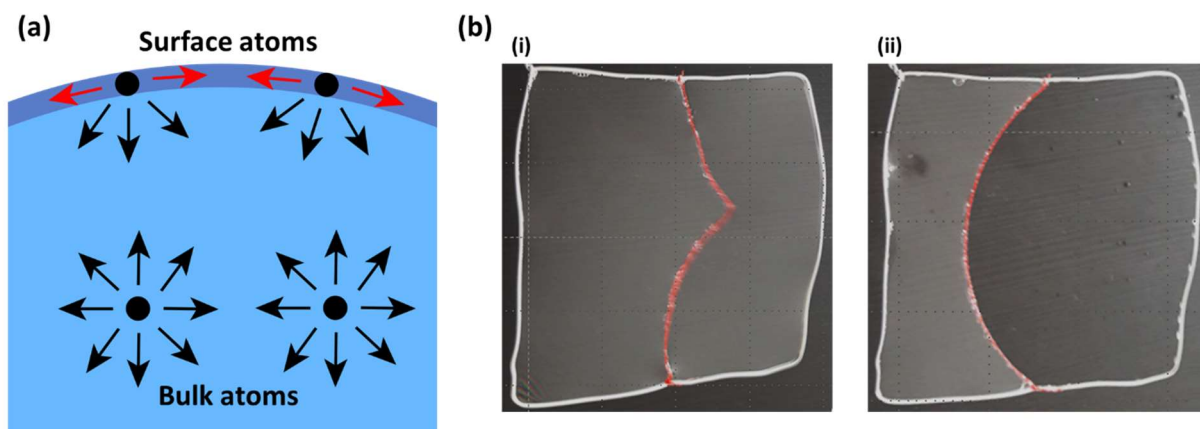


Figure 5 – Surface energy and surface tension of liquids. (a) Molecular origin of surface energy: schematic representation of atoms or molecules in the bulk and at the surface and their interactions with neighbors. (b) Soap bubble and string trick: (i) equilibrated water and soap solution films separated by a string, and (ii) rupture of equilibrium by removing of a film: the remaining film minimizes its surface by pulling on the string.

This minimization of the surface of a liquid in order to decrease the system energy produces a force, in the shape of a tension on the surface. This tension can be easily highlighted with the well-known soap bubble and string trick: a string is attached across a frame that are immersed in a water and soap

solution. The obtained solution films are at equilibrium with the string arbitrarily placed between them (Figure 5b.i). This equilibrium is broken by puncturing one the films: the system minimizes its energy by reducing the surface of the remaining solution film and thus pulling the string (Figure 5.ii). The force applied by the solution to the string to lower its surface is the so-called surface tension, expressed in N/m. It must be noted that this force also applies on the frame, which is too strong to be noticeably deformed. Surface tension and surface energy are equivalent (with $1 \text{ J/m}^2 = 1 \text{ N/m}$) and surface tension is often used when considering physico-chemical properties of liquids, such as wettability.

The surface tension of liquids is at the origin of the Laplace pressure. As previously mentioned, a liquid will self-organize into a round drop in absence of external constraint, and the surface tension will still tend to reduce this surface. This results in a higher pressure in the liquid drop than outside, following Eq. 1 with P_{in} and P_{out} the pressures inside and outside the drop, γ the surface tension and H the curvature of the interface.

$$P_{in} - P_{out} = 2\gamma H \quad \text{Eq. 1}$$

This assumption is however only valid for droplets much smaller than the capillarity length, given by Eq. 2. For larger drops, gravity forces will become larger than the surface tension forces, resulting in a pressure governed by hydrostatic instead of surface tension mechanisms.

$$l_c = \sqrt{\frac{\gamma}{\rho g}} \quad \text{Eq. 2}$$

1.2. Static wetting of a liquid on a smooth solid surface

As previously discussed, a system always tends to lower its energy until stability. For a liquid without external constraints, it leads to a round shape to minimize the surface on volume ratio. But what happens when a liquid is in contact with a solid? Both solid and liquid have surface tension to minimize, and only the liquid can move and rearrange. The system energy will thus be reduced thanks to the deformation of the liquid in contact with the solid. The round shape of the liquid will be conserved, but will be more or less “attached” to the solid, depending on their respective surface tension. The morphology of such a system can be predicted using Young’s Eq. 3⁴, with γ_{SG} , γ_{SL} and γ_{LG} corresponding to the interfacial tensions of solid/gas, solid/liquid and liquid/gas interfaces, respectively.

$$\cos \theta_Y = \cos \left(\frac{\gamma_{SG} - \gamma_{SL}}{\gamma_{LG}} \right) \quad \text{Eq. 3}$$

The solid/liquid interfacial tension depends on the affinity between the solid and the liquid, and will result in different liquid drop shapes (Figure 6). Wetting behaviors give various name to the corresponding surface, in particular when water is the liquid. For example, a liquid with a Young’s contact angle lower than 90° is denoted as “hydrophilic” from the Greek *hydro*, water, and *phileo*, love: that loves water (Figure 6a). If the Young’s contact angle is larger than 90° , the solid is denoted as “hydrophobic” from *phobos*, fear: that is afraid of water (Figure 6b). There are also extreme limits of these two behaviors, with the prefix “super”: superhydrophilicity, with a complete wetting of the solid by the liquid, characterized by a contact angle close to zero (Figure 6c), and superhydrophobicity characterized by a very low wetting of the solid, *i.e.* a water contact angle larger than 150° (Figure 6d).

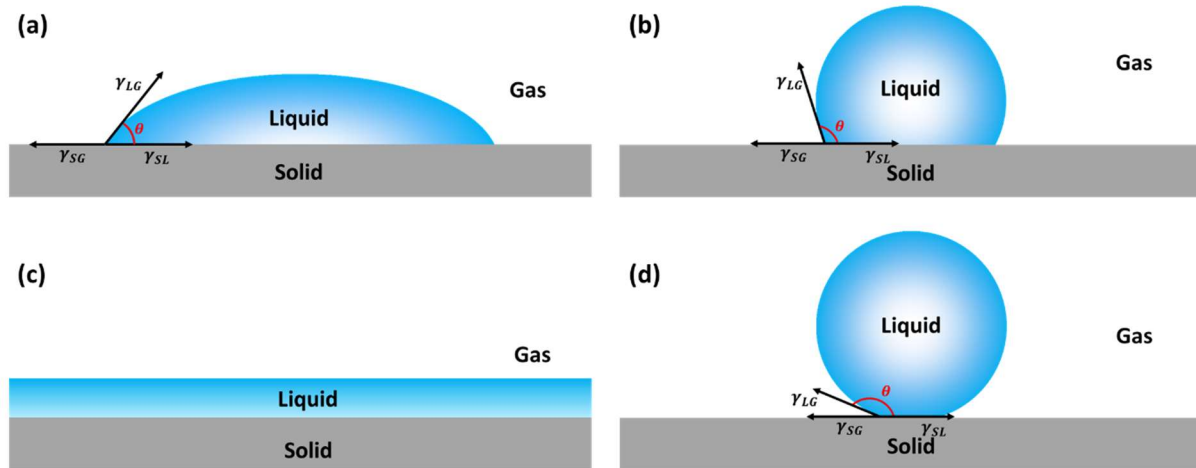


Figure 6 – Various wetting regimes of a solid by a liquid. As water is the liquid, solids with those wetting are denoted as (a) hydrophilic, (b) hydrophobic, (c) superhydrophilic, (d) superhydrophobic.

These names can be extended to other liquids changing the *hydro* part by suitable name such as *oleo* or *lipo* for oily liquids, *amphi* for both oil and water, or even *omni* or *hygro* for all types of liquids⁵. Terminology of surfaces with various wetting regimes will be discussed later.

1.3. Dynamic wetting: Moving a liquid on a smooth solid surface

After having described the static wettability of a liquid onto a solid surface, what happens when external forces are applied to move the liquid on the surface?

When talking about displacement of a liquid on a solid surface, it is in reality the moving of the triple line that is concerned. The triple line corresponds to the three-boundary zone where solid, liquid, and gas coexist. For example, the movement of the liquid can come from gravity with an inclined solid surface. As seen in Figure 7, when a liquid drop rolls on an inclined solid surface, the contact angle in front of the drop (at the advancing edge) is larger than the contact angle at the rear of the drop (at the receding edge). The same observation can be made in everyday life when observing water drops rolling on a window.

This difference of contact angle from advancing and receding edges can be explained by considering the energy needed to wet and dewet a solid. When a liquid drop advances on a solid, a new solid/liquid area is created in place of the previous solid/gas area at the front edge. At the rear edge, the opposite happens: a solid/liquid area is replaced by a solid/gas interface. Replacing a solid/gas interface by a solid/liquid interface is exoenergetic, and the opposite is logically endoenergetic. Makkonen⁶ pointed out that the energy released by the advancing edge could be equal to the energy needed for dewetting of the receding edge. This allows the wetting of a new surface area to power the dewetting on the receding side. However, the surface tension being precisely a surface property, it cannot store energy and thus transfer it to the opposite edge. In order to move a liquid droplet on a solid surface, energy must be given to the system because of the receding edge. This energy can come from gravity on an inclined plane, or from a mechanical stimulus.

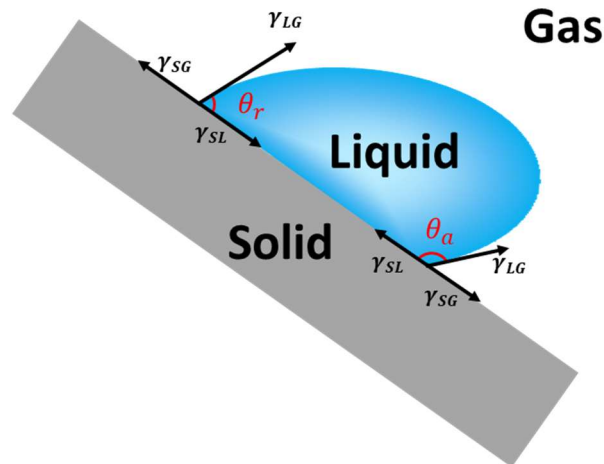


Figure 7 – Schematic representation of a liquid drop rolling on an inclined solid “phobic” surface

The equilibrium at the advancing edge is given by Eq. 4. As the advancing contact angle is the only free parameter of this equilibrium equation, the advancing contact angle has to be larger than the Young CA, in order to compensate the energy liberated by the newly created solid/liquid surface.

$$\gamma_{SL} = \gamma_{LG} (\cos \theta_Y - \cos \theta_a) \quad \text{Eq. 4}$$

The receding edge is then fueled by surface tension that pulls the triple line. In order to move the receding triple line, Eq. 5 must be equilibrated. As the receding contact angle is the only free parameter, it will decrease in order to let the liquid surface tension contribute to the motion.

$$\gamma_{SG} = \gamma_{LG} (\cos \theta_r - \cos \theta_Y) \quad \text{Eq. 5}$$

The difference of advancing and receding contact angle is called contact angle hysteresis and is usually denoted as $\Delta\theta$ or H . It reflects the ability of the liquid to easily move on the solid. A liquid wetting a solid with a high hysteresis will be hard to remove, whereas a liquid wetting a solid with low hysteresis results in an easy rolling-off, as water on a lotus leaf.

I.4. Conclusion

In this part, the surface energy of a liquids and solids have been defined based on the bonding energy of its constituents. This explains why a polymer has a lower surface energy than a ceramic or a metal. The Young’s contact angle has been introduced, as the angle of a given liquid on a perfectly smooth solid, reflecting their affinity.

Four wetting regimes have been described based on water wettability: superhydrophilicity, hydrophilicity, hydrophobicity, and superhydrophobicity.

The dynamic contact angles have been described as the advancing and receding contact angles, and the hysteresis, *i.e.* the difference between them, which come from the adhesion of the liquid to the solid.

II. Wettability of a rough surface: to superhydrophobicity and beyond

II.1. Complete wetting

Natural or artificial surfaces are rarely perfectly smooth and their wettability might be impacted by their texturing. When a liquid completely wets a textured surface, the resulting morphology (Figure 8a) is called the Wenzel's state. Robert Wenzel described this kind of wetting behavior in 1936⁷. In such a state, the solid/liquid interface has the same area as on a smooth surface, but on a tinier scale, because of the texturing. In these conditions, the apparent contact angle increase or decrease with the texturing is given by Eq. 6. The apparent contact angle depends on the "philic" or "phobic" property of the solid, *i.e.* its physico-chemical nature. θ_W is the Wenzel's apparent contact angle, r_W the roughness (defined as the real surface area divided by the projected area), and θ_Y is the Young's contact angle.

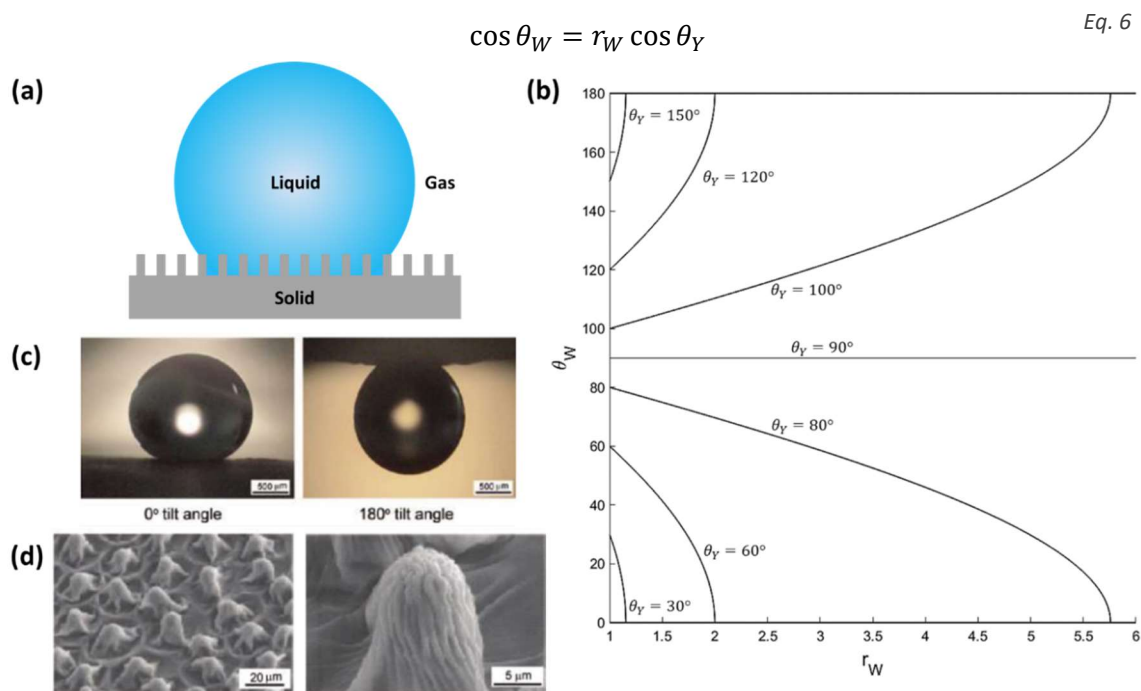


Figure 8 – Wenzel's state wetting of a liquid on a textured solid: (a) schematic representation of a "phobic" textured surface fully wetted by a liquid and (b) computed Wenzel's contact angle depending on intrinsic Young contact angle and roughness. (c) water droplet pinned on a Rosa Bairage and (d) corresponding surface texture observed by SEM. (c) and (d) are reprinted from⁸, Copyright 2010 American Chemical Society

When a textured solid surface is wetted by a liquid such as water in a Wenzel's state, its behavior could be exacerbated to a "super" behavior. In fact, if the solid is intrinsically hydrophilic, the resulting textured surface will tend to superhydrophilicity with a complete spreading of the drop. On the opposite, if the solid is intrinsically hydrophobic, the resulting textured surface will tend to superhydrophobicity with a water contact angle up to 180° (Figure 8b). Observing that chart, it is obvious that a poorly hydrophobic material needs a high roughness to reach superhydrophobicity. In the same time, a hydrophilic material could never be superhydrophobic according to the Wenzel's equation. Increasing the roughness of a hydrophilic surface would only lead toward superhydrophilicity.

The Wenzel's state is also characterized by very large contact angle hysteresis values, especially with high roughness and thus high contact angle values. A drop in a Wenzel's state is pinned into the texture because of the large interface area to wet and dewet in a tiny scale length. Such stickiness of a drop to a textured surface can be observed in nature on rose petals⁸ (Figure 8c-d) or with water-capturing insects like the desert beetle⁹, that uses this stickiness to collect condensed water vapor.

II.2. Partial wetting

When a liquid comes in contact with a textured surface, it may not fully wet the asperities. In some conditions that will be detailed later, the liquid can be held on top of the asperities and then sits on air like on a fakir carpet (Figure 9a). In such a particular wetting regime, surface tension prevents the liquid from going between asperities, *i.e.* resulting in a Wenzel's state. Such wetting morphology is denoted as the Cassie-Baxter's state¹⁰. For Cassie and Baxter, the apparent contact angle increases with air fraction at the interface, as water, and liquids in general, do not wet gas. The resulting interface area composed of only air has a virtual Young contact angle of 180°. They proposed Eq. 7, which averages the contact angle of the liquid with solid and gas, pondered by solid and gas fraction area f_S and f_G at the interface.

$$\cos \theta_{CB} = f_S \cos \theta_Y - f_G = f_S \cos \theta_Y + f_S - 1 \quad \text{Eq. 7}$$

When a liquid is standing on a textured surface in a Cassie-Baxter's state, its contact angle increases with gas fraction at the interface, as illustrated by Figure 9b. The gas fraction equal to 1 is a limit of the equation, as such state will not be a Cassie-Baxter's state but rather a liquid suspended in gas. This figure shows that every material could theoretically be turned superhydrophobic whatever its surface energy is, just by increasing the gas fraction at the interface in a Cassie-Baxter's state. However, stability criterions greatly limit this possibility and the higher the Young contact angle is, the better for both interface stability and high contact angle values. Detailed stability conditions of a Cassie-Baxter's state *versus* a Wenzel's state will be discussed later.

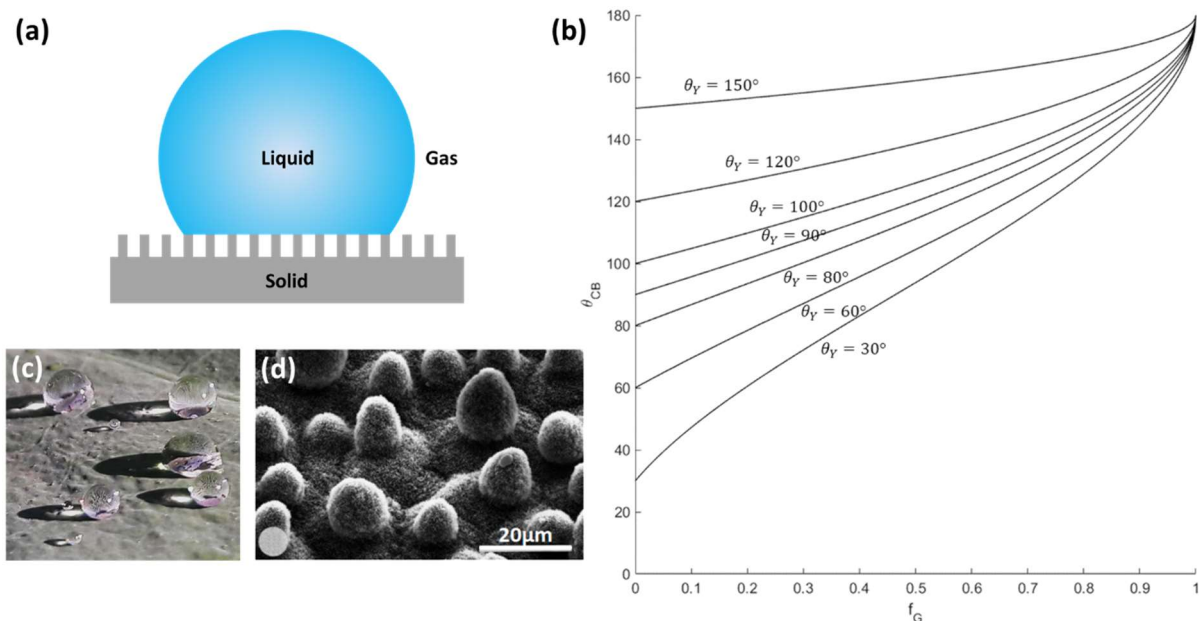


Figure 9 – Cassie-Baxter's partial wetting of a rough solid: (a) schematic representation of a "phobic" rough surface holding a liquid drop on top of its asperities and (b) computed Cassie-Baxter's contact angle depending on intrinsic Young's contact angle and gas (air) fraction at the interface. (c) water droplet on a lotus leaf and (d) corresponding surface texture observed by SEM. (d) is reprinted from¹¹, Copyright 1997 Springer Nature

The contact angle hysteresis of a liquid in a Cassie-Baxter's state is very low because of the lowering of the solid/liquid interfacial energy thanks to the large gas area at the interface. A low hysteresis traduces a low adhesion of a liquid drop to the textured surface, which then easily bounces and moves on the surface. However, Gao and McCarthy¹² demonstrated that contact angle and contact angle hysteresis does not result directly to the overall Cassie-Baxter's state interface but just to the interface at the triple line. They made different structures to investigate this point. A single smooth dot on a textured surface and a textured dot on a smooth surface. A water droplet was deposited on the dot, and then its volume was increased in order to be larger than the dot. When the triple-line of the drop

get out of the spot, contact angle would go from the dot's properties to the surface property. By doing so, they claimed: "How Wenzel and Cassie were Wrong". However, it must be noticed the surface has to be homogeneous to display such properties. So, in this case Wenzel's and Cassie-Baxter's models are still phenomenologically correct.

Low adhesion of liquids offers interesting properties to natural surfaces such as the well-known self-cleaning^{13,14} lotus leaf (Figure 9c-d) or the less-known springtail skin¹⁵, that repels low surface tension liquids such as ethanol or hexadecane. Numerous artificial surfaces have been created to mimic this behavior for drag reduction¹⁶, oil-water separation^{17,18}, anti-corrosion¹⁹, etc. and will be reviewed and discussed later.

Another way of achieving such properties is the use of Lubricant Impregnated Surface, known as LIS²⁰, LIPS, for Lubricant Impregnated Porous Surface²¹, or LESS, for Lubricant Entrenched Smooth Surface²². These surfaces aim to form a Cassie-Baxter's interface with a liquid but using a low surface tension liquid instead of gas, the immiscible low surface tension liquid acting as a lubricant. If such surfaces have interesting sliding properties and high pressure stability, possible contamination of the repelled liquid by the lubricant²³ and repellence selectivity (as immiscibility of the liquids is required) are strong limitations. As a consequence, such a lubricant-based approach will not be considered in this study.

II.3. Complete or partial wetting: Definition of superhydrophobicity

A surface is usually denoted as superhydrophobic if it exhibits a water contact angle larger than 150°. However, as previously discussed, different interface morphologies can lead to very different behavior in terms of liquid adhesion. However, superhydrophobicity is often associated to slippery behavior, considered for anti-fouling or self-cleaning properties. Thus, superhydrophobicity should be reserved to Cassie-Baxter's regime superhydrophobicity⁵, also denoted as slippery superhydrophobicity. Wenzel's superhydrophobicity can then be denoted as sticky superhydrophobicity. **For these reasons, superhydrophobicity will be defined as a surface exhibiting a water contact angle larger than 150°, with a hysteresis lower than 10°.**

If superhydrophobicity is an interesting property, repellence of other liquids with the same behavior is also of great interest. Such behavior with non-water liquids cannot be denoted as superhydrophobicity, even if they share the same properties. Repellence of liquids that are not water has traditionally been called superoleophobic²⁴, from the Latin *oleum*, oil, or superlipophobic from the Greek *lipo*, fats. But those liquids are not necessarily oil or fats, and oleophobicity has thus often been improperly used. The same goes with superamphiphobicity from the Greek *amphis*, of both sides, that could repel both water and oil, excluding liquids that are neither water nor oil. Some proposed to use superomniphobic, from the Latin *omnis*, all, that could repel anything. Marmur⁵ also proposed superhygrophobic, from the Greek *hygros*, wet, arguing that it refers to all liquids. However, as will be discussed later, a texture surface can rarely repel liquids of any surface tension. In fact, slippery behavior is often shown within a surface tension range, that goes from water (superhydrophobicity) to a chosen low surface tension liquid, that can be hexane²⁵, ethanol, etc.. It is thus impossible to have a single word for calling repelling surfaces beyond superhydrophobicity, and superomniphobicity or superhygrophobicity should be used. They could be completed by precisizing the lowest surface tension liquid they admit, meaning that they could repel all liquids with surface tension larger than that one. It must also be noted that superomniphobicity can only be reached with a Cassie-Baxter's interface, which is the only one that allows an increase of contact angle of liquids with low Young's contact angle values.

From now, Wenzel's and Cassie-Baxter's interfaces have been completely opposed. However, a mixed interface often exists in the shape of a Cassie-Baxter's interface with a partial Wenzel's wetting regime of the asperities (Figure 10). To account for this combination of the two models, roughness can be

added to the Cassie-Baxter's equation, leading to Eq. 8. Here, the roughness factor, r_S , refers to the roughness as defined by Wenzel, but only for the fully wetted area where a Wenzel's interface is established. When asperities are only top-wetted, $r_S = 1$ and the equation turns into the conventional Cassie-Baxter's one. When they are fully wetted, $f_G = 0$ and the equation turns into the Wenzel's one.

$$\cos \theta_{mix} = r_S f_S \cos \theta_Y - f_G \quad \text{Eq. 8}$$

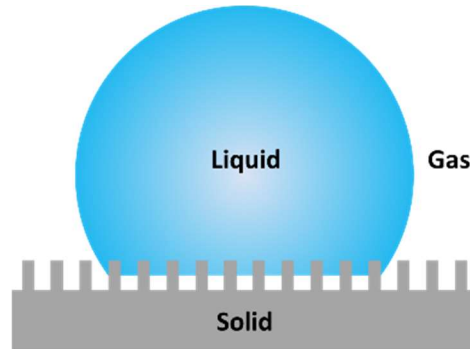


Figure 10 – Schematic representation of a Cassie-Baxter's and Wenzel's mixed interface

For hydrophobic materials, or more generally for solid/liquid couples with a Young contact angle larger than 90° , the texture and the air fraction work together in increasing the contact angle. Moreover, for regular pillars disposed as in Figure 10, the air fraction does not change with the liquid penetration depth. Hence, the more the liquid penetrates in the structure, the higher the contact angle is thanks to the combination of Wenzel's and Cassie-Baxter's behavior.

However, the combination of Wenzel's and Cassie-Baxter's wetting regimes is not favorable for slippery superhydrophobicity. The partial Wenzel's regime will govern concerning contact angle hysteresis, resulting in a sticky superhydrophobic surface. In order to keep a low adhesion of the liquid to the solid, the Wenzel's part has to be minimized, ultimately until a pure Cassie-Baxter's regime. Such a hybrid wetting regime can explain why some surfaces with a Cassie-Baxter's apparent interface, exhibit relatively high contact angle hysteresis.

Bico *et al.*²⁶ proposed a stability criterion for a Cassie-Baxter's state *versus* a Wenzel's state for a given surface texture. By comparing the Gibbs free energy of both interfaces using the interface solid fraction and the Wenzel's roughness, they proposed Eq. 9 for Cassie-Baxter's stability. The Young's contact angle has to be high enough to promote a Cassie-Baxter's state. The thermodynamically stable state will be the one which offers the smaller contact angle for a given texture. They also point out that for a Young contact angle between 90° and the value given by Eq. 9, a Cassie-Baxter's interface can exist in a metastable state. Based on Gibbs free energy calculations, Marmur²⁷ showed that a Wenzel's interface could always exist, in a stable or metastable state, as a condition of limit.

$$\cos(\theta_Y) < \frac{f_S - 1}{r_W - f_S} \quad \text{Eq. 9}$$

II.4. Cassie-Baxter's interface stability

The energy gap that has to be overpassed to go from a stable or a metastable Cassie-Baxter's state to a Wenzel's state can be considered as a threshold pressure, over which a Cassie-Baxter's interface will fully collapse into a Wenzel's state. Cui *et al.*²⁸ experienced this critical pressure with falling water drops on a superhydrophobic surface. Bouncing or pinning of a water drop falling from a given height depends on the critical pressure it can hold. They estimated the water-hammer pressure of their droplets of about 200kPa and compared this value with the capillary pressure of their surfaces. For this purpose, they used Eq. 10 where θ_a is the advancing contact angle and r the pore diameter of the

textured surface. They calculated a capillary pressure of about 300kPa, which is higher than the water-hammer pressure, explaining the bouncing of the water droplet. As capillary pressure increases with decreasing pore size, they suggested that the smaller the roughness scale, the higher the Cassie-Baxter's interface stability upon pressure.

$$P_c = \frac{-2\gamma_{LV} \cos(\theta_a)}{r} \quad \text{Eq. 10}$$

Tuteja *et al.*²⁹ proposed a calculation based on Gibbs free energy for this threshold pressure. They identified two interface rupture mechanisms: 1/ a forced penetration of the liquid into the texture, or 2/ a distortion of the liquid/gas meniscus. Depending on the texture geometry, one mechanism will dominate because of its lower energy. If the developed model is very geometry-dependent, it gives guidelines to increase the threshold pressure: using re-entrant asperities (or even doubly re-entrant geometries, that could virtually held an infinite pressure^{25,30}) and increase their height, as also suggested by Eq. 9.

The threshold pressure can also be reached by immersing a superhydrophobic surface in water, considering that underwater superhydrophobicity could be considered as thermodynamically stable, as theoretically demonstrated by Marmur³¹. Such a phenomenon have been observed by Helbig *et al.*¹⁵ on a springtail skin with a disappearance of the silvery air plastron during immersion in water with hydrostatic pressure about 400 kPa. Herminghaus³² also reported such a behavior on a smoketree leaf (*Cotinus Coggygria*) with a disappearance of the silvery plastron in a few seconds following an immersion in water at 20 cm depth, *i.e.* a hydrostatic pressure about 20 kPa. With the disappearance of this air plastron, the leaf was shown to be totally wetted, without recovering its properties upon pressure release.

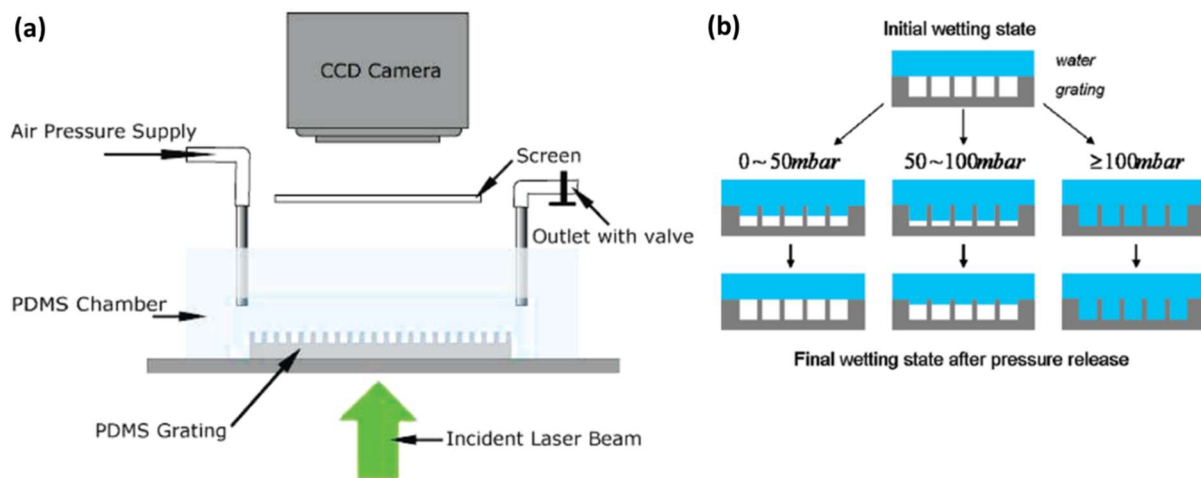


Figure 11 – Air plastron decay with pressure monitored by laser beam diffraction. (a) Scheme of the experimental set, (b) Corresponding interfaces upon pressure based on diffracted light analysis. Reprinted from ³³, Copyright 2010 American Chemical Society

Using a water fluidic chamber in order to apply a controlled hydrostatic pressure on a superhydrophobic textured PDMS, Lei *et al.*³³ studied the decay of the air plastron by beam diffraction (Figure 11a). Multiple air pockets trapped between asperities act as a diffracting grate, with the diffraction intensity directly related to the plastron shape and thickness. As shown in Figure 11b, when the pressure is increased from 0 to 5kPa, a penetration of water in the texture is observed, that is fully reversible after pressure release. With higher pressures, about 6kPa, such a mechanism is only partially reversible with a decay hysteresis corresponding to a pressure of 1kPa. Finally, when the pressure is about 10kPa, an irreversible Wenzel's regime is obtained.

Rathgen and Mugele³⁴ went further using a similar approach by following the diffraction intensity of an immersed hydrophobized textured silicon wafer with various incident angles (Figure 12a-b), at

various pressures. Using Rigorous Coupled Wave Analysis (RCWA), they were able to obtain the meniscus curvature for different applied pressures, considering their surface as perfectly monotonic. From the obtained curvature, they calculated the Laplace's pressure of the liquid. The later one was found to be equal to the applied hydrostatic pressure, validating the model for meniscus curvature calculation (Figure 12c).

They showed that the local water contact angle α linearly varies with pressure. When the pressure is lower than the atmospheric pressure, the local contact angle will be lower than the macroscopic Young's contact angle. For pressures up to 15 kPa, the local contact angle increases until reaching the macroscopic Young's contact angle. This meniscus bending is found to be fully reversible. However, when the pressure goes higher than a critical value, the local contact angle remains the same but the meniscus sag into an irreversible fully wetted Wenzel's state.

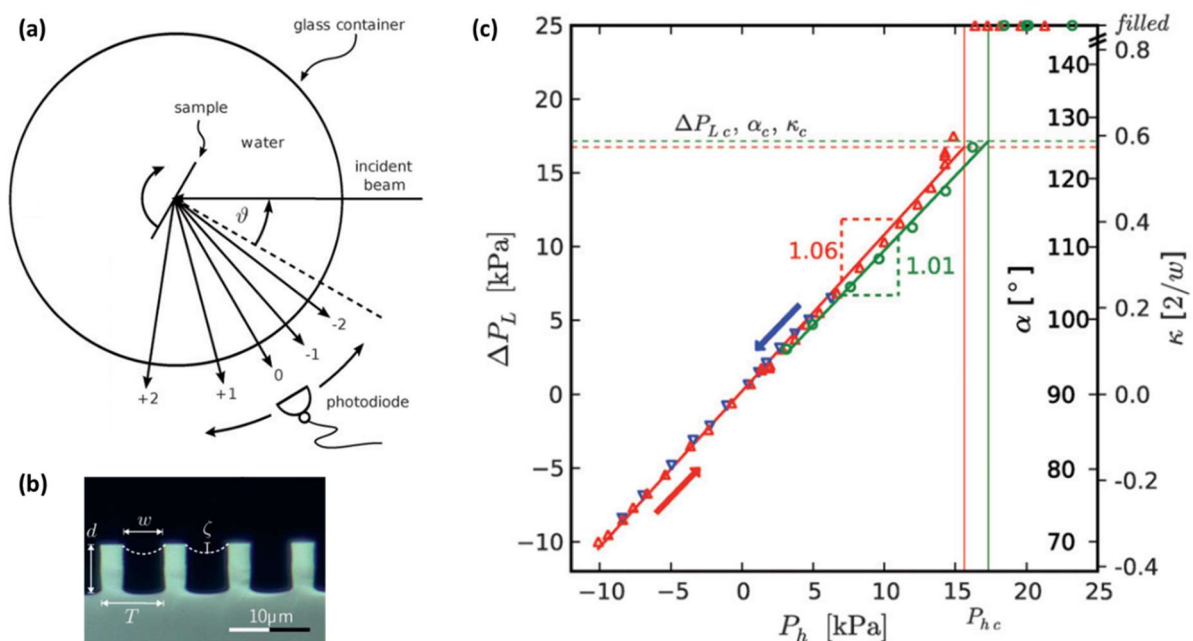


Figure 12 – Water/air meniscus shape under pressure monitored by laser beam diffraction. (a) Scheme of experimental set, (b) cross-view of the superhydrophobic sample (hydrophobized textured silicon wafer) and (c) plot of results: meniscus curvature κ and local contact angle α with the applied hydrostatic pressure (P_h) and the corresponding Laplace pressure (ΔP_L). Reprinted from³⁴, Copyright 2010 The Royal Society of Chemistry

They also point out that the collapse of a Cassie-Baxter's state into a Wenzel's state did not occur abruptly, but took several minutes. They attributed this slow transition to the kinetic of air diffusion in water: air bubbles can only "disappear" by diffusing in water or in the solid. When air was replaced by water vapor in the same experimental set, the transition from a Cassie-Baxter's to a Wenzel's state was found to be faster. This phenomenon can be associated to the condensation of water vapor, which is faster than diffusion of air in water.

A study of the plastron decay kinetic has been conducted by Poetes *et al.*³⁵ using a textured aluminum (obtained by bead-blasting) hydrophobized using a PTFE suspension (Figure 13a). They followed the plastron reflectivity over time for different immersion depths in water. Figure 13b shows the plastron reflectivity, that is related to its thickness, over time with immersion depths from 50 to 130 cm (corresponding to hydrostatic pressures from 50 kPa to 130 kPa). It appears that there are two regimes for the plastron decay: 1/ an incubation period with no observable decay that lasts longer with lower hydrostatic pressure (Figure 13d), and 2/ a faster decay of the plastron during about 2 hours.

Based on those results and on confocal microscopy observations, they proposed a mechanism for plastron decay over time (Figure 13c): trapped air slowly diffuses into water, leading to a thinner plastron. At some point, the plastron is so thin that it breaks into small bubbles, that then quickly

dissolve in water due to their higher Laplace's pressure, leaving a fully wetted surface. They also observed a remaining stable thin air plastron, especially visible for low depth immersed samples, while such plastron might be very unstable because of Laplace pressure. Despite this remaining nano-plastron, surfaces with a decayed plastron exhibit a Wenzel's behavior upon immersion removal. As a consequence, underwater superhydrophobicity could exist in a metastable state with a plastron decay strongly influenced by the hydrostatic pressure.

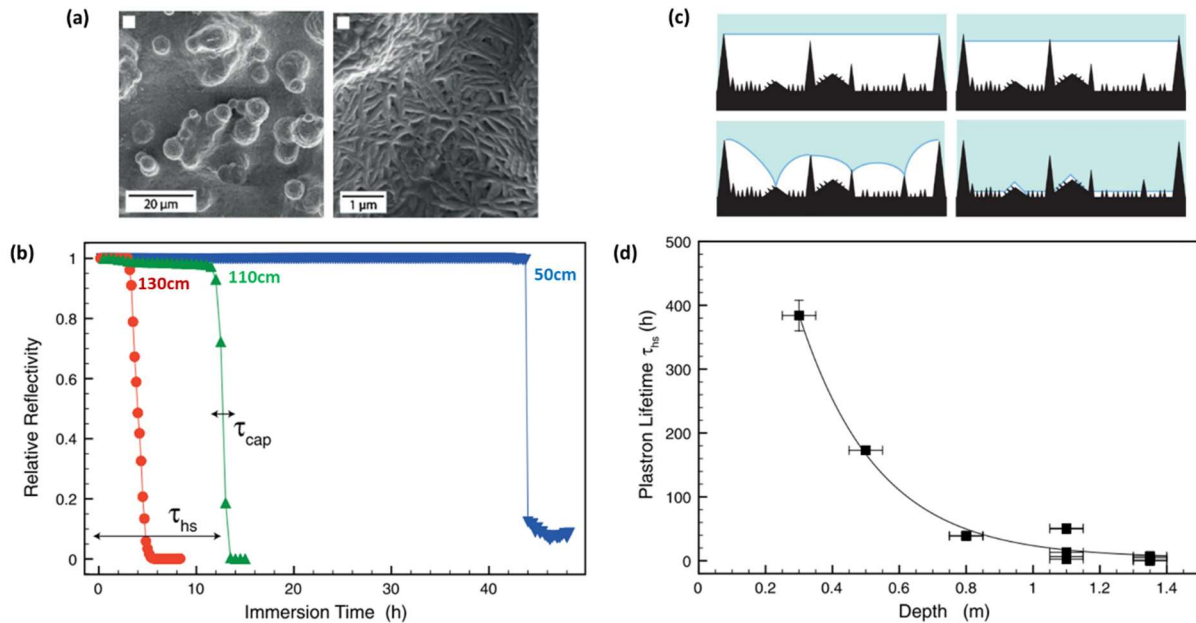


Figure 13 – Air plastron decay over time with different hydrostatic pressure monitored by relative reflectivity. (a) Sample surface observed by SEM, (b) plastron reflectivity decay over time for various immersion depth and thus hydrostatic pressure, (c) scheme of plastron decay mechanism, and (d) summary of plastron lifetime with immersion depth. Reprinted from³⁵, Copyright 2010 American Physical Society

II.5. Conclusion

Textured hydrophobic surfaces are considered to be the only way to achieve superhydrophobicity, *i.e.* a water contact angle larger than 150° . Behind this definition, two very different wetting regimes exist: 1/ the fully wetted Wenzel's regime and 2/ the hybrid liquid-on-air Cassie-Baxter's regime. These two regimes have been described considering the nature of the interface they form between the solid and the liquid, as well as their properties.

In particular, a Wenzel's regime is traduced by a high adhesion of the liquid to the solid, while the adhesion is very low with a Cassie-Baxter's regime. Hence, the Cassie-Baxter's wetting regime has been considered as the true superhydrophobicity. In fact, the associated properties such as anti-fouling, self-cleaning, or even drag reduction, are related to its low-adhesion property.

It has also been shown that a Cassie-Baxter's interface could always degenerate into a Wenzel's interface, considered as a loss of the interesting wetting properties. The conditions for a Cassie-Baxter's interface stability have been quickly described, and will be the main topic of the next chapter.

III. How to obtain superhydrophobic or even superomniphobic surfaces?

III.1. Reduction of surface energy

As previously discussed, superhydrophobicity can only be achieved through the combination of low surface energy and texturing, with a geometry promoting a Cassie-Baxter's state. For example, superhydrophobicity cannot be obtained for surfaces based on an epitaxial growth of perfluoroeicosane with perfect hexagonal organization of $-CF_3$ groups at the surface. Such a surface only exhibits a water contact angle of 119° , with a surface energy of $6,7\text{mJ/m}^2$ (against $22,5\text{mJ/m}^2$ for PTFE)³⁶. In fact, with such a smooth surface having a low surface energy, another way is required to reach superhydrophobicity.

However, Cassie-Baxter's superhydrophobicity can be achieved by reducing the surface energy of an already rough surface. For example, Zhang *et al.*³⁷ obtained a superhydrophobic wool textile by lowering its surface energy using polysiloxane (Figure 14.a-b). The surface texture remained the same (Figure 14.c-d). They achieved this surface energy reduction by accumulating a polyacrylate with grafted siloxane oligomers in the wool fibers. Thus, polyacrylate reacted with the fiber in order to fix the polymer to the textile, while the siloxane part preferably migrated to the fiber surface.

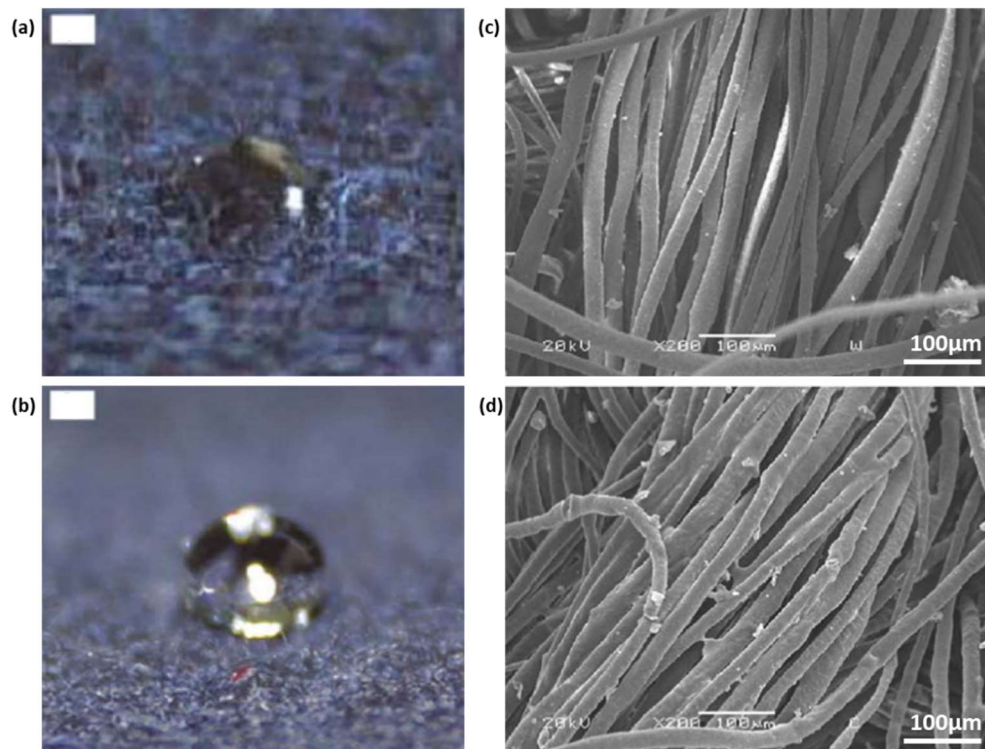


Figure 14 – Wool textile turned superhydrophobic by polysiloxane accumulation. (a) Water droplet on untreated superhydrophilic and (b) treated superhydrophobic wool textile. (c) SEM observation of the untreated and (d) treated fibers. Reprinted from ³⁷, Copyright 2008 Springer-Nature

In a similar way, in 2011 Wang *et al.*³⁸ turned a polyester textile from superhydrophilic to superomniphobic until hexadecane ($\gamma = 18,4\text{ mN/m}$)³⁹ (Figure 15 a-b). To do so, they coated the fibers with polypyrrole and a fluorinated alkyl silane. Such a coating was obtained by immersing the textile in an alcoholic solution of iron chloride with a fluorinated alkyl silane, followed by an exposition to pyrrole vapors that undergo further to polymerization. Figure 15 c-d clearly shows that the textile texturing has not been affected by the coating. The lower surface energy of the treated fibers is responsible of the turn of a superhydrophilic textile to a superomniphobic one.

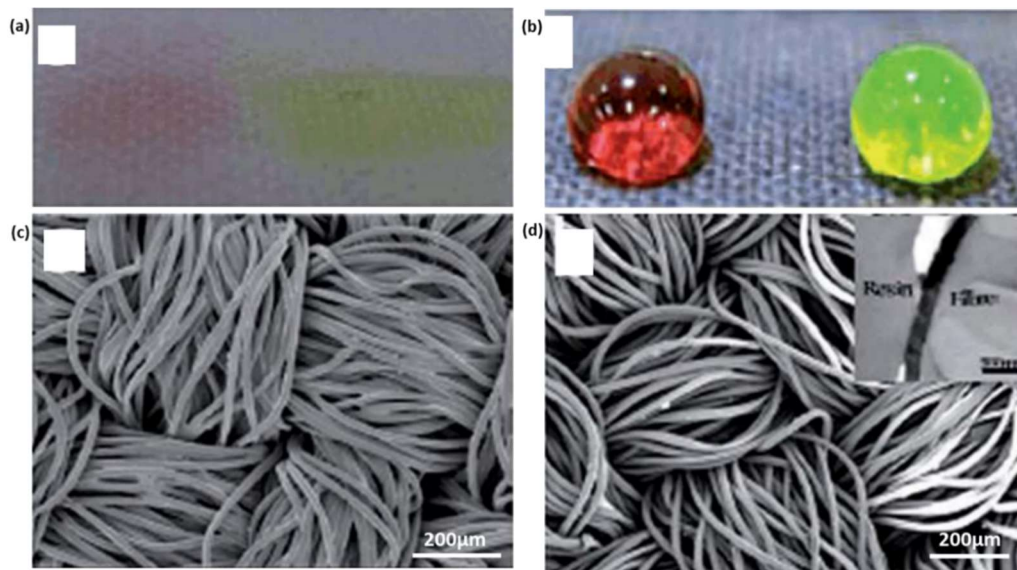


Figure 15 – Polyester textile turned superomniphobic until hexadecane, using a fluorinated alkyl silane. (a) Complete absorption of a red-colored hexadecane droplet and a green-colored water droplet by an untreated polyester textile, and (b) complete repellence of hexadecane and water by the treated superomniphobic polyester textile. (c) SEM observation of the fibers of untreated and (d) treated textile, showing no roughness differences. Reprinted from ³⁸, Copyright 2011 The Royal Society of Chemistry

With a different strategy, Calcagnile *et al.*¹⁸ obtained a superhydrophobic foam for oil/water separation from a commercially available polyurethane foam, modified with PTFE and iron oxide nanoparticles (Figure 16a). Unlike the previous examples, the surface is here textured by the PTFE nanoparticles, in addition to the surface energy reduction brought by the nanoparticles (see comparison between Figure 16b and c).

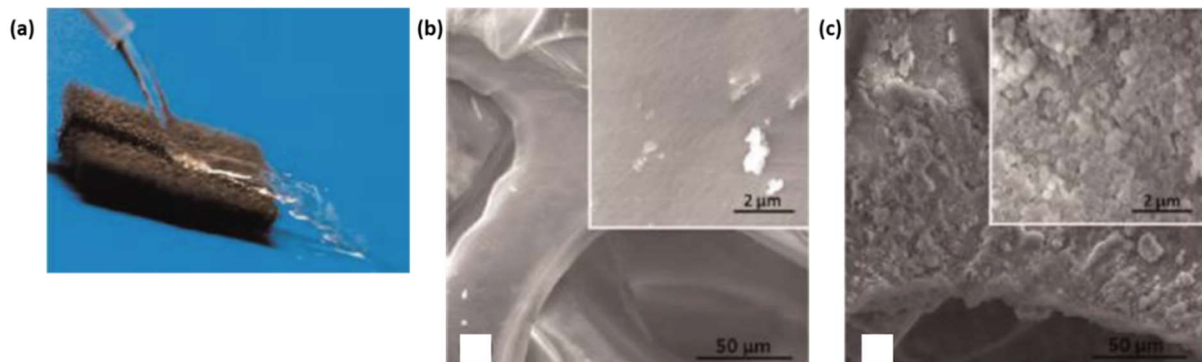


Figure 16 – Superhydrophobic polyurethane foam. (a) Water repelling polyurethane foam (b) SEM observation of untreated and (c) PTFE NP treated foam. Reprinted from ¹⁸, Copyright 2012 American Chemical Society

The reduction of the surface energy of textured surface can be efficiently achieved by grafting fluorinated compounds or polysiloxane to the surface. Low surface tension particles such as PTFE can also be deposited on the surface, bringing a nano-texturing in addition to the surface energy reduction. However, if the reduction of the surface energy is an effective approach for superhydrophobicity, the surface needs to be already textured. **How can a given material be textured to be superhydrophobic, or even superomniphobic?**

Table 1 – Summary of surface energy reduction approaches and resulting wettability

Substrate	Surface energy reduction	Wettability	Ref.
Smooth glass	Hexagonal pack of -CF ₃ groups	Hydrophobic ($\theta = 119^\circ$)	36
Wool textile	Polysiloxane grafting	Superhydrophobic	37
Polyester textile	Fluorinated silane grafting	Superoleophobic (hexadecane)	38
Polyurethane foam	PTFE nanoparticles deposition	Superhydrophobic	18

III.2. Processed textures

A better understanding of the Wenzel's and the Cassie-Baxter's superhydrophobicity equilibria has led to the development of experimental model textures that could be easily compared with theoretical models. In 2002, Yoshimitsu *et al.*⁴⁰ processed a patterned silicon surface using a micro-dicing machine. These authors obtained an anisotropic surface with uniaxial grooves (Figure 17a) and a quasi-isotropic surface with squared pillars (Figure 17b). After hydrophobization using a fluorinated silane coating, the surface with the squared pillar texture exhibits a Cassie-Baxter's superhydrophobicity, as well illustrated by Figure 17c.

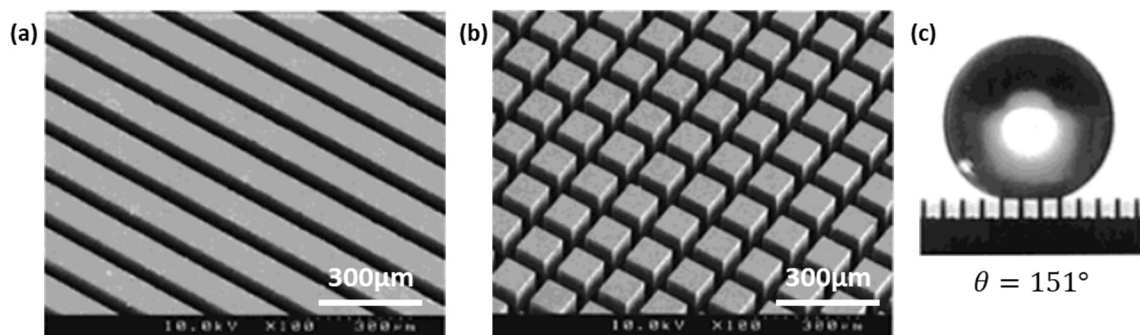


Figure 17 – Hydrophobized silicon surfaces patterned using a dicing machine. (a) Anisotropic surface with 49 μ m large and 160 μ m deep grooves separated by 96 μ m, (b) quasi-isotropic surface with squared pillar of 96 μ m large and 160 μ m height separated by 49 μ m, and (c) resulting wetting behavior with a water droplet seated on top of pillars. Reprinted from⁴⁰, Copyright 2002 American Chemical Society

In 2007, Zhang and Low⁴¹ have obtained perfectly-tailored grooves at both micrometric and nanometric scales using an imprinting process. They textured a polymer substrate (polystyrene or polymethylmethacrylate) by pressing it with a textured hard mold at a temperature above the glass transition. A nanoscale imprinting was then obtained with the same principle but at a temperature below the polymer glass transition (Figure 18a). The resulting surfaces have a very well-defined shape and the final morphology strongly depended on the orientation of the molds, leading to a large variety of surface morphologies (Figure 18b). The obtained surfaces are not found to be superhydrophobic, with too low water contact angle values probably resulting from a too low air fraction at the interface. However, their hydrophobicity is increased and the process shows a great versatility. Due to a high orientation of the asperities of these surfaces, a strong wettability anisotropy is observed.

Another way to obtain such regularly textured surfaces is photolithography, mimicking natural hoodoos that appear in some landscapes because of differential erosion. For example, Zhao *et al.*^{42,43} produced in 2011 silicon surfaces with grooves, as well as circular pillars. They could make these pillars with smooth (Figure 19a), or wavy (Figure 19b) sidewalls, or even with re-entrant nail-like geometry (Figure 19c). To do so, they used selective etching using plasma ion for smooth walls and nail-like pillars, and cyclic deep reactive ion etching for wavy walls pillars. The silicon surface was then hydrophobized by grafting an alkylsilane or a fluorinated silane, or even by coating PTFE using physical vapor deposition.

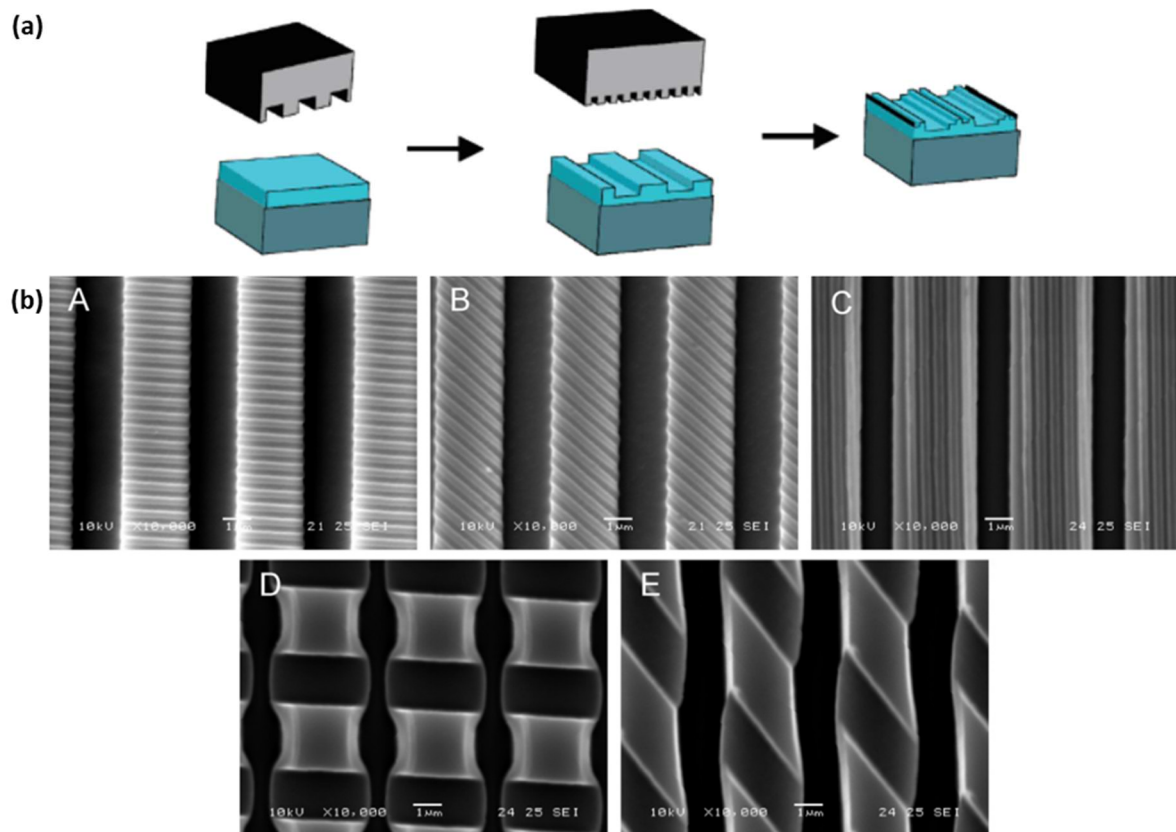


Figure 18 – Textured polymer surfaces obtained by micro and nano imprinting. (a) Scheme of the imprinting process: a polymer substrate is hot-pressed ($T > T_g$) using a hard microrough mold, and then cold-pressed ($T < T_g$) by a hard nanorough mold. (b) Resulting surfaces with various angle variations between the first and second mold: A, B and C are obtained by micro/nano imprinting, whereas D and E are obtained by a micro/micro imprinting. Reprinted from Zhang and Low⁴¹, Copyright 2007 American Chemical Society.

The three textures exhibit superhydrophobicity after hydrophobization, no matter the hydrophobizing agent, with a water contact angle around 155° and sliding angles lower than 10° . However, only the surface with wavy pillars coupled with fluorinated silane exhibits superoleophobicity, with a hexadecane contact angle of about 158° and a sliding angle of 10° . Nail-like pillars with fluorinated silane exhibits a relatively low hexadecane contact angle of 145° and a high sliding angle of 17° . The PTFE-covered surfaces show no sliding angle at all, probably because of a strong Wenzel's wetting behavior part.

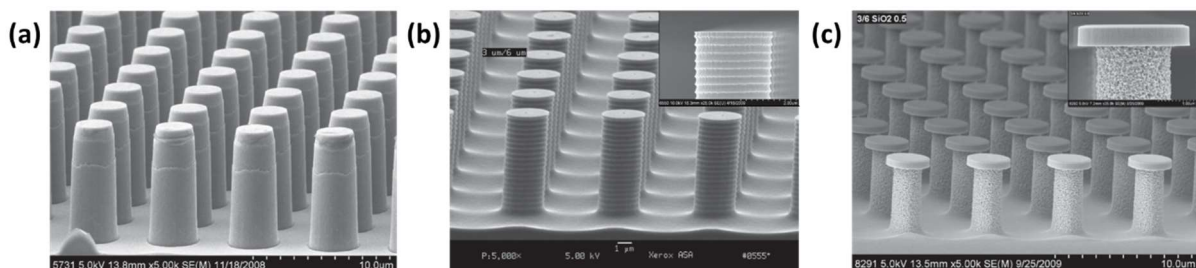


Figure 19 – Superhydrophobic patterned silicon surfaces. (a) Smooth sidewalls pillars, (b) wavy sidewalls pillars and (c) nail-like pillars, all obtained using photolithography, and of $3\mu\text{m}$ large, $7\mu\text{m}$ height and $3\mu\text{m}$ spaced. Reprinted from ⁴², Copyright 2011 American Chemical Society

If photolithography is a powerful tool to design perfectly-controlled textured surfaces, it could be time-consuming to produce numerous surfaces with the same texture. In 2010, Bhushan and Her⁸ replicated a pillar structure by molding epoxy resin in a negative template of a surface generated by photolithography. With a surface similar to the ones of Zhao *et al.*, they created a negative using

polyvinylsiloxane dental wax and pressing it with their master template, and then filled their negative template with epoxy resin. With such a method, numerous identical surfaces can be easily generated (Figure 20a), in order to compare the impact of another parameter on wettability: nanotexture. They covered their microtextured surfaces with epitaxial wax crystals using thermal evaporation (Figure 20b). By varying the wax content, they were able to change the morphology of these crystals, which were thicker and higher with increasing content, leading to stable Cassie-Baxter's behavior with different microtextures.

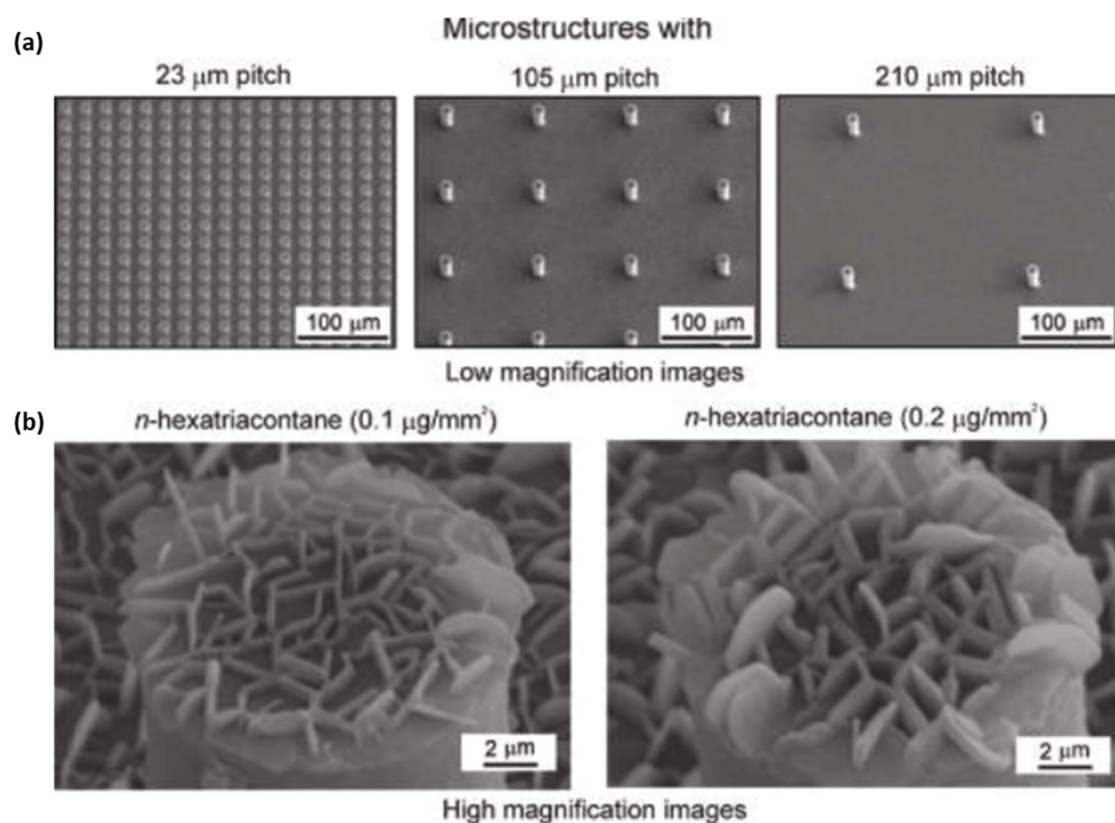


Figure 20 – Hierarchically textured superhydrophobic surface. (a) Molded epoxy resin surfaces with micropillars and (b) nanotexture made of hexatriacontane epitaxial crystals. Reprinted from ⁸, Copyright 2010 American Chemical Society

Zhao *et al.*⁴⁴ also obtained a superhydrophobic surface by replicating a Ginkgo leaf on a PDMS substrate (Figure 21a-b). This replication was simply obtained by pouring polysiloxane oil on a flattened Ginkgo leaf after a curing procedure. The obtained negative replica shows enhanced hydrophobicity, but only reached superhydrophobicity when it was laterally compressed, in order to increase the texturing through folding, and thus being closer to the original ginkgo leaf texture (Figure 21c-d). Thus, the negative replica of a superhydrophobic surface might thus not be superhydrophobic too. Further modification like increasing the texturing through micro-folding by compression can help reaching superhydrophobicity.

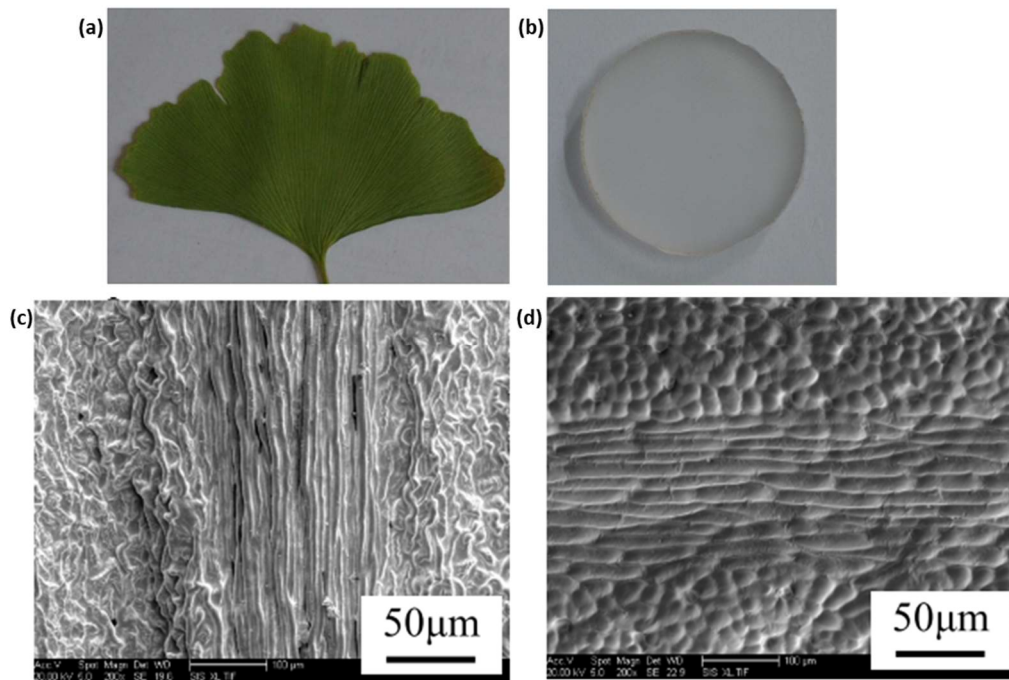


Figure 21 – Ginkgo leaf superhydrophobicity. (a) A natural Ginkgo leaf and (b) its PDMS negative replicated surface. (c) SEM observation of the natural Ginkgo leaf and (d) its negative replica. Reprinted from ⁴⁴, Copyright 2014 Trans Tech Publications

A texturing can also be generated on a silicon surface using laser etching, as done by Song *et al.*⁴⁵ in 2005. They produced superhydrophobic silicon surfaces with both micro and nano roughness, hydrophobized by an alkylsilane or a fluorinated silane. The microtexture (Figure 22a) comes from laser digging, that generates 5µm deep and 4µm large grooves, while the nanotexture is generated by the oxidation of silicon into SiO₂ particles and their deposition between grooves (Figure 22b). This hierarchical texturing, coupled with low surface tension thanks to the silane functionalization, led to superhydrophobicity with a water contact angle from 156 to 165° for all samples, whatever the silane nature and its deposition process (from solution or vapor). However, sliding angles were close to 0° for samples with silanes deposited using chemical vapor deposition, whereas samples hydrophobized by deposition from a solution had larger sliding angles, up to 17°.

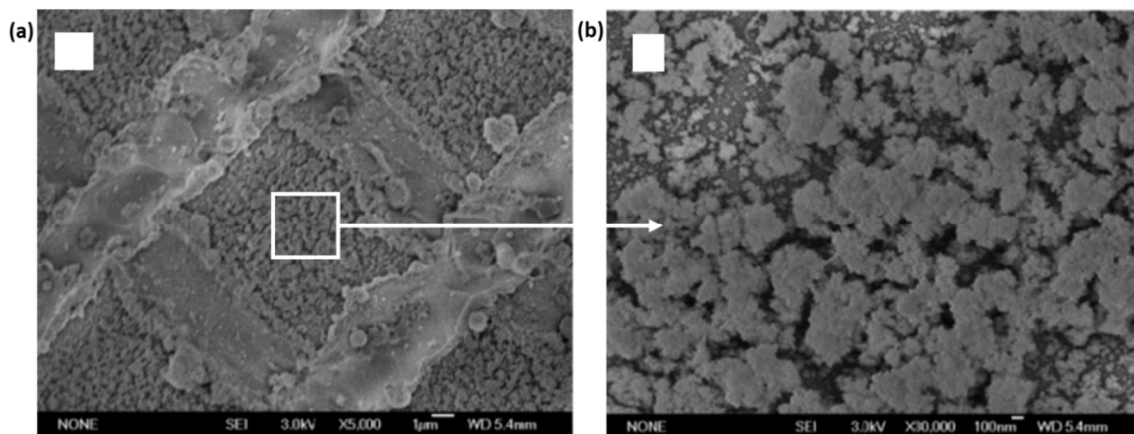


Figure 22 – Superhydrophobic silicon surface obtained using laser etching. (a) SEM observations of microtexture made of 5µm deep and 4µm large grooves and (b) nanotexture made of oxidized silicon sputtered chippings. Reprinted from ⁴⁵, Copyright 2005 American Chemical Society

Table 2 – Summary of superhydrophobic processed surfaces

Substrate	Texture		Surface energy reduction	Ref.
	Nature	Process		
Silicon	Squared pillars	Micro-dicing	Fluorinated silane coating	40
PS and PMMA	Orthogonal grooves	Imprinting	None	41
Silicon	Hoodos	Photolithography	PTFE or fluorinated silane coating	42
Epoxy resin	Hoodos	Molding	Epitaxially grown wax crystals	8
PDMS	Natural leaf folds	Molding and compression-folding	None	44
Silicon	Micrometric grooves and isotropic nanotexture	Laser etching	Fluorinated silane grafting	45

The various ways of producing tailored textured surfaces proved their efficiency for reaching superhydrophobicity. Moreover, the resulting surfaces are well-defined, facilitating their comparison with models. However, these approaches are time-consuming and cannot be easily applied to the production of large surfaces. It has however been shown by Song *et al.* that an isotropic nanotexturing combined with hydrophobization and a micro-texturing could lead to superhydrophobicity. **Isotropic texturing methods could thus permit to obtain superhydrophobic surfaces with fewer efforts.**

III.3. Isotropic textures

III.3.a. Texturation followed by surface tension lowering

As previously discussed, Poetes *et al.*³⁵ have investigated the Cassie-Baxter's interface stability under immersion, leading to the preparation of superhydrophobic surfaces with a simple two-step method. They textured an aluminum plate by blasting, and then reduced its surface tension by coating PTFE by spraying, also inducing a nanotexturing (Figure 13a). Texturation of aluminum can also be performed using chemical etching methods. For example, Weibel *et al.*⁴⁶ produced a hierarchically rough aluminum surface by chemically etching it using concentrated chloric acid to obtain a microroughness. A following anodization step generated a nano-porous anodic aluminum oxide layer. The hierarchically textured surface is then treated with an alkylsilane and coated with PTFE using physical vapor deposition (PVD), with PTFE, inducing an additional nanotexturing (Figure 23a). The resulting surface exhibits a Cassie-Baxter's regime superhydrophobicity with a water contact angle of 165° and a sliding angle lower than 3° (Figure 23b).

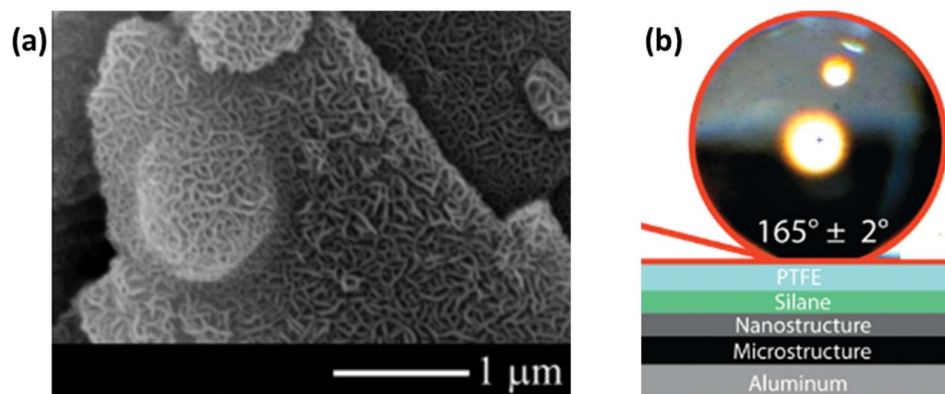


Figure 23 – PTFE coated textured alumina surface obtained from chemical etching and anodization followed by hydrophobization using an alkylsilane and PTFE. (a) SEM observation of the hierarchical roughness and (b) resulting superhydrophobicity of the treated aluminum. Reprinted from ⁴⁶, Copyright 2010 American Chemical Society

In 2020, Li *et al.*¹⁹ also obtained superhydrophobic textured surfaces from various metals such as zinc, copper or copper-zinc alloy. A smooth zinc layer was turned into a pillar-shape zinc oxide texture by hydrothermal reaction (Figure 24a). Copper was textured by chemical oxidation, resulting in a flower-like copper oxide texture (Figure 24b). Copper-zinc alloy was also chemically oxidized, resulting in a more separated flower-like copper oxide texture (Figure 24c). All three samples, after hydrophobization using pentadecafluorooctanoic acid, exhibit a Cassie-Baxter's regime superhydrophobicity, with a water contact angle around 160° and sliding angles lower than 6°.

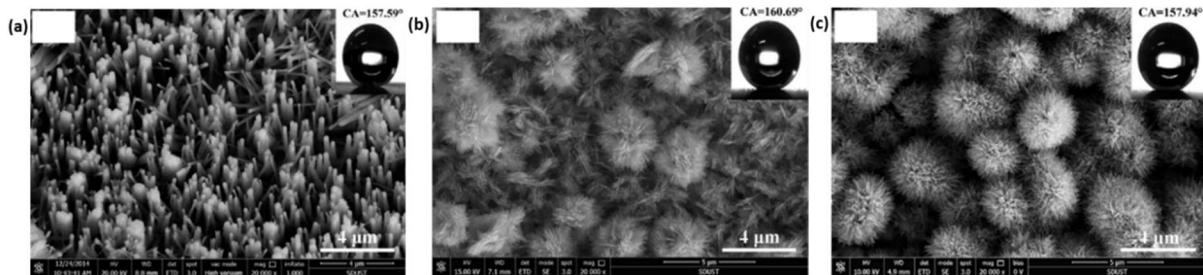


Figure 24 – Superhydrophobic metal oxide surfaces. (a) SEM observation of ZnO pillar-like texture, (b) CuO flower-like texture and (c) CuO in the presence of zinc flower-like texture, obtained from hydrothermal reaction or chemical oxidation of smooth zinc, copper, and brass surfaces, hydrophobized using a fluorinated acid. Reprinted from ¹⁹, Copyright 2020 American Chemical Society.

In a similar way, Hosono *et al.*⁴⁷ produced needle-shaped brucite-type cobalt hydroxide crystals using a bottom-up process: crystallization of the crystals on a substrate from a solution of hydrated cobalt chloride $\text{CoCl}_2 \cdot 6\text{H}_2\text{O}$ (Figure 25a-b). With a very high nanotexturing, obtained by generating cobalt oxide needle tip with a width of less than 10nm, hydrophobized using lauric acid, the resulting surface exhibits a Cassie-Baxter's superhydrophobicity with contact angle as large as 178°.

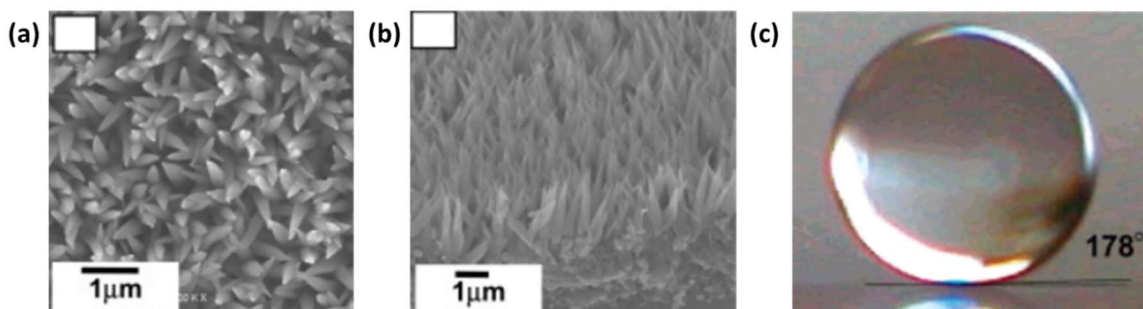


Figure 25 – Needle-like brucite-type cobalt oxide obtained by crystallization from solution, hydrophobized using lauric acid. (a) SEM observation from top and (b) and from side. (c) Resulting superhydrophobicity. Reprinted from ⁴⁷, Copyright 2005 American Chemical Society

Sarkar *et al.*⁴⁸ obtained larger structures by depositing silver from a solution of silver nitrate on a copper substrate using galvanic exchange reaction. When depositing silver on a copper substrate from a solution with only silver nitrate, a feather-like texture is obtained (Figure 26a), with a very low water contact angle because of the high surface energy of silver. But when benzoic acid is added in the silver nitrate solution, the deposited silver self-organizes into a flower-like shape with a high texturing (Figure 26b). Moreover, benzoic acid is found to be coated on the surface, thus reducing the surface energy, leading to a Cassie-Baxter's superhydrophobicity with a water contact angle and hysteresis measured at 162° and 2°, respectively.

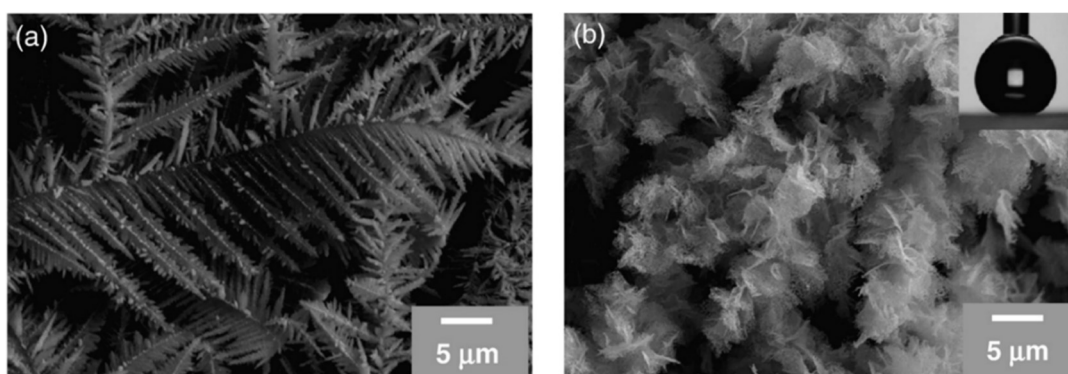


Figure 26 – Superhydrophobic silver coated surface. SEM observations of silver deposited on a copper substrate from a silver nitrate solution with (a) and without (b) benzoic acid. Reprinted from ⁴⁸, Copyright 2010 Elsevier

Zhai *et al.*⁴⁹ produced honeycomb-like superhydrophobic surfaces with hierarchical texturing from the degradation of polyelectrolyte multilayers further coated with silica nanoparticles, followed by hydrophobization. To do so, they immersed a film composed of 100 bilayers of poly(allylamine hydrochloride) and poly(acrylic acid) in an acidic solution. The resulting honeycomb-like textured surface does not exhibit superhydrophobicity, because of too high surface energy and too low texturing (Figure 27a). The texturing was increased by depositing 50 nm silica nanoparticles through dipping of the substrate in a nanosilica suspension (Figure 27b). Surface energy reduction was performed by grafting a fluorinated silane (tridecafluoro-1,1,2,2-tetrahydrooctyltrichlorosilane) using chemical vapor deposition (CVD). The resulting surface exhibits a Cassie-Baxter's regime superhydrophobicity, with a water contact angle of 172° and a sliding angle of 2°.

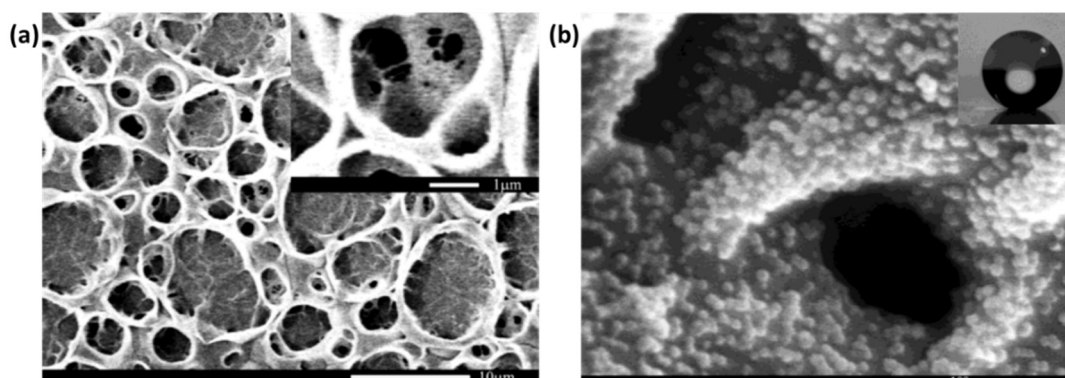


Figure 27 – Superhydrophobic honeycomb-like surface from polyelectrolyte multilayers. (a) Honeycomb-like micro-texturing is obtained by acidic treatment of poly(allylamine hydrochloride)/poly(acrylic acid) multilayers assembly, and (b) nanotexturing is obtained by silica nanoparticles deposition from a solution, followed by hydrophobization using fluorinated silane, and resulting superhydrophobicity. Reprinted from ⁴⁹, Copyright 2004 American Chemical Society

Table 3 – Summary of superhydrophobic isotropic textured surfaces after hydrophobization

Substrate	Texture		Surface energy reduction	Ref.
	Nature	Process		
Aluminum	Hills and valleys	Blasting	PTFE spray coating	35
Alumina	Micrometric flakes with nano-porosities	Chemical etching and anodization	PTFE coating (PVD)	46
Zinc, Copper, Zinc-copper alloy	Needles or flower-like	Chemical oxidation	Fluorinated acid grafting	19
Cobalt oxide	Needles	Epitaxial crystallization	Lauric acid grafting	47
Silver	Feather-like and flower-like	Galvanic exchange reaction	Benzoic acid grafting	48
Polyelectrolyte multilayers	Honeycomb-like	Acidic degradation and silica nanoparticles	Fluorinated silane grafting	49

Many isotropic texturing approaches can lead to superhydrophobicity after hydrophobization, from subtractive processes to controlled growth of crystals. However, the need of a hydrophobization step complexifies the surface treatment processes, limiting their industrial use. Moreover, the texturing process involved could require a lot of steps and very particular conditions to be effective. **There might be easier ways of texturing and reducing the surface tension of a surface.**

III.3.b. Use of hydrophobic particles

In order to generate superhydrophobicity on a large variety of substrates, coating is usually considered as such a process can be applied to metals, glass, or polymers. Superhydrophobic coatings bring both low surface tension and texturing. The texturing often comes from solid fillers like oxides nanoparticles.

For example, Chakrddhar *et al.*⁵⁰ obtained in 2011 a superhydrophobic coating by spraying a PDMS / zinc oxide nanoparticle blend on an aluminum substrate (Figure 28a). To do so, they dispersed zinc oxide nanoparticles in toluene and with PDMS and a curing agent. This mixture was then sprayed on an aluminum substrate and dried at room temperature, resulting in a superhydrophobic surface with a water contact angle of 155° and a sliding angle lower than 5°.

Zinc oxide nanoparticles were also used by Zhang *et al.*⁵¹ to produce a superhydrophobic coating on a PDMS substrate that do not strictly participate to superhydrophobicity (Figure 28b). Their zinc oxide nanoparticles hydrophobized by grafting a monolayer of octadecanethiol on their surface. The resulting hydrophobic nanoparticles were coated on the surface using a wet process: They were dispersed in deionized water, and the suspension was deposited on the PDMS substrate. The resulting surface is superhydrophobic with a water contact angle of 160° and a sliding angle lower than 2°. This surface is also superoleophilic, with dodecane fully wetting the surface. However, unlike common superhydrophobic surfaces, the coating recovers superhydrophobicity after a few seconds, dodecane being drawn by the PDMS underlayer.

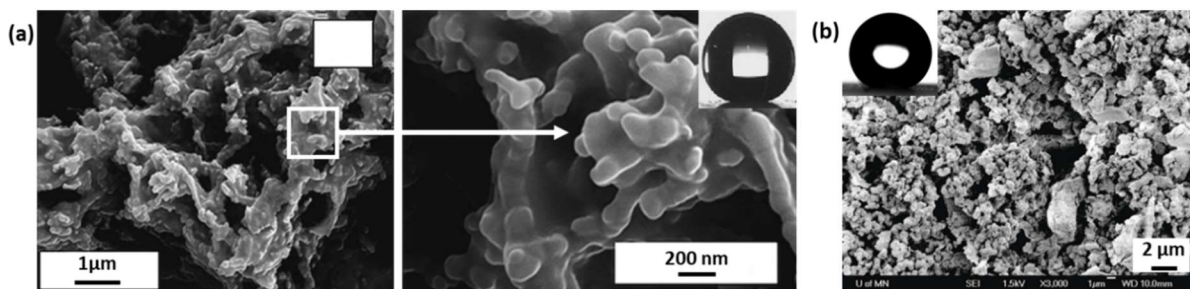


Figure 28 – Zinc oxide coated superhydrophobic surfaces. (a) ZnO/PDMS blend sprayed on an aluminum substrate, (b) Hydrophobic ZnO particles deposited on a PDMS substrate from solution. Reprinted from (a)⁵⁰ and (b)⁵¹ Copyright 2011 Elsevier and 2010 American Chemical Society, respectively.

However, the most used particle for texturing a surface by a coating process is silica, thanks to the variety of size and surface treatment available. For example, in 2018 Fourmentin *et al.*⁵² obtained a superhydrophobic polyurethane coating using hydrophobic fumed silica (Figure 29a). To obtain such a surface, a solution of poly(urethane-acrylate) and silica (60%_{wt}) in tetrahydrofuran was prepared, and coated on glass slides using a bar coater. The resulting cured surface exhibits a Cassie-Baxter's regime superhydrophobicity, with a water contact angle around 160° and a contact angle hysteresis of only 1°.

They were also able to tune the surface wetting behavior by varying the silica content (Figure 29b): for silica content up to 30%_{wt}, the surface was lowly textured, and remained hydrophilic; between 30 and 50%_{wt} silica content, the surface turned hydrophobic and even superhydrophobic, with water contact angles from 100° to 160°, but with large contact angle hysteresis from 100° to 140°, revealing a

Wenzel's regime. By changing the silica content from 50 to 60%_{wt}, they were thus able to turn a hydrophilic poly(urethane-acrylate) resin surface from a Wenzel's regime superhydrophobicity to a Cassie-Baxter's regime superhydrophobicity.

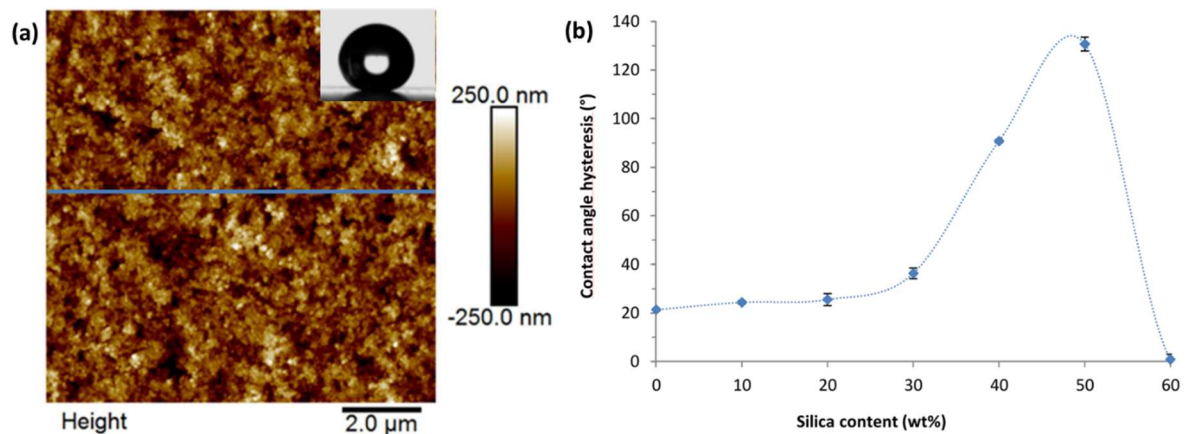


Figure 29 – Superhydrophobic poly(urethane-acrylate) resin textured using silica with tunable water adhesion. (a) AFM imaging of a Cassie-Baxter's superhydrophobic surface roughness with 60%_{wt} silica content, (b) Evolution of water contact angle hysteresis with silica content in the coating, linking roughness and surface wetting regime. Reprinted from ⁵², Copyright 2018 Elsevier

Söz *et al.*⁵³ obtained similar results using a hydrophobized fumed silica dispersed in a diluted solution of polystyrene in toluene (1/10 weight ratio of PS/silica). This solution was deposited on glass sides by spin-coating or doctor-blade coating and dried. Surfaces obtained using both spin-coating (Figure 30a) and doctor blade (Figure 30b) show a moderate microtexturing caused by large silica aggregate of around 10 μ m size, with a high nanotexturing attributed to silica nanoparticles. The resulting surfaces exhibit a Cassie-Baxter's regime superhydrophobicity, with a water contact angle around 161° and a contact angle hysteresis lower than 10° for the spin-coated surface, and a water contact angle of 162° with a contact angle hysteresis of 8° for the doctor-blade-coated surface with optimal processing conditions.

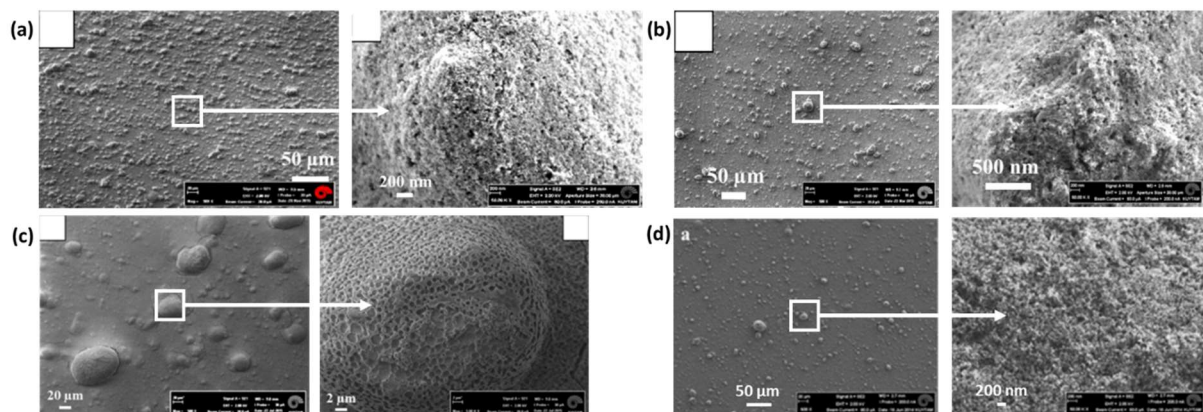


Figure 30 – Superhydrophobic silica coated surfaces. (a) Spin-coated and (b) doctor blade coated silica in a polystyrene matrix, (c) Spin-coated and (d) doctor blade coated fluorinated silica nanoparticles in an epoxy resin matrix. Reprinted from ⁵³, Copyright 2016 Elsevier

They also prepared superhydrophobic coatings from a diluted solution of epoxy-resin in methylene chloride with dispersed silica (1/10 weight fraction). However, for this coating to be superhydrophobic, it seems necessary to decrease the surface energy of silica by grafting polyperfluoroether on the nanoparticles surface. Surfaces coated with epoxy resin in diluted solution with dispersed fluorinated silica nanoparticles by spin-coating (Figure 30c) or doctor blade (Figure 30d) show a relatively low microtexturing combined with a high nanotexturing, with a singular crater-shape roughness for the

spin-coated sample. Despite their nanotexture shape differences, these two surfaces exhibit a Cassie-Baxter's superhydrophobicity with a water contact angle of 163° and a contact angle hysteresis lower than 4° .

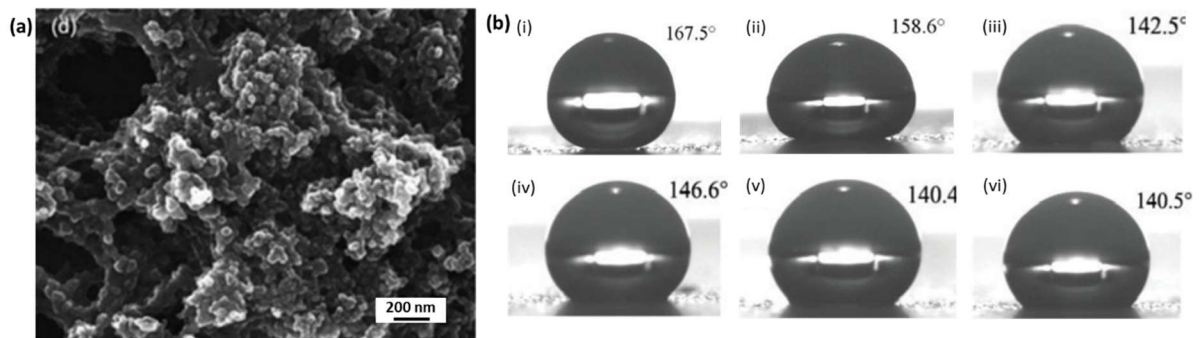


Figure 31 – Superomniphobic surface from a fluorinated silica coating. (a) SEM observation of the obtained superomniphobic surface and (b) resulting wettability with $5\mu\text{L}$ droplets of (i) water, (ii) diiodomethane, (iii) decahydronaphthalene, (iv) soybean oil, (v) diesel fuel, (vi) xylene. Reprinted from⁵⁴, Copyright 2008 Wiley

Using fluorinated silica nanoparticles, Sheen *et al.*⁵⁴ obtained superhydrophobic, and even superoleophobic surfaces (Figure 31a). They produced hydrophobic silica nanoparticles from a sol-gel route. These hydrophobic nanoparticles were dispersed in isopropanol and spin-coated on glass slides. The resulting superhydrophobic surface has a water contact angle of 168° and a sliding angle lower than 3° . It also repels low surface tension liquids such as diiodomethane, decahydronaphthalene, soybean oil, diesel fuel, and xylene, with contact angles of 159° , 147° , 141° , and 140° , respectively, and sliding angles lower than 3° (Figure 31b). For the later liquids, the value of 150° is not reached for contact angle values, but the low adhesion of droplets is characteristic of a Cassie-Baxter's regime: the produced surface could then be told superomniphobic, for surface tensions down to 23mN/m (corresponding to the xylene surface tension³⁹).

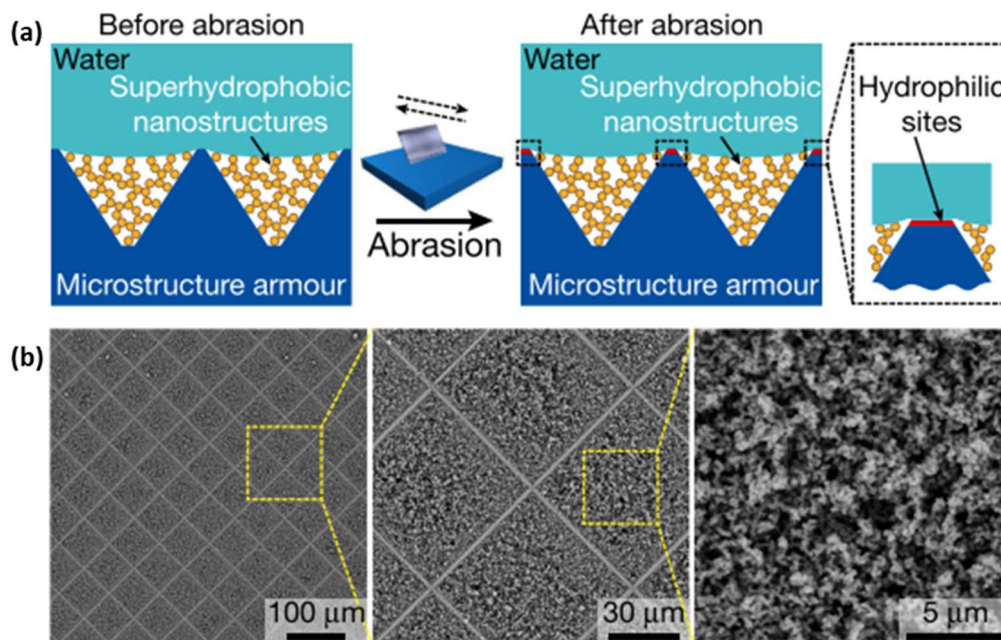


Figure 32 – Armored superhydrophobic surface consisting of a side-to-side pyramids silicon structure, obtained by photolithography, with voids filled by a superhydrophobic material: fluorinated silica nanoparticles. (a) Scheme of the armored surface viewed from the side, before and after abrasion, and (b) are SEM pictures of the obtained surface before abrasion, showing the armor silicon frame and the fluorinated nanoparticles. Reprinted from⁵⁵, Copyright 2020 Springer Nature

With similar silica nanoparticles, Wang *et al.*⁵⁵ produced in 2020 an armored superhydrophobic surface that can resist to a high degree of abrasion, thanks to a solid silicon frame consisting of side-to-side pyramids obtained by photolithography. The voids between each pyramid are filled with the superhydrophobic material, here fluorinated silica nanoparticles, with the pyramids tops being some unwanted but rare hydrophilic points (Figure 32). Upon abrasing the sample, the superhydrophobic fragile material is protected by the silicon pyramids, making the sample more resilient. However, after a strong abrasion, and even if some superhydrophobic material was still protected, the hydrophilic top-cut pyramids areas are too unfavorable for superhydrophobicity and then act as pinning points. Still, the abrasion resistance of such surface is very important, at the cost of a time-consuming process.

In 2009, Yang *et al.*⁵⁶ produced superhydrophobic surfaces using hierarchically textured CaCO_3 -silica composite particles. In fact, they mixed micrometer-size calcium carbonate particles with silica nanoparticles under violent stirring, and hydrophobized these composite particles using hexamethyldisilazane (Figure 33a). The resulting micro-nano particles were dispersed in a solution of PDMS with gasoline (with equal weight fractions of PDMS, particles and gasoline) containing curing agents, and the mix was sprayed on glass slides. After drying and curing, the surface clearly shows a hierarchical texturing, resulting in a Cassie-Baxter's regime superhydrophobicity with a water contact angle around 165° and a sliding angle lower than 5° (Figure 33b).

In 2017, Zhu *et al.*⁵⁷ also produced multiple-scales particles, using 500 nm and 25 nm silica particles. The two silica particles sizes were simply mixed and dispersed in xylene under ultrasonication. This suspension was then mixed with a crosslinked silanized polyacrylate and then sprayed on steel plates. After drying, the surface has a clearly visible hierarchical texturing at micro and nanoscale, and exhibits a Cassie-Baxter's regime superhydrophobicity, with a water contact angle of 156° and a sliding angle of 4° (Figure 33c). This coating is also quite resistant to abrasion, as the sliding angle stayed below 10° until 10 cycles of mechanical abrasion using sandpaper. With higher abrasion, the water contact angle stayed high, around 150° , but the sliding angle dramatically increases, demonstrating a transition into a Wenzel's regime.

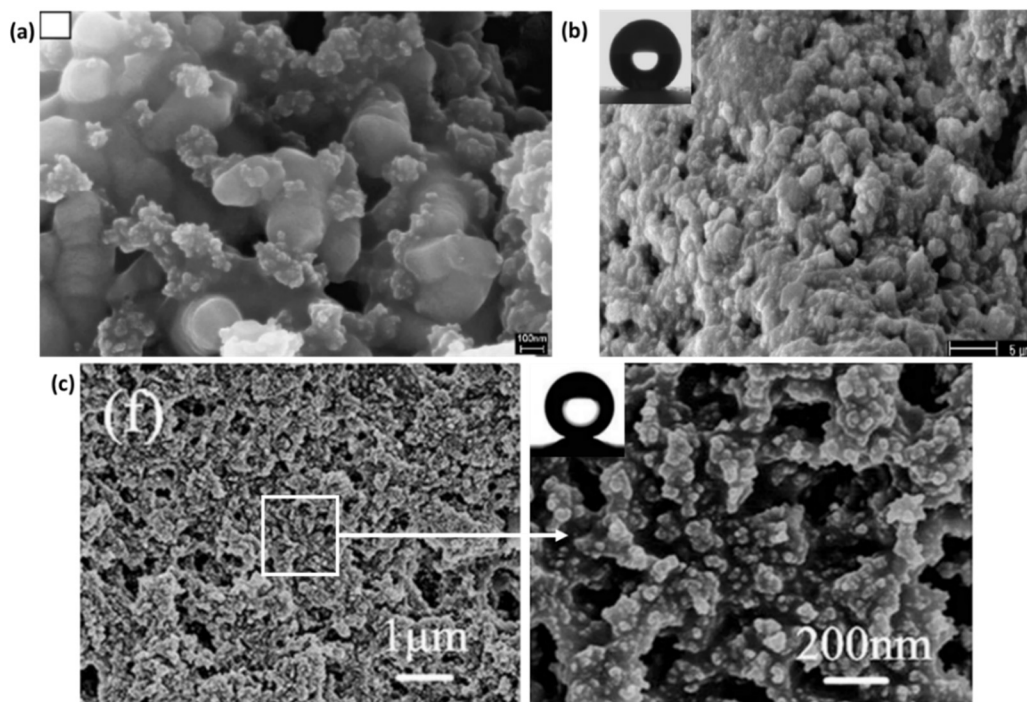


Figure 33 – Superhydrophobic surfaces from hydrophobized mulberry-like particles. (a) Bare silica nanoparticles on CaCO_3 microparticles, (b) silica nanoparticles on CaCO_3 microparticles mixed with PDMS and sprayed on a glass slide, and corresponding water CA. (c) Silica-on-silica multiple scales particle mixed with crosslinked silanized polyacrylate and sprayed on a steel plate, and corresponding water CA. Reprinted from (a, b)⁵⁶ and (c)⁵⁷, respectively, Copyright 2009 and 2017 Elsevier.

Srinivasan *et al.*⁵⁸ used nano-objects with higher aspect ratio: carbon nanotubes (CNT). They prepared CNT dispersible in a solvent, thus allowing better applicability, by adding poly(phenylenevinylene) oligomers (OPV) in chloroform, which have strong π interactions with CNT. The CNT + OPV suspension in chloroform was deposited on various substrates such as glass, mica or metals. The resulting surface is textured by randomly stacked CNT (Figure 34a), and exhibits a Cassie-Baxter's regime superhydrophobicity, with a water contact angle around 162° and a sliding angle lower than 2° , giving the surface self-cleaning and great water-repelling properties (Figure 34b-c). These coatings kept a stable superhydrophobicity overtime, with a water contact angle staying constant for at least 24h, and showing a good chemical resistance against both acidic and basic solutions.

Lv *et al.*⁵⁹ also used CNT as a filler in a superhydrophobic coating of poly(phenylene sulfide) (PPS) and silicon rubber (SR). To do so, they dispersed CNT in ethanol under ultrasonication, before adding PPS and SR in the solution (PPS:SR:CNT weight ratio is 0.7:0.3:0.0015). The mix was then sprayed on a heated aluminum substrate, to volatilize ethanol. The resulting surface is textured with dispersed SR particles and entangled CNT (Figure 34d), exhibiting a Cassie-Baxter's regime superhydrophobicity, with a water contact angle of 164° and a sliding angle of only 1° . It appears that a coating made in a similar way but without CNT still exhibits superhydrophobicity, but with a lower water contact angle of 152° : addition of CNT helps increasing the air fraction trapped on the surface, increasing superhydrophobicity. Such coating has a good thermal resistance, until 350°C , and a very good mechanical resistance to abrasion with a sliding angle staying below 10° after up to 5'000 abrasion cycles, with an abrasion weight loss being about three times lower than for a pure PPS coating.

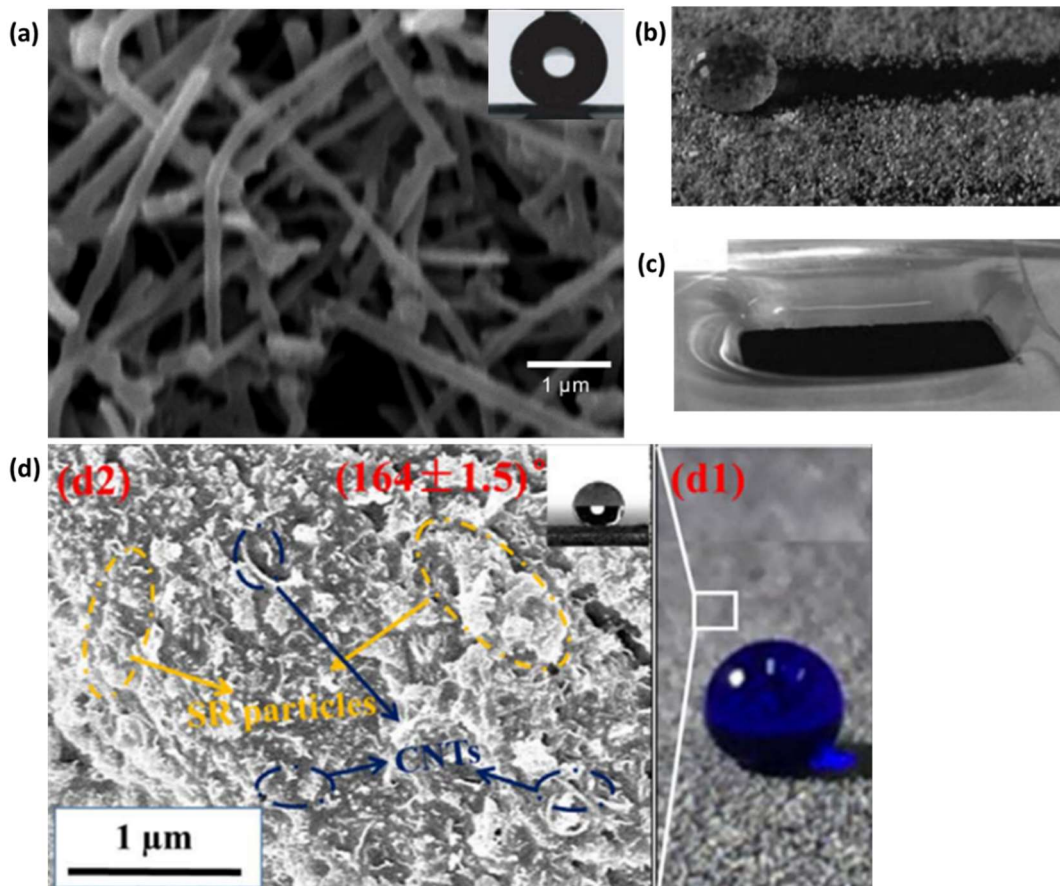


Figure 34 – Superhydrophobic surfaces from carbon nanotubes. (a) Randomly stacked CNT sprayed from a solution of CNT, OPV and chloroform, and resulting (b) self-cleaning and (c) water-repelling properties. (d) Poly(phenylene sulfide) sprayed coating, with silicon rubber particles and carbon nanotubes, and resulting wetting behavior. Reprinted from (a, b, c)⁵⁸ and (d)⁵⁹, Copyright 2008 Wiley and 2017 Elsevier, respectively.

In 2016, Perera *et al.*⁶⁰ obtained superhydrophobic surfaces using an original process of hydrophobic solid particle migration to the surface. They made low surface tension microparticle using diatomaceous earth modified by a fluorinated silane. The resulting particles were mixed with low viscosity binder solutions of epoxy resin or polyurethane in tetrahydrofuran, and the mix was coated on glass slides. During the coating drying, diatomaceous earth particles migrated to the surface, driven by their lower surface tension and thanks to the matrix low viscosity. When the particles were sufficiently fluorinated (more than 2%_wt of fluorosilane) and introduced in a large enough loading (more than 20%_wt), the resulting surface was sufficiently textured to be superhydrophobic, with a water contact angle around 160° (Figure 35a).

Using surface particles migration, Puretskiy *et al.*⁶¹ produced “self-healing” superhydrophobic surfaces from a fluorinated wax with incorporated silica nanoparticles. To do so, they mixed 1-iodo-1H,1H,2H,2H-perfluorodecane, a crystalline fluorinated wax with a melting point around 60°, with moderately hydrophilic silica nanoparticles (with size of 200nm) containing aminopropyl groups on their surface. The pure wax crystallizes into a fractally textured surface, leading to a large hydrophobicity, with a water contact angle of 127°. With the addition of 5%_wt or more of silica nanoparticles, the resulting surface is superhydrophobic, with a water contact angle of 152° and a contact angle hysteresis of only 1° (Figure 35b). The increased texturing comes from nanoparticles being pushed-out from the wax bulk during crystallization, thus covering the surface. This texturation mechanism allows simple recoveries of the texture after a mechanical break, by heating the coating above the wax melting point of 60°, and cooling it for the wax to recrystallize. Abrasion/recovery cycles have been conducted, and no loss of wetting properties have been reported through these cycles.

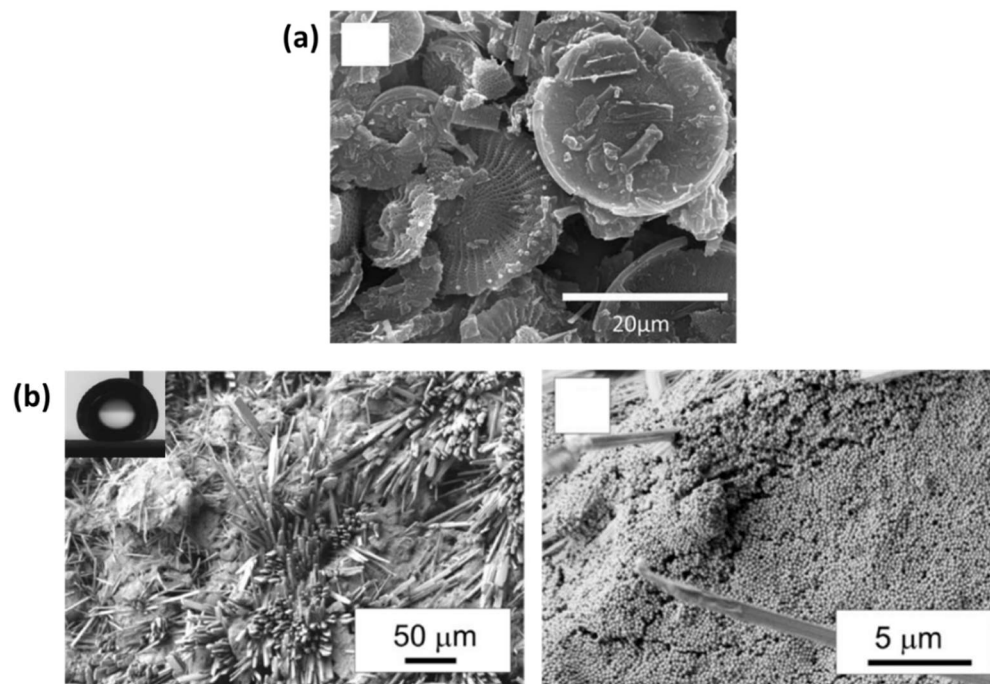


Figure 35 – Superhydrophobic surfaces using “floating” particles. (a) Fluorinated diatomaceous earth particles bound by polyurethane: particles migrate to the surface during drying of the coating. (b) Fluorinated wax crystals with silica nanoparticles “floating” at its surface: nanoparticles are expelled from the wax during crystallization. Reprinted from ⁶⁰ and ⁶¹, Copyright 2016 Wiley and 2012 American Chemical Society, respectively.

In 2003, Shirtcliffe *et al.*⁶² produced superhydrophobic sol-gel foams from organosilanes such as methyltriethoxysilane (MTEOS) or propyltriethoxysilane (PTEOS). Depending of the precipitation conditions, nanofeatures or microfeatures were obtained (Figure 36). As the silica is obtained from a slightly hydrophobic precursor, the foam with the tinier features exhibits a Cassie-Baxter’s regime superhydrophobicity without any further surface energy reduction, with a water contact angle of 155° and a hysteresis of 6°.

However, the foam with the larger features has a relatively high water contact angle of 153° , but also a high hysteresis of 16° . Cassie-Baxter's regime superhydrophobicity could still be obtained by either abrading the surface, thus reducing the contact angle hysteresis to 4° , or reducing the surface tension using trimethylsilyl- groups, thus reducing the contact angle hysteresis to 7° . The abrasion of the surface leading to superhydrophobicity is interesting, as most superhydrophobic surfaces lose their wetting properties when abraded.

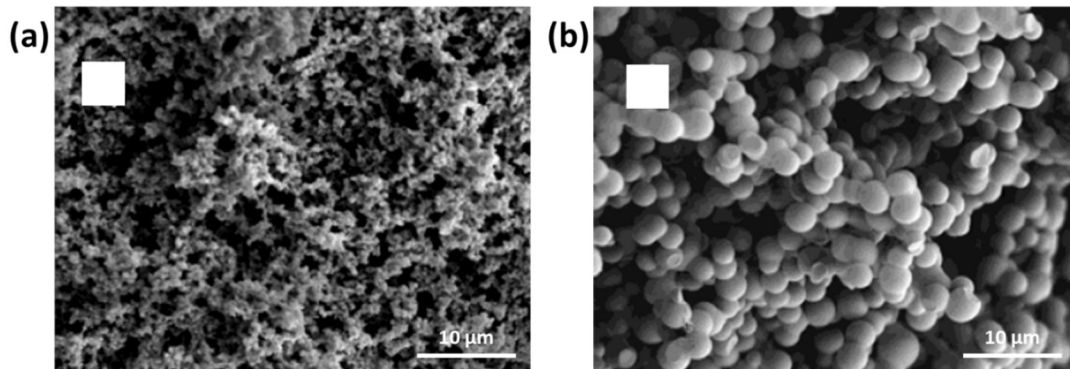


Figure 36 – Superhydrophobic organosilica sol-gel foams. (a) Foam slice with nanofeatures obtained from quick phase separation and (b) foam slice with microfeatures obtained from a slow phase separation. Reprinted from ⁶², Copyright 2003 American Chemical Society.

Texturing a surface by coating hydrophobic particles such as silica, zinc oxide or even carbon nanotube, as well as using such particles in the bulk and let them migrate to the surface, efficiently lead to superhydrophobicity. However, most of these processes require a fine tuning of the nanoparticles size and surface modification, or even assembly. For most approaches, a specific deposition technic is needed, limiting the transfer to low-value materials at an industrial scale.

Table 4 – Summary of superhydrophobic textured surfaces from hydrophobic particles

Substrate	Texture			Ref
	Particles	Binder	Process	
Aluminum	Zinc oxide	PDMS	Spraying	50
PDMS	Zinc oxide	None	ZnO-in-water deposition	51
Glass	Silica	Poly(urethane-acrylate)	Bar-coating	52
Glass	Silica	Polystyrene or epoxy resin	Spin-coating, bar-coating or doctor blade coating	53
Glass	Silica	None	Spin-coating	54
Silicon	Silica	None	Soot-templating	55
Glass	CaCO ₃ and silica	PDMS	Spraying	56
Steel	Silica (25 and 500nm)	Polyacrylate	Spraying	57
Glass, mica, metals	Carbon nanotubes	Poly(phenylenevinylene)	Solution deposition	58
Aluminum	Carbon nanotubes	Poly(phenylene sulfide) and silicon rubber	Spraying	59
Glass	Diatomaceous earth	Epoxy resin or polyurethane-in-THF	Unknown	60
None	Silica	Fluorinated wax	Surface migration	61
None	Silica	None	Sol-gel route	62

III.3.c. “Self-texturation” of polymers

III.3.c.i. Precipitation/crystallization of polymers from solutions

In 2003, Erbil *et al.*⁶³ proposed a very simple process to generate superhydrophobic polypropylene (PP) surfaces. By crystallizing and precipitating PP on a substrate from a xylene solution, they were able to obtain a highly porous coating, with intrinsically hydrophobic PP micrometric particles. Crystallization/precipitation rate was controlled by either the temperature, that affects the solvent evaporation rate, or by adding a non-solvent such as methylethylketone (MEK).

The surface obtained using the xylene/MEK solution appears to have smaller particles size than with pure xylene. This can be explained by the use of MEK, acting as a phase-separator for PP/solvent. With phase-separation, the nucleation rate is higher in the polymer-rich phase, leading to smaller particles (Figure 37a). For pure xylene solutions, the solvent evaporation rate, controlled through the drying temperature, has a major impact on the final morphology. The lower the drying temperature, the slower the crystallization and the higher the nucleation rate, resulting in a more crystalline coating with smaller particles (Figure 37b). The drying temperature has thus an impact on wetting properties, with a water contact angle decreasing from 155° to 138° with drying temperature increasing from 30°C to 70°C with pure xylene.

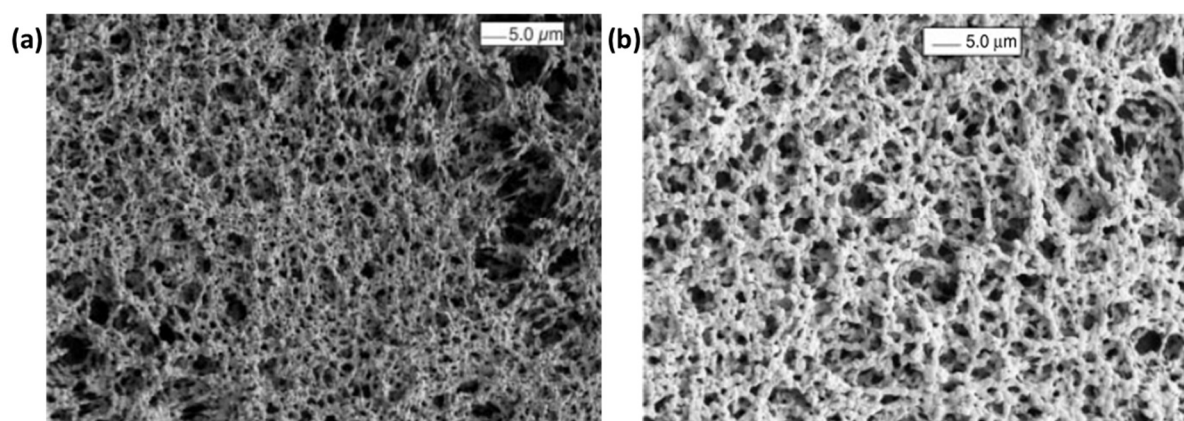


Figure 37 – Superhydrophobic coating from crystallization/precipitation of polypropylene. (a) Small PP particles obtained from precipitation and crystallization from a xylene/MEK solution, (b) Larger PP particles obtained from crystallization from a pure xylene solution. Reprinted from⁶³, Copyright 2003 American Association for the Advancement of Science

Such a PP crystallization and precipitation process have been widely reproduced in various conditions, in order to produce different particles shapes, or to simplify the process. For example in 2008, Rioboo *et al.*⁶⁴ made superhydrophobic PP surfaces from a pure xylene solution, with a coating drying at room temperature, thus allowing the preparation of larger surfaces. To do so, they prepared PP in pure xylene solutions at 135°C, and then cooled these solutions at around 60°C, just before gelation. These solutions were then coated on glass slides. The resulting surfaces were found to be superhydrophobic, with no observed impact of the polypropylene chain length, from 5'000 to 166'000 g/mol in number, or tacticity, on the resulting surface morphology.

In 2014, Hejazi *et al.*⁶⁵ obtained superhydrophobic PP surfaces from crystallization and precipitation, enhanced by the addition of zinc oxide particles instead of using a non-solvent. To produce such surfaces, they first dispersed ZnO nanoparticles in xylene. PP pellets were then added at a temperature of 120°C to allow their complete dissolution. The resulting solution was casted on glass slides using a spin-coater and dried. As ZnO particles increase the PP crystallization rate, they showed that these particles promote a hierarchical texturing, that is believed to be key for superhydrophobicity (Figure 38a).

They proposed a precipitation mechanism for PP/ZnO blends in xylene, with PP crystallizing around ZnO particles in the PP-rich phase, leading to microparticles. These microparticles are coated with

tinier PP nanoparticles, from a PP-poor phase, that crystallizes from homogenous nucleation sites (Figure 38b). This all process leads to a hierarchical texture of micrometric spheres coated with nanometric ones, exhibiting a Cassie-Baxter's regime superhydrophobicity. However, an excess of ZnO particles can destroy superhydrophobicity, as particles could then be present at the surface, thus lowering the surface energy.

For surfaces obtained using pure PP solution in xylene, they proposed a mechanism to explain the single-scale texturing (Figure 38c): in the PP-rich phase, PP and solvent separate through a co-continuity network, on top of which crystalline nanospheres from PP-poor phase crystallization deposits (Figure 38d). This single-scale texturing is not superhydrophobic, with a water contact angle of 140° only, whereas surfaces obtained using ZnO as a nucleating agent had a water contact angle of 165° with a sliding angle of 4° .

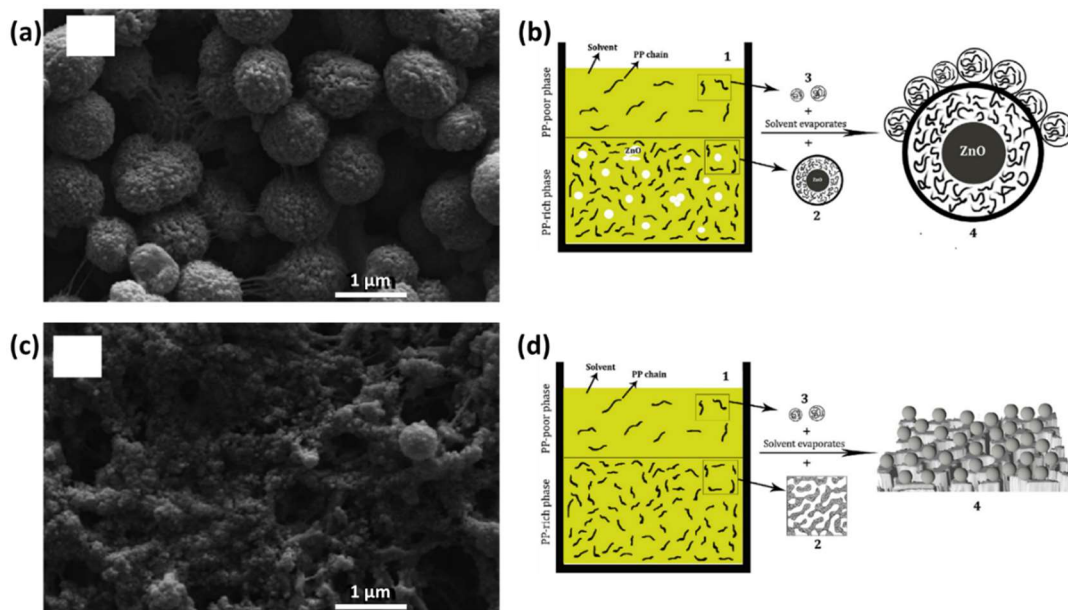


Figure 38 – Superhydrophobic PP surfaces obtained by precipitation from a xylene solution. (a) Superhydrophobic surface with a multiscale texture obtained using ZnO as a nucleating agent, and (b) proposed formation mechanism. (c) Non-superhydrophobic surface with a one-scale texture obtained from a pure xylene solution, and (d) proposed formation mechanism. Reprinted from ⁶⁵, Copyright 2014 Elsevier

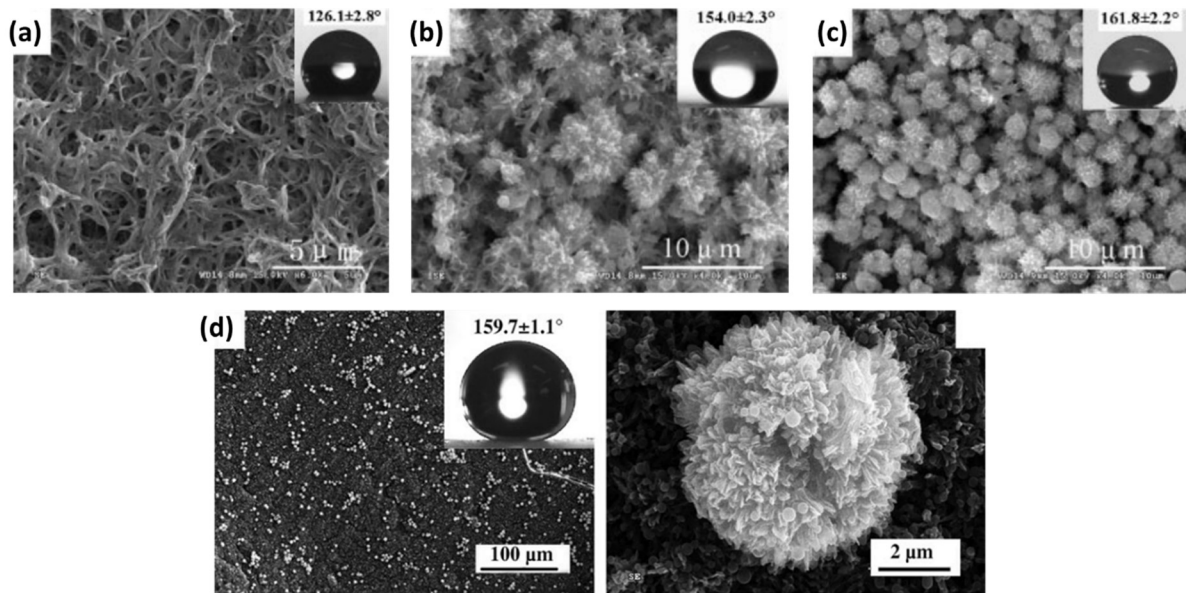


Figure 39 – Superhydrophobic polycarbonate surfaces. Precipitation from a DMF solution in air with (a) 0%, (b) 50% and (c) 75% relative humidity. (d) Precipitation from an acetone solution immersed in methanol. Reprinted from (a), (b), (c)⁶⁶ and (d)⁶⁷, Copyright 2005 and 2006 Wiley.

Zhao *et al.*^{66,67} obtained superhydrophobic surfaces from a similar process, using polycarbonate (PC) instead of PP, and DMF or acetone as a solvent. By swelling the PC sample with acetone by immersing it a few minutes, they were able to obtain a textured surface with high hydrophobicity (Figure 39a). However, in order to reach superhydrophobicity, they had to add a coagulator such as water or methanol to produce micrometric particles. The coagulator then acts as crystallization nuclei, leading to a hierarchical texturing, in a similar way to the one described by Hejazi *et al.*⁶⁵. The coagulator, a non-solvent, can be introduced in the solution by immersing the swollen PC sample directly into a solution of water or methanol (Figure 39d), by spraying it on the swollen PC, or simply by processing the PC in a humid atmosphere (with a relative humidity higher than 50%) (Figure 39b-c). The resulting flower-like hierarchically textured surface is superhydrophobic with water contact angles from 154° to 162°, and a sliding angle lower than 10°. Such process was also patented by Krishnan *et al.*⁶⁸ from the General Electric Company in 2007 (now abandoned).

In 2012, Cui *et al.*²⁸ followed a similar process to generate superhydrophobic hierarchically textured surfaces from PC and acetone, with a simple drying in air. They observed a strong relationship between the solvent exposure time and the resulting texture and thus superhydrophobicity after drying (Figure 40a). They estimated that a solvent exposure of at least 10 minutes was necessary for the surface to be sufficiently textured to have a water contact angle larger than 150°, and a relatively low sliding angle of 30°. Increasing the treatment duration over 30 minutes did not increase the superhydrophobicity, with a constant water contact angle around 152° and sliding angle of 30° (Figure 40b). They also showed that such surfaces had a strong Cassie-Baxter's regime superhydrophobicity upon pressure, with 9μL water droplets falling at 0.63 m/s on the surface not being pinned on it but simply bouncing.

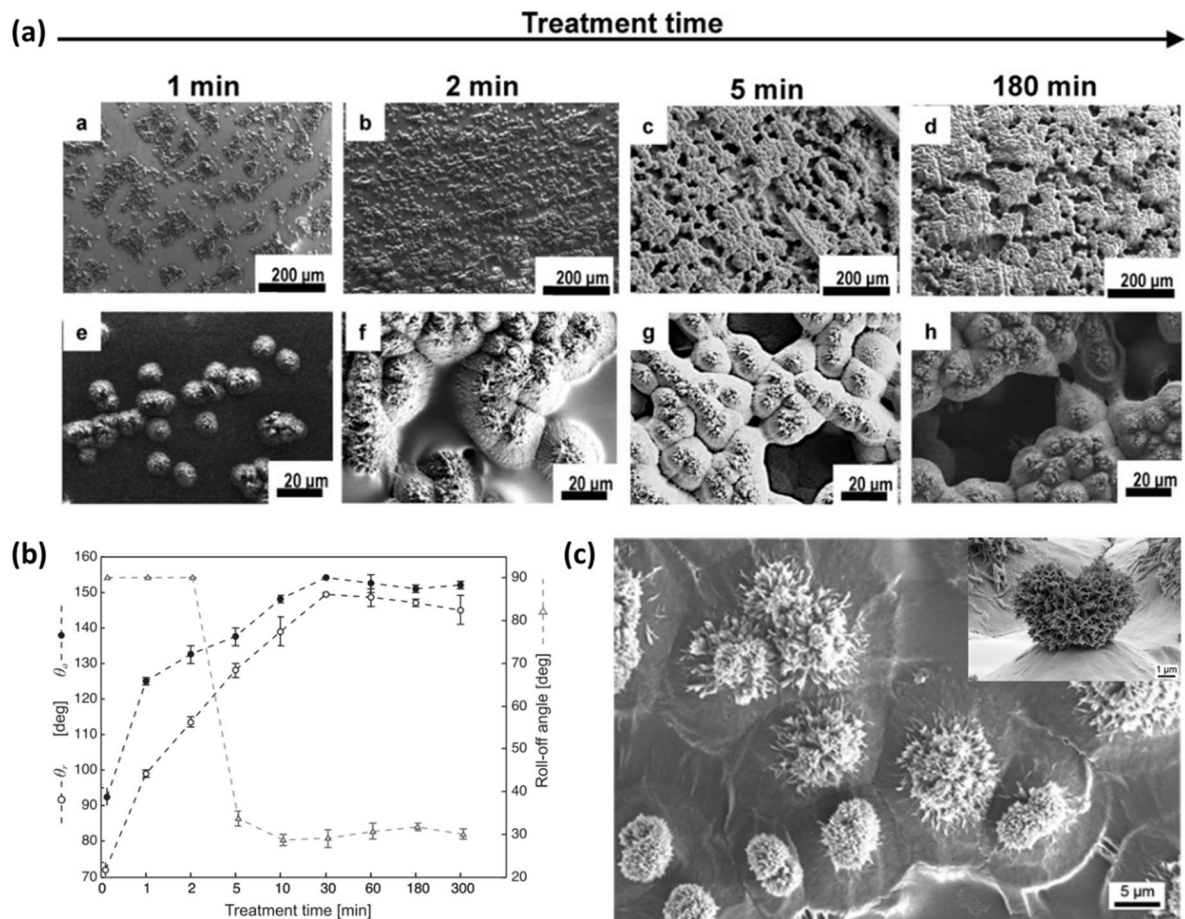


Figure 40 – Superhydrophobic PC surfaces from acetone solution. (a) PC surface roughness with immersion time in an acetone solution, and (b) corresponding water contact angle and sliding angle. (c) Superoleophobic PC surface with re-entrant asperities. Reprinted from (a), (b)²⁸ and (c)¹⁴, Copyright 2012 Elsevier and 2016 Springer-Nature, respectively.

Brown and Bhushan¹⁴ went further by adding nanoparticles in suspension in acetone, thus leading to a hierarchically textured surface with widely spaced large protrusion, with re-entrant angles (Figure 40c). Such surfaces exhibit Wenzel's regime superhydrophobicity, but after surface energy reduction using a fluorosilane, the resulting surface exhibits both superhydrophobicity, with a water contact angle of 165° and a sliding angle of 2°, as well as superoleophobicity with a hexane contact angle of 154° with a sliding angle of 5°. This superomniphobic surface had also a good mechanical resistance to abrasion, with no loss of superoleophobicity after 200 cycles of ball-on-flat tribometer wear experiment with 20mN load. With a higher load (45mN), the surface appears scratched, but the structure itself seems to resist, with a complete recovery of the superoleophobicity after a simple refluorination.

In 2018, Cheng *et al.*¹⁷ obtained a superhydrophobic and superoleophilic high density polyethylene (HDPE) sponge for water and oil separation, following a process similar to the one used by Erbil⁶³. They dissolved HDPE in xylene at 120°C, before adding ethanol in the resulting solution generating a phase separation. They obtained a superhydrophobic sponge by immersing a simple kitchen sponge into the resulting solution (Figure 41a). After at least three dipping and drying cycles, the resulting water contact angle was equal to 156°, thanks to HDPE intrinsic hydrophobicity and to the sheet-like structures obtained from precipitation (Figure 41b). Similar wetting properties were obtained on a smooth surface like a glass slide, or even on a copper mesh. However, the copper mesh holes were blocked, while the sponge main structure remained unchanged, permitting an efficient oil absorption.

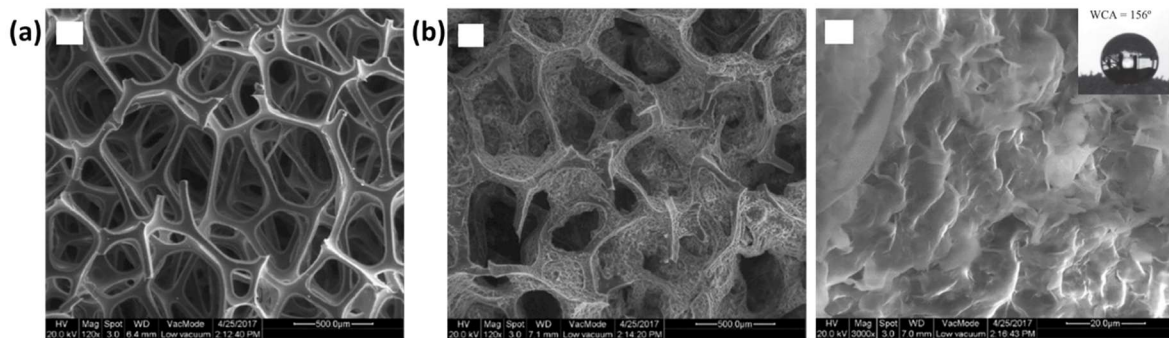


Figure 41 – Superhydrophobic and superoleophilic sponge. (a) Untreated kitchen sponge structure. (b) Kitchen sponge covered with HDPE deposited from a xylene/ethanol solution, preserving the sponge structure and adding a microstructure combined with hydrophobization, and corresponding water CA. Reprinted from ¹⁷, Copyright 2018 Elsevier

Xie *et al.*⁶⁹ obtained similar superhydrophobic surfaces in 2004 using polymethylmethacrylate (PMMA) combined with a fluorinated polyurethane (FPU). They first dissolved PMMA in dimethylformamide (DMF) at 5%_wt. The solution was then directly casted on a glass slide and dried. The resulting textured PMMA surface has a relatively high water contact angle of 140°, but also a strong adhesion of the water droplet to the surface, revealing a Wenzel's regime wetting (Figure 42a).

By dissolving at least 20%_wt of a fluorinated polyurethane with PMMA, while using the same procedure, the resulting surface turned out to be superhydrophobic, with a water contact angle of 166° and a sliding angle of 3° (Figure 42b). They assumed that the PMMA precipitation upon drying stayed unchanged with the addition of FPU. However, the FPU precipitated at the end of the drying, resulting in a covering of the PMMA microstructure with a low surface energy material. The combination of the texture obtained from PMMA precipitation and the low surface tension obtained by using FPU made the surface superhydrophobic.

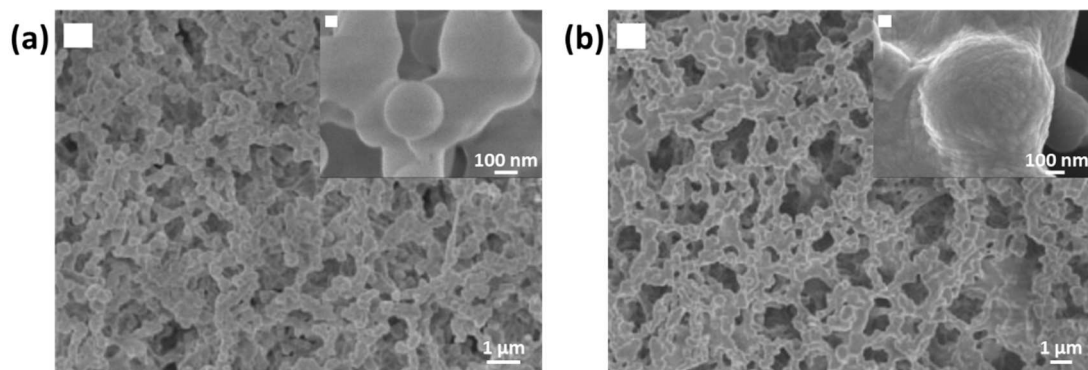


Figure 42 – Superhydrophobic PMMA/FPU textured surface. (a) Textured pure PMMA surface, exhibiting a Wenzel's wetting behavior, and (b) textured PMMA/FPU surface with a Cassie-Baxter's regime superhydrophobicity. Reprinted from ⁶⁹, Copyright 2004 Wiley

Such a process has been applied not only on PP, PC or PE, but to a large variety of polymers. For example, Sousa *et al.*⁷⁰ obtained superhydrophobic surfaces for bacterial colonization using poly(L-lactic acid) (PLLA), casted from a diluted solution (13%_wt PLLA in dioxane) on a smooth PLLA surface. After drying the coating, they obtained a textured surface composed of rounded protrusions which seems to be composed of nanometric fibrils, leading to a superhydrophobic behavior with a water contact angle of 154° (Figure 43a).

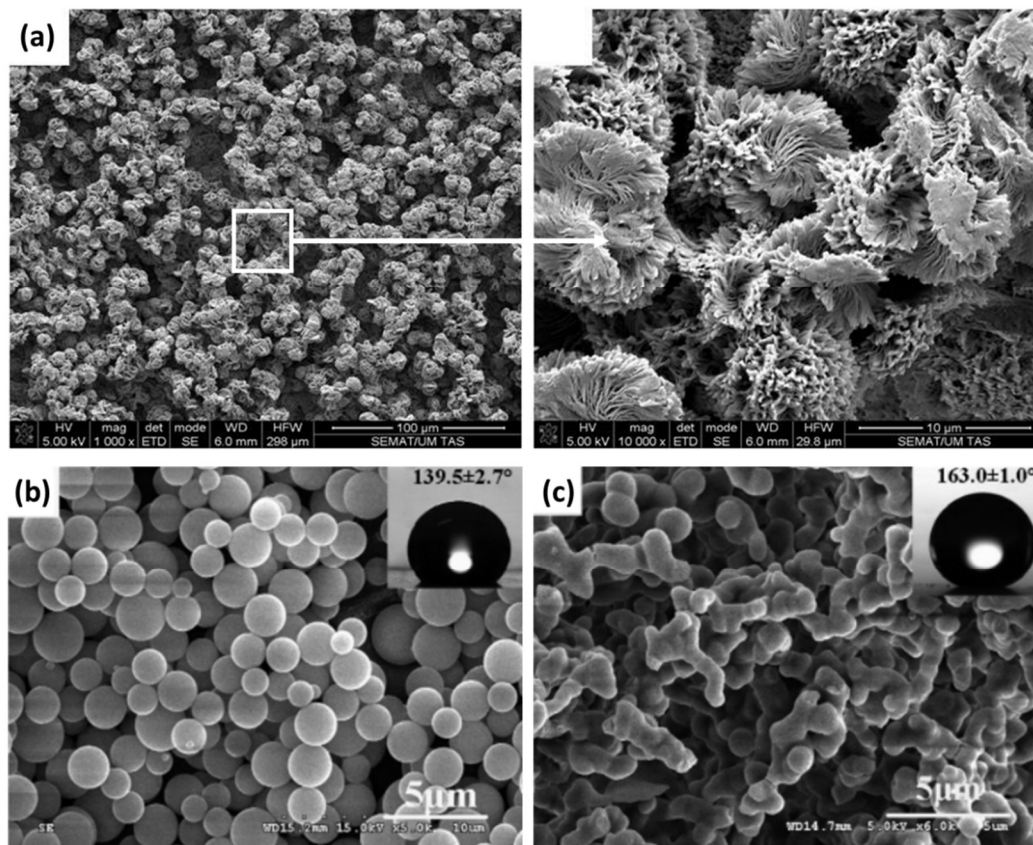


Figure 43 – Superhydrophobic textured surfaces from polymer precipitation. (a) Textured PLLA superhydrophobic surface from a PLLA/dioxane solution. (b) Textured hydrophobic PS surface from a PS/DMF solution casted in humid air. (c) Textured superhydrophobic surface from a PS-*b*-PDMS block copolymer casted from a DMF solution in humid air. Reprinted from (a)⁷⁰ and (b,c)⁷¹, Copyright 2011 Springer and 2005 American Chemical Society, respectively.

Zhao *et al.*⁷¹ obtained superhydrophobic surfaces from a polystyrene and polydimethylsiloxane block copolymer. They first tried to cast pure PS from a DMF solution on glass slides. When coating in dry air (relative humidity of less than 10%), the resulting surface was smooth. When the air was humid (with a RH of 605%), micrometric spheres of PS were obtained (Figure 43b). However, such a surface was only hydrophobic, with a water contact angle of 140°.

By repeating the same process with a PS-*b*-PDMS block copolymer, they were able to obtain a superhydrophobic textured surface, with a coalescent-sphere-like microstructure, and a water contact angle of 163° and a sliding angle of 7° (Figure 43c). They explained the texturing by the formation of PS-*b*-PDMS micelles upon drying, with a PS core and a PDMS shell. The micelle formation leads to round asperities that started to coalesce before being frozen when the drying was complete. Just like for PP or PC, non-solvent seems to play a key role in the precipitation process resulting in such textured surfaces. This non-solvent can be directly added to the solution or slowly diffused into the coated solution from a vapor form.

Superhydrophobic surfaces were also obtained by precipitating a polymer in a solvent and then spraying it on a substrate: Aruna *et al.*⁷² obtained such surface by dissolving PS in THF, adding ethanol as a non-solvent until the precipitation of the solution, revealed by the appearance of a white precipitate, and then spraying this solution on glass slides.

Werner *et al.*⁷³ patented such a process for the SweeTree Technologies AB Company in 2009, using CO₂ in supercritical conditions as CO₂ as a solvent, and provoking the precipitation of a hydrophobic substance such as stearic acid upon depressurization of the fluid, leading in a decrease of its solvency power. The hydrophobic substance is thus simultaneously precipitated and sprayed on a substrate, resulting in a textured superhydrophobic surface.

III.3.c.ii. Original processes

Original processes have also been proposed to generate superhydrophobic surfaces by crystallizing hydrophobic substances. For example, Niemietz *et al.*⁷⁴ extracted the epicuticular wax from Indian cress (*Nasturtium*) leaves, which consist of a mix of various aliphatic components with 27-29 carbon with primary or second alcohols or diols. They deposited this wax on glass slides by thermal evaporation, and observed that an ageing of the coating, at room temperature or in an oven at 50°C, leads to the grow of epicuticular wax crystals with a cylindrical shape. The resulting textured surface is superhydrophobic with a water contact angle up to 164° and a contact angle hysteresis down to 5° (Figure 44a).

In 2012, Pechook and Pokroy⁷⁵ have obtained similar superhydrophobic surfaces by crystallizing n-hexatriacontane wax by thermal deposition, as well as Bhushan *et al.*⁸. The just-coated surfaces exhibit hydrophobicity with a water contact angle of 116°. But as the coating were aged a few days at room temperature, the wax crystallized into epitaxial platelets, that after 100h of aging led to superhydrophobicity with a water contact angle of 156° (Figure 44b).

They later⁷⁶ produced a superhydrophobic surface from n-paraffin waxes of various chain lengths, by thermal deposition, decreasing the ageing time by increasing the temperature up to 40°C. With this process, they obtained surfaces with a one-scale texture (Figure 44c-d). Various structure were obtained from using different waxes, and hierarchically textured surfaces were also obtained (Figure 44e). To do so, they deposed a wax after another, provoking a crystallization of the second wax on the first crystals. Surfaces with a multiscale texture seems to have the same wetting behavior with water, with the same water contact angle and contact angle hysteresis as their monoscale counterparts. However, multiscale roughness seems to provide a stronger superhydrophobicity, with glycerol contact angle higher than for monoscale surfaces, with values up to 168°, while no indication of the contact angle hysteresis was provided. Hierarchically textured surfaces also show an increase of their pressure resistance, with a Cassie-Baxter's wetting regime kept longer upon droplet evaporation than with their monoscale counterparts, probably because of a reduced asperities size.

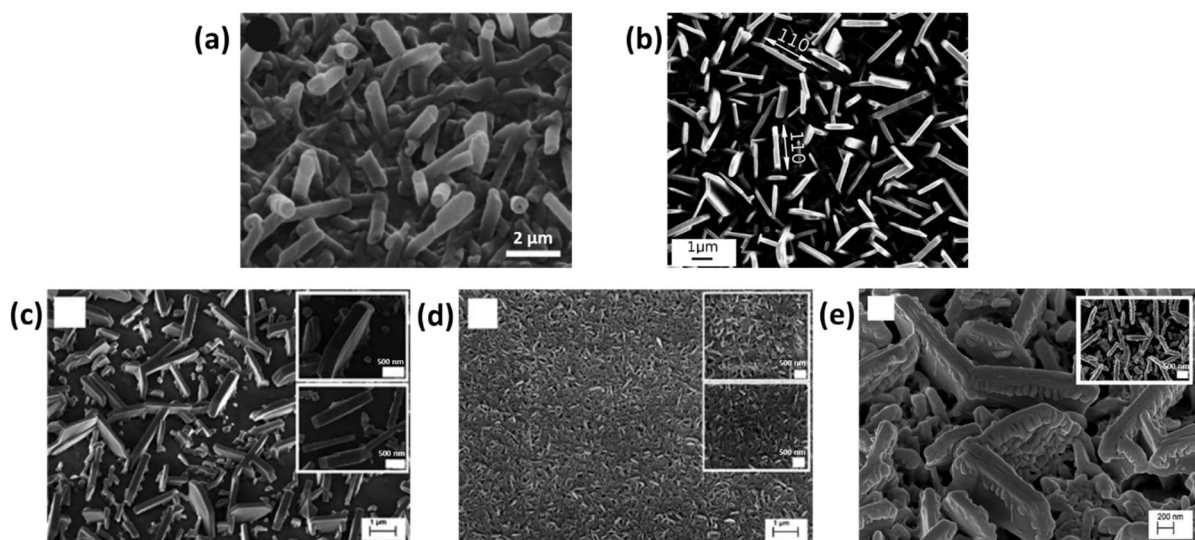


Figure 44 – Superhydrophobic surfaces from epitaxial wax crystals. (a) Indian cress wax recrystallized on a glass slide, (b) n-hexatriacontane thermally deposited on glass slide and aged, (c) $C_{36}H_{74}$ epitaxial wax crystals, (d) $C_{44}H_{90}$ epitaxial wax crystals, (e) $C_{36}H_{74}$ epitaxial wax crystals with $C_{44}H_{90}$ epitaxial wax crystals grown on it. Reprinted from (a)⁷⁴, (b)⁷⁵ and (c-e)⁷⁶, Copyright 2009 Elsevier, 2012 Wiley, and 2013 The Royal Society of Chemistry, respectively.

Rizvi *et al.*⁷⁷ obtained superhydrophobic and superoleophilic porous materials from a simple polymer foaming process. By fibrillating PTFE in a PP matrix using a twin-screw extruder with high shear, and then foaming this material using Sc-CO₂, they were able to produce a superhydrophobic foam with a water contact angle of 160°. To do so, a blend of PP with 3%_{wt} fibrillated PTFE was introduced in a

single-screw extruder at a temperature higher than the PP melting point, and 10%_{wt} SC-CO₂ was introduced. The PP/PTFE/CO₂ mix was transferred into a second single-screw extruder, with a barrel at a temperature lower than the PP melting point, in order to start the PP crystallization with a shish-kebab structure around PTFE fibrils. A rapid depressurization at the extruder die led to the foaming of the PP matrix, with the SC-CO₂ turning into its gaseous phase. The differences of viscosity between amorphous and crystalline phases led to the formation of an open-cells foam, with an un-foamed skin on the filament surface. After cutting the filament in order to reveal its inner texture, or after ultrasonication to break the un-foamed skin, the foam exhibits both superhydrophilicity and superoleophilicity, with a complete absorption of substances such as gasoline and repellence of water.

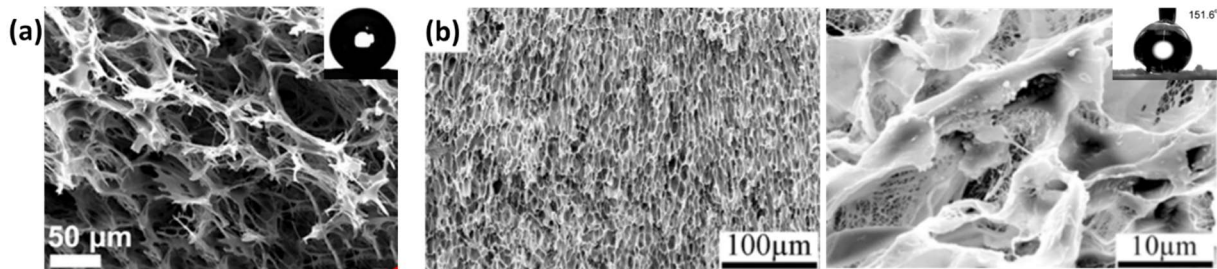


Figure 45 – Superhydrophobic polymer surfaces from foams. (a) Superhydrophobic and superoleophilic PP foam with PTFE fibrils from foaming with SC-CO₂ during and extrusion process, and (b) in a batch process. Reprinted from (a)⁷⁷ and (b)⁷⁸, Copyright 2014 and 2019 American Chemical Society, respectively.

Mi *et al.*⁷⁸ obtained similar superhydrophobic and superoleophilic porous materials with a batch-foaming process. In a first step, they mixed micrometric and nanometric PTFE particles in a PP matrix, using a dual-screw extruder. The PTFE microparticles were then fibrillated in the same twin-screw extruder at high temperature, leading to web-like structure. The resulting PP/PTFE composite was then foamed using Sc-CO₂: the blend was saturated with Sc-CO₂ at 20 MPa and 180°C, and a sudden pressure release leads the CO₂ to turn into its gaseous phase, leading to 10 μm large pores. During pores expansion, PTFE fibrils and nanoparticles are found to be staying at the surface, or even across the pores. The resulting foam surface exhibits a Cassie-Baxter's regime superhydrophobicity, with a water contact angle of 152° and a hysteresis of 5° (Figure 45c). When the inner structure of the foam is revealed, by slicing, fracturing or abrading with sandpaper, the superhydrophobicity was even higher, with a water contact angle up to 157°. The combination of dual-size PTFE particles with PP micropores seems to be at the origin of such wetting properties. In fact, PTFE nanoparticles reduce the surface energy and PTFE fibrils from PTFE microparticles increase the texturing and reduce the surface energy of the foam.

In summary, “self-texturing” polymers with a relatively low surface energy could permit the production of low-cost superhydrophobic surfaces. The materials and setups involved are relatively common, and lowly expensive. However, the toxicity of some solvents, as well as the batch-oriented production and the need of a post-treatment for some samples forbid its industrial transfer. Still, these methods are the most suitable for low-cost and industrially-friendly applications when compared to all the existing processes. From the inspiration given by such approaches, easy ways to texture a surface into superhydrophobicity will be investigated in the next chapters.

Table 5 – Summary of superhydrophobic surfaces from self-textured polymers

Substrate	Texture		Ref.
	Polymer	Process	
Glass	PP	Precipitation from a xylene/MEK solution	63
PP	PP	Precipitation from a xylene solution	64
Glass	PP	Precipitation from a xylene or xylene/ZnO solution	65
PC	PC	Crystallization/precipitation by immersing PC in acetone or DMF, additive with water or methanol	66–68
PC	PC	Crystallization/precipitation by immersing PC in acetone	28
PC	PC	Crystallization/precipitation by immersing PC in acetone with silica nanoparticles	14
Kitchen sponge	HDPE	Crystallization/precipitation from a xylene solution with ethanol	17
Glass	PMMA-FPU	Precipitation from a DMF solution	69
PLLA	PLLA	Precipitation from a dioxane solution	70
Glass	PS-b-PDMS	Precipitation from a DMF solution in humid conditions	71
Glass	PS	Precipitation by adjunction of ethanol in a THF solution, and spraying	72
Unspecified	Stearic acid	Precipitation from a Sc-CO ₂ solution during spraying (<i>i.e.</i> pressure release)	73
Glass	Natural or paraffinic waxes	Epitaxial crystallization by thermal evaporation	8,74,75,79
None	S-PEEK PAH/PAA polyelectrolyte multilayer	Complexation of S-PEEK with PAH, and aggregation with PAA, hydrophobized using a fluorosilane	80
None	PP with PTFE fibrils	Foaming PP with PTFE fibrils using Sc-CO ₂	77,78

III.4. Conclusion

It has been highlighted that there are numerous ways to achieve superhydrophobicity, by mimicking the natural surfaces or by producing completely tailored artificial surfaces. Superhydrophobicity can be brought on an already textured surface by lowering its surface energy, thanks to fluorinated substances for examples. On the opposite, a hydrophobic surface can be turned superhydrophobic by texturing it by etching, molding, self-organizing, *etc.* Superhydrophobicity can finally be brought to various substrate by depositing a coating that textures and reduces the surface energy of the solid in the same time.

However, most of these approaches are time-consuming and expensive, limiting their use for producing small superhydrophobic samples. When the materials or setups were not too expensive, the numerous required steps limit the transfer of such processes to an industrial scale.

Still, some interesting pathways are promising for producing superhydrophobic textured surfaces at a larger scale from hydrophobic thermoplastics. These approaches are:

- the use of fillers in the bulk that texture surface,
- using the self-organizing properties of polymer blends,
- foaming a polymer in a batch or continuous process, or
- precipitating a polymer from a solution.

These approaches will be further investigated in the following chapters.

IV. Chapter conclusion

Wettability is an essential surface property of materials as it governs adhesion. The wettability of a solid primarily depends on its surface energy, and the surface tension of the liquid. Nevertheless, the surface texture has also a key role in wetting by promoting adhesion or repellence, depending on the interface shape, homogeneous or heterogeneous. A homogeneous wetting, with liquid penetrating between asperities, is called a Wenzel's state. With such a wetting regime the solid/liquid adhesion is strong and the contact angle will spectacularly increase or decrease with the surface roughness depending on the Young contact angle of the solid/liquid couple. A heterogeneous wetting, with air trapped in the surface texture below the liquid, like a fakir carpet, is denoted as a Cassie-Baxter's state. Such a wetting regime leads to the liquid being in contact with only a fraction of the solid, the other fraction of the interface being in contact with air. Such an interface results in a low adhesion of the liquid, that is almost sliding on an air carpet. This reduced adhesion is traduced by a high contact angle, whatever the Young contact angle value.

The conditions of stability of Wenzel's and Cassie-Baxter's regimes were described. The transition from a Cassie-Baxter's to a Wenzel's regime occurs spontaneously or after applying a critical pressure on the interface. Even if a Wenzel's regime leads to a high contact angle with hydrophobic materials, a Cassie-Baxter's regime is more desirable for its low adhesion behavior.

Superhydrophobicity is in the same time a relatively common feature in Nature. An extensive research was done in the last two decades. Trying to mimic the Nature, in particular the lotus leaf, numerous superhydrophobic surfaces have been described and fabricated in the literature, from tailored monotonic pillars to isotropic particles stacks, coming with multiple processes. These processes are more or less simple, but always targeted the same goal; *i.e.* reducing the solid surface energy and texturing the surface to reach a stable superhydrophobicity. Other properties were sometimes considered, such as chemical resistance, abrasion resistance, magnetization, antibacterial behavior, electric conductivity, *etc.*

A promising way to easily reach superhydrophobicity is the use of hydrophobic polymers as the starting material, and texture them by various approaches. These approaches are for example using of fillers in the bulk that texture surface, using the self-organizing properties of polymer blends, foaming a polymer in a batch of continuous process, or precipitating a polymer from a solution. Simple ways of texturing a surface for superhydrophobicity will be the main focus of the following chapter, after the ideal texture would have been described.

Table 6 – Summary of studied superhydrophobic surfaces, depending on their texturing and surface energy reduction ways.

Texture		Surface energy		Ref.
Nature	Process	Nature	Process	
Wool textile	Weaving	PDMS	Grafting	37
Polyester textile	Weaving	Fluorinated silane	Grafting	38
PU foam	Foaming	PTFE	NP deposition	18
Silicon squared pillars	Micro-dicing	Fluorinated silane	Coating	40
PS and PMMA grooves	Imprinting	PS or PMMA	Intrinsic	41
Silicon hoodoos	Photolithography	PTFE or fluorinated silane	CVD	42
Epoxy resin hoodoos	Molding	Wax crystals	Thermal evaporation	8
PDMS folds	Molding and compression-folding	PDMS	Intrinsic	44
Silicon grooves	Laser etching	Fluorinated silane	Grafting	45
Aluminum Hills and valleys	Blasting	PTFE	Spraying	35
Alumina flakes with nanoporosities	Chemical etching and anodization	PTFE	PVD	46
Zinc, Copper, Zn-Cu alloy needles and flower-like	Chemical oxidation	Fluorinated acid	Grafting	19
Cobalt oxide needles	Epitaxial crystallization	Lauric acid	Grafting	47
Silver feather-like and flower-like	Galvanic exchange reaction	Benzoic acid	Grafting	48
Polyelectrolyte multilayers honeycomb-like	Acidic degradation and silica deposition	Fluorinated silane	Grafting	49
ZnO particles with PDMS	Spraying	PDMS	Matrix	50
ZnO particles	Solution deposition	PDMS	Substrate	51
Silica particles with PUA	Bar-coating	PUA	Matrix	52
Silica particles with PS or epoxy resin	Spin-coating, bar-coating, doctor-blade	PS or epoxy resin	Matrix	53
Silica particles packing	Spin-coating	Fluorinated silane	Grafting	54
	Soot-templating	Fluorinated silane	Grafting	55
	Surface migration	Fluorinated wax	Matrix	61
	Sol-gel route	Fluorinated silane	Sol-gel	62
CaCO ₃ and silica particles with PDMS	Spraying	PDMS	Matrix	56
Silica particles (25-500nm) with PA	Spraying	PA	Matrix	57
Carbon nanotubes	Solution deposition	PPV	Matrix	58
	Spraying	PPS and SR	Matrix	59
Diatomaceous earth	Coating (?)	Epoxy resin or PU	Matrix	60
Bead-like packs	Precipitation from xylene solution (with a non-solvent)	PP	Intrinsic	63–65
	Precipitation from DMF	PMMA-FPU	Intrinsic	69
	Precipitation from DMF in humid conditions	PS-b-PDMS	Intrinsic	71
	Precipitation from solvent (THF/ethanol or SC-CO ₂)	PS	Intrinsic	72,73
Flower-like	Crystallization/precipitation after solvent immersion	PC	Intrinsic	14,28,66–68
	Precipitation from dioxane	PLLA	Intrinsic	70
Flakes	Crystallization/precipitation from xylene/ethanol	HDPE	Intrinsic	17
Epitaxial waxes	Crystallization from thermal evaporation	Natural or paraffinic waxes	Intrinsic	8,74,75,79
Open cells foam with fibrils	Foaming PP with fibrillated PTFE	PP and PTFE	Intrinsic	77,78

V. References

1. Gilman, J. J. Direct Measurements of the Surface Energies of Crystals. *J. Appl. Phys.* **31**, 2208–2218 (1960).
2. Wu, S. Calculation of interfacial tension in polymer systems. *J. Polym. Sci. Part C Polym. Symp.* **34**, 19–30 (2007).
3. Owens, D. K. & Wendt, R. C. Estimation of the surface free energy of polymers. *J. Appl. Polym. Sci.* **13**, 1741–1747 (1969).
4. Young, T. An Essay on the Cohesion of Fluids. *Philos. Trans. R. Soc. London* **95**, 65–87 (1805).
5. Marmur, A. Hydro- hygro- oleo- omni-phobic? Terminology of wettability classification. *Soft Matter* **8**, 6867 (2012).
6. Makkonen, L. A thermodynamic model of contact angle hysteresis. *J. Chem. Phys.* **147**, 064703 (2017).
7. Wenzel, R. N. Resistance of solid surfaces to wetting by water. *Ind. Eng. Chem.* **28**, 988–994 (1936).
8. Bhushan, B. & Her, E. K. Fabrication of Superhydrophobic Surfaces with High and Low Adhesion Inspired from Rose Petal. *Langmuir* **26**, 8207–8217 (2010).
9. Parker, A. R. & Lawrence, C. R. Water capture by a desert beetle. *Nature* **414**, 33–34 (2001).
10. Cassie, A. B. D. & Baxter, S. Wettability of porous surfaces. *Trans. Faraday Soc.* **40**, 546 (1944).
11. Barthlott, W. & Neinhuis, C. Purity of the sacred lotus, or escape from contamination in biological surfaces. *Planta* **202**, 1–8 (1997).
12. Gao, L. & McCarthy, T. J. How Wenzel and Cassie Were Wrong. *Langmuir* **23**, 3762–3765 (2007).
13. Guldin, S. *et al.* Self-Cleaning Antireflective Optical Coatings. *Nano Lett.* **13**, 5329–5335 (2013).
14. Brown, P. S. & Bhushan, B. Durable, superoleophobic polymer–nanoparticle composite surfaces with re-entrant geometry via solvent-induced phase transformation. *Sci. Rep.* **6**, 21048 (2016).
15. Helbig, R., Nickerl, J., Neinhuis, C. & Werner, C. Smart Skin Patterns Protect Springtails. *PLoS One* **6**, e25105 (2011).
16. McHale, G., Newton, M. I. & Shirtcliffe, N. J. Immersed superhydrophobic surfaces: Gas exchange, slip and drag reduction properties. *Soft Matter* **6**, 714–719 (2010).
17. Cheng, Y. *et al.* Facile preparation of high density polyethylene superhydrophobic/superoleophilic coatings on glass, copper and polyurethane sponge for self-cleaning, corrosion resistance and efficient oil/water separation. *J. Colloid Interface Sci.* **525**, 76–85 (2018).
18. Calcagnile, P. *et al.* Magnetically Driven Floating Foams for the Removal of Oil Contaminants from Water. *ACS Nano* **6**, 5413–5419 (2012).
19. Li, H., Peng, Y., Yu, S. & Yin, X. Both slender pillars and hierarchical structures achieving superhydrophobicity and the comparison of their properties. *Appl. Surf. Sci.* **505**, 144524 (2020).
20. Smith, J. D. *et al.* Droplet mobility on lubricant-impregnated surfaces. *Soft Matter* **9**, 1772–1780 (2013).

21. Brown, P. S. & Bhushan, B. Liquid-impregnated porous polypropylene surfaces for liquid repellency. *J. Colloid Interface Sci.* **487**, 437–443 (2017).
22. Wang, J. *et al.* Viscoelastic solid-repellent coatings for extreme water saving and global sanitation. *Nat. Sustain.* **2**, 1097–1105 (2019).
23. Jacobi, I., Wexler, J. S. & Stone, H. A. Overflow cascades in liquid-infused substrates. *Phys. Fluids* **27**, (2015).
24. Yong, J., Chen, F., Yang, Q., Huo, J. & Hou, X. Superoleophobic surfaces. *Chem. Soc. Rev.* **46**, 4168–4217 (2017).
25. Panter, J. R., Gizaw, Y. & Kusumaatmaja, H. Multifaceted design optimization for superomniphobic surfaces. *Sci. Adv.* **5**, (2019).
26. Bico, J., Thiele, U. & Quéré, D. Wetting of textured surfaces. *Colloids Surfaces A Physicochem. Eng. Asp.* **206**, 41–46 (2002).
27. Marmur, A. Wetting on Hydrophobic Rough Surfaces: To Be Heterogeneous or Not To Be? *Langmuir* **19**, 8343–8348 (2003).
28. Cui, Y., Paxson, A. T., Smyth, K. M. & Varanasi, K. K. Hierarchical polymeric textures via solvent-induced phase transformation: A single-step production of large-area superhydrophobic surfaces. *Colloids Surfaces A Physicochem. Eng. Asp.* **394**, 8–13 (2012).
29. Tuteja, A., Choi, W., Mabry, J. M., McKinley, G. H. & Cohen, R. E. Robust omniphobic surfaces. *Proc. Natl. Acad. Sci.* **105**, 18200–18205 (2008).
30. Zhang, J. & Zhao, H. Pinning and wetting stability of liquids on superoleophobic textured surfaces. *Surf. Innov.* **2**, 103–115 (2014).
31. Marmur, A. Underwater superhydrophobicity: Theoretical feasibility. *Langmuir* **22**, 1400–1402 (2006).
32. Herminghaus, S. Roughness-induced non-wetting. *Europhys. Lett.* **52**, 165–170 (2000).
33. Lei, L., Li, H., Shi, J. & Chen, Y. Diffraction Patterns of a Water-Submerged Superhydrophobic Grating under Pressure. *Langmuir* **26**, 3666–3669 (2010).
34. Rathgen, H. & Mugele, F. Microscopic shape and contact angle measurement at a superhydrophobic surface. *Faraday Discuss.* **146**, 49 (2010).
35. Poetes, R., Holtzmann, K., Franze, K. & Steiner, U. Metastable Underwater Superhydrophobicity. *Phys. Rev. Lett.* **105**, 166104 (2010).
36. Nishino, T., Meguro, M., Nakamae, K., Matsushita, M. & Ueda, Y. The Lowest Surface Free Energy Based on –CF₃ Alignment. *Langmuir* **15**, 4321–4323 (1999).
37. Zhang, B. T. *et al.* Fabricating superhydrophobic surfaces by molecular accumulation of polysiloxane on the wool textile finishing. *Colloid Polym. Sci.* **286**, 453–457 (2008).
38. Wang, H., Xue, Y. & Lin, T. One-step vapour-phase formation of patternable, electrically conductive, superamphiphobic coatings on fibrous materials. *Soft Matter* **7**, 8158–8161 (2011).
39. Jasper, J. J. The Surface Tension of Pure Liquid Compounds. *J. Phys. Chem. Ref. Data* **1**, 841–1010 (1972).
40. Yoshimitsu, Z., Nakajima, A., Watanabe, T. & Hashimoto, K. Effects of Surface Structure on the Hydrophobicity and Sliding Behavior of Water Droplets. *Langmuir* **18**, 5818–5822 (2002).

41. Zhang, F. & Low, H. Y. Anisotropic wettability on imprinted hierarchical structures. *Langmuir* **23**, 7793–7798 (2007).
42. Zhao, H., Law, K. Y. & Sambhy, V. Fabrication, surface properties, and origin of superoleophobicity for a model textured surface. *Langmuir* **27**, 5927–5935 (2011).
43. Zhao, H. & Law, K. Y. Directional self-cleaning superoleophobic surface. *Langmuir* **28**, 11812–11818 (2012).
44. Zhao, X. L., An, W. W., Yan, J. C., Yu, H. C. & Wang, L. Q. Wettability of Polymeric Bionic Surface Replicated from Ginkgo Leaves. *Key Eng. Mater.* **625**, 736–741 (2014).
45. Song, X., Zhai, J., Wang, Y. & Jiang, L. Fabrication of Superhydrophobic Surfaces by Self-Assembly and Their Water-Adhesion Properties. *J. Phys. Chem. B* **109**, 4048–4052 (2005).
46. Weibel, D. E. *et al.* Adjustable Hydrophobicity of Al Substrates by Chemical Surface Functionalization of Nano/Microstructures. *J. Phys. Chem. C* **114**, 13219–13225 (2010).
47. Hosono, E., Fujihara, S., Honma, I. & Zhou, H. Superhydrophobic perpendicular nanopin film by the bottom-up process. *J. Am. Chem. Soc.* **127**, 13458–13459 (2005).
48. Sarkar, D. K. & Saleema, N. One-step fabrication process of superhydrophobic green coatings. *Surf. Coatings Technol.* **204**, 2483–2486 (2010).
49. Zhai, L., Cebeci, F. C., Cohen, R. E. & Rubner, M. F. Stable superhydrophobic coatings from polyelectrolyte multilayers. *Nano Lett.* **4**, 1349–1353 (2004).
50. Chakradhar, R. P. S., Kumar, V. D., Rao, J. L. & Basu, B. J. Fabrication of superhydrophobic surfaces based on ZnO–PDMS nanocomposite coatings and study of its wetting behaviour. *Appl. Surf. Sci.* **257**, 8569–8575 (2011).
51. Zhang, J., Pu, G. & Severtson, S. J. Fabrication of Zinc Oxide/Polydimethylsiloxane Composite Surfaces Demonstrating Oil-Fouling-Resistant Superhydrophobicity. *ACS Appl. Mater. Interfaces* **2**, 2880–2883 (2010).
52. Fourmentin, A., Galy, J., Charlot, A. & Gérard, J.-F. Bioinspired silica-containing polyurethane-acrylate films: Towards superhydrophobicity with tunable water adhesion. *Polymer (Guildf)*. **155**, 1–12 (2018).
53. Söz, C. K., Yilgör, E. & Yilgör, I. Simple processes for the preparation of superhydrophobic polymer surfaces. *Polymer (Guildf)*. **99**, 580–593 (2016).
54. Sheen, Y., Huang, Y., Liao, C., Chou, H. & Chang, F. New approach to fabricate an extremely super-amphiphobic surface based on fluorinated silica nanoparticles. *J. Polym. Sci. Part B Polym. Phys.* **46**, 1984–1990 (2008).
55. Wang, D. *et al.* Design of robust superhydrophobic surfaces. *Nature* **582**, 55–59 (2020).
56. Yang, J. *et al.* A novel method to fabricate superhydrophobic surfaces based on well-defined mulberry-like particles and self-assembly of polydimethylsiloxane. *Appl. Surf. Sci.* **255**, 3507–3512 (2009).
57. Zhu, B. *et al.* Superhydrophobic coating with multiscale structure based on crosslinked silanized polyacrylate and nanoparticles. *Surf. Coatings Technol.* **331**, 40–47 (2017).
58. Srinivasan, S., Praveen, V. K., Philip, R. & Ajayaghosh, A. Bioinspired Superhydrophobic Coatings of Carbon Nanotubes and Linear π Systems Based on the “Bottom-up” Self-Assembly Approach. *Angew. Chemie* **120**, 5834–5838 (2008).

59. Lv, C. *et al.* A fluorine-free superhydrophobic PPS composite coating with high thermal stability, wear resistance, corrosion resistance. *Prog. Org. Coatings* **110**, 47–54 (2017).
60. Perera, H. J., Khatiwada, B. K., Paul, A., Mortazavian, H. & Blum, F. D. Superhydrophobic surfaces with silane-treated diatomaceous earth/resin systems. *J. Appl. Polym. Sci.* **133**, 36–38 (2016).
61. Puretskiy, N., Stoychev, G., Synytska, A. & Ionov, L. Surfaces with Self-repairable Ultrahydrophobicity Based on Self-organizing Freely Floating Colloidal Particles. *Langmuir* **28**, 3679–3682 (2012).
62. Shirtcliffe, N. J., McHale, G., Newton, M. I. & Perry, C. C. Intrinsically superhydrophobic organosilica sol-gel foams. *Langmuir* **19**, 5626–5631 (2003).
63. Erbil, H., Demirel, A. L., Avci, Y. & Mert, O. Transformation of a Simple Plastic into a Superhydrophobic Surface. *Science (80-.)*. **299**, 1377–1380 (2003).
64. Rioboo, R. *et al.* Superhydrophobic Surfaces from Various Polypropylenes. *Langmuir* **24**, 9508–9514 (2008).
65. Hejazi, I. *et al.* Role of nanoparticles in phase separation and final morphology of superhydrophobic polypropylene/zinc oxide nanocomposite surfaces. *Appl. Surf. Sci.* **293**, 116–123 (2014).
66. Zhao, N. *et al.* Fabrication of biomimetic superhydrophobic coating with a micro-nano-binary structure. *Macromol. Rapid Commun.* **26**, 1075–1080 (2005).
67. Zhao, N. *et al.* A lotus-leaf-like superhydrophobic surface prepared by solvent-induced crystallization. *ChemPhysChem* **7**, 824–827 (2006).
68. Krishnan, K. *et al.* Method to modify surface of an article and the article obtained therefrom. *Pat. N° US 20070009709A1* (2017).
69. Xie, Q. *et al.* Facile Creation of a Super-Amphiphobic Coating Surface with Bionic Microstructure. *Adv. Mater.* **16**, 302–305 (2004).
70. Sousa, C. *et al.* Superhydrophobic poly(L-lactic acid) surface as potential bacterial colonization substrate. *AMB Express* **1**, 34 (2011).
71. Zhao, N. *et al.* Superhydrophobic surface from vapor-induced phase separation of copolymer micellar solution. *Macromolecules* **38**, 8996–8999 (2005).
72. S.T., A., P., B., Richard, E. & Basu, B. J. Properties of phase separation method synthesized superhydrophobic polystyrene films. *Appl. Surf. Sci.* **258**, 3202–3207 (2012).
73. Werner, O. P., Wagberg, L.-E. R., Turner, C. K. & Quand, C. Method to prepare superhydrophobic surfaces on solid bodies by rapid expansion solutions. *Pat. N° WO2009005465A1* (2009).
74. Niemietz, A., Wandelt, K., Barthlott, W. & Koch, K. Thermal evaporation of multi-component waxes and thermally activated formation of nanotubules for superhydrophobic surfaces. *Prog. Org. Coatings* **66**, 221–227 (2009).
75. Pechook, S. & Pokroy, B. Self-assembling, bioinspired wax crystalline surfaces with time-dependent wettability. *Adv. Funct. Mater.* **22**, 745–750 (2012).
76. Pechook, S. & Pokroy, B. Bioinspired hierarchical superhydrophobic structures formed by n-paraffin waxes of varying chain lengths. *Soft Matter* **9**, 5710 (2013).
77. Rizvi, A., Chu, R. K. M., Lee, J. H. & Park, C. B. Superhydrophobic and oleophilic open-cell foams from fibrillar blends of polypropylene and polytetrafluoroethylene. *ACS Appl. Mater. Interfaces*

- 6, 21131–21140 (2014).
78. Mi, H.-Y. *et al.* Highly Durable Superhydrophobic Polymer Foams Fabricated by Extrusion and Supercritical CO₂ Foaming for Selective Oil Absorption. *ACS Appl. Mater. Interfaces* **11**, 7479–7487 (2019).
79. Koch, K., Dommissé, A., Niemietz, A., Barthlott, W. & Wandelt, K. Nanostructure of epicuticular plant waxes: Self-assembly of wax tubules. *Surf. Sci.* **603**, 1961–1968 (2009).
80. Li, Y., Li, L. & Sun, J. Bioinspired Self-Healing Superhydrophobic Coatings. *Angew. Chemie Int. Ed.* **49**, 6129–6133 (2010).

CHAPTER 2 – DESIGNING SUPERHYDROPHOBIC SURFACES

Designing superhydrophobic surfaces

I. Literature Review	54
I.1. Wenzel’s and Cassie-Baxter’s wetting regimes balance	54
I.2. Effect of asperities size	55
I.3. Role of multi-scale roughness	56
I.4. Re-entrant asperities	58
I.5. Conclusion: Definition of an ideal superhydrophobic surface	59
II. Modeling superhydrophobicity as easily as possible	60
II.1. Model definition	60
II.2. Application to model surfaces	62
II.3. Conclusion	67
III. Confronting the model to the reality	68
III.1. Patterned and isotropic surfaces	68
III.2. Critical pressure prediction	69
III.3. Conclusion	71
IV. Chapter conclusion	72
V. References	73

For numerous applications, designing and producing superhydrophobic surfaces is a crucial issue. Differences between a fully wetted Wenzel’s regime and a partially wetted Cassie-Baxter’s regime have been highlighted in the first chapter. Through natural and artificial examples, a guideline has emerged: hydrophobicity and texturing together can successfully lead to slippery superhydrophobicity. However, the combination of these properties was not always successful in making superhydrophobic surfaces with a Cassie-Baxter’s regime. Various pathways led to very different-looking surfaces with the same properties, and some look-alike surfaces had different wetting behaviors. It is thus important to define some criterions and guidelines for the design of superhydrophobic surfaces, before looking for how to obtain the desired surface topography. At first, a quick review of the criteria proposed in the literature for reaching slippery superhydrophobicity will be presented. Then a simple model of prediction of a Cassie-Baxter’s interface stability with the topography parameters will be defined, and confronted to real surfaces. This model aims at giving a better understanding of the wetting behaviors, and also simple guidelines for the design of superhydrophobic surfaces

I. Literature Review

I.1. Wenzel's and Cassie-Baxter's wetting regimes balance

Since the early 2000s, superhydrophobicity have been considered through the competition between the Wenzel's and Cassie-Baxter's wetting regimes. Because slippery superhydrophobicity, or "lotus leaf effect" has become the main objective when talking about superhydrophobicity, the Wenzel's regime is considered as the unwanted state, and efforts have been performed to describe Cassie-Baxter's regime stability criterions. In 2002, Bico *et al.*¹ compared the surface energy variation corresponding to a displacement of a triple line in a Wenzel's² (Eq. 11) or Cassie-Baxter's³ (Eq. 12) regime.

$$dF = r(\gamma_{SL} - \gamma_{SV})dx + \gamma_{LV}dx \cos \theta^* \quad \text{Eq. 11}$$

$$dF = \phi_S(\gamma_{SL} - \gamma_{SV})dx + (1 - \phi_S)\gamma_{LV}dx + \gamma_{LV}dx \cos \theta^* \quad \text{Eq. 12}$$

$$\cos \theta_W = r \cos \theta_Y \quad \text{Eq. 13}$$

$$\cos \theta_{CB} = \phi_S \cos \theta_Y - (1 - \phi_S) \quad \text{Eq. 14}$$

Where r is the roughness, ϕ_S the surface area fraction at the interface, θ^* the apparent contact angle γ_{SL} , γ_{SV} and γ_{LV} the surface energy of solid/liquid, solid/vapor and liquid/vapor interfaces, and θ_Y the Young's contact angle⁴, respectively.

Minimizations of Eq. 1 and Eq. 12 lead to the Wenzel's (Eq. 13) and Cassie-Baxter's (Eq. 14) equations, respectively. As the wetting regime associated with the lower surface energy variation will be thermodynamically stable, Bico *et al.* proposed Eq. 15 for Cassie-Baxter's regime stability criterion. According to this equation, the Young contact angle has to be large enough for a stable Cassie-Baxter's regime, *i.e.* the solid has to be hydrophobic enough. To widen the range of acceptable Young contact angles, the roughness can be increased (very high roughness leading to the condition $\cos \theta_Y < 0$, meaning a just strictly hydrophobic solid), as well as the solid surface area ϕ_S . Bico *et al.* also pointed out that for a value of θ_Y between the minimal value from Eq. 15 and 90° , a Cassie-Baxter's wetting regime could exist in a metastable state.

$$\cos \theta_Y < \frac{\phi_S - 1}{r - \phi_S} \quad \text{Eq. 15}$$

Marmur⁵ used a similar approach in 2003, by calculating the Gibbs free energy of a fully wetted (Wenzel's regime) or partially wetted (Cassie-Baxter's regime) surface. He proposed an equation for the Gibbs free energy depending on the radius of the drop, the wetted area fraction, and the roughness of the wetted area. Thus, he was able to calculate the system energy for various penetration depths of a drop into the roughness, from a Cassie-Baxter's to a Wenzel's regime using Eq. 16.

$$G^* = F^{-2/3}(\theta^*)[2 - 2 \cos \theta^* - \Phi(f) \sin^2 \theta^*] \quad \text{Eq. 16}$$

with

$$F(\theta^*) = (2 - 3 \cos \theta^* + \cos^3 \theta^*) \quad \text{Eq. 17}$$

and

$$\Phi(f) = r_f f \cos \theta_Y + f - 1 \quad \text{Eq. 18}$$

Where θ^* is the apparent contact angle, θ_Y the Young contact angle, f the fraction of wetted area at the interface, and r_f the roughness of the wetted area, respectively.

$$\frac{d^2(r_f f)}{df^2} > 0 \quad \text{Eq. 19}$$

Considering a hydrophobic surface, *i.e.* $\cos \theta_Y < 0$ and Eq. 16, Marmur showed that a local minimum of G^* corresponding to a Cassie-Baxter's regime stable or metastable state, Eq. 19 has to be fulfilled. This implies that the roughness and the wetted area fraction could be translated to equations, and thus hardly applies to irregular natural surfaces.

1.2. Effect of asperities size

The previous calculation made no assumption of the texture size or shape effect on Cassie-Baxter's regime stability, assuming a constant wetted area fraction or roughness. However, Gao and McCarthy⁶ have realized an experience to investigate the importance of multiple lengths scale to reach superhydrophobicity. These authors compared the advancing and receding angles of a patterned surface with flat-top and nanotextured asperities, using a crosslinked polymethylsiloxane (Figure 46a). The flat-top asperities led to a 20° hysteresis, whereas the nanotextured asperities led to a neglectable hysteresis, with the same advancing angles. They explained this difference in contact angle hysteresis by a change in the kinetic of the contact line recession, caused by a decrease of the transition energy between each pinning sites, *i.e.* between each metastable states. The additional roughness and air area fraction from the nanoroughness can be neglected, as the advancing angle value did not change. Thus, the reduction of asperity size could lead to a lower contact angle hysteresis.

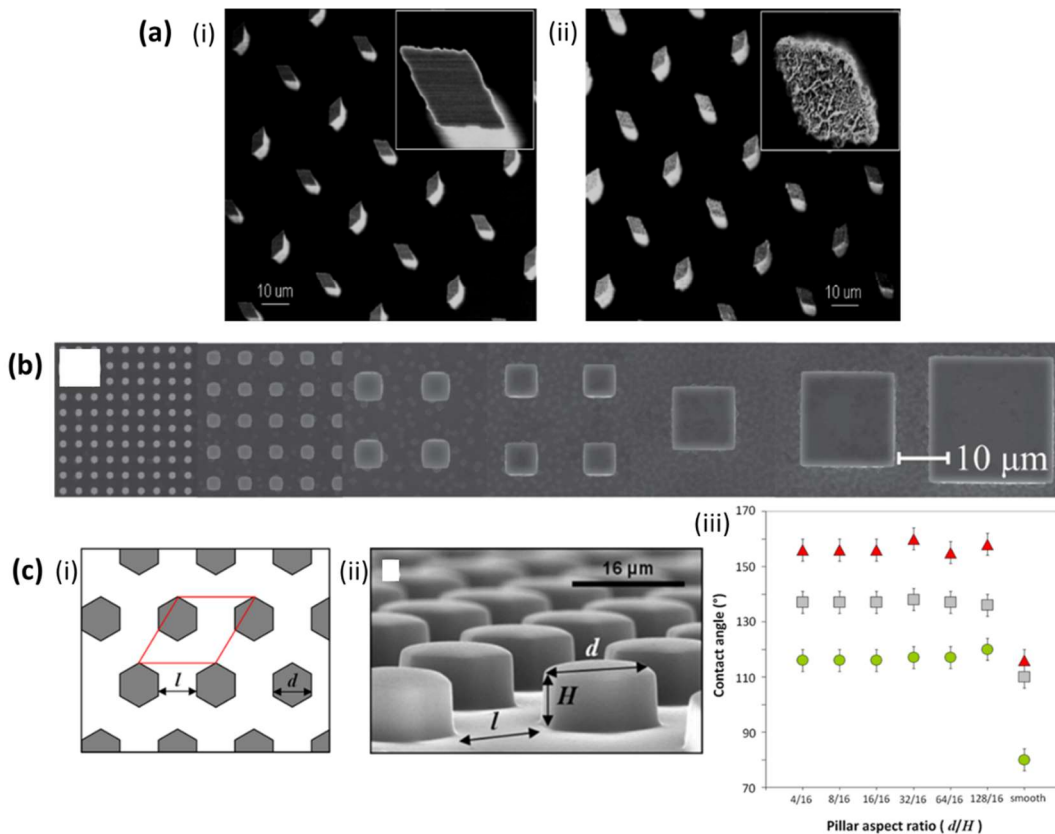


Figure 46 – Scale length impact on contact angle and hysteresis. (a) Rhombus pillars of $4 \times 8 \mu\text{m}$ large and $40 \mu\text{m}$ height, separated by a tenth micrometers, with (i) flat tops and (ii) nanorough tops; (b) Square pillars with increasing scale length from 2 to $40 \mu\text{m}$ with a $30 \mu\text{m}$ height and a constant solid area fraction of 0.16; (c) Hexagonal pillars with (i) constant length and distance kept equal with values from 4 to $128 \mu\text{m}$ and (ii) constant height of $16 \mu\text{m}$, and (iii) resulting equilibrium (\square), advancing (Δ), and receding (\circ) contact angles. (a), (b) and (c) are reprinted from ^{6,7} and ⁸ respectively, Copyright 2006, 2012 and 2014, American Chemical Society

Lv and Hao⁷ used this difference of hysteresis with the length scale to design a surface on which a droplet can move, powered by scale gradient (Figure 46b). When placing a water droplet on this surface, and increasing its radius through water addition, the droplet expanded exclusively toward the

larger scale. When the droplet volume was kept constant but the surface was subjected to vibrations, the droplet then moved from the tinier scale to the larger one. They explained this behavior by comparing the “triple line energy” with the asperity area to dewet. The liquid surface tension will be stronger in comparison with the solid/liquid interfacial energy for smaller asperities, because of a reduced area to dewet. This conclusion is similar to the one of Gao and McCarthy of reduction of the transition energy between pinning sites.

However, Hisler *et al.*⁸ did not observe a scale influence on the contact angle nor hysteresis for samples with an identical surface area fraction Φ_s , and various roughness values (Figure 46c.i-ii). For all these surfaces, they measured a water advancing contact angle around 157° , and a receding contact angle around 118° , with a hysteresis of 39° (Figure 46c.iii): the scale seems to have no impact on both the water CA and its hysteresis. They explained such invariance by calculating pinning and depinning energies, showing an invariance of each term with the length/distance ratio. However, it's surprising that a water droplet with a Cassie-Baxter's wetting regime exhibits such a high hysteresis, even if a Wenzel's wetting regime does not seem to be obtained neither, with no variation of the contact angle with the roughness. Moreover, as pointed out by Makkonen⁹, energy liberated at the advancing edge of a triple line cannot be transferred to the receding edge. The energy liberated at the advancing edge is dissipated into thermal energy, and the receding edge is fueled by whatever causes the motion, (gravity, kinetic energy, ...).

The question of the impact of scale length on contact angle and its hysteresis does not appear to be completely answered, with contradictory observations and assumptions.

1.3. Role of multi-scale roughness

By observing natural superhydrophobic surfaces, it became clear that a multiscale roughness was mandatory for slippery superhydrophobicity. As a consequence, numerous artificial surfaces have been produced mimicking natural surfaces and their multiscale roughness^{10–14}.

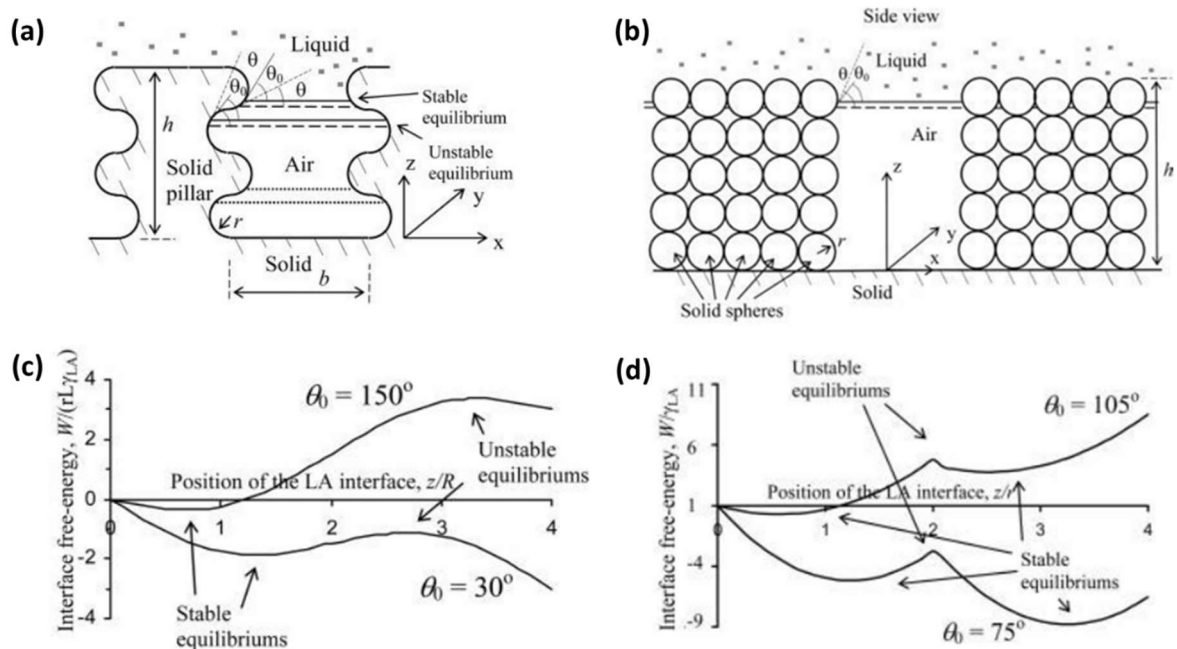


Figure 47 – Study of a Cassie-Baxter's interface stability with (a) monoscale and (b) hierarchical roughness, and (c-d) resulting interface free energy for mono- and multiple scale roughness, respectively. Reprinted from ¹⁵, Copyright 2007 American Chemical Society

Nosonovsky¹⁵ explained how important was this multiscale roughness through calculation of the free energy of single-scale and multiscale surfaces. By a biomimetic approach, following the lotus leaf superhydrophobic surface roughness, he modeled surfaces with smooth cylindrical micropillars following a hexagonal pattern (Figure 47a), or nanospheres-constituted pillars, with the same size and distribution as smooth pillars (Figure 47b). The interface free energy was plotted against the penetration depth of the liquid/air interface for both surfaces (Figure 47c-d), showing stable and unstable equilibrium in both cases. However, the multiscale surface exhibits a more stable equilibrium, with a higher energy gap before collapsing into a Wenzel's regime, even with relatively low Young's contact angle (here noted θ_0). Thus, he highlights that multiscale roughness can help reaching a stable Cassie-Baxter's regime, due to the surfaces being more "convex", and even claims that this multiscale roughness was mandatory. The observation of natural superhydrophobic surfaces also points in that direction.

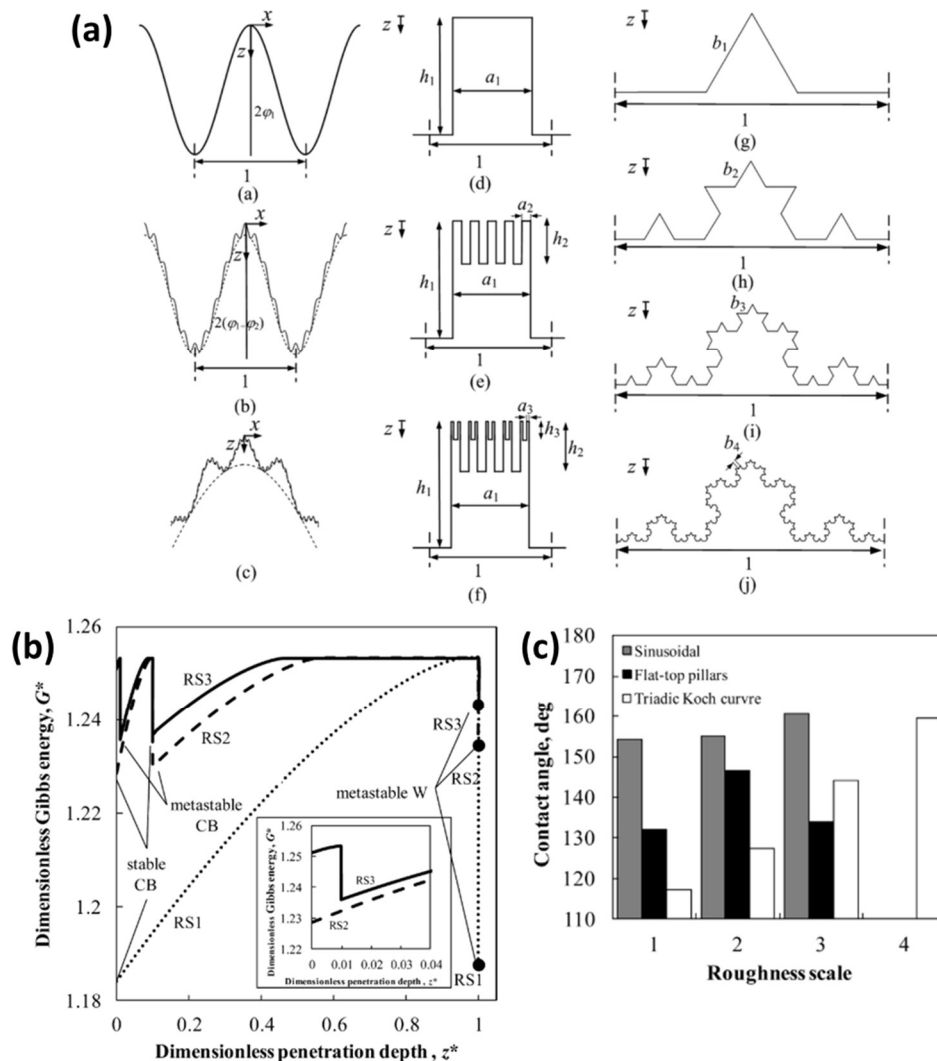


Figure 48 – Impact of multiscale roughness on the wetting properties. (a) Studied topographies, based on (a-c) sinusoidal curvature, (d-f) flat-top pillars, and (g-j) triadic Koch curve. (b) Resulting free energy of the system with liquid penetration depth for flat-top pillars, with 1, 2 or 3 roughness scales. (c) Calculated water contact angle with the number of roughness scales, for sinusoidal, flat-top pillars and triadic Koch curve topographies. Reprinted from ¹⁶, Copyright 2012 American Chemical Society

Later, Bittoun and Marmur¹⁶ studied the free energy changes of model surfaces with up to 3 hierarchical roughness scales, with different shapes: a sinusoidal curvature, flat-top pillars, and a triadic Koch topography (Figure 48a). For each 2D topography, with one, two or three hierarchical scales, they calculated the free energy of the system with the penetration depth of the liquid between

the asperities, from a pure Cassie-Baxter's regime to a fully wetted Wenzel's regime. For flat-top pillars (Figure 48b), a single roughness scale leads to a stable Cassie-Baxter's state with no penetration depth, and a metastable Wenzel's state at the completed penetration depth (full wetting of the surface by the liquid). With additional roughness scales, metastable Cassie-Baxter's states also exist, at low and very low penetrations depths. On the opposite, with triadic Koch topography, multiscale roughness appeared mandatory to allow a metastable Cassie-Baxter's state. For sinusoidal curvature topographies, the added-value of multiscale roughness varied with the signal amplitude, *i.e.* geometry, of the surface. With low amplitude, multiscale roughness was mandatory to create metastable or stable Cassie-Baxter's states, whereas with higher amplitude, a stable Cassie-Baxter's state exists even with a single roughness scale.

Moreover, the impact of the number of hierarchical roughness scale on the apparent contact angle (Figure 48c) seems different for each topography: a slight contact angle increase for sinusoidal curvature, a contact angle increase followed by a decrease for flat-top pillars, and a steady contact angle increase for triadic Koch topography. All these observations conducted the authors to claim that even if multiscale roughness is often beneficial for stability and contact angle. It could not be always of interest, and it mostly depends on the geometry of asperities.

1.4. Re-entrant asperities

In 2008, Tuteja *et al.*¹⁷ made surfaces that could repel low surface tension liquid such as pentane (15,7mN/m), thanks to asperities with re-entrant angles from electrospun fibers and micro-hoodoos. They also proposed some criterions in order to reach superomniphobicity thanks to re-entrant textures. Two adjusting parameters were considered to design superomniphobic surfaces with re-entrant asperities: a spacing ratio D^* , and a stability ratio A^* (Eq. 22), leading to the "robustness height" H^* (Eq. 20) and the "robustness angle" T^* (Eq. 21). The spacing ratio is obtained by dividing the texture period length by the asperity length; for example, with parallel fibers of radius R spaced by a length D ,

$$D^* = \frac{R+D}{R}.$$

$$H^* = \frac{(1 - \cos \theta)R l_c}{D^2} \quad \text{Eq. 20}$$

$$T^* = \frac{l_c \sin(\theta - \psi_{min})}{2D} \quad \text{Eq. 21}$$

$$\frac{1}{A^*} = \frac{1}{H^*} + \frac{1}{T^*} \quad \text{Eq. 22}$$

Where θ is the local contact angle, R the radius of the round asperity, l_c the capillary length of the liquid, D the spacing of asperities, and ψ_{min} the minimum re-entrant angle achievable (Figure 49a).

When $H^* < T^*$, the pressure applied by the liquid on the interface will provoke a penetration in-between the asperities, resulting in a change of the Cassie-Baxter's regime, into a Wenzel's regime at a given pressure.

If $H^* > T^*$, the pressure applied by the liquid on the interface will provoke an increase in the local contact angle θ , resulting in a sagging of the interface into higher depths. As the stability ratio A^* computes the two robustness ratios, the authors focused on maximizing the spacing and stability ratios together. They considered that the minimum value of $A^* = 1$ corresponded to a stable Cassie-Baxter's wetting regime. Also, the higher the value of both A^* and D^* , the better for the interface stability and contact angle.

Following this study, numerous artificial surfaces with re-entrant asperities have been described, displaying superoleophobicity^{18,19} or even complete superomniphobicity²⁰. For example, Liu and Kim²¹ considered nail-like pillars with a doubly re-entrant geometry (Figure 49b). By carefully designing these doubly-re-entrant pillars with an overhang, the authors were able to repel numerous liquids with

surface tensions from 72 to only 10mN/m by using only untreated, *i.e.* hydrophilic, silica (Figure 49c). The Nature itself also considers re-entrant asperities to repel low surface tension liquids, like the springtail skin for example²².

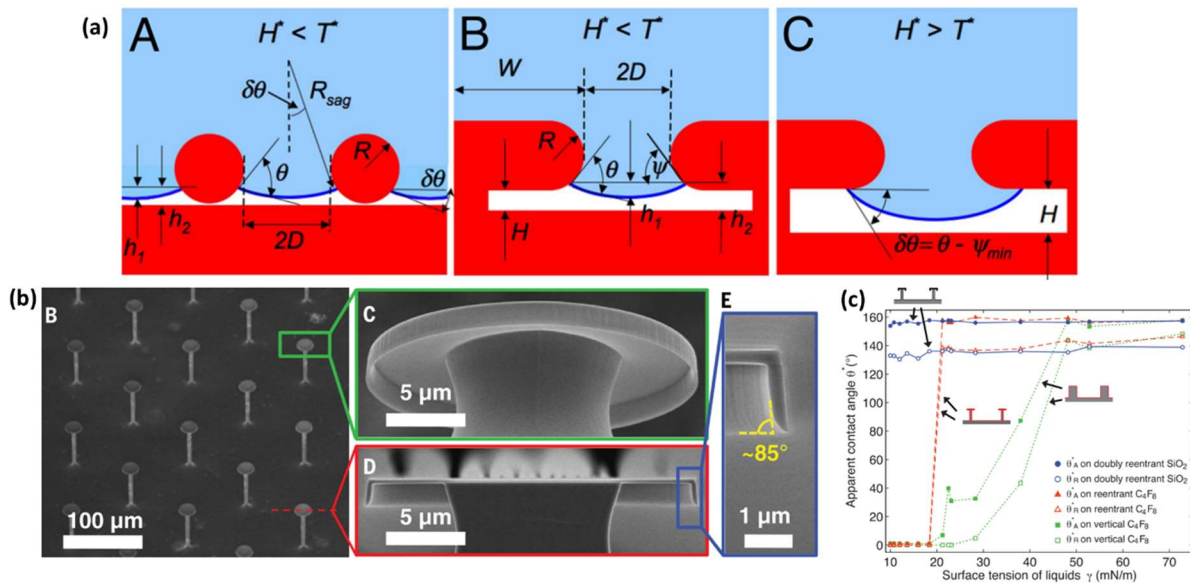


Figure 49 – Re-entrant asperities and corresponding wetting properties. (a) Scheme of re-entrant asperities and corresponding calculation parameters: (A) fibers and (B-C) micro-hoodoos. (b) Doubly re-entrant nail-like asperities with superomniphobicity, and (c) corresponding contact angle with various surface tension liquids. Reprinted from (a)¹⁷ and (b-c)²¹, Copyright 2008 The National Academy of Science of the USA and 2014 American Association for the Advancement of Science, respectively.

1.5. Conclusion: Definition of an ideal superhydrophobic surface

Based on models, calculations and studies of natural or artificial superhydrophobic surfaces, the characteristics of an ideal surface are found to be:

- Intrinsically hydrophobic materials*,
- Textured surface,
- Low solid surface area fraction,
- Multiscale roughness, at micro and nanoscale,
- Re-entrant geometry of asperities.

*However, it must be noted that with re-entrant asperities, the first criterion, intrinsic hydrophobicity, is no longer mandatory, even if it would reinforce the interface stability. In addition, some studies (Gao and McCarthy's⁶ and Lv and Hao's⁷) suggest that asperities must be as small as possible, whereas others authors have shown no difference of hysteresis with the asperities scale (Hisler *et al.*⁸). Thus, it is hard to conclude on this point from a literature survey.

This ideal surface has been targeted by numerous researchers following various approaches, with various resulting topographies. However, there is still a need for simple but effective guidelines to help designing superhydrophobic or even superomniphobic surfaces. A model, as simple as possible, needs to be developed in order to give robust predictions of a Cassie-Baxter's interface stability and contact angle.

II. Modeling superhydrophobicity as easily as possible

II.1. Model definition

As previously stated, a Cassie-Baxter's interface is formed when a liquid droplet is held by air pockets trapped in the surface roughness. The contact angle of a liquid drop on such a surface increases with the fraction of air at the interface, following the Cassie-Baxter's equation (Eq. 14). This equation clearly shows that for enhancing superhydrophobicity, the solid fraction at the interface must be minimized, by replacing solid/liquid interface by liquid/gas interface.

In the same time, for such interface to be stable, surface tension must prevent the liquid from falling into the cavities because of the pressure applied on the interface, leading to an undesired Wenzel's state. Thus, is there a compromise to overcome in order to achieve stable superhydrophobicity? Which conditions allow the maximization of the air fraction at the interface with sufficient counterbalance due to the surface tension for preventing an equilibrium destabilization? These questions can be easily answered by calculating for a defined interface the maximum applied pressure before destabilization, the corresponding air fraction, and the final contact angle at macroscale.

The pressure P is exerted by the liquid on the interface because of either the liquid's weight, the hydrostatic pressure during immersion, etc. The force which is opposed to this pressure, F_S , comes from the surface tension that applies at each point of the interface triple line (solid/liquid/gas interface), considering the maximum local contact angle as equal to the Young's contact angle²³ (Figure 50a). Nevertheless, only the normal contribution of the surface tension, *i.e.* perpendicular to the macroscopic surface, acts to maintain the equilibrium (Eq. 23).

$$F_S = \gamma^{LV} \cdot l \cos(\theta_Y - \psi + 90^\circ) \quad \text{Eq. 23}$$

Where γ^{LV} is the surface tension of the liquid, l is the length of the triple line, θ_Y is the Young contact angle, and ψ is the angle between the 2D surface and the wall of the asperity.

For a given surface texture, *i.e.* for given l , ψ and S_{air} parameters, the equilibrium is reached between the force exerted by the pressure (obtained by dividing the pressure by the air surface S_{air}) and the surface tension force F_S for $P = P_{max}$ (Eq. 24). When this critical pressure is reached, the Cassie-Baxter's interface is no longer stable: the liquid meniscus between each asperity is bend at its maximum, forming a local contact angle equal to the macroscopic Young contact angle. The interface will then sag into a hybrid or pure Wenzel's wetting regime, resulting in a loss of the slippery property of the Cassie-Baxter's interface (Figure 50b). Thus, this latter interface is considered stable for pressure values lower than P_{max} .

$$P_{max} = \frac{-\gamma l \cos(\theta_Y - \psi + 90^\circ)}{S_{air}} \quad \text{Eq. 24}$$

It must be noticed that this model is only valid as the force exerted by the pressure and surface tension are opposed. This requirement limits the applicability of this model to a liquid/solid system for which the normal contribution of the surface tension is positive, *i.e.* for $\theta_Y > \psi$. If this condition is not satisfied, the surface tension could never counterbalance the liquid weight. Thus, the liquid will sag between asperities, leading to an undesired Wenzel's regime. Still, a Cassie-Baxter's equilibrium could be observed stealthily as a transition state according to Bico *et al.*¹. Moreover, asperities must be high enough in order to avoid the liquid meniscus from touching the bottom of the cavity, thus leading to a Wenzel's regime (Figure 50c). The maximum meniscus height is related to θ_Y , ψ , and to the maximum distance between each asperity, D_{max} (D is defined as the distance between asperities in a square pattern, Table 1). The minimum required height of asperities, denoted as H_{min} , can be calculated using Eq. 25, according to equations leading to D_{max} (tabulated for each studied asperity shape in Table 1). If the asperity height is lower than this minimum value, the transition from the Cassie-Baxter's state

to the Wenzel’s state will come from the bending of the meniscus provoking a wetting of the cavities bottom instead of a sagging after the maximum bending. This results in a Cassie-Baxter’s to Wenzel’s regime transition at a lower critical pressure, meaning a lower interface stability²¹. As a first approximation, H_{min} can be considered to be at least equal to the distance between asperities D for the model to be valid.

$$H_{min} = \frac{D_{max}}{2 \cos(\psi + 90^\circ - \theta_Y)} \times (1 - \sin(\psi + 90^\circ - \theta_Y)) \quad \text{Eq. 25}$$

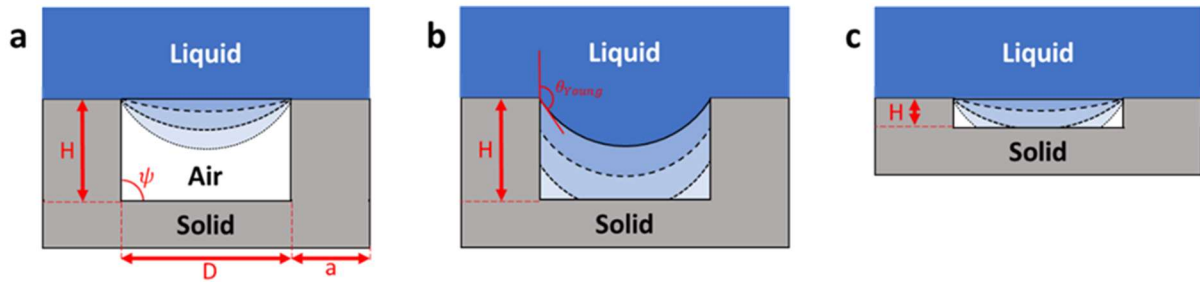


Figure 50 – Schemes of the deformation of the liquid/air interface with pressure and stability rupture. (a) Bending of the liquid meniscus with increasing pressure, from a flat (solid line) solid/liquid interface with no applied pressure to a bended meniscus forming a local contact angle equal to Young contact angle at maximum applied pressure (pointed line), and intermediate bending with local contact angle lower than the Young contact angle value. (b) Sagging of the bended solid/liquid interface when the maximum pressure is overpassed ($P > P_{max}$): the initial Cassie-Baxter’s state turn into a Wenzel’s state over time, passing by hybrid wetting state. (c) Formation of a Wenzel’s interface for pressure values below the maximum calculated pressure for a system with a too low asperities height ($H < H_{min}$): the bending of the meniscus with increasing pressure leads to a wetting of the void floor at lower pressure and thus meniscus curvature than with a sufficient height. This last case is excluded from the current model.

Table 7 – Relevant size parameters of asperities having different shapes

Asperity shape	“Cell” structure (asperity is in blue and air is in white)	Triple line length (l)	Air surface (S_{air})	Maximum distance between asperities (D_{max})
		$l = \pi a$	$S_{air} = (a + D)^2 - \pi \left(\frac{a}{2}\right)^2$	$D_{max} = D\sqrt{2} - (1 - \sqrt{2})a$
		$l = 4a$	$S_{air} = D^2 + 2aD$	$D_{max} = D\sqrt{2}$
		$l = 4a$	$S_{air} = (a + D)^2 - 5\left(\frac{a}{3}\right)^2$	$D_{max} = \left(D + \frac{2a}{3}\right)\sqrt{2}$
		$l = \frac{44}{9}a$	$S_{air} = (a + D)^2 - 5\left(\frac{a}{3}\right)^2$	$D_{max} = \left(D + \frac{4a}{9}\right)\sqrt{2}$

II.2. Application to model surfaces

The described model can be applied on patterned surfaces such as the one based on column asperities having a circular section arranged following a square pattern by varying its parameters, *i.e.* the distance between each asperity, D , and their width, a . The maximum stability pressure P_{max} and the Cassie-Baxter's contact angle θ_{CB} have been calculated for each parameters value. From these calculations, guidelines could be proposed to design effective and robust superhydrophobic surfaces. Other asperities patterns have also been studied, such as square (Figure 54), cross (Figure 55) and multiple-arms cross (Figure 56) sections, and their particularity will be discussed later.

For a water / polyethylene reference system ($\gamma_{water} = 72.8 \text{ mN/m}$, $\theta_Y = 95^\circ$), when calculating the Cassie-Baxter's contact angle and the interface equilibrium for D from 100 nm to 1 mm for straight ($\psi = 90^\circ$) and circular section pillars having diameters from 1 μm to 1 mm (Figure 51), one can observe:

- The interface stability, evaluated from the maximum pressure before transition from a Cassie-Baxter's to a Wenzel's regime, decreases with increasing distance between the pillars D ,
- The interface stability increases with decreasing asperities width a ,
- The Cassie-Baxter's contact angle increases with increasing distance between asperities D ,
- The Cassie-Baxter's contact angle decreases with increasing pillar width a .

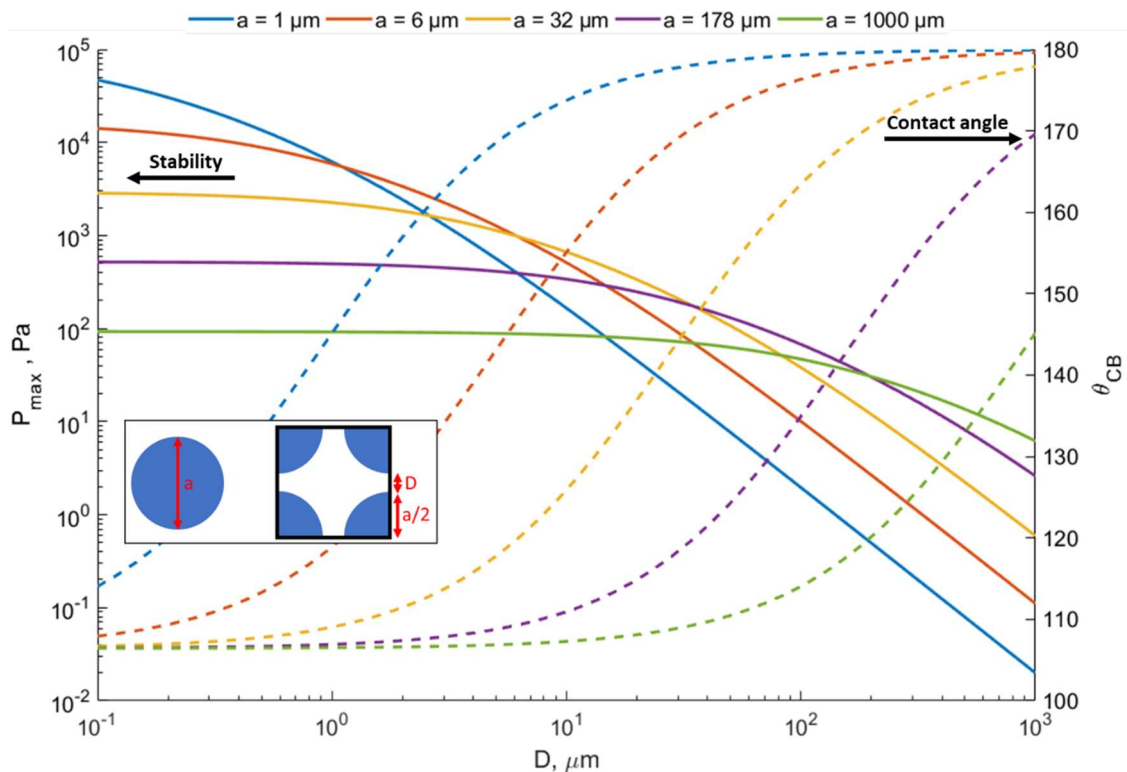


Figure 51 – Application of the proposed model to a regularly patterned surface based on polyethylene circular pillars: Changes of the interface stability (evaluated from the maximum pressure before transition from Cassie-Baxter's to Wenzel's state) and contact angle with pillar spacing D , and width a . Solid lines correspond to stability and dashed lines correspond to contact angle.

These observations are backed by the study of Eq. 14 and Eq. 24, respectively the Cassie-Baxter's equation, and the equation of the surface tension force. The Cassie-Baxter's equation for contact angle clearly shows that for the contact angle to increase, the air fraction might be maximized. This can be done by increasing the air surface at the interface. Figure 52 shows that an increase of the air surface S_{air} is expected when increasing the asperities spacing distance D or increasing the asperities width a . The increase of S_{air} is also responsible for an increase of the weight of the wetting liquid exerted

on the liquid/air interface. In the same time, Figure 52 shows no impact of the asperities spacing distance D on the triple line length, with a regular increase of this length with the asperities width a . As the ratio between the triple line length l and the air surface at the interface S_{air} have a major impact on the surface tension force for a given system (*i.e.* fixed surface tension, Young's contact angle and asperities angle), as expressed by Eq. 24, an increase of the air surface leads to simultaneously a weight increase and a surface tension force decrease, thus logically leading to a reduced critical pressure. That is why an increase of the spacing distance D leads to a decrease in interface stability. Moreover, as the triple line length l increases linearly with a , whereas the air surface S_{air} increases with the square of a , an increase of this width will result in a decrease of the interface stability.

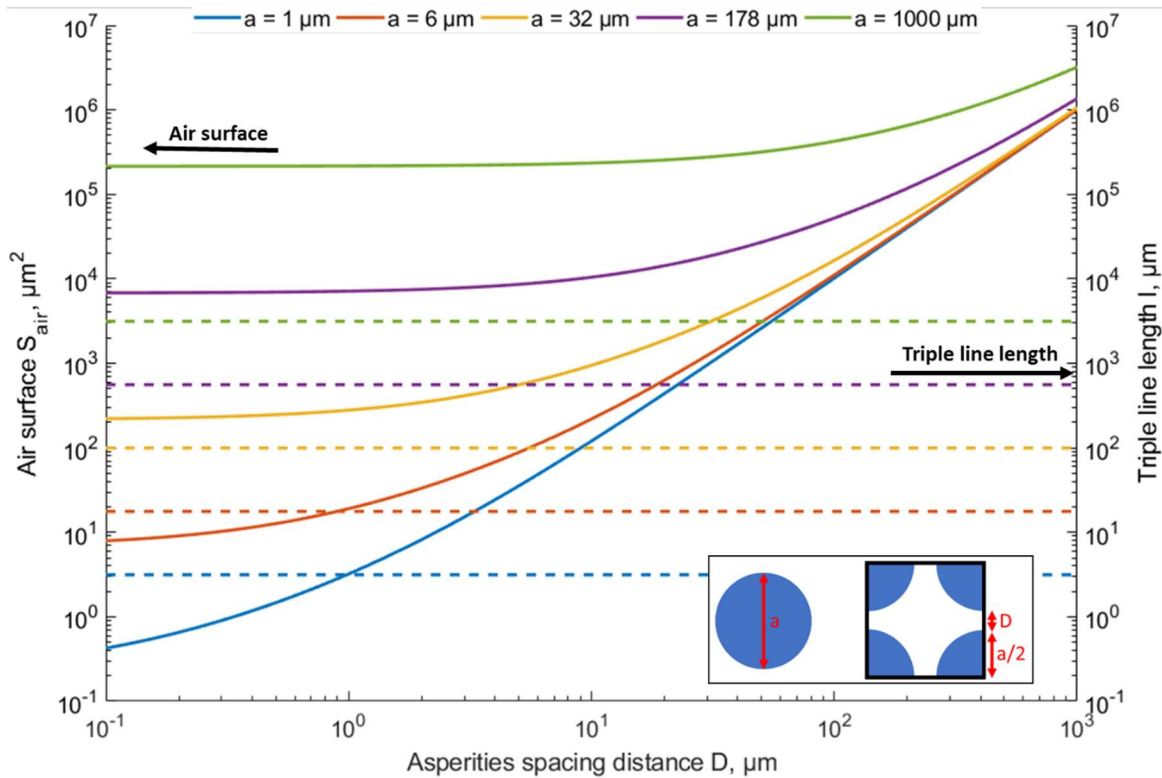


Figure 52 – Evolution of the air surface S_{air} and triple line length l with spacing distance D and asperities width a for circular asperities following a squared pattern, as shown in the insert. Solid lines correspond to air surface and dashed lines correspond to triple line length.

Therefore, there is a compromise between D and a dimensions for reaching a stable superhydrophobicity regime. In fact, D has to be as low as possible to increase the interface stability, but as high as possible to reach high air fraction and consequently a high Cassie-Baxter's contact angle. Concerning the pillar width a itself, it must be as low as possible in order to reach both high interface stability and a high contact angle. This compromise can be highlighted by plotting the interface stability, *i.e.* the maximum suitable pressure P_{max} , and the Cassie-Baxter's contact angle versus the D/a ratio for different values of a (Figure 53). From such a model, it is clear that pillar width is the key parameter for the Cassie-Baxter's interface stability, as the maximum pressure which can be sustained by the interface before collapsing is obtained with the tiniest pillars. One can notice that for D/a lower than 0.1, the interface stability is not significantly influenced by D/a values. It can be explained by the air fraction at the interface due to the asperities shape being significantly greater than the one from their spacing. However, such surface patterns offer very poor superhydrophobicity behavior, as the Cassie-Baxter's contact angle is then lower than 110° due to the low trapped air fraction. To get θ_{CB} exceeding 150° , *i.e.* a superhydrophobic behavior, D/a must be larger than a lower limit D/a_{min} in order to get enough interface air fraction. For example, considering a water/HDPE ($\theta_Y = 95^\circ$)

patterned surface with circular pillars, a f_{air} larger than 0.85 is needed for θ_{CB} to be larger than 150° . This condition leads to a minimum D/a ratio of 1.3 (Eq. 26).

$$f_{air} = \frac{S_{air}}{S_{Tot}} = \frac{(a + D)^2 - \pi \left(\frac{a}{2}\right)^2}{(a + D)^2} > 0.85 \quad \text{Eq. 26}$$

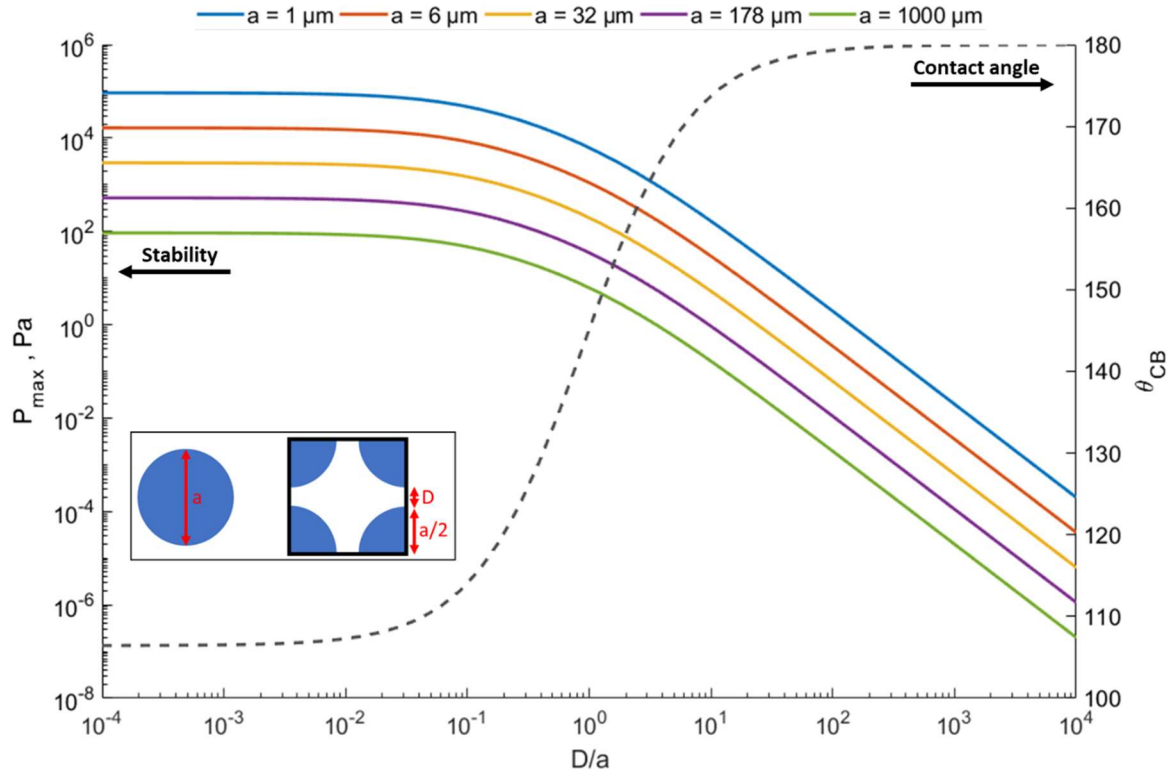


Figure 53 – Change of the interface stability and contact angle with spacing on asperity size ratio D/a for circular asperities from 1 to 1,000 μm . Solid lines correspond to stability, and dashed line correspond to contact angle (numerical application based on polyethylene and water). The insert shows the considered asperities shape.

Table 8 – Calculated maximum D/a ratio allowing interface stability for a given maximum pressure P_{max} with a given vertical surface tension contribution (from θ_Y and ψ) and asperity width a for circular asperities following a square pattern. 20Pa correspond to the pressure exerted by a 2mm water drop on a surface due to its weight, and 1,000Pa correspond to a 10cm deep immersion of the surface in water.

D/a max (Circles)	$\theta_Y - \psi + 90^\circ = 95^\circ$		$\theta_Y - \psi + 90^\circ = 110^\circ$		$\theta_Y - \psi + 90^\circ = 125^\circ$	
	$P_{max} = 20 \text{ Pa}$	$P_{max} = 1000 \text{ Pa}$	$P_{max} = 20 \text{ Pa}$	$P_{max} = 1000 \text{ Pa}$	$P_{max} = 20 \text{ Pa}$	$P_{max} = 1000 \text{ Pa}$
$a = 0.1 \mu\text{m}$	99	13.3	198	27	258	35.7
$a = 0.5 \mu\text{m}$	44	5.5	88	11.6	115	15.4
$a = 1 \mu\text{m}$	31	3.6	62	8	81	10.6
$a = 5 \mu\text{m}$	13.3	/	27	3	35.7	4.2
$a = 10 \mu\text{m}$	9	/	19	2	25	2.7
$a = 50 \mu\text{m}$	3.6	/	8	/	10.6	/
$a = 100 \mu\text{m}$	2.3	/	5.4	/	7.2	/
$a = 500 \mu\text{m}$	/	/	2	/	2.7	/

The D/a upper limit for the interface equilibrium, D/a_{max} , is directly related to the maximum D/a ratio which allows a stable Cassie-Baxter's interface with a given liquid pressure. For a higher D/a , the Cassie-Baxter's state will turn into a Wenzel's state. Such limits for circular section pillars are shown in Table 8. The upper limit of D/a ratio increases with decreasing asperity size a and increasing the normal component of the surface tension. The normal component of the surface tension can be

increased either by increasing the Young contact angle, θ_Y , from a lower surface energy solid or by decreasing asperities angle to the surface ψ (using for example re-entrant asperities). For example, taking a condition of stability of 1 kPa, corresponding approximately to a water column of 10cm held by the interface, D/a upper limit for $a = 1\mu\text{m}$ and $\theta_Y - \psi + 90^\circ = 95^\circ$ and 110° are 3.6 and 8, respectively.

As previously mentioned, similar calculations have been made with different asperities shape, such as squares (Figure 54), crosses (Figure 55), and multiple-arms crosses (Figure 56). Squares and crosses have a similar perimeter with a different air fraction, while crosses and multiple-arms crosses have a similar air fraction with different perimeters (Table 8).

First of all, it must be noted that Cassie-Baxter’s contact angle changes have not a strong influence. In fact, the changes with asperities width a and spacing distance D remain the same for the four systems. However, changes of stability with a and D are different for squares asperities. This might be because of the absence of a negative part in the S_{air} calculation for this system. An increase of a for very low values of D has a very little impact on the stability, asperities being almost at the contact one from another (with squares, asperities in contact leads to $S_{air} = 0$). As a consequence, all stability curves are converging at very low values of D in Figure 54a. Despite this difference, the conclusion from these observations are still the same: a lower D/a value leads to a greater stability and a lower contact angle.

However, calculations using Eq. 26 show that the asperity shape has an effect on D/a_{min} , with asperities with larger S_{air} for given D and a , leading to lower D/a_{min} , with values from 1.6 to 0.9 for square and cross (or multi-arms) sections respectively, for $\theta_Y = 95^\circ$ and f_{air} higher than 0.85 (polyethylene/water reference system).

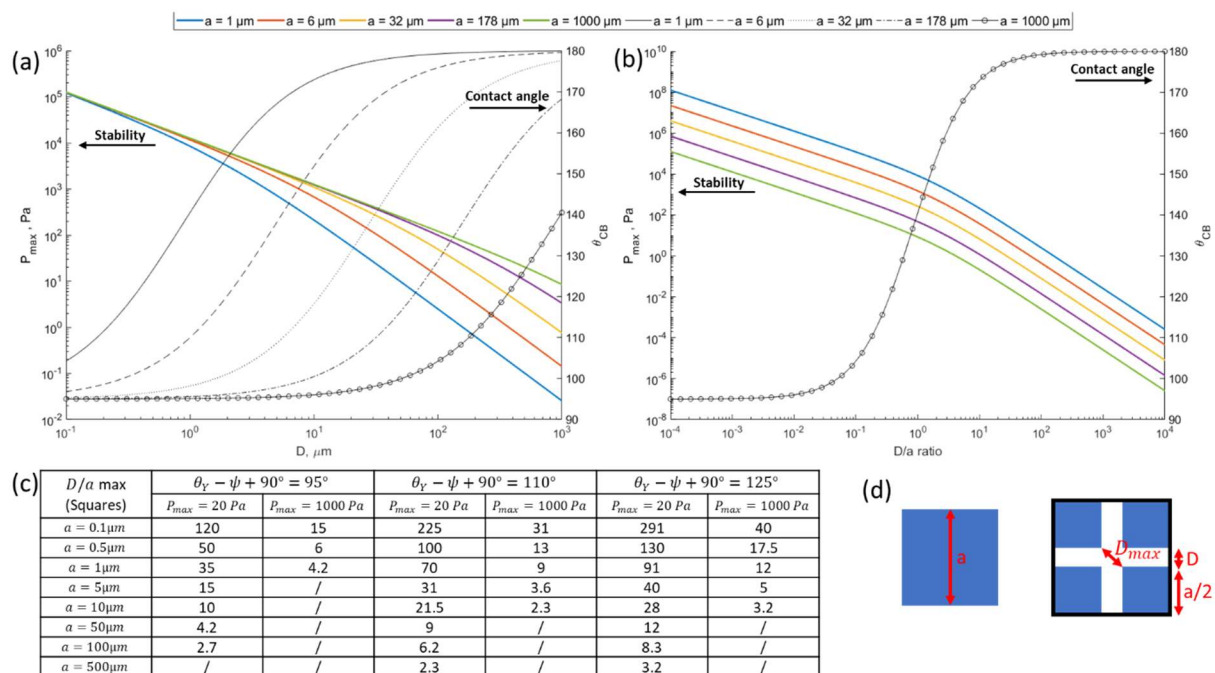


Figure 54 – Application of the proposed model to patterned surfaces based on square section pillars. (a) Changes of the interface stability (evaluated from the maximum pressure before transition from Cassie-Baxter’s to Wenzel’s state) and contact angle with pillar spacing, D , for circular section pillars from 1 to 1,000 μm large. (b) Change of the interface stability and contact angle with spacing on asperity size ratio D/a for circular asperities from 1 to 1,000 μm . (c) Calculated maximum D/a ratio allowing interface stability for a given maximum pressure P_{max} with a given vertical surface tension contribution (from θ_Y and ψ) and asperity width a . (d) Asperity shape and parameters used for application of the model

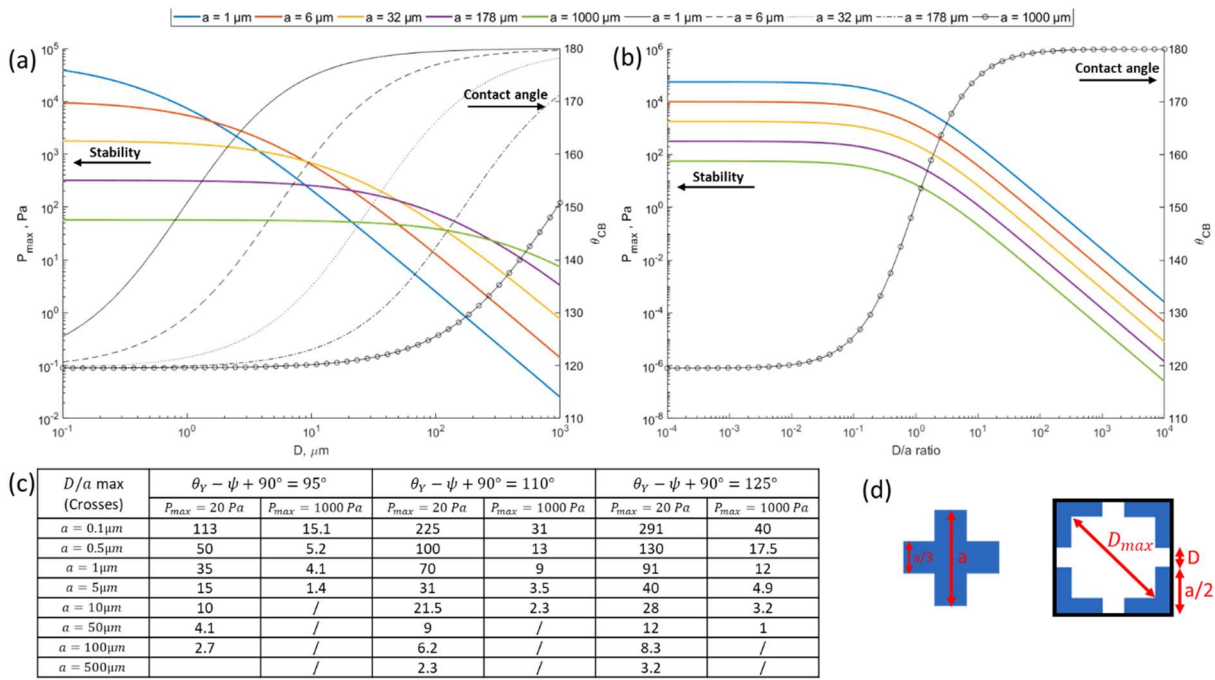


Figure 55 – Application of the proposed to model patterned surfaces based on cross section pillars. (a) Changes of the interface stability (evaluated from the maximum pressure before transition from Cassie-Baxter’s to Wenzel’s state) and contact angle with pillar spacing, D , for circular section pillars from 1 to 1,000 μm large. (b) Change of the interface stability and contact angle with spacing on asperity size ratio D/a for circular asperities from 1 to 1,000 μm . (c) Calculated maximum D/a ratio allowing interface stability for a given maximum pressure P_{max} with a given vertical surface tension contribution (from θ_Y and ψ) and asperity width a (d) Asperity shape and parameters used for application of the model

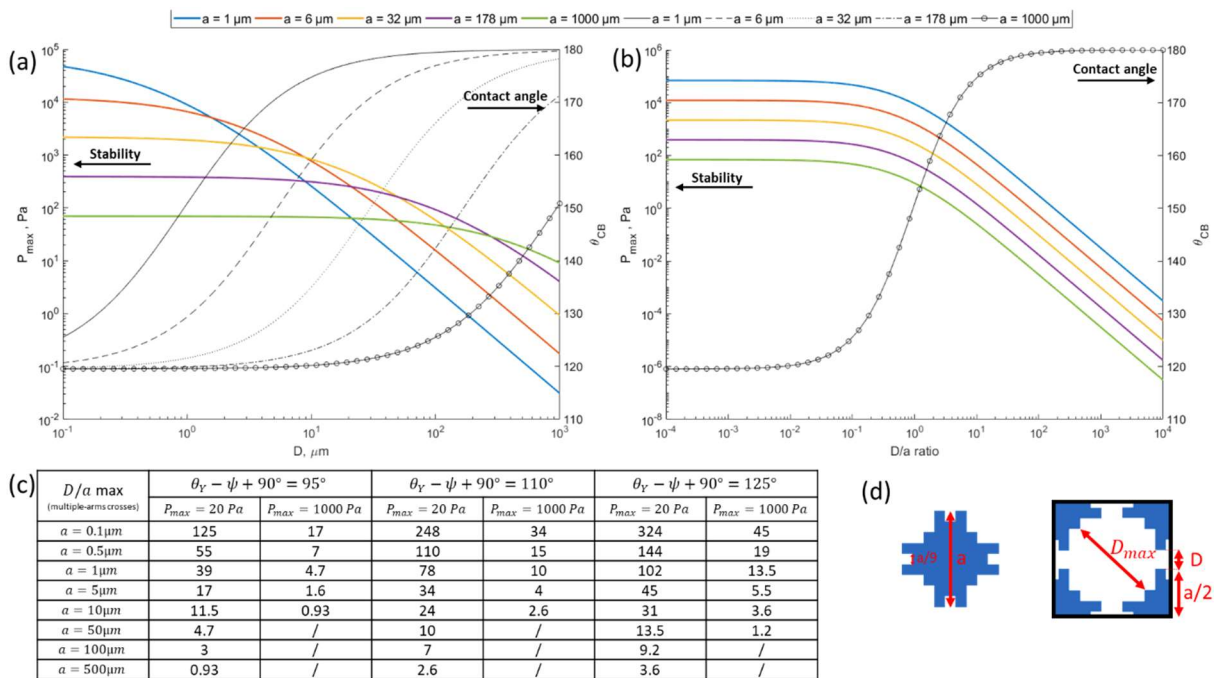


Figure 56 – Application of the proposed model to patterned surfaces based on multiple-harms cross section pillars. (a) Changes of the interface stability (evaluated from the maximum pressure before transition from Cassie-Baxter’s to Wenzel’s state) and contact angle with pillar spacing, D , for circular section pillars from 1 to 1,000 μm large. (b) Change of the interface stability and contact angle with spacing on asperity size ratio D/a for circular asperities from 1 to 1,000 μm . (c) Calculated maximum D/a ratio allowing interface stability for a given maximum pressure P_{max} with a given vertical surface tension contribution (from θ_Y and ψ) and asperity width a (d) Asperity shape and parameters used for application of the model

II.3. Conclusion

According to the described model, in order to have a stable slippery superhydrophobicity regime, asperities should be as small and as close as possible, with a lower limit of the D/a ratio obtained using Eq. 26, considering a minimum of f_{air} given by the Cassie-Baxter's equation.

All calculations have been performed considering monotonically patterned surfaces: a non-monotonic pattern would have locally different wetting behaviors, resulting in a macroscopic stability corresponding to the one of the weakest microscopic part. A water drop would indeed roll on the surface until being pinned on a defect, leading to a local Wenzel's regime, no matter the wetting regime around the defect: The macroscopic wetting regime always corresponds to the less favorable microscopic one.

III. Confronting the model to the reality

III.1. Patterned and isotropic surfaces

Some of the results reported in the literature on superhydrophobic surfaces have been analyzed according to geometrical characteristics of the surface topography in order to apply the previously described model. For example, Bhushan *et al.*²⁴ processed a surface by molding an epoxy resin as cylinders (Figure 57a) and coated the surface with hexatriacontane wax (Figure 57b). The surfaces with the lower wax content display different wetting behavior, *i.e.* from slippery Cassie-Baxter's superhydrophobicity (contact angle of 164° with 3° hysteresis) for 23 μm spaced pillars to sticky Wenzel's superhydrophobicity (contact angle of 152° with 87° hysteresis) for pillars spaced by 105 μm. For larger spacing, the resulting surface is even not superhydrophobic as a contact angle of 135° was measured. Thus, considering such an experimental approach, double scale surfaces were obtained as often considered as a required condition for reaching superhydrophobicity^{6,25,26}. The impact of the nanoscale texturisation combined with the microscale patterning will be discussed later.

Such results can be confronted with our model considering circular section asperities perpendicular to the surface ($\psi = 90^\circ$) for a Young contact angle θ_Y equal to 110° for water on a hexatriacontane-coated surface. It results that the lower limit for D/a ratio is about 1.0, according to Eq. 26 and the Cassie-Baxter's equation (Eq. 14) with such θ_Y . According to the values reported in Figure 2c, the upper limit of D/a ratio for a 2mm water column, exerting a pressure of approximately 20Pa, on such surface is close to 19. The surface having the higher pillar density exhibits a ratio $D/a = 23/14 = 1.6$, *i.e.* in-between D/a lower and upper limits. In addition, the pillar height is almost twice their spacing. Thus, all conditions are met and the resulting wetting behavior of the surface is in good agreement with the prediction of the model, *i.e.* a stable Cassie-Baxter's superhydrophobicity.

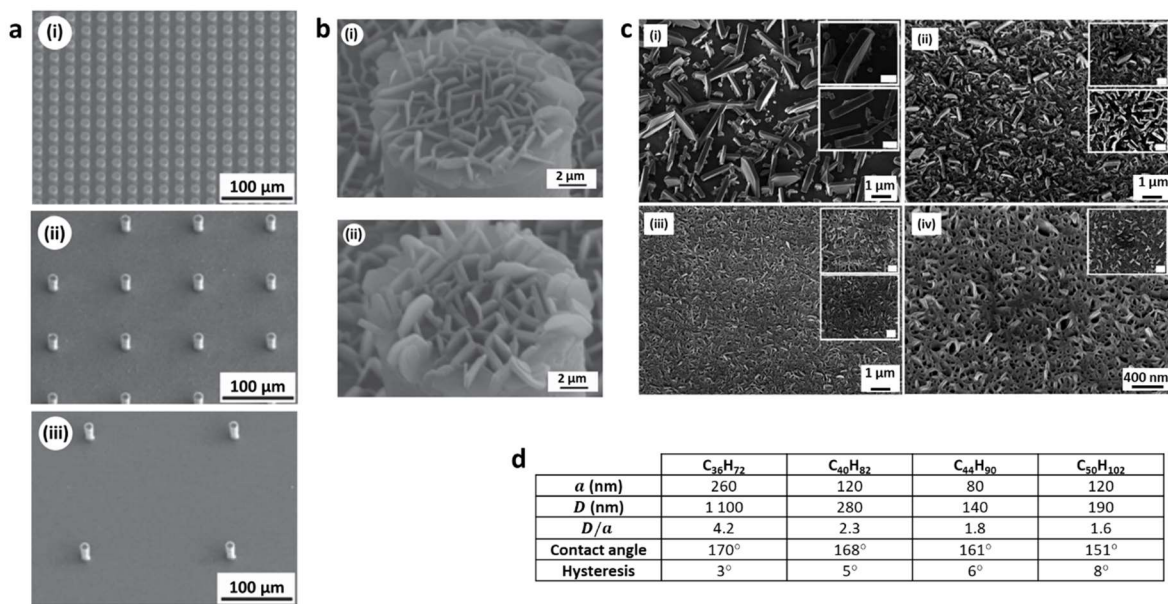


Figure 57 – Superhydrophobic surfaces reported in the literature. (a) Molded epoxy micropillars of 14 μm large and 30 μm height and spaced by (i) 23, (ii) 105, and (iii) 210 μm from Bhushan *et al.*²⁴. (b) Epitaxial hexatriacontane wax on top of micropillars: (i) low and (ii) large wax content from Bhushan *et al.*²⁴. (c) Epitaxial waxes crystals from *n*-paraffin of chain lengths of 36, 40, 44, and 50 carbon respectively (i-iv), from Pechook *et al.*¹³. (d) Size, spacing distance, and height of the *n*-paraffin wax crystals and resulting contact angle reported for the surfaces represented in (c). (Reprinted respectively from ²⁴ and ¹³, Copyright 2010 American Chemical Society and 2013 Royal Society of Chemistry.)

For the surface displaying a Wenzel's regime of superhydrophobicity, the texture ratio $D/a = 105/14 = 7.5$ is included between upper and lower D/a limits: the expected result should be a Cassie-Baxter's regime. However, the pillar height is about a third of their spacing distance, which is well below the minimum pillar height for the liquid to be suspended between two asperities. That's

why the interface collapses into a Wenzel's interface with no trapped air pocket, resulting in a large hysteresis. Same conclusions can be drawn for the third surface with widely spaced pillars which displays the lower contact angle due to the lower pillar density.

When increasing the wax content (Figure 57b(ii)), the three surfaces having different spacing distance between pillars display a slippery superhydrophobicity behavior (water contact angles from 166 to 168° with 3° hysteresis). For such surfaces, the previously described model predicts instability for Cassie-Baxter's interface. Such results could be associated to the major change in nanotexture that occurred with increasing wax content. Using an image analysis, the height, thickness, and spacing distance of the wax crystals have been determined. For a low wax content, wax crystals are approximately 150 nm thick, 500 nm tall, and spaced by 800 nm. For D/a close to 5.3 and such tiny size, the Cassie-Baxter's interface is expected to be stable. Nevertheless, their height is once again too low to ensure stable Cassie-Baxter's interface. Thus, a Wenzel's behavior occurs at nanoscale, increasing the local contact angle and hysteresis but compensated in the first case by the microscale topography. For a higher wax content, crystals are found to be approximately 300 nm thick, 1 μm tall, and spaced by 900 nm. With a D/a value close to 3 and a small asperities size, and with sufficiently height asperities, a stable superhydrophobic Cassie-Baxter's interface is obtained at nanoscale. A smooth surface coated with such wax crystals would display a slippery superhydrophobicity regime because of its nanoscale patterning and the microscale texture would have no impact on Cassie-Baxter's interface stability under pressure, even if it could lead to a larger contact angle.

An intermediate behavior can exist for a nanoscale texture which is only able to sustain low liquid pressure. Such a surface would display a Wenzel's wettability behavior at nanoscale on top of the asperities, but a Cassie-Baxter's wettability regime at microscale, where the liquid pressure on the nanoroughness would be lower because of the pinning on the microroughness. Such combined nano and micro scales texture would exhibit a Cassie-Baxter's superhydrophobicity regime even with a pillar height which appears to be too low. However, this type of surface structure would lead to very unstable behavior which will easily collapse under pressure.

Same types of nanotextures have been obtained by Pechook *et al.*¹³ by evaporating n-paraffin waxes composed of different chain lengths, *i.e.* from C_{36} to C_{50} , on a silicon substrate. The resulting epitaxial wax crystals covered surfaces (Figure 57c) exhibit Cassie-Baxter's slippery superhydrophobicity behavior with a decreasing contact angle and increasing hysteresis with increasing chain length (Figure 3d). The parameters a and D have been also measured using ImageJ software to evaluate the D/a ratio (Figure 57d). According to the authors, the crystals height is the same as their size at least equal to their spacing distance. Thus, according to our model, $H > H_{min}$ is always verified for those surfaces. The decrease of water contact angle combined with an increase of hysteresis with increasing chain length of the n-paraffin can be directly associated with the decreasing D/a . In fact, as D/a decreases, the trapped air fraction f_{air} also decreases, leading to a lower contact angle and a higher hysteresis. For lower chain lengths, the wax crystals are more spaced and the contact angle is higher. Nevertheless, the model predicts a lower stability for such surface structures. Thus, the best choice may not be the $\text{C}_{36}\text{H}_{72}$ wax for reaching stable slippery superhydrophobicity, even if it exhibits the largest contact angle because of the compromise between maximum pressure held by an interface and high contact angle.

III.2. Critical pressure prediction

Threshold pressure predicted by the model can be easily compared with air plastron stability under pressure measurements made by Lei *et al.*²⁷. The authors immersed in a fluidic chamber a superhydrophobic PDMS surface made of cylindrical pillars of 5 μm radius (R), 50 μm height and organized following a pseudo-triangular lattice with constants of 20 (a_1), 22,4 (a_2) and 22,4 μm (a_3) (Figure 58a.i). They followed the diffracting intensity at 0th and 1st order to compute qualitatively the

air plastron thickness variations with pressure, up to 10kPa (Figure 58a.ii). The authors observed an increase of the 0th order and decrease of 1st order diffraction intensities for pressure up to 2kPa, followed by an inversion (decrease of 0th order and increase of 1st order) for higher pressures. For a pressure lower than 5kPa, the phenomenon was observed to be totally reversible (Figure 58a.iii). After applying a pressure of 6kPa, the phenomenon was only partially reversible, with a remanence corresponding to a 1kPa pressure. When applying a pressure as high as 10kPa, the diffraction intensity went very low, and no recovery was observed.

When applying the model to this experimental surface, the air surface at the interface S_{air} for such pseudotriangular lattice is given by Eq. 27. Thus, the triple line length is $2\pi R$. Taking a surface tension value for water equal to 72,8mN/m and a Young contact angle for water/PDMS equal to 105°, the maximum pressure held by the interface before sagging is 1.83kPa. The D/a ratio value is close to unity, and the air fraction is about 0.8, which is enough when combined with the PDMS strong hydrophobicity for reaching a water contact angle calculated at 148° using the Cassie-Baxter's equation (measured by the authors at 150°).

$$S_{air} = \frac{a_2 \left(\sqrt{a_1^2 - \left(\frac{a_2}{2}\right)^2} + \sqrt{a_3^2 - \left(\frac{a_2}{2}\right)^2} \right)}{2} - \pi R^2 \quad \text{Eq. 27}$$

Where a_1 , a_2 and a_3 are the pseudo-triangular lattice parameters and R the asperities radius.

The value of maximum pressure held by the texture before sagging of the interface of 1.83kPa can be compared to the pressure value corresponding to the maximum in 0th order and minimum of 1st order diffraction intensity, about 2kPa. These limits of diffraction intensity represent the bending of the meniscus due to increasing pressure. When the predicted maximum pressure is reached, the interface sags between asperities, without reaching a stable Wenzel's state. For a higher pressure, the sagging goes so deep that a fully wetted Wenzel's state is reached.

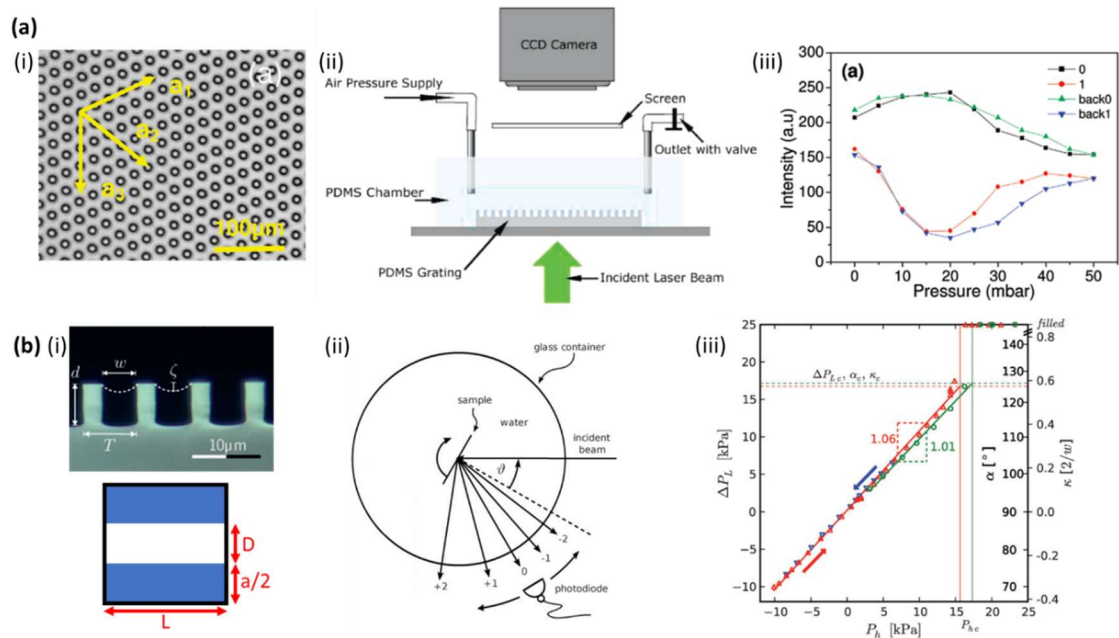


Figure 58 – Measuring the pressure effect on the interface stability. (a) (i) PDMS textured surface with cylindrical pillars, (ii) diffraction of light by the air plastron of the immersed surface experimental set scheme, and (iii) resulting measurements of diffracted intensity with applied pressure. (b) Fluorinated silicon textured surface with streaks (i) optical microscopy view and lattice cell representation, (ii) scheme of the experimental set for measuring the meniscus curvature, and (iii) resulting results: curvature and local contact angle variation with hydrostatic pressure and Laplace pressure corresponding to the curvature of the meniscus. Reprinted from ²⁷ and ²³ respectively, Copyright 2010 American Chemical Society and The Royal Society of Chemistry.

Rathgen and Mugele²³ have conducted a similar experiment with a fluorinated textured superhydrophobic surface based on rectangular streaks of $5\mu\text{m}$ width for $6\mu\text{m}$ depth, spaced by $3\mu\text{m}$. This surface can also be seen as linear asperities of $3\mu\text{m}$ width and $6\mu\text{m}$ height, spaced by $5\mu\text{m}$, with an infinite length (Figure 58b.i). Measuring the diffracted light (Figure 58b.ii) and using the Rigorous Coupled Wave Analysis (RCWA), the authors were able to calculate the meniscus curvature from their diffraction data, and follow its variations with pressure, from -10 to 25kPa (Figure 58b.iii). They observed that the meniscus curvature, *i.e.* local contact angle, varies linearly with the pressure. A negative curvature is observed when a negative pressure was applied, while an increasing curvature is evidenced when the pressure increased above the atmospheric pressure. When the pressure is higher than 17kPa , the curvature did not continue to increase, but an irreversible decay of the plastron was observed. The Cassie-Baxter's state has degenerated into a Wenzel's state. At the maximum applied pressure before non-reversibility, the local contact angle corresponds to the macroscopic Young's contact angle, as hypothesized by the model.

To compare this maximum sustained pressure to the one predicted by the model, the air area at the interface is $S_{air} = DL$, the triple line length is $l = 2L$, and the air fraction is $f_{air} = \frac{D}{D+a}$. The streak length L simplifies in the maximum pressure held calculation, and leads to a value of 14.6kPa taking $\theta_Y = 120^\circ$, according to authors. This calculated pressure is of the same order of magnitude as the measured one, close to 17kPa . Moreover, when considering re-entrant pillars, having a tilting angle $\psi = 84^\circ$, corresponding to a change of only 6° , the new calculated value is $17,1\text{kPa}$. Thus, it can be observed that the calculation is very sensitive to asperities tilt angle, and the accuracy of the predicted value strongly depends on asperities dimensions and angles measurements.

III.3. Conclusion

After applying the model on theoretical surfaces, it was successfully confronted to result published for real patterned and isotropic surfaces. The model well predicts a superhydrophobic or not surface behavior. It was possible to explain wettability differences between some surfaces through the model conclusions and guidelines. This allows the prediction of the maximum critical pressure value for textured surfaces in good adequation with the measured values. However, these predictions are very sensitive to the entry values such as the Young contact angle or the asperities tilting angle. Thus, this model might be used to evaluate order of magnitude order maximum pressure sustained rather than precise values.

Based on confrontations of the proposed model to real surfaces, the model can be considered as robust enough. Guidelines can be confidently defined to design superhydrophobic surfaces from proper texturing.

IV. Chapter conclusion

A quite simple model allowing an accurate prediction of a surface superhydrophobicity based on few geometrical parameters has been described. This model aims to contribute to the understanding and design of slippery superhydrophobic surfaces and their stability under immersion. The model is based on the balance between the pressure applied by the liquid and the surface tension permitting a stable Cassie-Baxter's regime. The simplicity of this model allows its use with few surface geometry parameters, *i.e.* the asperities width, their spacing distance, and their tilting with the macroscopic surface, in addition with conventional wetting characteristics such as surface tension or Young's contact angle. Asperities height is a limit of this model as well as asperities tilting angle that must be strictly lower than the Young's contact angle. This model has been successfully confronted to experimental results published in the literature for patterned surfaces. For each type of surface texture, the model has been able to explain the wettability behavior. If a Cassie-Baxter's interface is stable under some conditions, the resulting surface is slippery superhydrophobic, whereas it will be sticky superhydrophobic with a Wenzel's regime if the maximum pressure is overpassed.

Based on this model and its confrontation to experimental results, an ideal surface can be described in order to reach super stable superhydrophobicity or even superomniphobicity regimes. This ideal surface would have:

- Re-entrant asperities, at an angle $\psi \rightarrow 0$,
- Tiny section asperities ($1\mu\text{m}$ or less, the lower the better),
- Spaced by at least their own size or the double.

If a periodical surface patterning is not mandatory, the overall interface stability will be leveled-down to the weaker part, so the surface should be homogeneous to improve the overall superhydrophobicity. In addition, a multiscale roughness is not mandatory to reach stable superhydrophobicity regime, even if it could help reaching very high contact angle without decreasing the interface stability.

V. References

1. Bico, J., Thiele, U. & Quéré, D. Wetting of textured surfaces. *Colloids Surfaces A Physicochem. Eng. Asp.* **206**, 41–46 (2002).
2. Wenzel, R. N. Resistance of solid surfaces to wetting by water. *Ind. Eng. Chem.* **28**, 988–994 (1936).
3. Cassie, A. B. D. & Baxter, S. Wettability of porous surfaces. *Trans. Faraday Soc.* **40**, 546 (1944).
4. Young, T. An Essay on the Cohesion of Fluids. *Philos. Trans. R. Soc. London* **95**, 65–87 (1805).
5. Marmur, A. Wetting on Hydrophobic Rough Surfaces: To Be Heterogeneous or Not To Be? *Langmuir* **19**, 8343–8348 (2003).
6. Gao, L. & McCarthy, T. J. The “Lotus Effect” Explained: Two Reasons Why Two Length Scales of Topography Are Important. *Langmuir* **22**, 2966–2967 (2006).
7. Lv, C. & Hao, P. Driving Droplet by Scale Effect on Microstructured Hydrophobic Surfaces. *Langmuir* **28**, 16958–16965 (2012).
8. Hisler, V. *et al.* Model Experimental Study of Scale Invariant Wetting Behaviors in Cassie–Baxter and Wenzel Regimes. *Langmuir* **30**, 9378–9383 (2014).
9. Makkonen, L. A thermodynamic model of contact angle hysteresis. *J. Chem. Phys.* **147**, 064703 (2017).
10. Zhu, B. *et al.* Superhydrophobic coating with multiscale structure based on crosslinked silanized polyacrylate and nanoparticles. *Surf. Coatings Technol.* **331**, 40–47 (2017).
11. Yan, Y. Y., Gao, N. & Barthlott, W. Mimicking natural superhydrophobic surfaces and grasping the wetting process: A review on recent progress in preparing superhydrophobic surfaces. *Adv. Colloid Interface Sci.* **169**, 80–105 (2011).
12. Li, H., Peng, Y., Yu, S. & Yin, X. Both slender pillars and hierarchical structures achieving superhydrophobicity and the comparison of their properties. *Appl. Surf. Sci.* **505**, 144524 (2020).
13. Pechook, S. & Pokroy, B. Bioinspired hierarchical superhydrophobic structures formed by n-paraffin waxes of varying chain lengths. *Soft Matter* **9**, 5710 (2013).
14. Cui, Y., Paxson, A. T., Smyth, K. M. & Varanasi, K. K. Hierarchical polymeric textures via solvent-induced phase transformation: A single-step production of large-area superhydrophobic surfaces. *Colloids Surfaces A Physicochem. Eng. Asp.* **394**, 8–13 (2012).
15. Nosonovsky, M. Multiscale roughness and stability of superhydrophobic biomimetic interfaces. *Langmuir* **23**, 3157–3161 (2007).
16. Bittoun, E. & Marmur, A. The role of multiscale roughness in the lotus effect: Is it essential for super-hydrophobicity? *Langmuir* **28**, 13933–13942 (2012).
17. Tuteja, A., Choi, W., Mabry, J. M., McKinley, G. H. & Cohen, R. E. Robust omniphobic surfaces. *Proc. Natl. Acad. Sci.* **105**, 18200–18205 (2008).
18. Brown, P. S. & Bhushan, B. Durable, superoleophobic polymer–nanoparticle composite surfaces with re-entrant geometry via solvent-induced phase transformation. *Sci. Rep.* **6**, 21048 (2016).
19. Zhao, H., Law, K. Y. & Sambhy, V. Fabrication, surface properties, and origin of superoleophobicity for a model textured surface. *Langmuir* **27**, 5927–5935 (2011).

20. Panter, J. R., Gizaw, Y. & Kusumaatmaja, H. Multifaceted design optimization for superomniphobic surfaces. *Sci. Adv.* **5**, (2019).
21. Liu, T. & Kim, C. J. Turning a surface superrepellent even to completely wetting liquids. *Science (80-.)*. **346**, 1096–1100 (2014).
22. Helbig, R., Nickerl, J., Neinhuis, C. & Werner, C. Smart Skin Patterns Protect Springtails. *PLoS One* **6**, e25105 (2011).
23. Rathgen, H. & Mugele, F. Microscopic shape and contact angle measurement at a superhydrophobic surface. *Faraday Discuss.* **146**, 49 (2010).
24. Bhushan, B. & Her, E. K. Fabrication of Superhydrophobic Surfaces with High and Low Adhesion Inspired from Rose Petal. *Langmuir* **26**, 8207–8217 (2010).
25. Yamamoto, M. *et al.* Theoretical Explanation of the Lotus Effect: Superhydrophobic Property Changes by Removal of Nanostructures from the Surface of a Lotus Leaf. *Langmuir* **31**, 7355–7363 (2015).
26. Bhushan, B. & Nosonovsky, M. The rose petal effect and the modes of superhydrophobicity. *Philos. Trans. R. Soc. A Math. Phys. Eng. Sci.* **368**, 4713–4728 (2010).
27. Lei, L., Li, H., Shi, J. & Chen, Y. Diffraction Patterns of a Water-Submerged Superhydrophobic Grating under Pressure. *Langmuir* **26**, 3666–3669 (2010).

CHAPTER 3 – EXPLORING SIMPLE TEXTURING METHODS TO REACH SUPERHYDROPHOBICITY

Exploring simple texturing methods to reach superhydrophobicity

I. Review of relevant routes to produce textured surfaces.....	79
I.1. Texturing using particles	79
I.1.a. Particles deposition on the surface	79
I.1.b. Particles dispersed in the bulk	80
I.2. Porous membranes and foams	81
I.2.a. Removing a phase of an immiscible polymer blend	81
I.2.b. Foaming a thermoplastic using supercritical CO ₂	81
I.2.c. Using blend interfaces to enhance foam nucleation	83
I.3. Conclusion	84
II. Materials and methods.....	85
II.1. Materials	85
II.2. Processing techniques.....	86
II.2.a. Processing polymer blends.....	86
II.2.b. Sc-CO ₂ foaming	87
II.2.c. Blown-film extrusion.....	88
II.3. Characterization methods	88
II.3.a. Scanning Electron Microscopy.....	88
II.3.b. Surface roughness measurements	89
II.3.b.i. Mechanical profiler	89
II.3.b.ii. Atomic Force Microscopy.....	89
II.3.c. Wettability measurements	89
III. Texturing from fillers	90
III.1. Classical fillers	90
III.2. Glass microspheres	92
III.3. Organic particles.....	94
III.3.a. PTFE microparticles	94
III.3.b. UHMWPE particles	94
III.4. Conclusion	96
IV. Immiscible polymer blends	97
IV.1. Polyethylene / polyethyleneoxide immiscible blend	97
IV.2. Filled PE/PEO immiscible blend filled based on hydrophilic silica.....	99
IV.3. Filled HDPE/PEO immiscible blend based on hydrophobic silica	100
IV.4. Filled HDPE/PEO immiscible blends based on PTFE microparticles	101
IV.5. Conclusion	103
V. Batch foaming using supercritical carbon dioxide	104
V.1. Foaming HDPE and PP with Sc-CO ₂	104
V.1.a. Influence of the foaming temperature.....	104
V.1.b. Influence of the depressurization rate	107
V.1.c. Influence of fillers as nucleating agents	108
V.1.c.i. Filled high-density polyethylene	108
V.1.c.ii. Filled polypropylene.....	110
V.2. Foaming immiscible polymer blends.....	112
V.2.a. Polypropylene / polystyrene immiscible blend	112
V.2.a.i. PP/PS 50/50 blends	112
V.2.a.ii. 70/30 PP/PS blends	113
V.2.b. Polypropylene / polyethylene immiscible blend	114
V.3. Conclusion	116
VI. Continuous foaming process (extrusion).....	117
VI.1. Blowing agents	117
VI.2. Extrusion of polyethylene foams.....	120
VI.2.a. Influence of the CBA loading	120
VI.2.b. Influence of the CBA compound.....	122

VI.2.c.	Influence of the nucleating agents	123
VI.2.d.	Extruding a HDPE foam with a high matrix viscosity	124
VI.3.	Conclusion	126
VII.	Chapter conclusion	127
VIII.	References.....	129

After describing the ideal texture required for a hydrophobic surface to be superhydrophobic in the last chapter, the different relevant routes to produce such textures have been investigated. In addition to the literature review of the first chapter, a brief overview of the manufacturing processes leading to textured surfaces and to superhydrophobicity will be reported. Three major routes can be evidenced:

- Adding fillers to texture the polymer surface,
- Considering immiscible polymers blends,
- Foaming a thermoplastic surface using supercritical CO₂.

An additional route for producing textured surfaces suitable for superhydrophobicity will be considered, as a derivative of the third route, *i.e.* directly extruding thermoplastic foams.

For these four texturing routes, some of the obtained surfaces will be presented, and an understanding of the texturing mechanisms will be attempted, in order to optimize the final surface morphology. The texture and wettability of surfaces will be characterized by SEM, and water contact angle and hysteresis measurements, respectively. Strengths and weaknesses of each texturing method will be discussed, as well as some potential perspectives to go on the current study, or use it for other applications that superhydrophobicity.

I. Review of relevant routes to produce textured surfaces

I.1. Texturing using particles

To obtain a superhydrophobic textured surface, nanoparticles deposition is the most common strategy, as discussed in the first chapter. However, the use of nanoparticles on the surface can sometimes involve complex nanoparticles assemblies or surface-modified particles. Here, only the easiest ways to produce a textured surface have been reported, with some of them even showing a superhydrophobic behavior.

I.1.a. Particles deposition on the surface

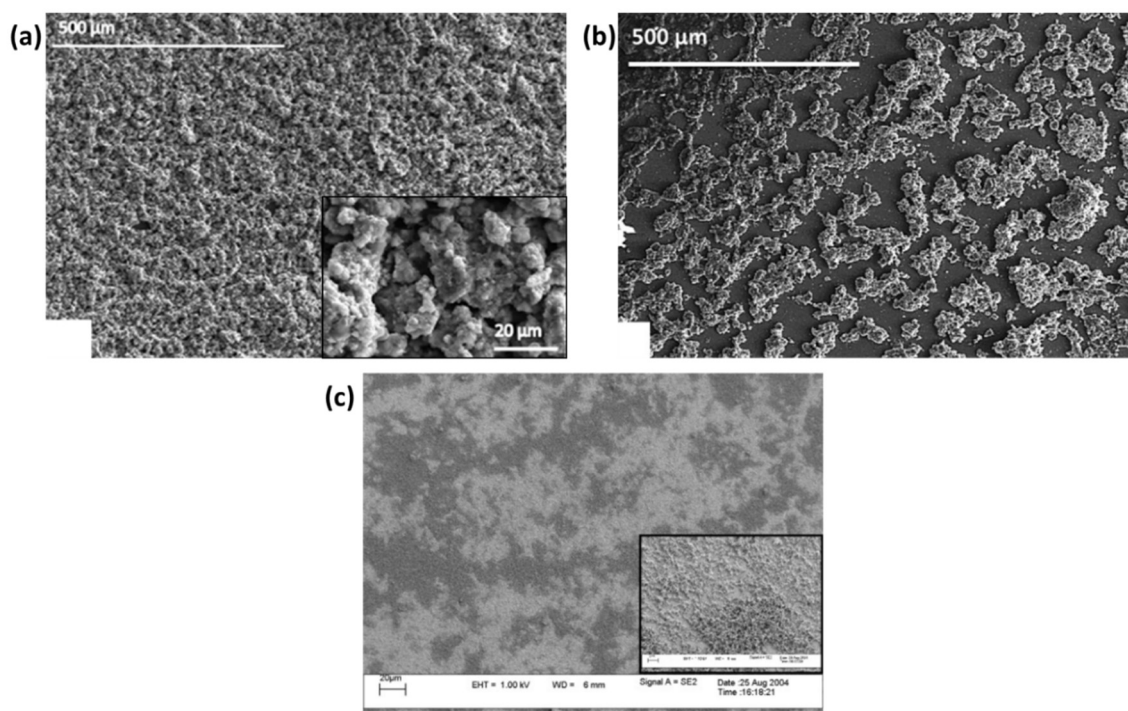


Figure 59 – SEM micrographs of textured surfaces obtained by depositing nanoparticles on a substrate by (a,b,c) spray or (d) spin-coating. (a) Zinc oxide nanoparticles at 100g.L^{-1} in a PDMS-in-white-spirit solution, sprayed on a silicon wafer¹. (b) Silica nanoparticles at 20g.L^{-1} in a PMMA-in-toluene solution, sprayed on a silicon wafer¹. (c) SiO_2 nanoparticles at $40\%_{\text{wt}}$ in a polystyrene-in-chloroform solution, spin-coated on glass substrate². Reprinted from (a,b)¹, (c)², Copyright 2014 Elsevier and 2005 American Chemical Society, respectively.

For example, Manoudis and Karapanagiotis¹ obtained a superhydrophobic surface by simply spraying a $7\%_{\text{wt}}$ PDMS-in-white-spirit solution containing 100g.L^{-1} of alumina nanoparticles (27-43nm) on a silicon wafer (Figure 59a). They were also able to obtain similar surfaces using other nanoparticles such as silica (7nm), tin oxide (22-43nm) or zinc oxide (40-100nm).

The nanoparticles bring their own texturing to the surface, which is amplified by the spray deposition process that leads to a stacking of the particles, and the PDMS covers these particles, reducing the surface energy ($\gamma_{\text{PDMS}} = 21.5\text{mN/m}$)³. They used the same process using a thermoplastic, poly(methyl methacrylate) (PMMA) at $5\%_{\text{wt}}$ in toluene with a low silica nanoparticles fraction of 20g.L^{-1} , and obtained a similarly textured surface. However, the silicon wafer coverage was not fully complete, probably because of the shrinkage of the thermoplastic after solvent evaporation (Figure 59b).

Yüce *et al.*² also designed superhydrophobic surfaces by spin-coating a preparation of $40\%_{\text{wt}}$ silica nanoparticles in a polystyrene-in-chloroform solution. The resulting surface displayed an important texturing at nanoscale, with nanoparticles aggregates leading to a porous surface which can be favorable to superhydrophobicity (Figure 59c). The surface energy of the sample was reduced by both

the use of a hydrophobic grade silica and the use of PS as the polymer matrix, which is also hydrophobic.

They proved that even when using a deposition process that intrinsically generates less texturing than spraying, such surfaces could be obtained when the nanoparticles concentration is sufficiently high. As Fourmentin *et al.*⁴, whose work has been detailed in the first chapter, the authors observed a major impact of the nanoparticles content in the blend on the resulting surface wetting behavior, with a threshold around 40-60%_{wt} of nanoparticles in the coating. However, all these texturing routes require nanoparticles-filled polymer solutions, which are specific to the deposition process, such as spraying or spin-coating.

1.1.b. Particles dispersed in the bulk

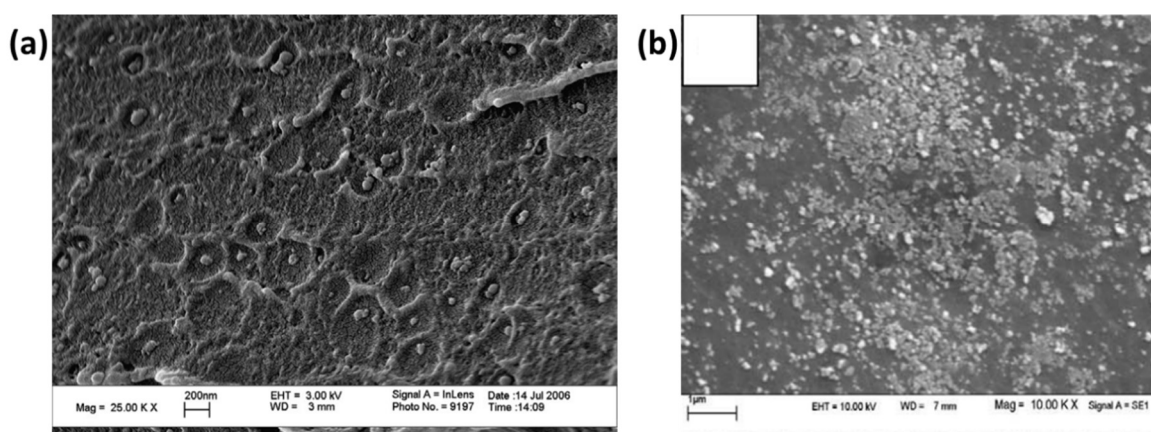


Figure 60 – SEM observations of textured surfaces obtained by hot-pressing polymer/particles nanocomposites. (a) Hot-pressed 2%_{wt} Al₂O₃ in polycarbonate film⁵. (b) Hot-pressed 5%_{wt} hydrophilic silica in poly(ethylene terephthalate) film⁶. Reprinted from ^{5,6}, Copyright 2008 and 2010 Elsevier.

Chandra *et al.*⁵ obtained textured surfaces of hot-pressed polycarbonate films containing alumina nanoparticles (96nm) coated by a poly(styrene-maleic anhydride) copolymer. The purpose of their work was to produce a PC nanocomposite with improved mechanical properties without altering its transparency. If their goal was far from the current project application, the fact that they obtained a textured surface using a filming process that typically produces relatively smooth samples is interesting.

Using only 2%_{wt} of alumina nanoparticles, they obtained a textured surface with the formation of a cellular structure composed of nanoparticles on the surface (Figure 60a). If such approach could be used with higher loads of nanoparticles, a surface sufficiently textured to be superhydrophobic could be obtained.

Similarly, Parvinzadeh *et al.*⁶ obtained a textured poly(ethylene terephthalate) film by hot-pressing a PET containing 5%_{wt} of hydrophilic silica. The surface of the resulting film shows an important concentration of silica nanoparticles. This feature leads to a relatively important textured surface despite the low nanoparticles concentration (Figure 60b). By increasing the particles content and tuning their surface energy, using hydrophobic silica for example, a superhydrophobic surface could theoretically be obtained by pressing or extruding a filled thermoplastic.

Based on these works, it seems that the surface texturing using nanoparticles could be achieved relatively easily by a surface deposition or with nanoparticles emerging from the bulk. If the surface deposition approach has proved to lead to superhydrophobic surfaces, it requires a high particles content. With a lower particles fraction, surfaces textured by using emerged particles are an interesting route. Nevertheless, such a route has not proven its ability to lead to superhydrophobic surfaces yet.

1.2. Porous membranes and foams

1.2.a. Removing a phase of an immiscible polymer blend

Another strategy to easily produce textured thermoplastic is to mimic the membranes and foams production. Then, the bulk morphology has to be “transferred” to the surface for superhydrophobicity. A few routes leading to interesting bulk morphologies will be reported as inspirations source for surface texturing.

Trifkovic *et al.*⁷ obtained porous membranes with a very reduced pores size from removing one phase of a co-continuous immiscible polymers blend. To do so, they mixed a neat polyethylene (PE) or a maleic anhydride grafted one (PE-g-MA) with a poly(ethylene oxide) (PEO), in equivolumetric proportions (50/50%_{vol}). The maleic anhydride grafting acts as a compatibilizer between PE and PEO. Thus, the two polymers phases are reduced thanks to the decrease of the interfacial tension.

By mixing these polymers in a twin-screw extruder, they obtained a co-continuous immiscible blend, resulting in a porous membrane after removing PEO with water. They observed that the process had an influence on the resulting phases size, with the blend exposed to the larger shear having tinier phases (Figure 61a and b). On the other hand, they observed a major impact of the MA grafts, that act like a compatibilizer, on the resulting polymers phases. With a neat PE/PEO blend prepared in the same condition as the sample in Figure 61a, they now have phases larger than 10 μm (Figure 61c).

Based on the Cassie-Baxter’s interface stability model, such surface morphologies are believed to be favorable to superhydrophobicity. In fact, asperities have almost the same size as the porosities, *i.e.* above 10 μm , and the residual polymer is hydrophobic. However, the expect air fraction at the interface of about 50% might be too low to give the surface a sufficiently large water contact angle. Still, modifications of the blend proportions could help solve this problem, but could also induce a change in the final morphology, as well as a loss of mechanical properties. Moreover, such porosity must be present on the surface of the sample, and not only in the bulk as in the current example.

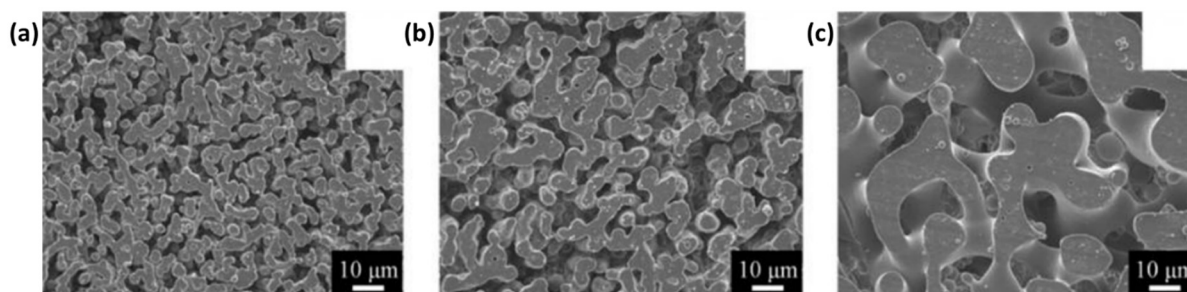


Figure 61 – SEM observations of sliced polyethylene or polyethylene-grafted-maleic anhydride/poly(ethylene oxide) immiscible polymer blends after PEO removal. (a), (b) correspond to various mixing conditions of PE-g-MA/PEO 50/50 blends, from the greater mixing time (a) to the lesser (b), whereas (c) is a PE/PEO 50/50 blend compounded with the same conditions than (a). Reprinted from ⁷, Copyright 2012 American Chemical Society.

1.2.b. Foaming a thermoplastic using supercritical CO₂

To produce directly porous thermoplastic foams, supercritical carbon dioxide (Sc-CO₂) is a powerful path. In fact, Sc-CO₂ has many advantages such as the diffusivity of a gas and the density of a liquid, while being a low-cost process. Depending on the pressure and the temperature, the Sc-CO₂ will be more or less soluble in a given polymer⁸, resulting in a phase separation. Thus, CO₂ “bubbles” appear in the material and grow, powered by the pressure difference between these bubbles and the pressure applied to the material.

Goel and Beckman⁹ produced microcellular PMMA foams using Sc-CO₂. The authors obtained a microcellular foam, with porosities of around 1 μ m with a limited dispersity (Figure 62a). They attributed this reduced porosity size to both low temperature foaming and high saturation time, considering that it favors a homogeneous cell nucleation, and thus a greater nucleation rate.

With a similar autoclave foaming process, Reignier *et al.*¹⁰ used crystallization to reduce the cells size. To do so, they simply add talc (5%_{wt}) as a nucleating agent for poly(ϵ -caprolactone). Such process resulted in cells of less than 10 μ m of diameter with a small dispersity (Figure 62b). This foam was also reported to have open porosities, which is quite rare for a CO₂-foamed polymer.

They attributed the reduced cell size and open-cell behavior to a change of the matrix viscoelastic properties through temperature due to the addition of talc, the polymer stiffness being mainly governed by its crystallinity. The smaller cells were obtained when foaming the polymer below the polymer crystallization temperature when swollen by CO₂.

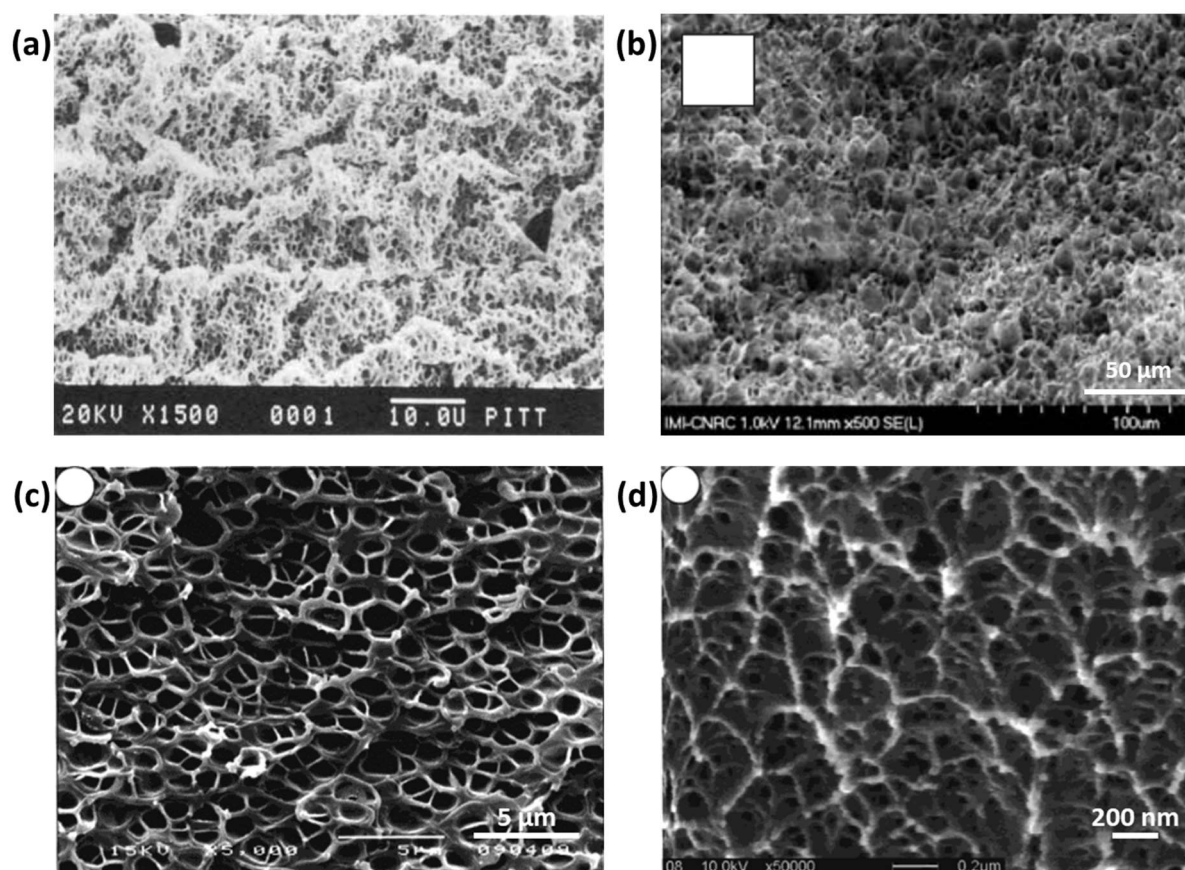


Figure 62 – SEM observations of thermoplastics foam inner structures obtained using carbon dioxide. (a) PMMA foamed at 40°C after a 24h exposure of Sc-CO₂ at 34.47MPa.⁹ (b) Poly(ϵ -caprolactone) filled with 5%_{wt} of talc foamed at 30°C after a CO₂ exposure of 3h at 6.41MPa and 70°C.¹⁰ (c) Polyimide and (d) polysulfone foamed in a glycerol bath at 170°C and 260°C respectively, after a CO₂ exposure at 5MPa and 25°C.¹¹ Reprinted from (a)⁹, (b)¹⁰, and (c,d)¹¹, Copyright 1994 Wiley, 2007 SAGE Publications, and 2002 American Chemical Society, respectively.

Krause *et al.*¹¹ obtained open nanocellular foams using polyimide and polysulfone, by foaming these polymers at a temperature below their glass transition. They obtained a nanocellular foam with an unfoamed skin due to CO₂ diffusion near the sample interface. With polyimide, cells are about 1 μ m large with a polygonal shape and a relatively low dispersity (Figure 62c). With polysulfone, the cells are even smaller and open, with a diameter of a few nanometers and a more irregular shape (Figure 62d).

The described morphologies obtained by foaming thermoplastics using Sc-CO₂ are interesting for superhydrophobicity, as they produced morphologies with small cells. However, they are only inner morphologies, observed after a freeze-fracture of the sample, and the surface of these samples

remains smooth for most of the cases. Moreover, the processes involved require a long time for cooling the samples in various liquids at a controlled rate.

I.2.c. Using blend interfaces to enhance foam nucleation

Another way to produce microcellular foams consists in the use of polymer blends. The interface will increase the nucleation rate, leading to a larger cells density and lower cells size. For example, Liao and Nawaby¹² have obtained a skinless microcellular foam from a poly(L-lactic acid)/poly(D,L-lactic acid) blend in 70/30 weight fractions.

The resulting sample had tiny open porosities, with a skinless morphology, meaning that the sample surface was porous. When observing the inner structure of the foamed sample, it appears that there are very disperse cells sizes, that appear to have been formed from cells walls fracture (Figure 63a). Some cells seem to have coalesced a longer time than others, resulting in such a high size dispersity.

The authors claimed to have been able to generate an open-cells morphology thanks to their fine tuning of the matrix stiffness, due to crystallinity. In fact, addition of PDLLA reduced the PLLA crystallinity, thus permitting the sample to have intermediate viscoelastic properties between PDLLA and PLLA. Moreover, in comparison with polyolefin, poly(lactic-acid) in general is found to have a greater CO₂ solubility. For example, the solubility of CO₂ in PLA is about 500mg per gram of polymer at 3.2MPa and 0°C¹², against only 10mg CO₂/g polymer for polystyrene at 2.5MPa and 200°C¹³. Thanks to the skinless morphology obtained, and with a reduced porosities size, such morphology could be very interesting for superhydrophobicity, even if PLA is slightly hydrophilic.

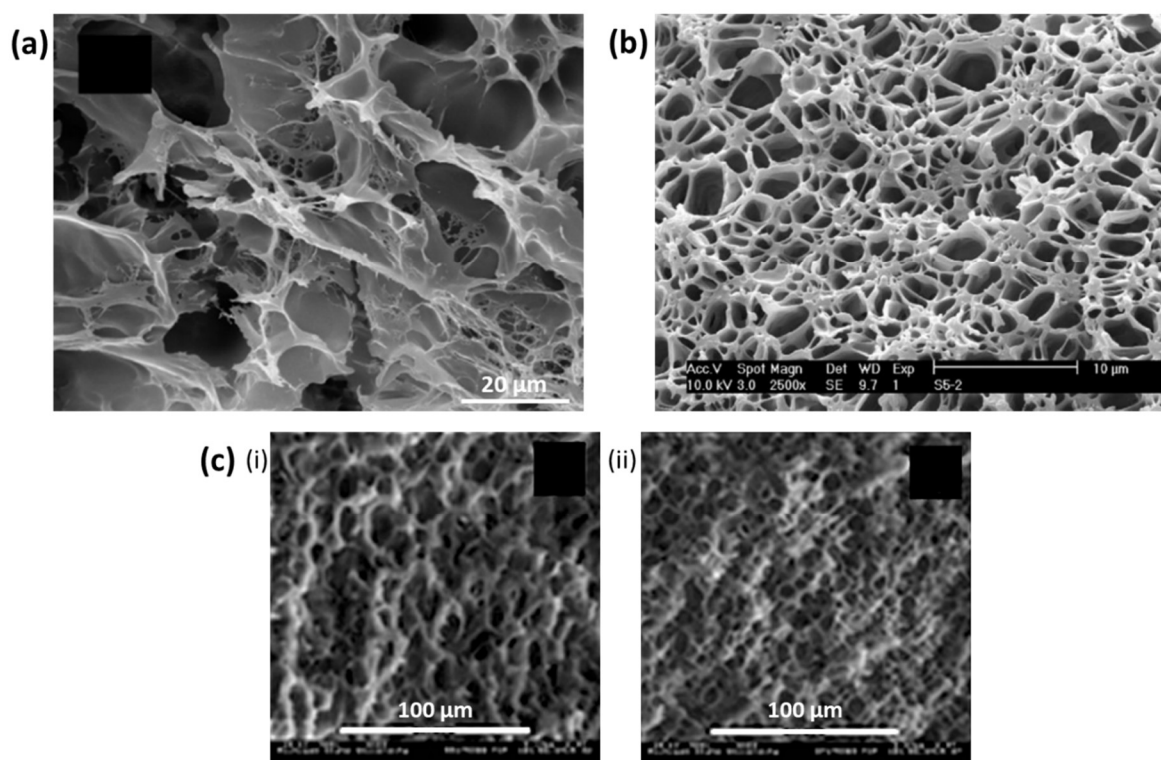


Figure 63 – SEM observation of foamed thermoplastics blends. (a) Poly(L-lactic acid)/poly(D,L-lactic acid) blend in 70/30 proportions foamed in water at 90°C, after a CO₂ exposure at 2.8MPa and 0°C for 24h.¹² (b) PP/PS 70/30 blend foamed at 179°C, after a Sc-CO₂ exposure at 19MPa and 179°C for 10h.¹⁴ (c) HDPE/PP blend in (i) 50/50 and (ii) 30/70 proportions foamed in glycerin at 175°C, after a CO₂ exposure at 5.5MPa at room temperature for 24h.¹⁵ Reprinted from (a)¹², (b-c)¹⁴ and (c)¹⁵, Copyright 2012 American Chemical Society, 2011 Wiley, and 2004 Society of Plastics Engineers, respectively.

Huang and Xu¹⁴ obtained very interesting morphologies with immiscible polypropylene/polystyrene blends (PP/PS) in various proportions. In particular, PP containing 30%_wt of PS was found to have a microcellular morphology with a large air fraction when foamed (Figure 63b). Such a morphology is due to a heterogeneous nucleation in the PS dispersed phase and at the PP/PS interface. The heterogeneous nucleation leads to an increased number of nucleation sites and thus a higher cell density and reduced cells size, of about 10^{13} cells/cm³ and 150nm, respectively.

Moreover, as the CO₂ solubility in PP is relatively high in comparison to PS, the PP phase could act as a CO₂ reservoir within the polymer. It also appeared from observation of other foams obtained using blends in different PP/PS proportions that the cell growth takes place mainly in the PS phase, the PP phase being stiffer. Even if the samples had a non-porous skin, the obtained morphology is very favorable to superhydrophobicity, with porosities of less than 10µm, thin cell walls and PP and PS intrinsic hydrophobicity.

Rachtanapun *et al.*¹⁵ also obtained microcellular foams HDPE/PP blends with various compositions. Depending on the HDPE/PP proportions, slightly different morphologies were obtained. With 50/50 proportions, the polymer phases are co-continuous and the foamed sample has relatively large cells with thick walls (Figure 63c.i). With 30/70 proportions, the polypropylene phase is dispersed within the HDPE matrix, and the foamed sample has smaller rounded asperities with a reduced size dispersity and relatively thin walls (Figure 63c.ii).

Once again, the authors attributed such a microcellular morphology formation to a heterogeneous nucleation of the cells at the HDPE/PP interfaces. In addition, they could adapt the stiffness of the matrix by the compounding, limiting the cell growth and coalescence. However, such samples were still found to have a dense skin and a smooth surface.

1.3. Conclusion

In addition to different routes to produce superhydrophobic surfaces detailed in the first chapter, it has been shown that easier processes can lead to morphologies leading to superhydrophobicity, according to the understanding from the interface stability model.

These routes are:

- Deposition of particles at the surface,
- Surface emergence of nanoparticles dispersed in a thermoplastic,
- Removal of a given phase from a co-continuous immiscible polymer blend,
- Foaming thermoplastic surfaces.

However, if all these ways seem to be suitable for producing superhydrophobic surfaces, they all have drawbacks that must be overpassed. For example, the nanoparticles nature and content need to be tuned in order to have well textured surfaces. For foams, a similar surface morphology as the one observed in their core is required, rather than their conventional dense skin. All these routes will be investigated in the following chapter, focusing on designing textured superhydrophobic surfaces using simple and inexpensive materials and processes.

II. Materials and methods

II.1. Materials

Four references of high-density polyethylene (HDPE) from Total were considered (Table 9). These resins have been selected mainly for their use in packaging. One polypropylene resin was also investigated, *i.e.* PPH4060 from Total.

The crystallinity of the HDPE resins is traduced by their density, crystalline polyethylene being denser than amorphous polyethylene. The viscosity of these resins is given by their melt index (MI), following the ASTM standard D1238. The 5502-R3 resin is thus the more viscous one, followed by BM593, M6040 and HD6081.

Polystyrene (PS), low-density polyethylene (LDPE) and poly(oxy-ethylene) (PEO) were also occasionally used as matrixes or for blends with HDPE or PP. Relatively viscous resins of PS and LDPE were used. PEO was supplied by Sigma Aldrich and has a molecular weight around 100kg/mol according to the supplier, permitting it to act as a fully entangled polymer, while being able to easily dissolve in water.

Polymers were used as received as pellets, except for PEO which was received as a fine powder. Surface tension measurements were done on smooth samples by measuring their contact angles with water and diiodomethane.

Table 9 – Polymer considered in this study

Polymer		HDPE	HDPE	HDPE	HDPE	PP	PS	LDPE	PEO
Supplier		Total	Total	Total	Total	Total	Total	Total	Sigma Aldrich
Reference		5502	BM593	M6040	HD6081	PPH4060	PS1070	FE8000	181986
Melt index	Conditions	2.16kg 190°C	2.16kg 190°C	2.16kg 190°C	2.16kg 190°C	2.16kg 230°C	5kg 200°C	2.16kg 190°C	-
	Value (g/10min)	0.25	0.27	4.0	8.0	3.0	1.6	0.8	-
Density		0.954	0.959	0.960	0.960	0.905	1.05	0.924	1.13
Melting point (°C)		136	134	137	135	168	-	111	65
Surface tension (mN/m, at 25°C)		41.2	37.5	36.2	37.8	31.2	42.3	38.1	43

Table 10 – Silica particles considered in this study

Reference	HDK® S13	HDK® H20	Aerosil® 200	Aerosil® R812
Supplier	Wacker	Wacker	Evonik	Evonik
Type	Pyrogenic	Pyrogenic	Pyrogenic	Pyrogenic
Nature	Hydrophilic	Hydrophilic	Hydrophilic	Hydrophobic
Specific surface area	110-140 m ² /g	170-230 m ² /g	200 ±25 m ² /g	230-290 m ² /g
Surface modification	None	Dimethylsiloxo	None	Hexamethyldisilazane
Water contact angle*	-	63° ±11°	-	137° ±7°

Four different fumed silica nanoparticles were: hydrophilic ones (Wacker HDK® S13 and Evonik Aerosil® 200), and hydrophobic ones (Wacker HDK® H20 and Evonik Aerosil® R812) (Table 10).

Surface tension measurements were performed on films made of compressed silica particles. Nevertheless, with hydrophilic particles (Aerosil® 200 and HDK® S13), the film instantaneously absorbed the water droplet, *i.e.* water completely wet such silica particles. With other silica particles, the measured water contact angle gives a trend of hydrophilicity of hydrophobicity, because of the compressed silica film roughness.

Other types of particles, *i.e.* organic or inorganic ones, were also considered as fillers or as texturing agents, such as talc, calcium carbonate (CaCO₃), ultra-high molecular weight polyethylene (UHMWPE) or poly(tetrafluoroethylene) (PTFE) (Table 11).

Table 11 – Particles (organic or inorganic) considered in this study

Type	Talc	Calcium carbonate	UHMWPE	PTFE	Glass beads
Reference	Luzenac A3	-	GUR4150	430935	GL019B4-1345
Supplier	Imerys	-	Ticona	Sigma Aldrich	Mo-Sci
Average particles size	~ 1µm	<50µm	~ 100µm	~ 1µm	13-45µm

II.2. Processing techniques

II.2.a. Processing polymer blends

Polymer blends with additives such as organic or inorganic particles were processed using a twin-screw micro-extruder. The used twin-screw micro-extruder was a DSM Xplore MC15 extruder, equipped of conical co-rotating screws in a heated barrel that allow re-circulation of the matter with a total volume of 15mL (Figure 64).

The desired blend compounds were classically introduced in the micro-extruder turning at 100rpm and heated a homogeneous temperature from 160°C to 220°C for HDPE and from 180°C to 220°C for PP, and mixed for 3 to 5 minutes prior to extrusion. Blends were typically extruded into strands and cut into pellets using a pelletizer, or kept as a strand, or even extruded as a film using a 0.2mm film die. For films, the material was cooled right out of the die using an air jet, and the film was uniaxially pulled, resulting in a thickness from 50µm to 400µm depending on the operating conditions.



Figure 64 – DSM Xplore® MC15 micro-extruder

II.2.b. Sc-CO₂ foaming

Foaming a thermoplastic using a gas like CO₂ in a subcritical or supercritical state usually requires two main steps: swell the material with CO₂, and quickly breaking the polymer/CO₂ miscibility, for example by quenching the pressure. In this second step, the CO₂ that is no longer miscible within the material will phase-separate into bubbles. These bubbles will grow depending on the material viscosity, and the pressure difference between the bubble and the material. This pressure difference powers the cells growth, and the material will oppose a resistance to this growth through its elongational viscosity.

Thermoplastic foams presented in the current chapter using Sc-CO₂ have been obtained using a batch-foaming apparatus, schematically described in Figure 65. The foaming chamber is a 300cm³ steel cylinder hermetically closed by pinching, fed with gaseous CO₂ that can be liquefied using a high-pressure pump.

The chamber temperature and pressure are computer-monitored by the electric heater unit and the exhaust valve. The exhaust flow rate is controlled by opening or closing a bit the flow control valve. In a typical experiment, the flow control valve is fully opened, but it can occasionally be only 75%, 50% or 25% opened, from the larger flow rate to the smaller one. The precise flow rate cannot however be controlled or measured, due to the extreme speed of the pressure quench.

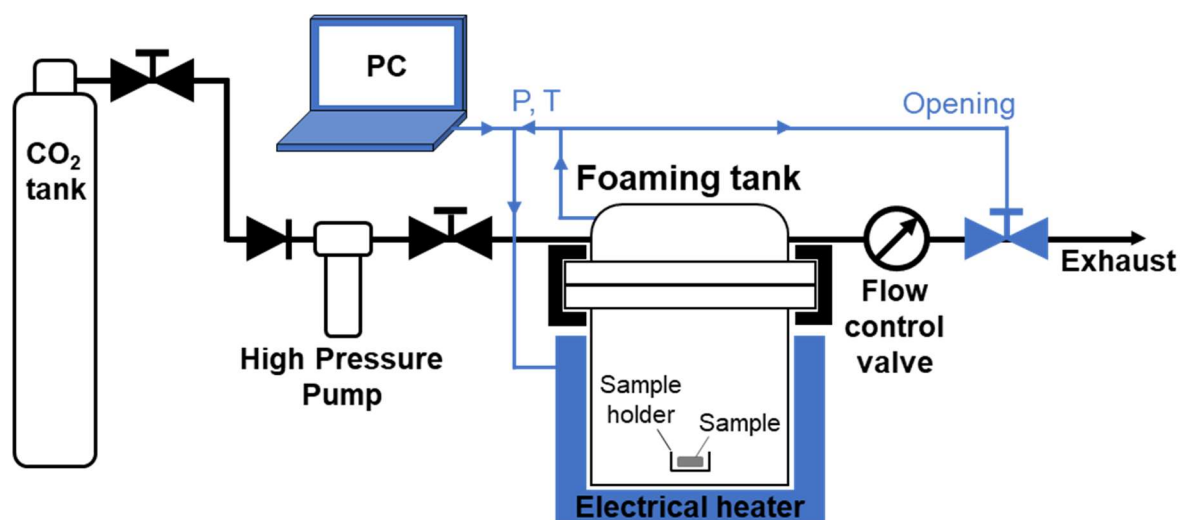


Figure 65 – Scheme of the Sc-CO₂ batch foaming apparatus consisting of a 300cm³ tank fed with CO₂ using a high-pressure pump and an electric heater. Pressure and temperature are computer-monitored. The foaming tank, from Parr, is designed to work at a maximum pressure of 20MPa and a maximum temperature of 350°C.

A typical foaming experiment of a thermoplastic such as HDPE or PP consists of the following steps:

- The sample is placed in the foaming chamber, that is then sealed and flushed with CO₂. CO₂ is then introduced and pressurized thanks to the high-pressure pump. Above the saturating vapor pressure of CO₂, a part of the gas condensates into liquid CO₂.
- The pressure vessel is then completely isolated from the CO₂ feeding part and the chamber is heated up to the exposure temperature. This temperature elevation is coupled by a pressure increase. Once the desired conditions are reached, the system is maintained for a given time, typically from 1 to 5 hours, to reach the equilibrium of CO₂ diffusion in the material.
- The system is then cooled down to the foaming temperature (about 3°C/min). Once the desired foaming temperature is reached, the pressure is instantly released by commanding the opening of the exhaust valve. This depressurization also induces a cooling of the system at temperatures below the foaming temperature.

A foaming experiment using this process is characterized by the sample nature, the exposure conditions (temperature and pressure), and the foaming conditions (temperature and flowing rate). All samples that have been foamed using such a process are then sliced using a razor blade. As Sc-CO₂ is well-known to generate smooth-skin samples and closed cells, the foams surface was not furtherly investigated but its smoothness was always confirmed.

II.2.c. Blown-film extrusion

To produce thermoplastic films, a lab-scale blown-film extruder setup was used (Collin Tech-line BL50T with a E20T extruder, Figure 66). This setup is composed of a single-screw extruder that melts, transports and compresses the matter. The polymer goes through a heated ring die of 1mm thick and 30mm large, and the formed sheath is inflated using compress air, and cooled using an air flow all around the die.

A typical blown-film extrusion experiment is performed with an extruder heated at a temperature from 180°C to 230°C from the hopper to the end. The extruder screw is typically rotating at 25rpm, leading to a pressure from 5 to 15MPa at the end of the extruder. The residency time of the material from the hopper to the ring die is of about 2 minutes when the screw is operating at 25rpm. The film thickness depends on the uniaxial stretching rate and of the inflating rate.

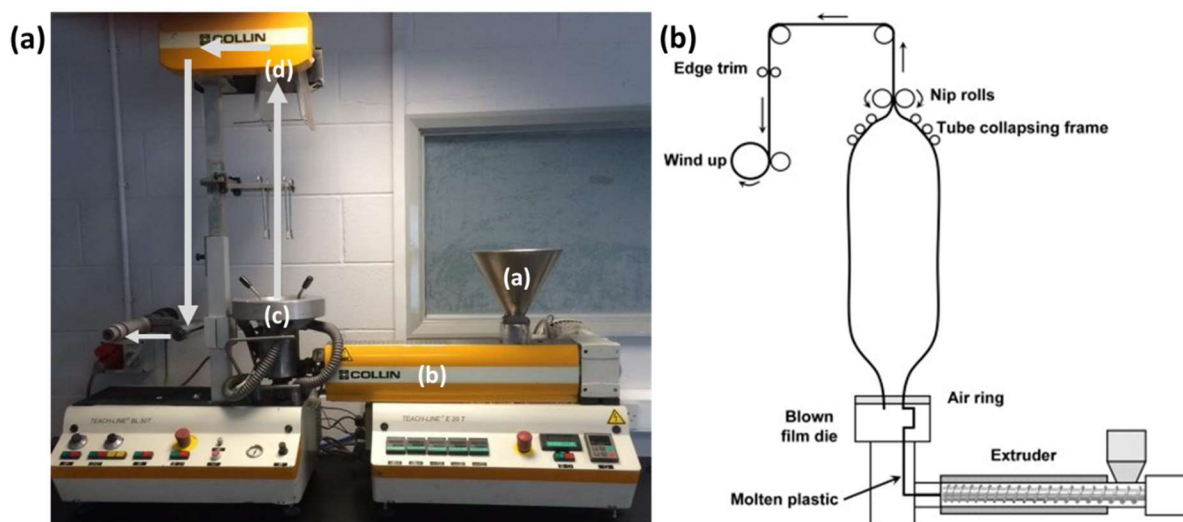


Figure 66 – Blown-film extruder apparatus. (a) Collin Tech-line® BL 50T blow film system with a Collin Tech-line® E20T extruder. (A) Hopper, (B) single-screw extruder for material melting and compression, (C) ring die of 30mm diameter and 1mm thick, with a film cooling by air flow, (D) rollers for film pinching and drawing., and (b) corresponding scheme, from ¹⁶. Copyright Elsevier 2017.

II.3. Characterization methods

II.3.a. Scanning Electron Microscopy

In order to characterize the sample surface texture and determine asperities shape and size, scanning electron microscopy (SEM) was systematically performed on the obtained samples. After a surface preparation process depending on the sample particularities (cutting for bulk-foamed samples, drying to solvent-exposed samples, etc.), the samples were metalized with gold at an electrical current of 30mA for 90s, at a distance of 5cm.

Samples were then observed using a TESCAN Vega microscope. Observations were made using a secondary electron detector and an acceleration tension of 10kV, and a working distance of 10mm.

Some experiments focusing on the samples extreme surface were performed using a Zeiss Merlin Compact VP from the Centre Technologique des Microstructures (CTμ) of Lyon. With an acceleration

tension of only 1kV and a working distance of around 5mm, it was possible to obtain good quality pictures with a very limited electron penetration depth, depicting the samples most extreme surface.

II.3.b. Surface roughness measurements

II.3.b.i. Mechanical profiler

Surface topography of the process samples were characterized using a Veeco Dektak 150 mechanical profiler. However, even by using the smallest available stylus for such an apparatus (radius of $2.5\mu\text{m}$), asperities were often too small to be fairly measured. The results obtained from such a method will thus not be presented in this thesis as they bring no useful additional information.

II.3.b.ii. Atomic Force Microscopy

AFM measurements were not performed on samples with the smallest asperities because of a too high depth of voids between these asperities, that would have damaged the apparatus. If the lateral resolution of AFM would have been interesting for measuring distances and heights on the obtained samples, the risk of damages prohibited its use.

Asperities sizes and shape have thus been measured from SEM pictures using the ImageJ software for discrete or complete measurements, that permitted to determine sizes distribution for example.

II.3.c. Wettability measurements

The surface wettability and surface tension have been characterized by measuring the contact angle with water or diiodomethane. Advancing and receding contact angle were measured using the sessile drop technique, and hysteresis was calculated from these values (ISO 19403-6:2017, Figure 67a-b).

An alternative way to obtain such values consists in measuring the static contact angles of a drop after deposition and after liquid removal from the drop (Figure 67c-d). The static measurement technique has been employed for most contact angle measurements for its simplicity, and was found to provide values consistent with the ones obtained using the dynamic technique. Measurements were made using a DataPhysics Instruments OCA15 apparatus.

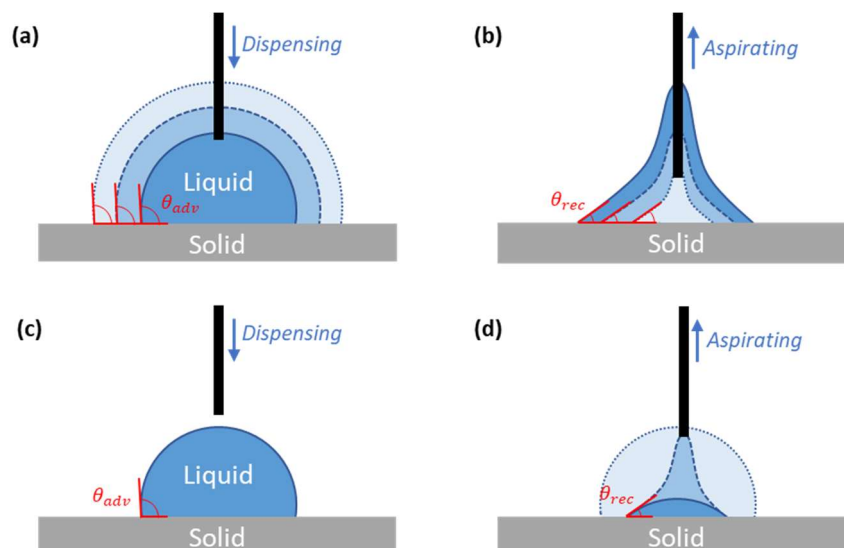


Figure 67 – Measuring advancing and receding contact angle with the sessile drop technique. (a) Advancing and (b) receding contact angle measurement on advancing and receding triple lines due to liquid addition or removal from a drop (dynamic measurement), and simplified measurement technique for (c) advancing and (d) receding contact angle at equilibrium after drop deposition and liquid removal.

III. Texturing from fillers

III.1. Classical fillers

The first route to texture a HDPE surface was considered from the incorporation of silica by a film extrusion (Figure 68). Two types of fumed silica were used: a hydrophilic and a hydrophobic one (Wacker HDK® S13 and H20). Various amounts of silica were introduced in HDPE (BM593) (from 6 to 22%_{vol}, *i.e.* 11%_{wt} to 34%_{wt}) at 200°C (Figure 69).

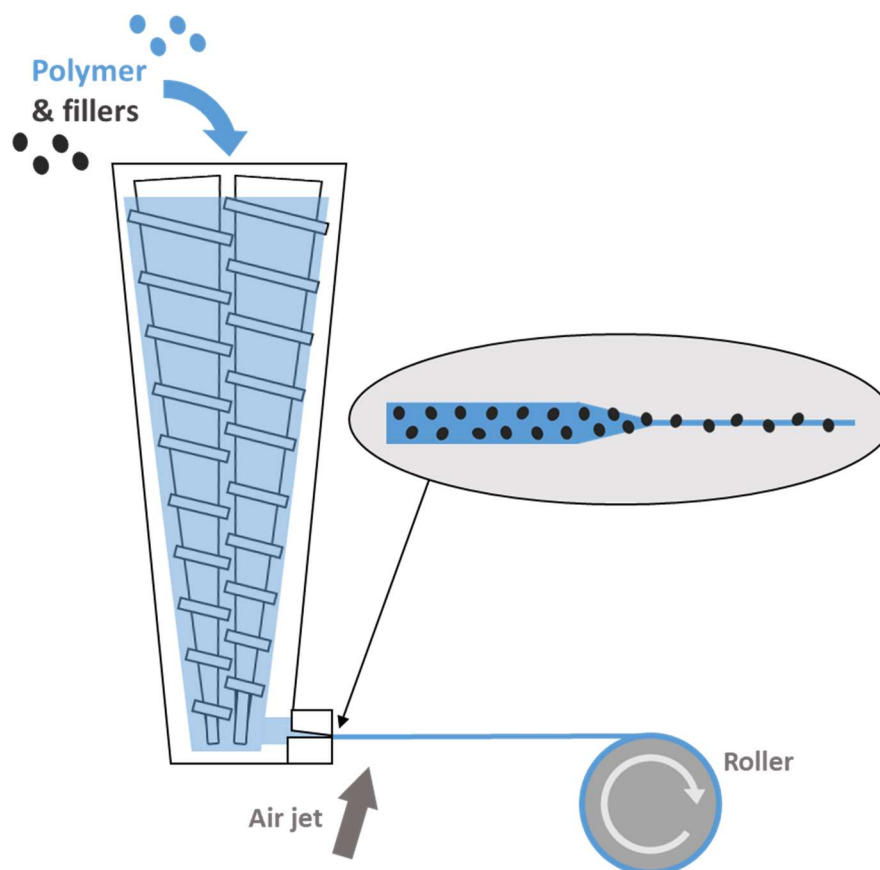


Figure 68 – Scheme of the texturing from fillers route. Polymer and fillers are introduced in a twin-screw extruder, and extruded into a film, leading to emerge particles during the film shrinking.

The silica content has a major impact on the film surface topography, *i.e.* 22%_{vol} silica filled HDPE (Figure 69c,d) appearing to be more textured than 6%_{vol} filled HDPE (Figure 69a,b). As expected, the hydrophilic silica is less dispersible in HDPE than the hydrophobic one. Also, a more pronounced texturing is expected with higher silica content. On the other side, the hydrophobic H20 silica leads to a surface displaying a more pronounced texturing, with larger aggregates (Figure 69b,d) than the hydrophilic S13 silica (Figure 69a,c).

Despite the effective texturing of the surfaces from addition of fumed silica, the water contact angles did not significantly increase. Asperities are not sufficiently distinct to define their size, width or spacing distance, to confront these data with the stability model requirements.

As an extruded neat HDPE film has a water contact angle of 100° and hysteresis of 19°, the higher water contact angle measured with silica-filled samples was 116° for the 22%_{vol} H20-filled HDPE (Table 12). In addition, the contact angle hysteresis on the textured surfaces were always higher than on the neat film (from 21 to 30°, Table 12). The increase of the contact angle might be caused by the existence of a Wenzel's regime in such conditions.

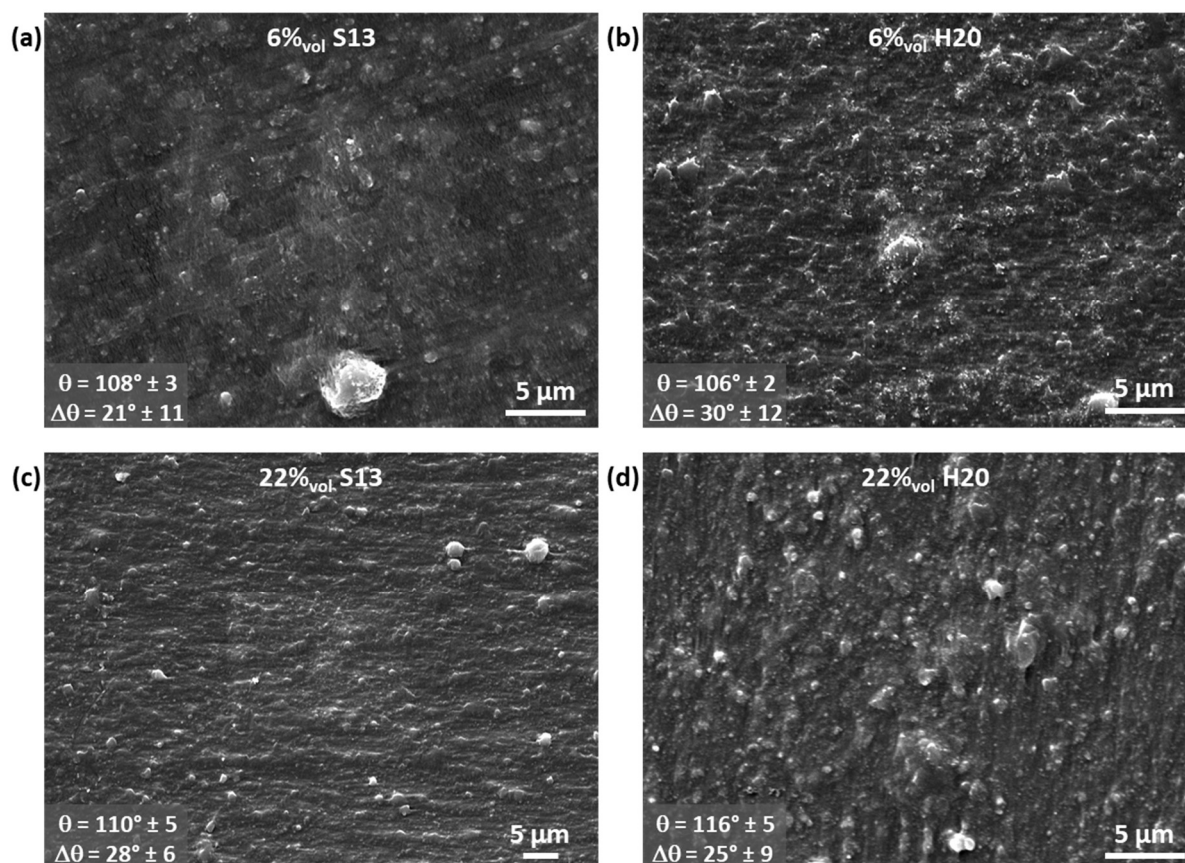


Figure 69 – SEM observation of surfaces based on HDPE (BM593) filled with various amount of hydrophilic and hydrophobic silica. (a,b) HDPE filled with 6%_{vol} (11%_{wt}) of silica, and (c,d) 22%_{vol} (34%_{wt}) of silica. (a,c) HDPE with hydrophilic Wacker S13 silica, and (b,d) HDPE with hydrophobic Wacker H20 silica.

Based on the work of Yüce *et al.*² or Fourmentin *et al.*⁴, it could be expected that such a texture is appropriate for superhydrophobicity with a silica content up to 50%_{vol} (63%_{wt}). Nevertheless, such a silica content can not be reached with such a processing (twin-screw extrusion).

If the incorporation of silica nanoparticles in the bulk allowed a texturing of the surface of an extruded film, the obtained texture did not lead to superhydrophobicity. To achieve superhydrophobicity, high contents of silica (larger than 50%_{vol}) must be reached according to previous works. Such highly filled blends display a very high viscosity, limiting their processing into films.

Table 12 – Water contact angle and hysteresis of surfaces processed from HDPE filled with silica, depending on silica content and nature.

Matrix	Silica	Volume fraction (%)	θ_{adv} (°)	$\Delta\theta$ (°)
HDPE	None	0	100±3	19±9
HDPE	Wacker S13	6	108±3	21±11
HDPE	Wacker S13	22	110±5	28±6
HDPE	Wacker H20	6	106±2	30±12
HDPE	Wacker H20	22	116±5	25±9

III.2. Glass microspheres

Another strategy was investigated, by using glass microspheres with a diameter of 13 to 45 μm from the Mo-Sci company (Figure 70a). They have been incorporated in HDPE (BM593) and extruded as a film at 200°C or 220°C. Due to their larger size and thus reduced specific surface compared to silica nanoparticles, larger amounts of such particles were able to be incorporated in HDPE without being too stiff. That is why up to 50%_{wt}, or 35%_{vol}, microspheres have been successfully introduced in HDPE, as well as a lower loading of 38%_{wt}, or 23%_{vol} (Figure 71)

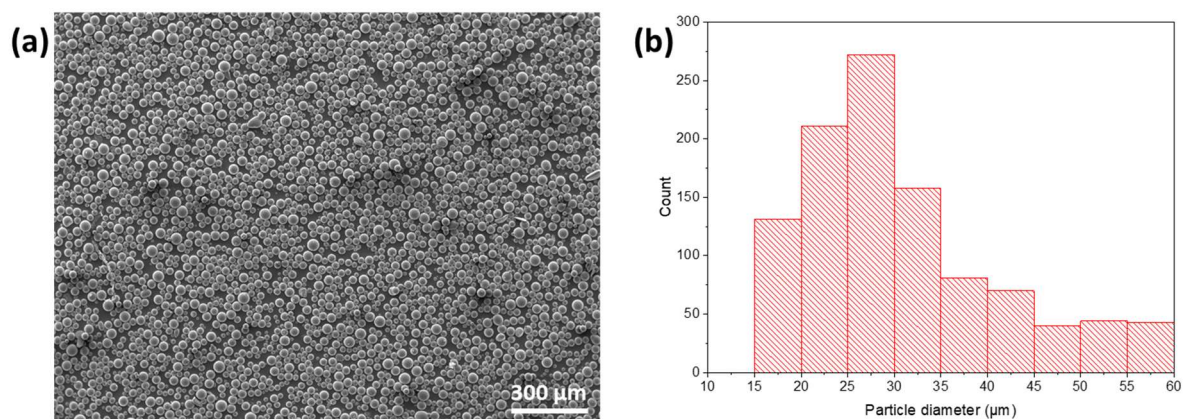


Figure 70 – Glass beads of about 30 μm average diameter. (a) SEM micrograph of the microspheres before introduction in HDPE, and (b) corresponding size distribution from SEM image analysis using ImageJ.

For HDPE filled with 23%_{vol} of microspheres (Figure 71a), a clear texturing is obtained due to a partial fissuring of the film. This fissuring results from a poor adhesion between the matrix and the particles, generating a delamination and crack propagation phenomenon as the film is pulled out of the extruder die. Such a phenomenon is well illustrated by the fact that all particles at the surface of the film are de-bonded from the matrix from the same side, corresponding to the pulling direction. The surface of a HDPE film filled with 23%_{vol} of microspheres is only hydrophobic (Table 13).

The incorporation of 35%_{vol} of microspheres in HDPE under the same processing conditions leads to a different surface with no sharp fracture of the matrix, but smoother waves due to the same matrix/particles decohesion (Figure 71b). Such a surface is poorly hydrophobic (Table 13), despite a higher particle loading.

When the same blend is compounded and extruded at a lower temperature (200°C), a similar morphology as for the 23%_{vol} filled HDPE is obtained, with sharp cracks caused by matrix/particle decohesion (Figure 71c). Here, even if the particles loading is greater, the density of particles and cracks on the surface does not appear to be significantly greater than with 23%_{vol} of microspheres. Still, this third sample surface is more hydrophobic than the two firsts (Table 13).

From the stability model point of view, such surfaces can be seen as having a spacing distance of about 30 μm (corresponding to the microspheres average diameter) and an asperities width larger than this value (due to the low density of voids on the surface). The surface is quite heterogeneous with some “asperities” being smaller than a tenth micrometers, and others being larger than 50 μm . With a D/a ratio below unity, the air fraction at the interface might be too low for the surface to have a water contact angle larger than 150°.

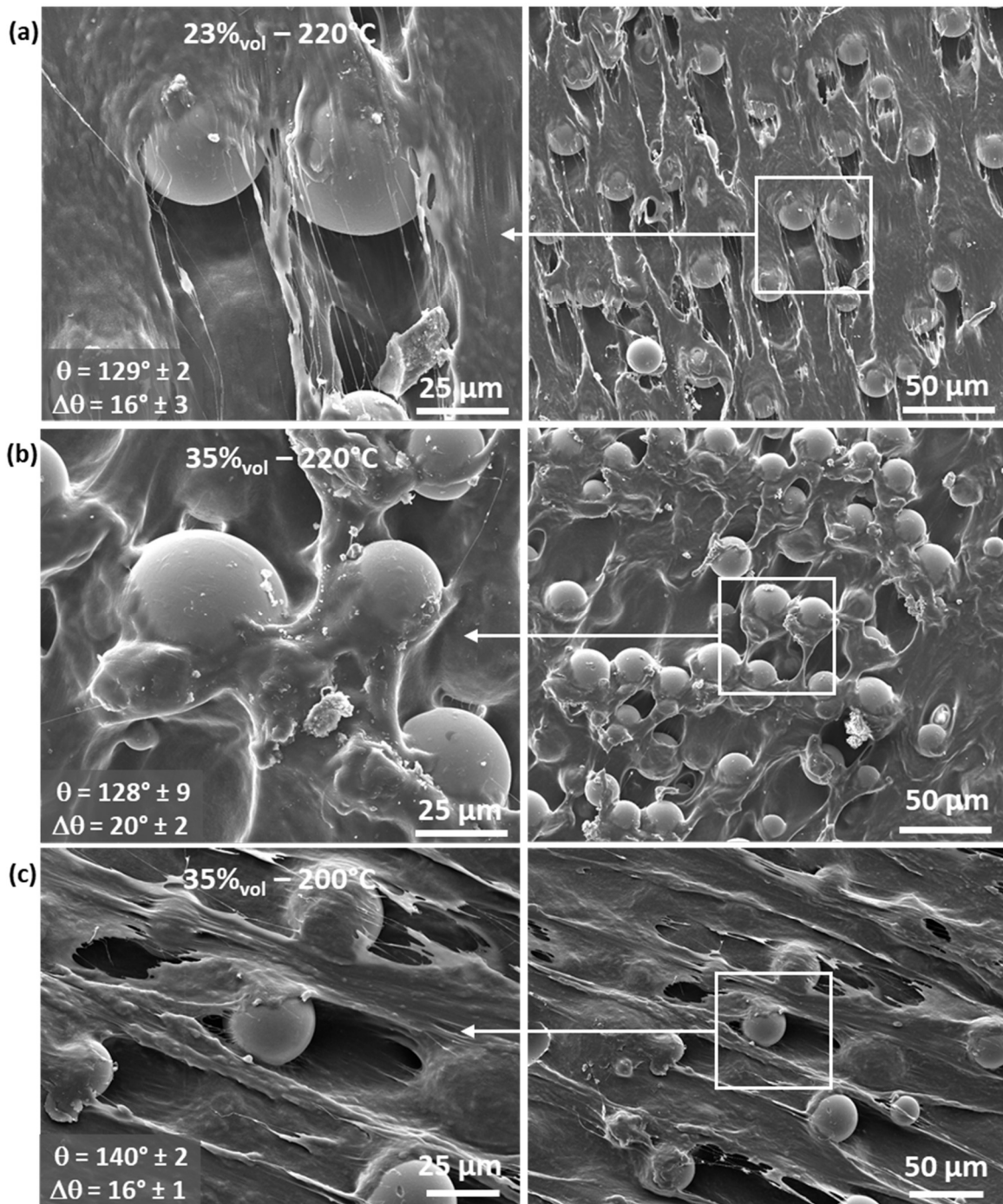


Figure 71 – SEM micrographs of glass microspheres-filled HDPE films. (a) HDPE (BM593) filled with 23%_{vol} glass microspheres, (b,c) 35%_{vol} glass microspheres. (a) and (b) are compounded and extruded at 220°C, and (c) is compounded and extruded at 200°C.

In summary, the use of glass microspheres as surface texturing fillers in HDPE led to an effective texturing of the film surface due to matrix/particle debonding generating cracks. However, the resulting texture scale might be too important to obtain a superhydrophobic surface. Thus, as the scale of the texture depends on the particles diameter, smaller objects have to be used in order to obtain stable superhydrophobic surfaces. In addition, as the glass particles are hydrophilic, de-bonded particles could act as pinning points for a water droplet: the use of hydrophobic particles is required.

Table 13 – Water contact angle and hysteresis of HDPE (BM593) filled with 13-45 μm diameter glass microspheres depending on the particles loading and extrusion temperature.

Matrix	Microspheres volume fraction (%)	Extrusion temperature ($^{\circ}\text{C}$)	θ_{adv} ($^{\circ}$)	$\Delta\theta$ ($^{\circ}$)
HDPE	-	-	100 \pm 3	19 \pm 9
HDPE	23	220	129 \pm 2	16 \pm 3
HDPE	35	220	128 \pm 9	20 \pm 2
HDPE	35	200	140 \pm 2	16 \pm 1

III.3. Organic particles

III.3.a. PTFE microparticles

To overpass the size and hydrophilicity limitations of glass microspheres, 1 μm polytetrafluoroethylene (PTFE) particles were mixed with HDPE in order to texture the surface from cracks generation. 20%_{vol} of PTFE particles were incorporated in HDPE (BM593) which was extruded into a film at 200 $^{\circ}\text{C}$. The resulting surface has a very low texturing, with a few cracks larger than the average particle size, and a few PTFE particles on the film surface (Figure 72).

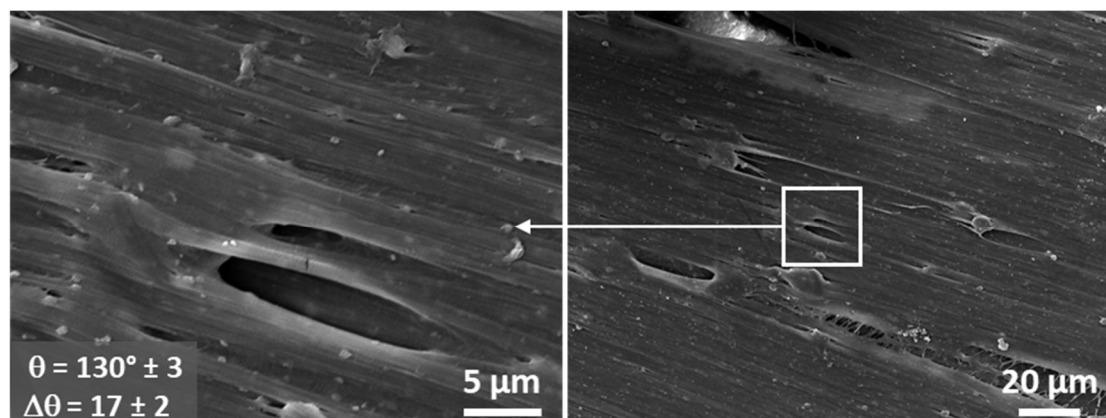


Figure 72 – SEM micrographs of a HDPE film surface containing 20%_{vol} PTFE microparticles at different magnifications.

Interestingly, despite a relatively low local texturing, the film is found to be strongly hydrophobic (Table 14). This high hydrophobicity could be associated with the presence of some PTFE particles on the surface leading to texturing and low surface energy ($\gamma_{\text{PTFE}} = 22.5\text{mN/m}$)¹⁷. The size of PTFE particles seems to be too small to effectively create a defect which could initiate cracks, despite the poor HDPE/PTFE adhesion. At the same time, there is not enough particles to effectively texture the surface by themselves.

Table 14 – Water contact angle and hysteresis of HDPE (BM593) film filled with PTFE particles.

Matrix	Particles	Volume fraction (%)	θ_{adv} ($^{\circ}$)	$\Delta\theta$ ($^{\circ}$)
HDPE	-	-	100 \pm 3	19 \pm 9
HDPE	PTFE	20	130 \pm 3	17 \pm 2

III.3.b. UHMWPE particles

Due to the favorable compatibility with HDPE, ultra-high molecular weight polyethylene (UHMWPE, GUR4150) particles were investigated as a surface texturing filler. Thus, UHMWPE particles (from 20%_{vol} to 50%_{vol}) were incorporated in HDPE (BM593) and extruded into a film at 200 $^{\circ}\text{C}$ and 220 $^{\circ}\text{C}$ for

the highest UHMWPE content. Even with the lowest UHMWPE content, a textured film is obtained, with stretched PE strings and lumps (Figure 73a). Such a morphology could be due to an increased stiffness of the blend. This surface morphology led to an increase of the hydrophobicity, but not enough to reach superhydrophobicity (Table 15).

With a UHMWPE content of 33%_{vol}, a similar morphology is obtained, but the texturing does not seem to be significantly improved (Figure 73b). The obtained morphology only leads to a higher hydrophobicity (Table 15). When looking closely at the stretched strings zones, the morphology seems favorable to superhydrophobicity, with 1 μ m large asperities (strings), and 2-3 μ m spacing distances. However, this favorable texture is only located at some limited areas.

When further increasing the UHMWPE content up to 50%_{vol}, the extruder temperature was increased to 220°C to manage the blend viscosity increase. The resulting film has a lower texturing in comparison to previous films without any stretched PE strings and only large UHMWPE lumps on the surface (Figure 73c). This could be due to a too important temperature for the HDPE matrix to generate cracks. This surface does not display a higher hydrophobicity than a neat HDPE film (Table 15).

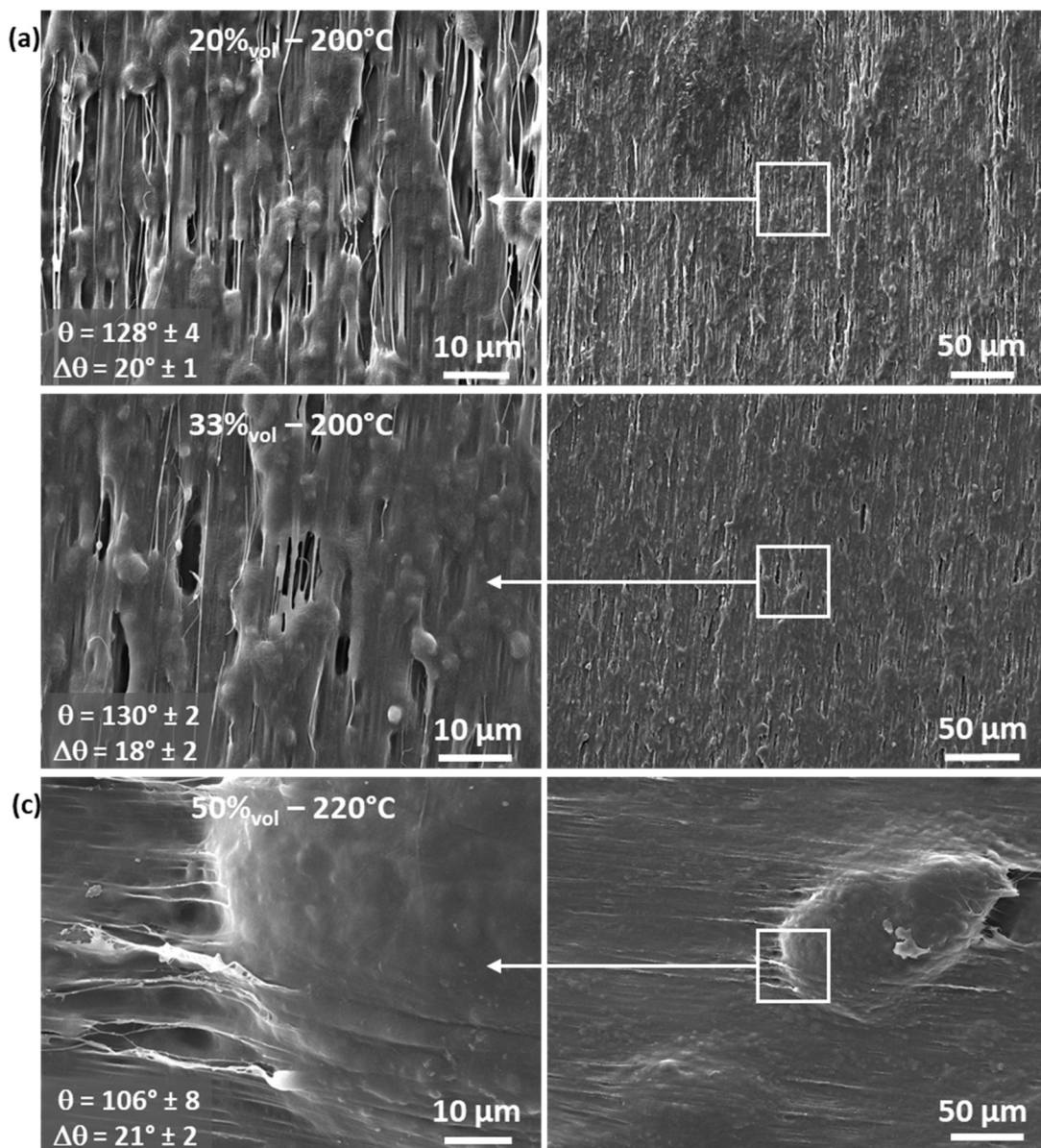


Figure 73 – SEM observation of HDPE (BM593) films containing (a) 20%_{vol}, (b) 33%_{vol}, and (c) 50%_{vol} UHMWPE particles.

For such a route, in order to generate a significant surface texture during the film processing, the matrix viscosity needs to be high enough to induce stretching of the UHMWPE domains, *i.e.* for forming PE strings. However, a too high UHMWPE content requires a temperature increase for processability, which acts against the UHMWPE particles stretching

Table 15 – Water contact angle and hysteresis of HDPE (BM593) films filled with UHMWPE particles, depending on the particle loading.

Matrix	Particles	Volume fraction (%)	θ_{adv} (°)	$\Delta\theta$ (°)
HDPE	-	-	100±3	19±9
HDPE	UHMWPE	20	128±4	20±1
HDPE	UHMWPE	33	130±2	18±2
HDPE	UHMWPE	50	106±8	21±2

III.4. Conclusion

Few attempts to texture the surface of HDPE films by incorporating various types of fillers in the molten state have been investigated. Addition of silica nanoparticles, glass microspheres, or polymer microparticles (PTFE or UHMWPE) have led to a surface texturing of the surface through various mechanisms.

When adding silica nanoparticles up to 22%_{vol} in HDPE, the film surface was textured, as nanoparticles are observable at the surface, but not enough to reach superhydrophobicity.

When adding larger particles such as glass microspheres to HDPE from 23%_{vol} to 35%_{vol}, a texturing due to polymer/particles interface debonding was observed. Such interfacial cracks are due to matrix/particle decohesion, leading to grooves of sizes close to the particles. Such textures are of interest, but the quite large asperities and their limited surface density only led to an increase of the hydrophobicity.

When smaller polymer particles such as 1µm-PTFE particles are incorporated in HDPE, such crack mechanisms cannot be longer observed. This low level of texturing, even if PTFE particles have a low surface energy, only leads to hydrophobicity.

The use of UHMWPE particles as surface texturing fillers in HDPE was also investigated. The surfaces obtained after an extrusion processing at 200°C display an important texturing. The texturing mechanism is due to the stretching of UHMWPE domains, leading to microscale strings oriented in the extrusion direction.

For higher UHMWPE contents and temperatures, the stretching of the UHMWPE domains is no longer observed. These domains only lead to large bumps on the film surface, leading to a limited texturing level. The use of UHMWPE only led to an increase of the hydrophobicity, in particular for low particle content processed at the lowest temperature.

The incorporation of particles in HDPE, and the processing as films only led to a higher hydrophobic character, the generation of surface textures. In order to reach superhydrophobicity, it is expected that a higher content of particles is required. However, such higher contents lead to processing limitations of such blends

IV. Immiscible polymer blends

IV.1. Polyethylene / polyethyleneoxide immiscible blend

Based on the work of Trifkovic *et al.*⁷, immiscible blends of HDPE and poly(ethylene oxide) (PEO) have been process in co-continuous phases conditions (Table 16). To do so, HDPE (BM593) and PEO were mixed in 40/60, 50/50, and 60/40 weight proportions and extruded as a film at 180°C after a 5min blending time. The 200 μ m thick films were immersed in deionized water for 48h to remove the water-soluble PEO phase, and then dried in a vacuum oven at 60°C overnight (Figure 74).

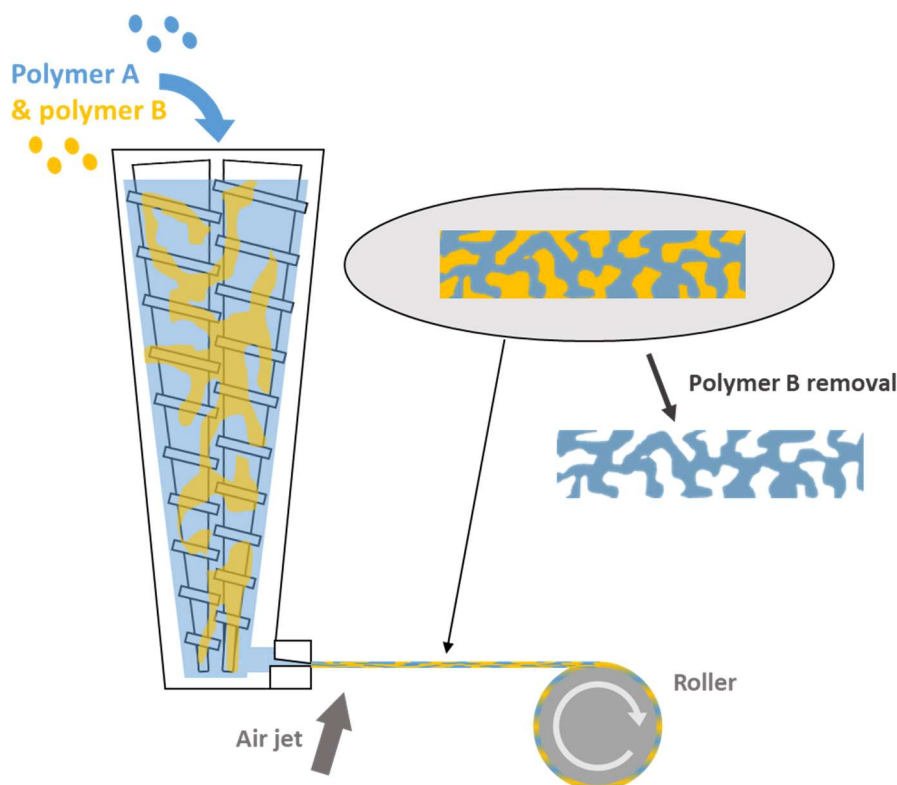


Figure 74 – Scheme of the texturing from immiscible polymer blends route. Polymers are introduced in a twin-screw extruder, and extruded into a film. The polymer B (PEO) is then removed by dissolution in water, revealing a porous polymer A (HDPE) surface textured film.

Table 16 – Summary of PE/PEO blends realized, with their volume and weight proportions, and the presence of a compatibilizer.

HDPE/PEO (% _{vol})	PE/PEO (% _{wt})	Compatibilizer
36/64	40/60	None
46/54	50/50	None
56/44	60/40	None
46/54	50/50	5% _{wt} hydrophilic silica (Aerosil®200)
46/54	50/50	5% _{wt} hydrophobic silica (HDK®H20)
46/54	50/50	5% _{wt} hydrophobic silica (Aerosil®R812)
46/54	50/50	5% _{wt} PTFE microparticles
46/54	50/50	10% _{wt} PTFE microparticles

Because of the final air fraction at the interface directly depends on the PEO fraction, various PE/PEO proportions have been investigated. These proportions were chosen close to the equivolumetric conditions, *i.e.* having a porous structure without losing the film integrity.

For a PEO content of 64%_{vol}, the surface displays rounded HDPE phases observable after the PEO removal (Figure 75a), leading to a poorly cohesive film. The spherical asperities of about 10 μ m, as well as the strings in-between only leads to a higher hydrophobicity character than neat HDPE (Table 17).

For 54%_{vol} of PEO, a co-continuous morphology is observed after PEO removal (Figure 75b). If some spherical asperities are connected with tiny strings, the main morphology is an entangled phase with rounded protrusions. This film is stronger and can be manipulated with no particular precautions, and the water-removal of PEO did not destroyed any part of it. Nevertheless, the surface morphology of such sample is not as good as the previously described one, and is only hydrophobic (Table 17).

When HDPE is considered as the main polymer in the blend (44%_{vol} of PEO), a HDPE continuous phase is unambiguously observed after the PEO removal (Figure 75c). This surface morphology revealed more cavities than protrusions, confirming a PEO-in-HDPE morphology. Again, some spherical asperities connected by stretched strings are displayed on this surface. Nevertheless, the generated texture does not lead to superhydrophobicity (Table 17).

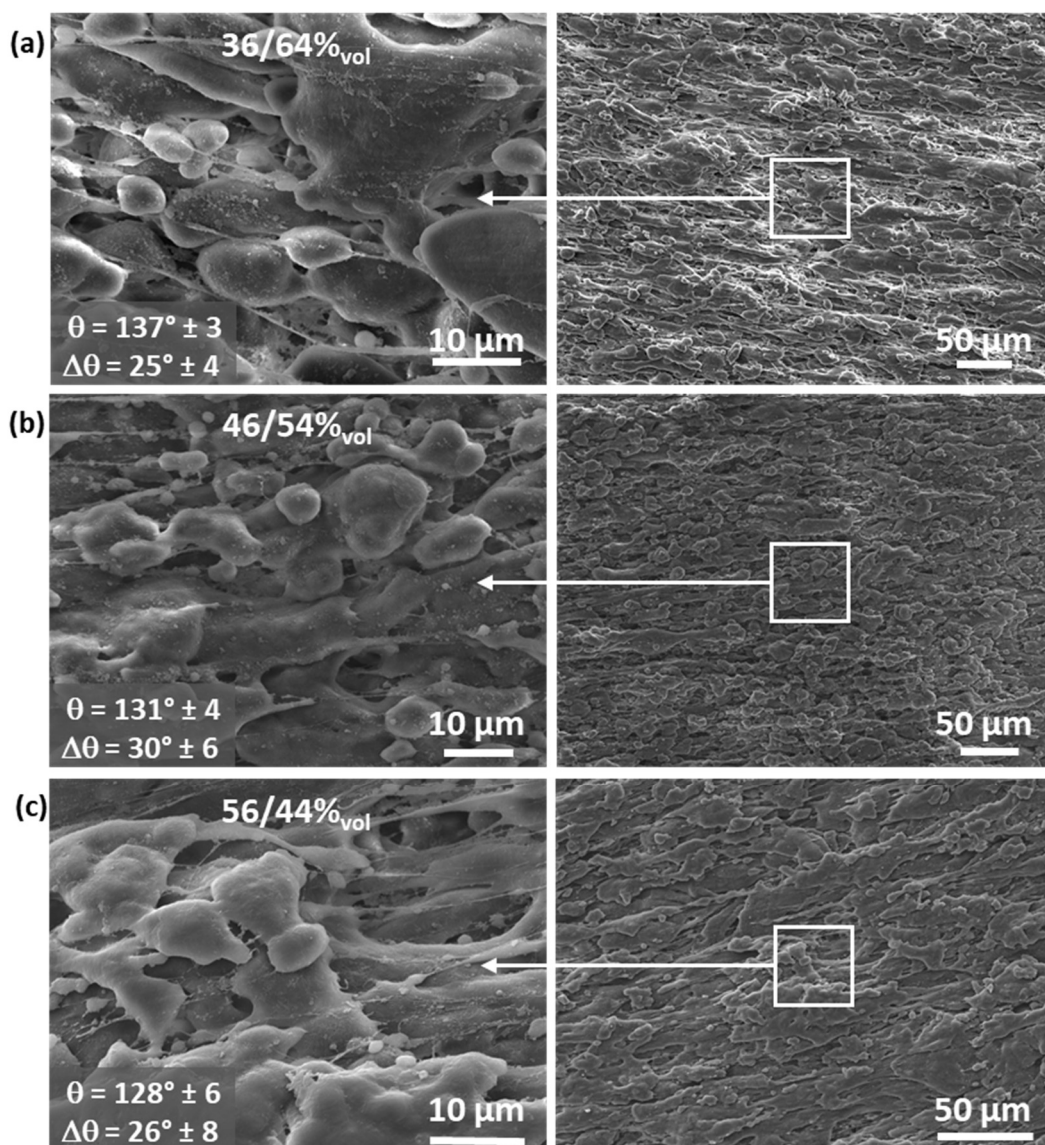


Figure 75 – SEM micrographs of PE/PEO immiscible blends surface after PEO removal for various PE/PEO volumetric proportions: (a) 36/64, (b) 46/54, and (c) 56/44.

From these three samples with various PEO contents, which were processed under the same conditions one can conclude that the expected blend morphologies were obtained, with an additional effect of the film stretching. The surface texture of the sample with a dispersed HDPE phase in a PEO matrix (36/64%_{vol}) looks as the most interesting for superhydrophobicity. Nevertheless, such a film has a very low integrity after the PEO removal, and cannot be considered. The 46/54%_{vol} HDPE/PEO blend was thus chosen as a reference.

The objective, starting from this hydrophobic surface, is now to promote the texturing, by reducing the domains sizes. In fact, the resulting asperities scale directly depends on the HDPE phases, and the spacing distance depends on the PEO phases. With the HDPE/PEO balance in favor of PEO, the D/a (spacing distance on asperities width) ratio is thus expected to be slightly higher than unity.

Table 17 – Water contact angle and hysteresis of HDPE/PEO immiscible blends (after PEO removal) depending on the volume proportions.

HDPE/PEO (% _{vol})	θ_{adv} (°)	$\Delta\theta$ (°)
100/0 (pure HDPE)	100±3	19±9
36/64	137±3	25±4
46/54	131±4	30±6
56/44	128±6	26±8

IV.2. Filled PE/PEO immiscible blend filled based on hydrophilic silica

To reduce the size of the final texture obtained from immiscible polymer blends, the addition of a compatibilizer is well-known for its efficiency. Compatibilizers reduce the interfacial energy between the phases through shielding, stabilizing smaller domains. The use of nanoparticles such as silica^{18,19} or clay^{20,21} was proposed as a powerful and easy route to compatibilize immiscible polymer blends.

In order to shield the HDPE/PEO interface, hydrophilic silica nanoparticles (Aerosil® 200) were incorporated in the blend. This silica was used for its high specific area and its hydrophilicity, considering that it will thus be more compatible with the PEO phase. As reported in numerous papers¹⁸⁻²¹, the HDPE surface is effectively covered by silica nanoparticles (Figure 76).

The phase size reduction in comparison with the neat HDPE/PEO blend with the same proportions is not very significant. As expected, the silica nanoparticles effectively act as a texturing agent at a nanoscopic scale despite their low content. Due to the hydrophilic nature of the silica nanoparticles, such a surface was found to be superhydrophilic, *i.e.* water droplets are completely and instantaneously absorbed by the sample.

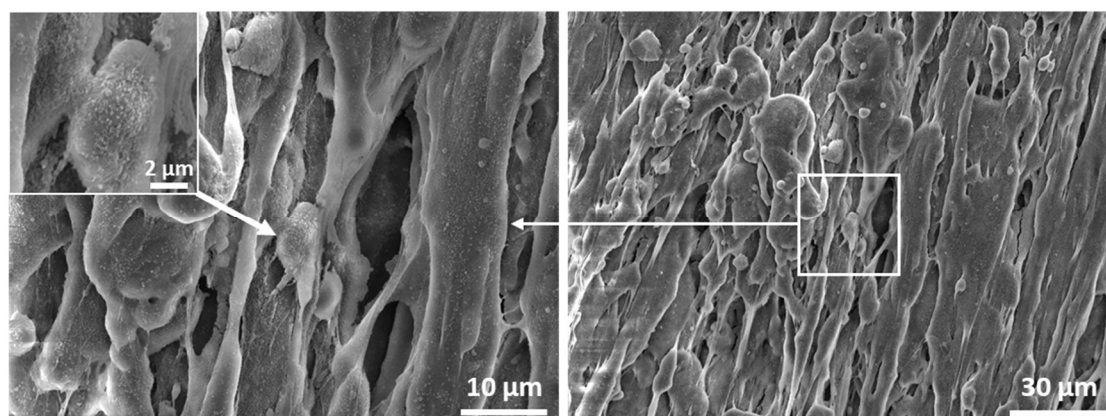


Figure 76 – SEM micrographs of a HDPE/PEO immiscible blend based on 46%_{vol} HDPE (BM593) after PEO removal, containing 5%_{wt} hydrophilic silica (Aerosil® 200)

Addition of silica nanoparticles to a HDPE/PEO immiscible blend leads to slightly reduce the phases size, and to increase the texturing at the nanoscale. Nevertheless, the hydrophilicity of these particles acts against the search of superhydrophobicity. The use of hydrophobic silica nanoparticles could be an answer to this issue, even if a lower texturing level at nanoscale is expected due to nanoparticles being more embedded in the HDPE phase.

IV.3. Filled HDPE/PEO immiscible blend based on hydrophobic silica

In order to decrease the HDPE phases size, *i.e.* increase the surface texturing level, as well as adding a nanotexture to the surface without turning it superhydrophilic, the use of hydrophobic silicas was investigated. Two different silicas were used, HDK® H20 and Aerosil® R812 (the first being slightly hydrophilic and the last one truly hydrophobic).

As 5%_{wt} of these silica nanoparticles were dispersed in a HDPE/PEO blend (containing 46%_{vol} of HDPE), the resulting surface is found to be poorly textured. In particular, the HDPE domains are found to be larger and more stretched, leading to long and oriented domains rather than spherical asperities (Figure 77). It also demonstrated that with Aerosil® R812, less silica nanoparticles were found at the HDPE surface after the PEO removal. Such a disappearance of the silica nanoparticles could be explained by a localized higher concentration within the HDPE phases (rather than at the HDPE/PEO interface due to a better compatibility).

Due to such an increased HDPE/silica compatibility, the interface shielding effect of such nanoparticles could be reduced in comparison with the surface process using hydrophilic silica (Figure 77a-b).

Due to the HDK® H20 hydrophilicity, the film surface was found to be hydrophilic (Table 18). As Aerosil® R812 is truly hydrophobic, it results in a hydrophobic HDPE surface after PEO removal (Table 18).

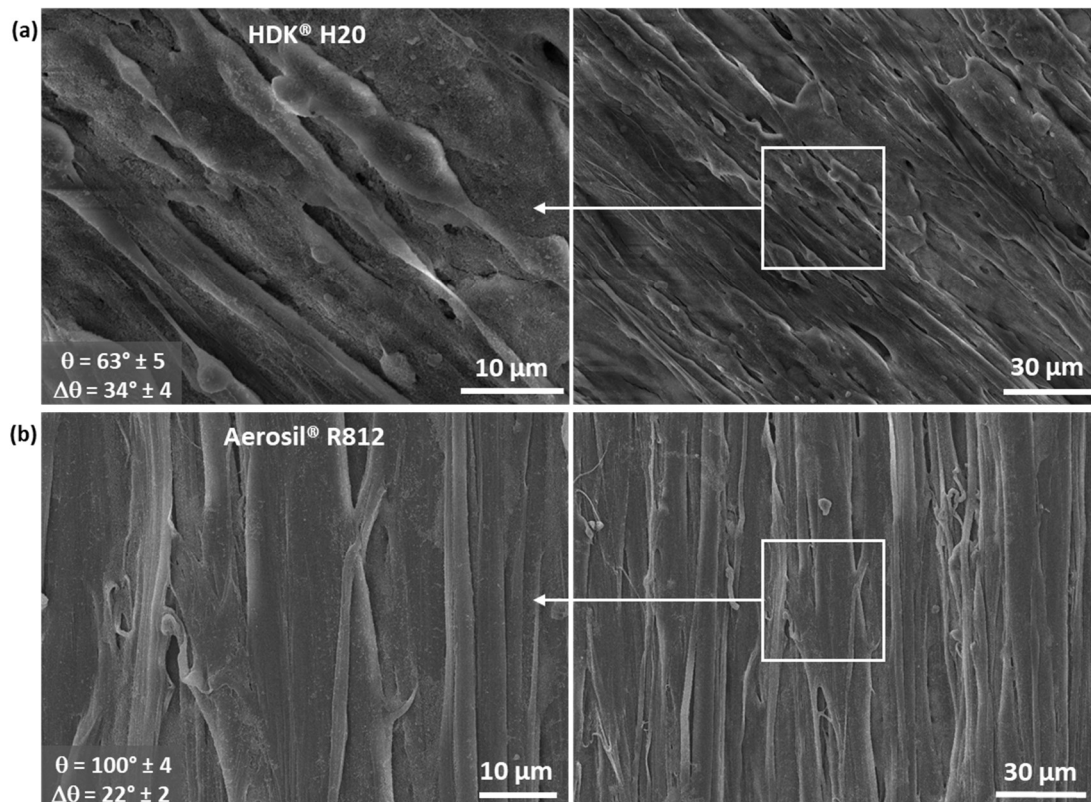


Figure 77 – SEM micrographs of HDPE/PEO immiscible blends surface with 46%_{vol} HDPE (BM593) after PEO removal, containing 5%_{wt} "hydrophobic" silicas: (a) HDK® H20, and (b) Aerosil® R812.

Aerosil® R812 are intrinsically hydrophobic particles, at the opposite of HDK® H20 or Aerosil® 200. Nevertheless, even with Aerosil® R812 particles, the resulting HDPE texture does not allow to reach superhydrophobicity, despite the generation of a nanotexture from silica nanoparticles. Surfaces have a hydrophobic character similar to a neat HDPE film, and less hydrophobic than a unfilled HDPE/PEO blend surface.

HDPE/PEO blends containing silica nanoparticles do not lead to superhydrophobicity (after PEO removal), mainly because of the silica hydrophilicity.

Table 18 – Water contact angle and hysteresis for HDPE/PEO blends filled with hydrophobic silica nanoparticles (after PEO removal).

HDPE/PEO (%vol)	Compatibilizer	θ_{adv} (°)	$\Delta\theta$ (°)
100/0 (pure HDPE)	-	100±3	19±9
46/54	None	131±4	30±6
46/54	5% _{wt} hydrophobic silica (HDK®H20)	63±5	34±4
46/54	5% _{wt} hydrophobic silica (Aerosil®R812)	100±4	22±2

IV.4. Filled HDPE/PEO immiscible blends based on PTFE microparticles

PTFE microparticles, previously used as a texturing agent of HDPE, were incorporated in HDPE/PEO blends. Here, the strategy is mainly the use of the HDPE/PEO interface as a preferential localization site for PTFE microparticles, allowing their emergence at the surface after the PEO removal. With such a strategy, and effective texturing is expected with low particles contents.

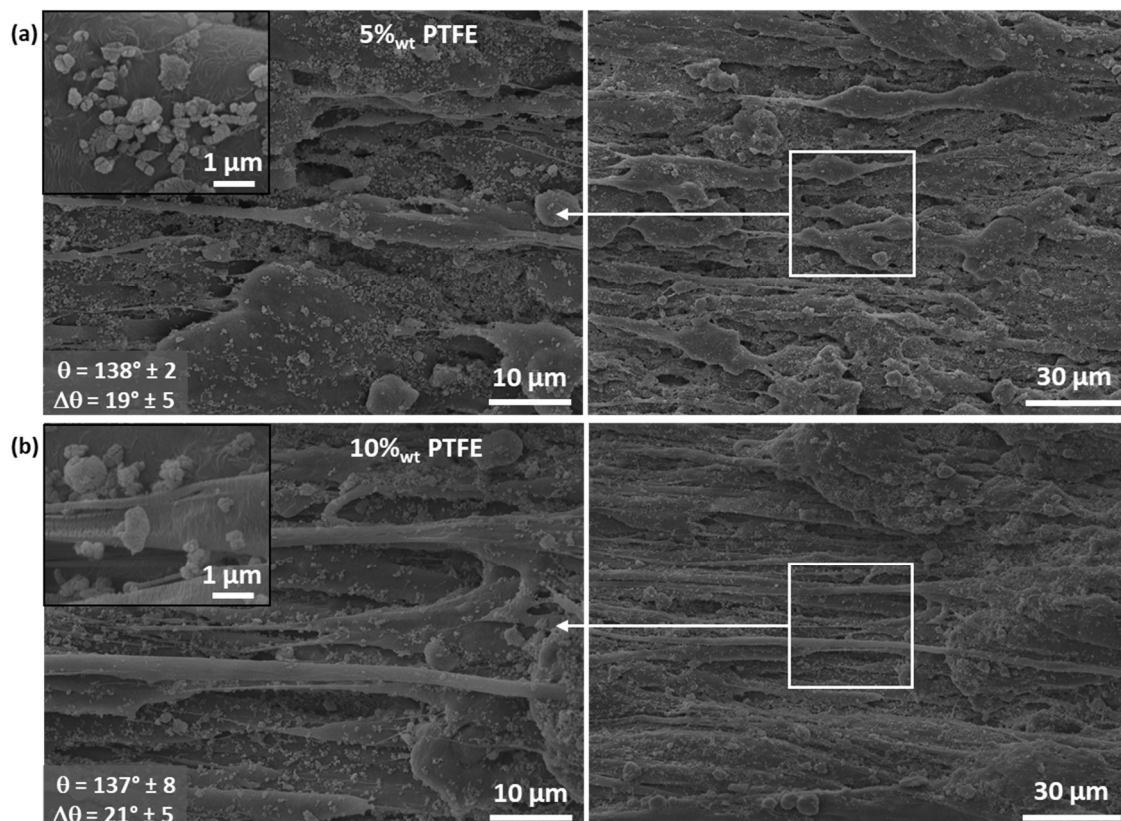


Figure 78 – SEM micrographs of HDPE/PEO immiscible blends surface based on 46%vol HDPE (after PEO removal), and (a) 5%_{wt}; (b) 10%_{wt} PTFE microparticles

From SEM analysis of the resulting textured surface (Figure 78a), the goal of bringing PTFE microparticles to the surface seems to be reached. PTFE particles of less than a micrometer are all over the film surface, heterogeneously dispersed. Some parts of the surface appear to be fully “coated” with these microparticles, while other parts suffer from a few micrometers spacing between each particle. Such a spacing of the particles can be directly linked to the interface extension during the film pulling. The stretching of the film causes the elongation of some phases where the PTFE particles are attached, thus separating particles that could have been close. In addition, as the particles seem to be mainly out of the HDPE phase, PTFE particles could have been removed during the PEO extraction.

With 5%_{wt} of PTFE particles in the HDPE/PEO blend (46/54%_{vol}), an effective texturing at scales of less than one micrometer and of a few tenth micrometers is observed. Despite such a texturing and the hydrophobicity of the particles, the surface was not found to be superhydrophobic (Table 19). At the smaller scale, asperities are about half a micrometer large and about the same height. However, their spacing is too important, of a few micrometers and even more in some areas, for the resulting texture to hold a stable Cassie-Baxter’s interface according to the model. If a and D/a values satisfy the model requirements, the asperities height is too low with such large spacing distances. Moreover, there are too much uncovered areas of HDPE for the nanoscale texture to make the surface superhydrophobic by itself.

With 10%_{wt} of PTFE particles in the HDPE/PEO blend (46/54%_{vol}), the PTFE particles density on the surface appears to be very similar to the one of the blend containing only 5%_{wt} particles (Figure 78b). The spacing of these particles does not seem to come from a lack of particles within the blend, but to the interfaces stretching during the film pulling and/or their loss during the PEO removal. This second film, with a higher PTFE particle loading, has a hydrophobicity similar to the 5%_{wt} PTFE loaded film (Table 19). Such an observation tends to confirm the hypothesis of an elongation of HDPE phases leading to a distancing of the PTFE particles.

Table 19 – Water contact angle and hysteresis for HDPE/PEO immiscible blends filled with PTFE particles (after PEO removal).

HDPE/PEO (% _{vol})	Compatibilizer	θ_{adv} (°)	$\Delta\theta$ (°)
100/0 (pure HDPE)	-	100±3	19±9
46/54	None	131±4	30±6
46/54	5% _{wt} PTFE microparticles	138±2	19±5
46/54	10% _{wt} PTFE microparticles	137±8	21±5

The use of the HDPE/PEO interface to localize PTFE particles on the surface with reduced contents has been demonstrated to be very effective. With only 5%_{wt} of PTFE particles dispersed, a maximum surface concentration of the particles has been reached. However, due to the stretching of the film, the particles were distanced from the others. The resulting textured surfaces are highly hydrophobic, but not superhydrophobic due to the too important particles spacing distances.

IV.5. Conclusion

Textured films were obtained from immiscible blends of HDPE and PEO having various compositions after PEO washing. Films with lower contents of HDPE were more textured, with mainly a dispersed HDPE phase in a PEO matrix morphology. Such films display have a large water contact angle but are poorly cohesive and very brittle after the PEO phase elimination. Films containing almost 50%_{vol} HDPE were sufficiently cohesive to be manipulated without any particular precaution. However, their texturing was reduced and they were found to be less hydrophobic.

The addition of hydrophilic silica nanoparticles as a compatibilizer led to a neglectable polymer phases size reduction, but induced an additional texture at the nanoscale. This texturing is due to nanoparticles being localized at the former PE/PEO interface. However, due to the hydrophilicity of these nanoparticles, the resulting surface was found to be superhydrophilic.

The replacement of these nanoparticles by more hydrophobic ones led to a lower texturing at a nanoscale. Because of their higher compatibility with HDPE, particles are well dispersed in the HDPE phases and not at the former interface. The resulting films are only slightly hydrophobic, with wetting properties similar to the ones of untextured HDPE. The HDPE/PEO interface was also used to localize PTFE particles at the surface with low particles contents. However, due to the interface stretching during the film pulling, the particles are too widely spaced for superhydrophobicity, even if the surface hydrophobicity is increased.

Such an approach of texturing HDPE from immiscible blends with a water-soluble polymer such as PEO was found to be effective. However, such a route requires an additional treatment for PEO elimination. Moreover, a large amount of PEO need to be removed, constituting a major waste generation even if PEO could be recovered by drying or precipitation processes.

V. Batch foaming using supercritical carbon dioxide

v.1. Foaming HDPE and PP with Sc-CO₂

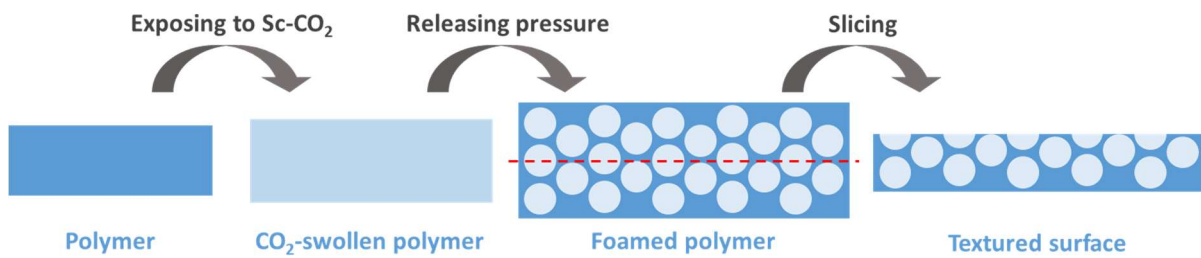


Figure 79 – Scheme of the texturing from Sc-CO₂ foaming route. Polymer are introduced in pressure barrel and swelled with Sc-CO₂, then foamed during the pressure release. The foamed polymer is sliced to reveal a textured surface.

V.1.a. Influence of the foaming temperature

According to the literature and the Cassie-Baxter's interface stability model, a foam surface needs to display small cells to be superhydrophobic. To reduce the cells size, the growth must be limited during the foaming while the cells nucleation density must be kept high. To fulfill these requirements, a large amount of Sc-CO₂ must be dissolved in the matrix prior to foaming, *i.e.* an important Sc-CO₂ pressure, for increasing the cells density⁹. At the same time, the matrix viscosity must be large enough to limit the cells growth. HDPE is a good candidate for such growth limitation due to its relatively high viscosity and its large crystallinity. By foaming HDPE close to its crystallization temperature, the pressure release will induce a temperature decrease that will cross the crystallization temperature of the matrix, leading to an important viscosity increase.

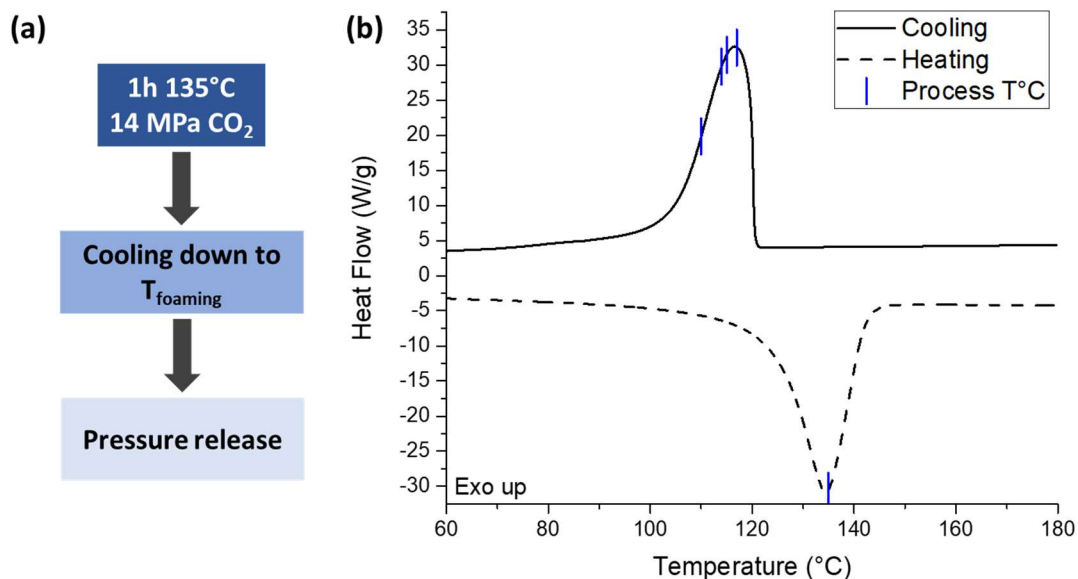


Figure 80 – (a) Foaming process and (b) corresponding temperatures on a HDPE (BM593) DSC thermogram showing melting (dash line) and crystallization (solid line) peaks, and process temperatures (denoted on the crystallization exotherm) (Heating and cooling rates are 10K.min⁻¹)

The impact of the foaming temperature on the cells size with HDPE was studied by exposing HDPE (BM593) pellets to Sc-CO₂ at 14MPa and 135°C for 1h, then cooling it at a temperature close to the maximum of the DSC crystallization peak (Figure 80b) and releasing the pressure instantly with a fully

opened flow control valve. The exposure temperature has been chosen to have HDPE in the molten state, promoting the CO₂ diffusion through the amorphous phase. In such conditions, the CO₂ diffusion equilibrium was found to be reached for 1h of exposure, as longer exposure times led to similar morphologies. The foaming temperatures were varied from 117°C to 110°C, *i.e.* at or below the maximum crystallization peak.

The resulting foams are shown in Figure 81, and the cells size distributions in Figure 81e (from the SEM pictures using the ImageJ software).

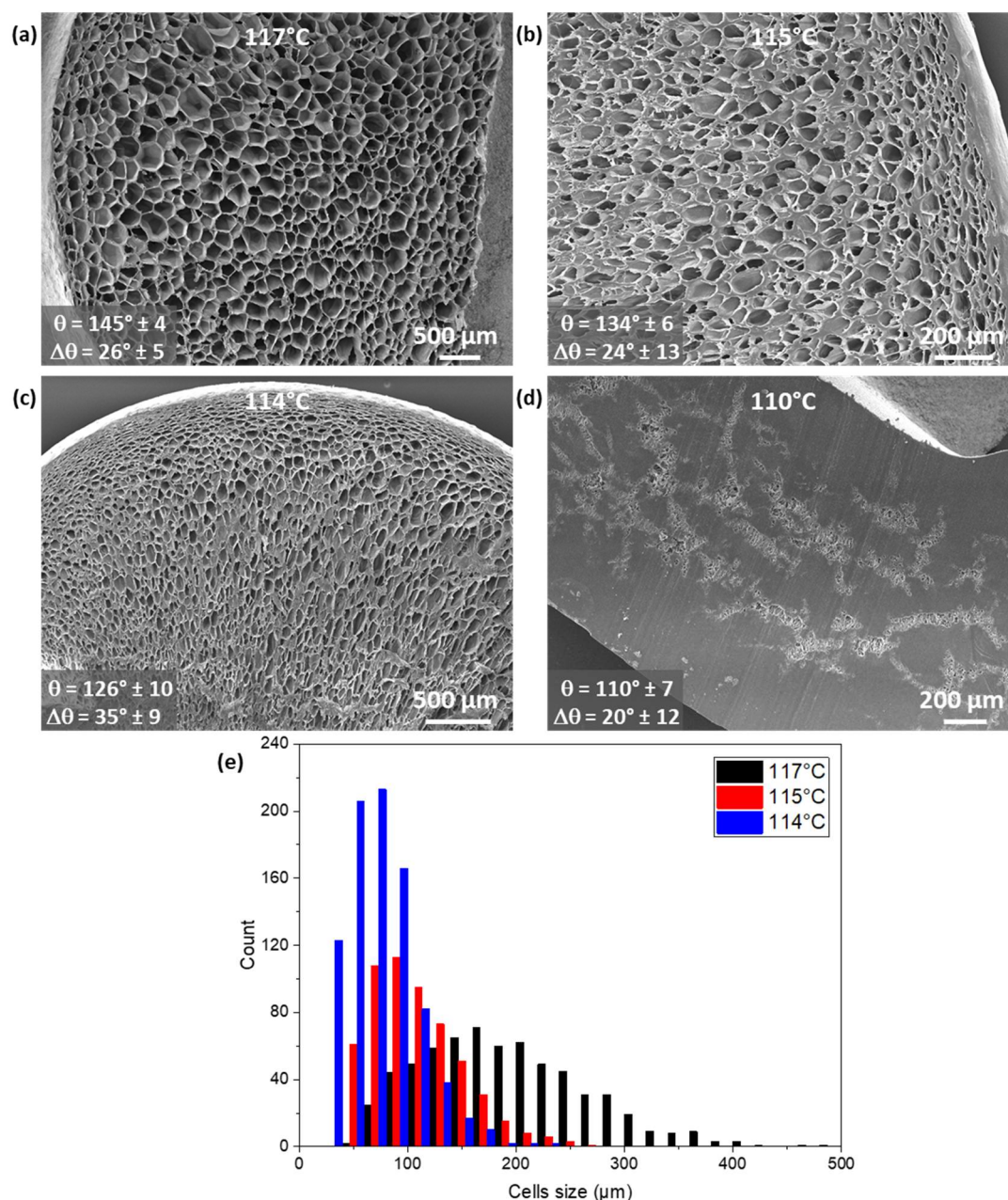


Figure 81 – Effect of foaming temperature on the cells size of HDPE (BM593). The polymer has been exposed to Sc-CO₂ at 14MPa and 135°C for 1h, then cooled at (a) 117°C, (b) 115°C, (c) 114°C, and (d) 110°C for a pressure release at a 100% flow control valve opening. (e) Size distribution of the cells from samples foamed at 117°C, 115°C and 114°C, measured from SEM pictures using ImageJ.

The first observation that can be made when considering samples foamed at temperatures between 117 and 114°C is that all the samples display closed-cells morphologies, with an unfoamed skin. In addition, all samples have cells with relatively thin walls. Such features are characteristic of Sc-CO₂

foaming of thermoplastics from the molten state. When the foaming temperature is lower than the crystallization temperature, for example 110°C, the sample is almost unfoamed. The crystallization upon cooling induces a CO₂ desorption and strongly increases the matrix viscosity.

Even if the samples were chosen to be as thin as possible (2mm large pellets), a gradient of cell sizes is observed for most of the samples. This phenomenon can be attributed to a temperature gradient through the sample thickness due to a low thermal conductivity during the cooling, either controlled or induced by the pressure release.

With thicker samples, this temperature gradient leads to even broader cells size dispersion, as reported in Figure 82 (HDPE foam obtained in the same conditions for a 1cm large sample). In addition to the broad cells size distribution, the temperature gradient induces a temperature shift in the matrix core. This shift results in a foamed sample when the foaming temperature is set at 110°C, whereas a smaller sample under the same conditions is found to be almost unfoamed. The observed inner structure is thus not representative of the foaming temperature, and is very sensitive to the cooling rate.

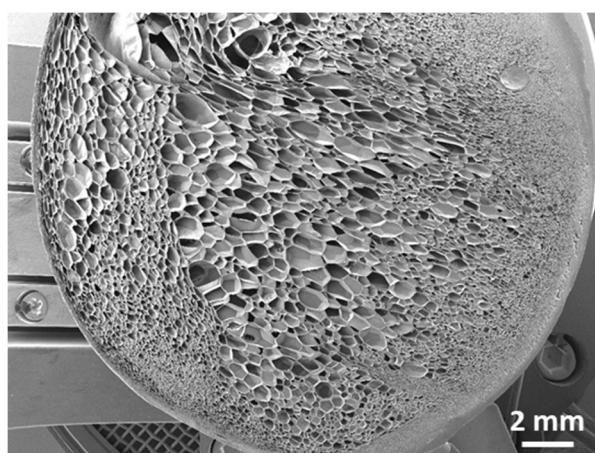


Figure 82 – Large HDPE (BM593) sample foamed by Sc-CO₂ at 110°C after an exposure at 14MPa and 135°C for 1h.

For HDPE foamed at 117, 115 or 114°C, the surface revealed by slicing displays thin asperities (cells walls) of about 10µm, and voids (cells) of hundreds of micrometers. These morphologies do not fulfill the Cassie-Baxter's interface stability model requirements. The surfaces still exhibit high hydrophobic behaviors with a limited adhesion (contact angle hysteresis) (Table 20). A hybrid Wenzel's and Cassie-Baxter's interface might be obtained on these surfaces.

By comparing the samples obtained at foaming temperatures of 117°C, 115°C, 114°C, and 110°C, the expected temperature effect can be confirmed: the lower the temperature of foaming is, the quicker the crystallization will occur, resulting in an increase of the matrix viscosity, limiting the cells growth. It is also observed that lower foaming temperatures led to less-dispersed cells size, probably because of a limitation of the cells coalescence: the cells all nucleate and grow in a similar way, leading to such a low dispersion. At some point, for example foaming HDPE at 110°C, the matrix viscosity is too important for the cells to grow. The energy needed to form a gas bubble in the resulting very viscous matrix is then larger than the diffusion energy, and the CO₂ molecules diffuse out of the sample without being able to precipitate.

Table 20 – Water contact angle and hysteresis of HDPE (BM593) foamed at different temperatures after a 1h exposure to Sc-CO₂ at 14MPa and 135°C.

Foaming temperature (°C)	θ_{adv} (°)	$\Delta\theta$ (°)
117	145±4	26±5
115	134±6	24±13
114	126±10	35±9

110	110±7	20±12
-----	-------	-------

It has been demonstrated the major influence of the foaming temperature on the final foam morphology. Smaller cells are generated at lower temperatures, *i.e.* close to the crystallization temperature. The sample thickness was also shown to be of importance, as a too thick sample will induce temperature gradients or even shifts. As a consequence, the 115°C foaming temperature was chosen, because it is a compromise between the average cell size and broadness of size distribution, *i.e.* tiny cells with a low dispersity.

V.1.b. Influence of the depressurization rate

The depressurization rate can have a double effect during foaming. First, a slower pressure release slightly reduces the pressure difference inside and outside the cells, lowering the energy of cells expansion. At the same time, a slower pressure release also slows down the temperature decrease, allowing a longer grow time for the cells before the matrix being too viscous. To know which of these antagonist effects is predominant, a viscous HDPE (5502-R3) was foamed at 115°C after a CO₂ exposure at 17MPa for 5h with a flow control valve opening of 100%, 50%, or 25% (Figure 83).

It must be noted that these experiments have been conducted with a higher CO₂ pressure in comparison with the first test, in order to increase the cell nucleation density, as an increased pressure at a given temperature will lead to a larger amount of CO₂ dissolved in the matrix.

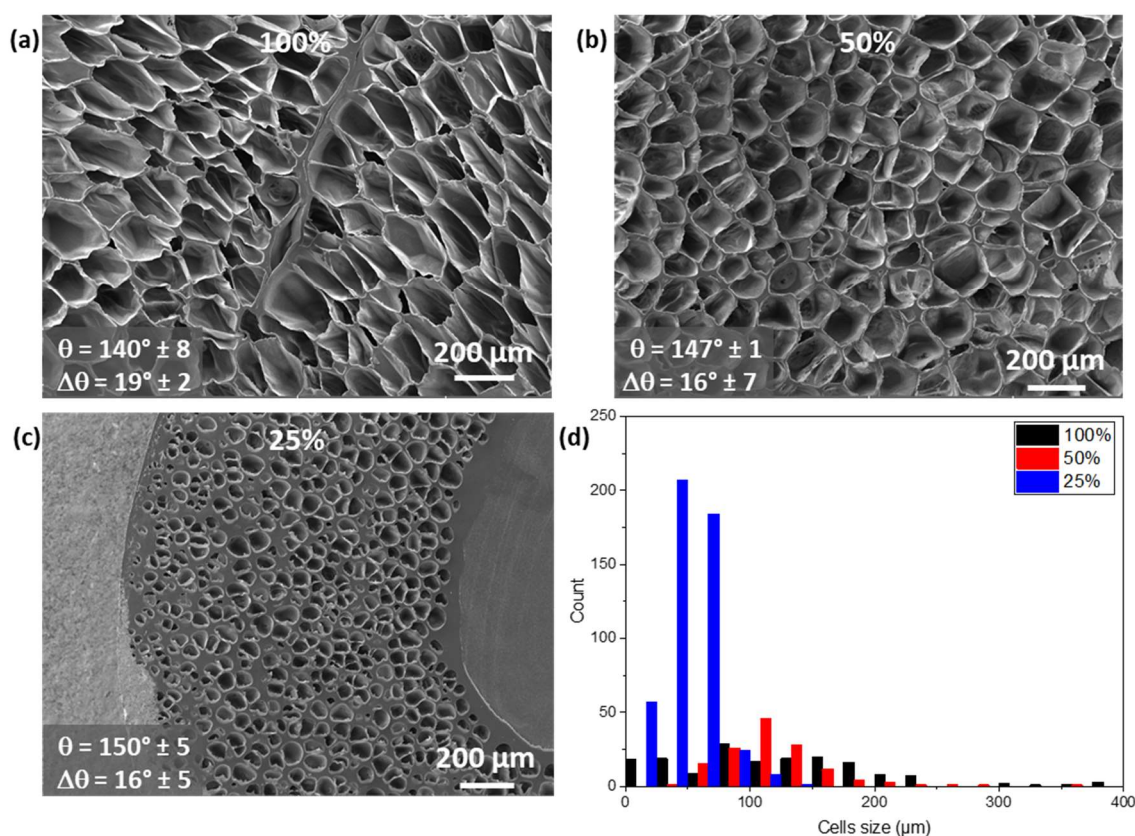


Figure 83 – Influence of the depressurization flow rate on the cells size of HDPE (5502-R3). SEM micrographs of HDPE exposed to Sc-CO₂ at 17MPa and 135°C for 5h and foamed at 115°C with a flow control valve opened at (a) 100%, (b) 50%, and (c) 25%. (d) Cells size distribution of the foamed HDPE as a function of the depressurization flow rate (from SEM pictures using the ImageJ software).

The comparison of the HDPE foams resulting from depressurizing with a fully-opened (100), half-opened (50%) and quarter-opened (25%) exhaust valve show a clear trend. The slower the depressurization rate is (in the given conditions), the smaller the cells are (Figure 83). The cell size

distribution is also narrower with a reduced depressurization rate (Figure 83d). On the opposite, the cells walls got thicker when the depressurization rate is reduced, suggesting a limitation of the cells growth.

The three foams display closed-cells morphologies, with average cell size from 150 to 50 μm , and walls thickness from 5 to 20 μm . All the resulting surfaces are highly hydrophobic (Table 21). The foam obtained with the lowest depressurization rate could almost be denoted as superhydrophobic, with a water contact angle of exactly 150°, but the hysteresis is still too important. None of these surfaces is slippery superhydrophobic. Such a behavior can be caused by a too low air fraction at the interface, too large asperities (flat surfaces), or hybrid Wenzel's and Cassie-Baxter's interface.

It must be noted that D/a upper and lower limits values from the Cassie-Baxter's interface stability model were based on discrete asperities over an extended gaseous area. Here, the gaseous areas are discrete, with a continuous solid area: D/a upper and lower limits given by the model might be taken as guidelines rather than as precise predictions, in particular with such different surface morphologies.

Table 21 – Water contact angle and hysteresis of HDPE (5502-R3) foamed at 115°C depending on the flow control valve opening, after an exposure to Sc-CO₂ at 17MPa and 135°C for 5h.

Flow control valve opening	θ_{adv} (°)	$\Delta\theta$ (°)
100%	140 \pm 8	19 \pm 2
50%	147 \pm 1	16 \pm 7
25%	150 \pm 5	16 \pm 5

Promising results were obtained by foaming a viscous HDPE close to its crystallization temperature, with a low depressurization rate in order to limit the cells growth. Nevertheless, cells walls thickness was still too important, even if these cells were smaller. Thus, there is a need to limit the cells growth while increasing drastically their nucleation density.

V.1.c. Influence of fillers as nucleating agents

To increase the cell nucleation density, as well as increasing the matrix viscosity, fillers such as talc or calcium carbonate are usually incorporated^{22–26}. The inorganic structure of these particular fillers enhances the cells density thanks to a higher heterogeneous nucleation rate. In addition, such particles could lead to an open-cells morphology due to cells walls breakage upon stretching, due to matrix/particle decohesion from stress concentration. The reinforcing effect of fillers on the matrix could also be a way to limit the cells growth.

V.1.c.i. Filled high-density polyethylene

Blends of HDPE (BM593) containing 10%_{wt} fillers such as calcium carbonate (CaCO₃) and talc were extruded at 200°C into a strand and cut into pellets of about 2mm large for foaming experiments. As HDPE has an intrinsically good crystallization rate, no change in the crystallization behavior was expected nor was observed with fillers. The crystallization and melting temperatures of neat and loaded HDPE were unchanged, as well as the crystallinity yield (Figure 84).

The expected influence of these fillers concerns the cells nucleation, and the increase of the matrix viscosity. However, as the foaming is performed close to the crystallization temperature, the latter effect could almost be neglected. In fact, crystallization is the major contributor to changes of the matrix viscosity over this temperature range.

These three samples were foamed at 115°C with the lowest depressurization rate (flow control valve opened at 25%), after being saturated with Sc-CO₂ at 17MPa and 140°C. The resulting foam inner morphology as well as the cells size distribution are shown in Figure 85.

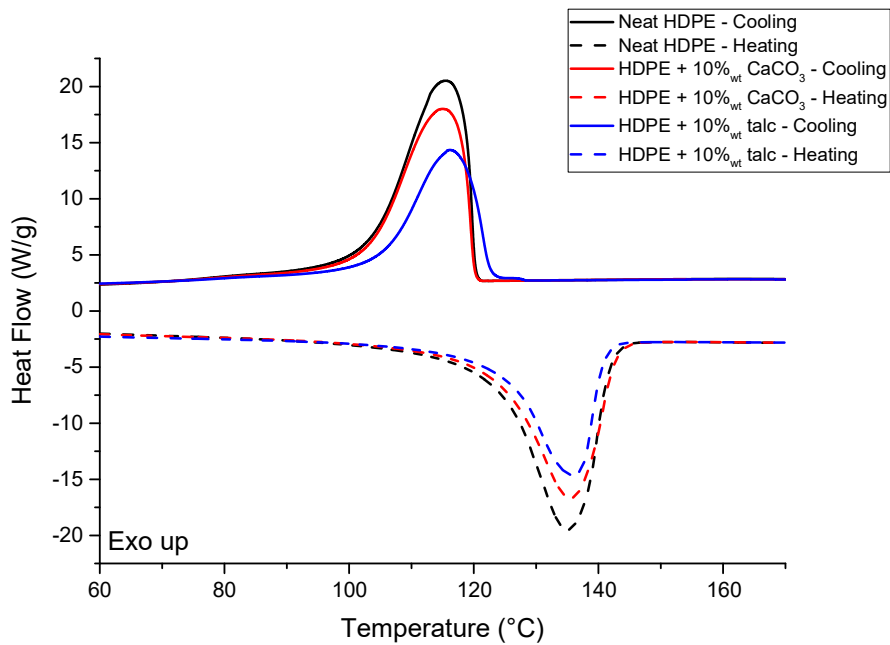


Figure 84 – DSC thermograms of neat HDPE (BM593) and HDPE filled with 10%_{wt} of talc or calcium carbonate. (Heating and cooling rates are 10K.min⁻¹)

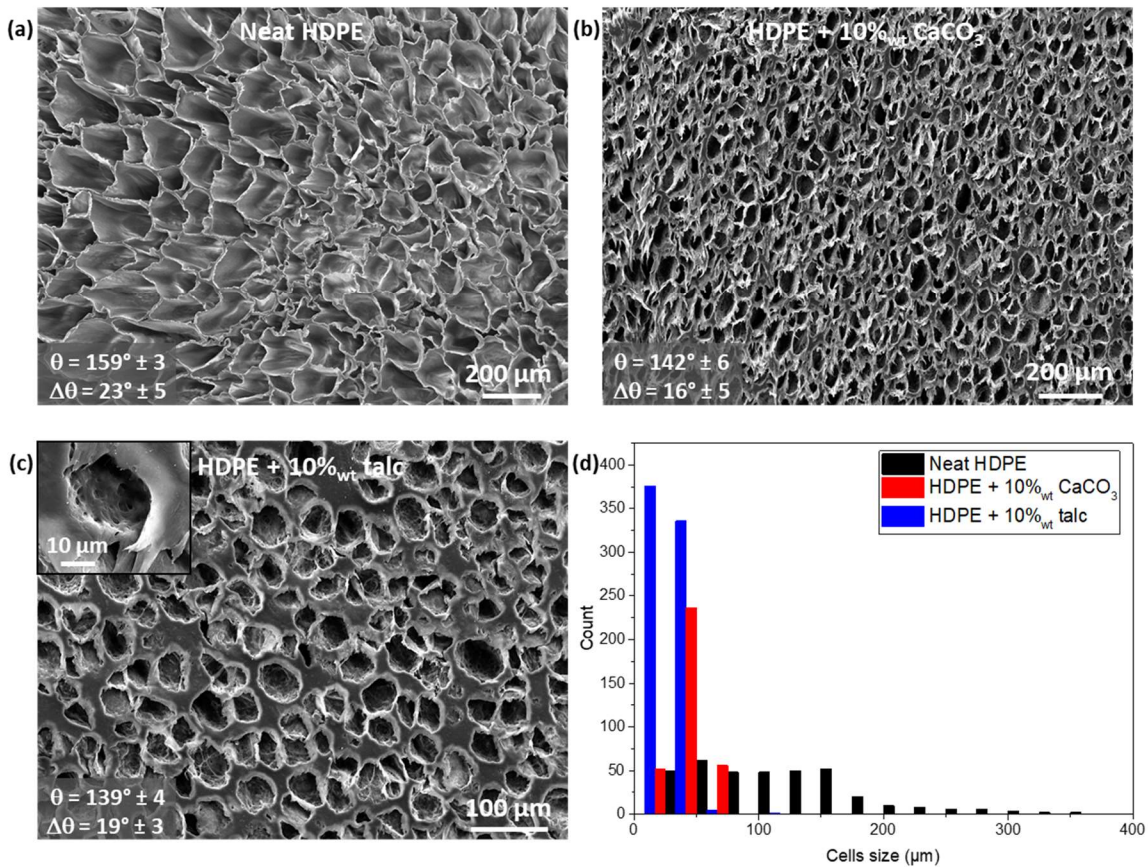


Figure 85 – Influence of the presence of fillers in the cells size and size distribution of HDPE (BM593), after an exposure to Sc-CO₂ at 17MPa and 140°C for 5h followed by a cooling at 115°C and pressure release at the lowest depressurization rate (flow control valve opened at 25%). SEM micrographs of (a) Neat HDPE, (b) HDPE containing 10%_{wt} CaCO₃, and (c) HDPE containing 10%_{wt} talc. (d) Size distribution of the cells (from SEM using ImageJ).

Neat HDPE (BM593) foamed at 115°C with at the lowest depressurization rate (25% opening of the flow control valve) (Figure 85a) has a morphology different from the HDPE (5502-R3) sample foamed under the same conditions (Figure 83c). In fact, the cells are larger with a broader size distribution (Figure 85d, black). These ones were stretched during the expansion step, and display thin walls (about 5µm).

When adding 10%_{wt} of calcium carbonate in HDPE, and foaming such sample under the same conditions, tinier cells are obtained with a narrower size distribution, and thicker walls (about 10µm) (Figure 85b). The average cell size is close to 50µm, and the size distribution is contained in a 75µm range (Figure 85d, red).

When 10%_{wt} of talc is used as the filler, the cells are smaller than with CaCO₃ (about 30µm), with a narrow size distribution (Figure 85d). The cells are rounded, have thick walls (about 20µm) and some of them seem to be opened, or at least touching each other and locally resulting in really thin walls.

In addition, the cells walls appear to be textured by micro-porosities (Figure 85c). Such a morphology could be the manifestation of the walls breakage due to the presence of hard talc particles within the polymer. Similar web-like texturing of the cells walls was observed by Miller *et al.*²⁷, with larger cells.

Table 22 – Water contact angle and hysteresis of foamed HDPE (BM593) containing fillers such as CaCO₃ or talc, saturated with Sc-CO₂ at 17MPa and 135°C and foamed at 115°C with a 25% opening of the flow control valve.

Sample	θ_{adv}	$\Delta\theta$
Neat HDPE	159°±3	23°±5
HDPE + 10% _{wt} CaCO ₃	142°±6	16°±5
HDPE + 10% _{wt} talc	139°±4	18°±3

With large cells and thin walls, the foam obtained from neat HDPE is sticky superhydrophobic with a hybrid Wenzel's and Cassie-Baxter's interface (Table 22). Such an interface is obtained because of the very high value of spacing distance on asperities width ratio (D/a). With CaCO₃ or talc, this ratio is lower (from 5 to 1), but the asperities are larger (from 10 to 20µm). These filled HDPE foams have a high hydrophobic behavior, but are not superhydrophobic (Table 22).

A cells size reduction has been successfully obtained by using fillers such as calcium carbonate or talc as cells nucleating agents. In addition to the size reduction, a web-like texturing of the cells walls has been observed. Even if the average cell size is lower than the one reported by Miller *et al.*²⁷, the scale of the foam morphology is still too large to lead to slippery superhydrophobicity, even if large water contact angle values are reported.

V.1.c.ii. Filled polypropylene

Foaming experiments have also been conducted using polypropylene. The addition of nucleating agents into PP is known to affect its crystallinity, modifying its viscosity variations upon cooling. 20%_{wt} of talc was incorporated in PP (PPH4060) at 200°C and extruded into a strand and cut into pellets for foaming experiments.

The comparison of the DSC thermogram of neat PP and PP filled with 20%_{wt} of talc (Figure 86d) shows that talc increases the crystallization temperature of PP up to 130°C. The melting behavior of these two materials remains the same (melting temperature of about 165°C). PP containing talc is expected to have smaller cells than neat PP, due to a faster viscosity increase due to its higher nucleation rate. In addition, smaller cells with thicker walls and some in-cell imperfections due to breakage of the walls are expected, as with HDPE. The two PP samples (neat or filled with 20%_{wt} talc) were foamed at 130°C with a fully opened flow control valve, after a Sc-CO₂ saturation at 155°C and 17MPa for 5h.

When neat PP is foamed at 130°C, large cells are formed, with quite thick walls (about 20µm). Some of the cells also appear to be opened, with connections through cracked cell walls (Figure 86a). The cells size distribution is relatively broad, with the most of the size values being between 150 and 200µm (Figure 86c). With such cells size and walls dimensions, a stable Cassie-Baxter's interface leading to superhydrophobicity is not established. The water droplets get pinned on the large cells walls, simply leading to hydrophobicity (Table 23).

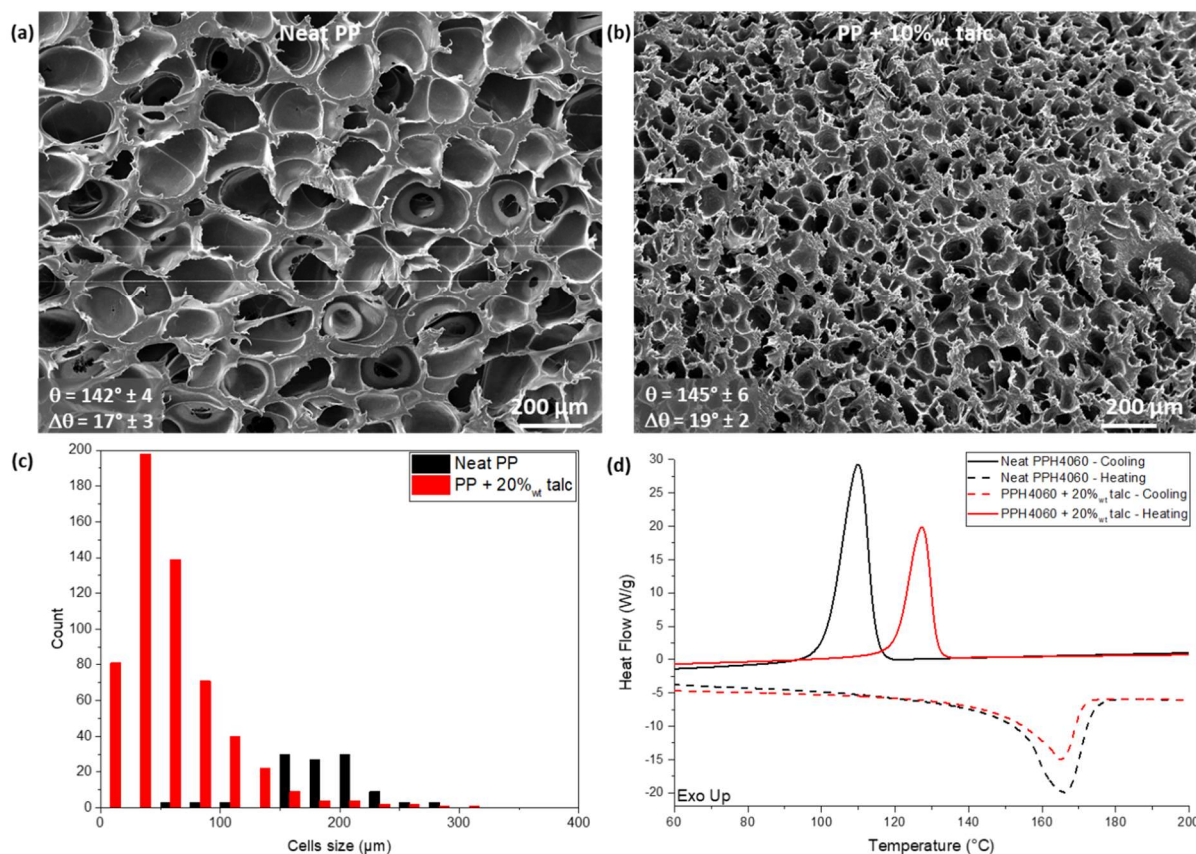


Figure 86 – Influence of the presence of nucleating agents on the cells size and distribution of PP (PPH4060). SEM micrographs of (a) Neat PP and (b) PP containing 20%_{wt} talc. (c) Size distribution of the cells (from SEM using ImageJ). (d) DSC thermograms of neat PP and PP filled with talc (Heating and cooling rates are 10K.min⁻¹).

When PP filled with 20%_{wt} of talc is foamed (in the same conditions), smaller cells (about 30µm) with a narrower distribution (range of about 100µm) are obtained (Figure 86c). The cells walls have about the same thickness as for neat PP (about 20µm), suggesting that the cells growth phenomenon proceeded similarly. The cells size reduction could be associated to an increase of cell nucleation. In fact, talc is known to be a powerful cell nucleation promoter. However, even if the cells size is reduced in comparison with previous samples, the asperities (cells walls), are still too large for slippery superhydrophobicity (Table 23).

Table 23 – Water contact angle and hysteresis of foamed PP (PPH4060) containing talc as a nucleating agent, saturated with Sc-CO₂ at 17MPa and 155°C and foamed at 130°C with a fully opened flow control valve.

Sample	θ_{adv}	$\Delta\theta$
Neat PP	142°±4	17°±3
PP + 20% _{wt} talc	145°±6	19°±2

As for HDPE, the addition of talc as a nucleating agent led to a major reduction of the cells size. However, such a size reduction is still insufficient for the sliced foam surface to be superhydrophobic.

Foaming thermoplastics such as HDPE or PP led to various inner morphologies, depending on the nature of the polymer, the presence of fillers as cell nucleation agents, or on the processing

parameters. The obtained morphologies are theoretically favorable to superhydrophobicity according to their dimensions. The D/a ratio is always larger than unity, but too large to lead to slippery superhydrophobicity. In particular, cells walls thickness is always larger than $5\mu\text{m}$, and often than $10\mu\text{m}$. Such large asperities are strong pinning points for water droplets, leading to adhesion to the surface. Nevertheless, this adhesion is lower than with a fully wetted Wenzel's interface.

Reducing the dimension of such morphologies would permit to reach superhydrophobicity from sliced thermoplastics foams. Such a reduction strategy should be achieved from foaming immiscible polymer blends, as smaller morphologies were reported in the litterature^{14,15}.

V.2. Foaming immiscible polymer blends

V.2.a. Polypropylene / polystyrene immiscible blend

Huang *et al.*¹⁴ described foams having cells of only a few micrometers large from PP/PS blends using Sc-CO₂ (foaming at 179°C after a Sc-CO₂ exposure at 19MPa and 120°C for 10h).

In a similar way, blends of PP (PPH4060) and PS (PS1070) in 70/30 and 50/50 weight fractions were extruded at 200°C into a strand, and cut into pellets. The prepared PP/PS immiscible blend were saturated with Sc-CO₂ at 18MPa and 180°C for 5h, and then foamed at 180°C, 150°C or 120°C at the higher depressurization rate (fully opened flow control valve). The foaming at 180°C was done to mimic the Huang *et al.* experiment, with PP and PS being melted at such high temperature. At 150°C and 120°C, the crystallization temperature of PP is closer to the foaming temperature, theoretically leading to a cells growth rate reduction.

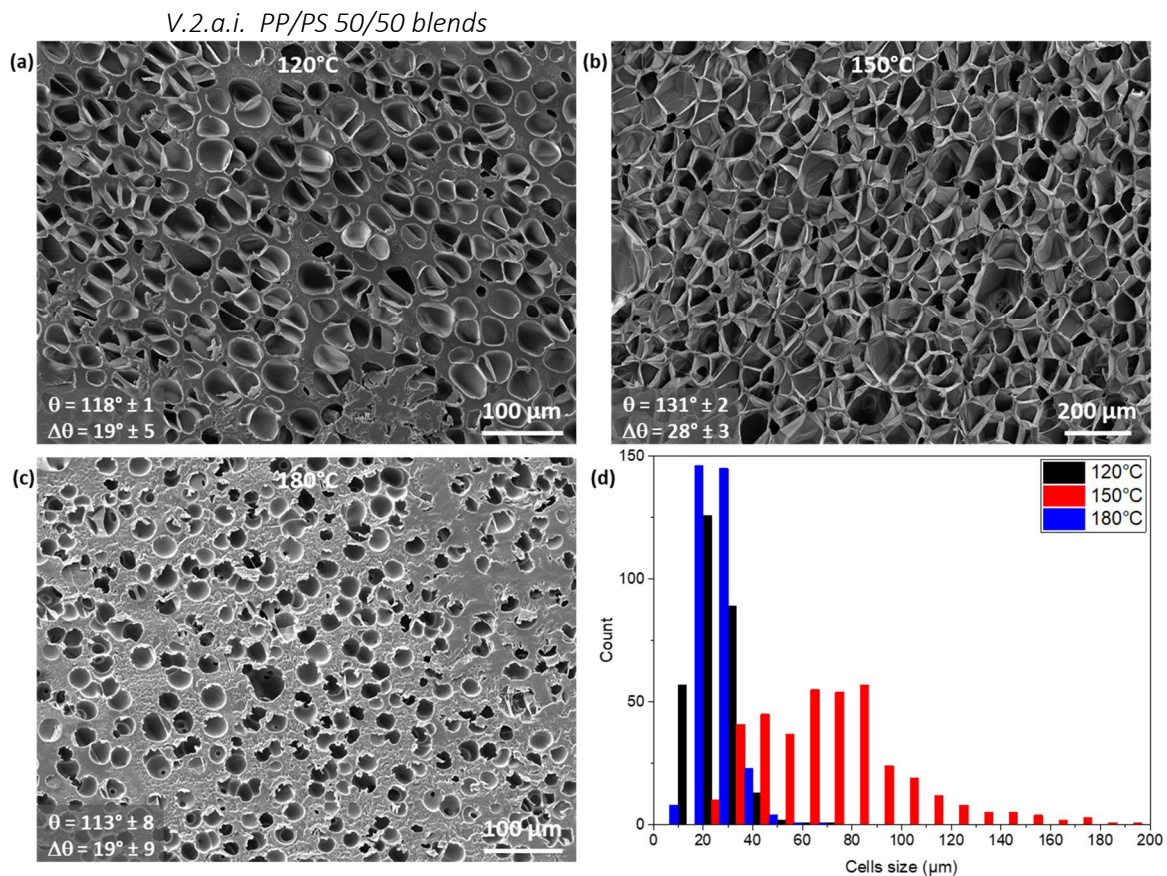


Figure 87 – Influence of the foaming temperature on the cells size and distribution of a PP/PS (PPH4060/PS1070N) blend in 50/50 weight proportions, after an exposure to Sc-CO₂ at 18MPa and 180°C for 5h followed by a cooling at (a) 120°C, (b)

150°C, and (c) 180°C, i.e. no cooling, and pressure release with the flow control valve fully opened, observed by SEM. (d) Size distribution of the cells (from SEM using ImageJ).

50/50 PP/PS foamed at 120°C after a CO₂ saturation at 180°C displays spherical closed cells, with walls of various thickness, from 1 to 20µm (Figure 87a). These cells are all less than 50µm large, with a narrow size distribution (Figure 87d). Even if the cells size is reduced in comparison with neat PP foams, the thick walls act as pinning site for water droplets. Such a surface structure is found to be slightly more hydrophobic than unfoamed PP (Table 24). Air fraction appears to be too low with such a morphology to be superhydrophobic. In addition, polystyrene is known to be only poorly hydrophobic (water contact angle of only 91°¹⁷).

When this blend is foamed at 150°C, the sliced surface interestingly shows polygonal cells with thin walls (about 5µm) (Figure 87b). The cells size distribution is broad, with an average value of 80µm (Figure 87d). Such a morphology is very similar to the ones obtained using HDPE, but with slightly reduced dimensions. However, even if the large air fraction at the interface is favorable to large water contact angles, the Cassie-Baxter's stability conditions are not reached (Table 24).

When the foaming temperature is as high as 180°C, i.e. the closest conditions to the ones of Huang *et al.*, a very peculiar structure is obtained. This foam has almost perfectly spherical cells, largely spaced ones to others. Some cells are in contact, and even opened (Figure 87c). These cells have narrow size distribution, with an average value of 30µm (Figure 87d), and a distance of about. Once again, even if the D/a ratio seems favorable to a Cassie-Baxter's interface stability, the cells size is too large and the air fraction is too low for making this surface superhydrophobic (Table 24).

V.2.a.ii. 70/30 PP/PS blends

When the PP phase is the major one (70/30%_{wt}), the morphologies obtained after foaming using the same conditions as the 50/50 blends are very different. For the blend foamed at 120°C after a Sc-CO₂ saturation at 180°C, the sliced surface shows no porosity in the dispersed PS phase, but a decohesion of the PP and PS phases (Figure 88a). Very rare and deformed porosities are obtained in such conditions, leading to a hydrophobicity (Table 24).

The same blend foamed at 150°C shows open porosities with poorly-defined cells and some PS spherical phases still unfoamed (Figure 88b). Despite the presence of open porosities in the foam inner structure, its surface remained smooth. The sliced surface is again strongly hydrophobic but not superhydrophobic (Table 24).

When the blend is foamed at 180°C, a completely open-porosity morphology is obtained. The cells are large and includes only some tenths of micrometers "bridges" (Figure 88c). Such morphology dimensions, despite the large air fraction at the interface, are obviously too large to reach superhydrophobicity (Table 24).

Surprisingly, the PS phase does not seem to be foamed in the 70/30 blends, whereas the foamed phase remains uncertain in the 50/50 blend, as the two phases are expected to be co-continuous²⁸. With the 50/50 PP/PS blend, the foaming temperature plays a major role on the final inner morphology of the foam, with isolated closed cells at both low (120°C) and high (180°C) temperatures. The only change concerns the spacing distance of cells between the two conditions. At 150°C, a morphology consisting in polygonal cells with low wall thickness was obtained.

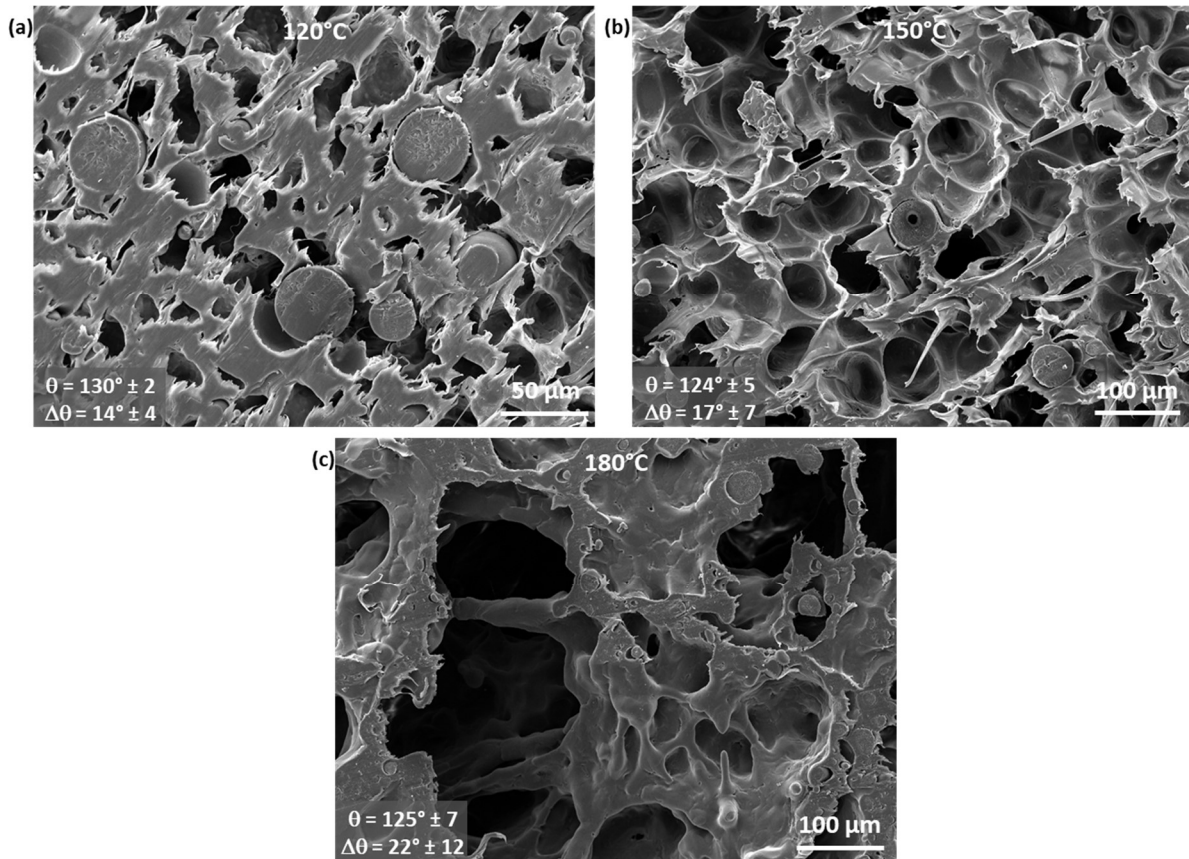


Figure 88 – Influence of the foaming temperature on the cells size and distribution of a PP/PS blend in 70/30 weight proportions, after an exposure to Sc-CO₂ at 18MPa and 180°C for 5h followed by a cooling at (a) 120°C, (b) 150°C, and (c) 180°C, and pressure release with the flow control valve fully opened, observed by SEM.

When PP is the most abundant polymer in the blend, the cells seem to expand within this phase. At low temperature (120°C), the cell growth only emphasizes a PP/PS phases decohesion. At higher temperatures (from 150°C to 180°C), relatively large and badly defined opened porosities are obtained. Again, none of these foam morphologies were found to be superhydrophobic, all materials have an unfoamed skin.

Table 24 – Water contact angle and hysteresis of foamed 50/50 and 70/30 PP/PS (PPH4060 and PS1070N) immiscible blend, saturated with Sc-CO₂ at 18MPa and 180°C and foamed at 120°C, 150°C or 180°C, at the fastest depressurization rate (fully opened flow control valve).

PP/PS (% _{wt})	Foaming temperature (°C)	θ_{adv} (°)	$\Delta\theta$ (°)
50/50	120	118±1	19±5
50/50	150	131±2	28±3
50/50	180	113±8	19±9
70/30	120	130±2	14±4
70/30	150	124±5	17±7
70/30	180	125±7	22±12

V.2.b. Polypropylene / polyethylene immiscible blend

Following the work of Rachtanapun *et al.*¹⁵ on microcellular PP/HDPE blends foams, blends of PP (PPH4060) and HDPE (5502-R3) have been prepared in 50/50 and 70/30 weight fractions and extruded at 200°C into a strand. The strand was cut into pellets that were foamed at 120°C at the fastest depressurization rate (fully opened flow control valve), after a Sc-CO₂ exposure at 180°C and 18MPa

for 5 hours. These 50/50 and 70/30 fractions are expected to lead to different blends morphologies: co-continuous and HDPE-in-PP dispersed phases, respectively²⁹.

The 50/50 PP/HDPE blend foamed at 120°C has almost spherical opened cells, with some cells close ones to others, and some other cells separated by thicker walls (Figure 89a). Such a morphology was not found to be superhydrophobic (Table 25).

When the PP/HDPE proportions are turned to 70/30, the blend foamed at 120°C has slightly smaller cells, with again spherical opened cells with poorly defined edges (Figure 89b). Such a surface was neither found to be superhydrophobic (Table 25). The presence of smooth areas of about a tenth micrometers between porosities might act as pinning sites for water.

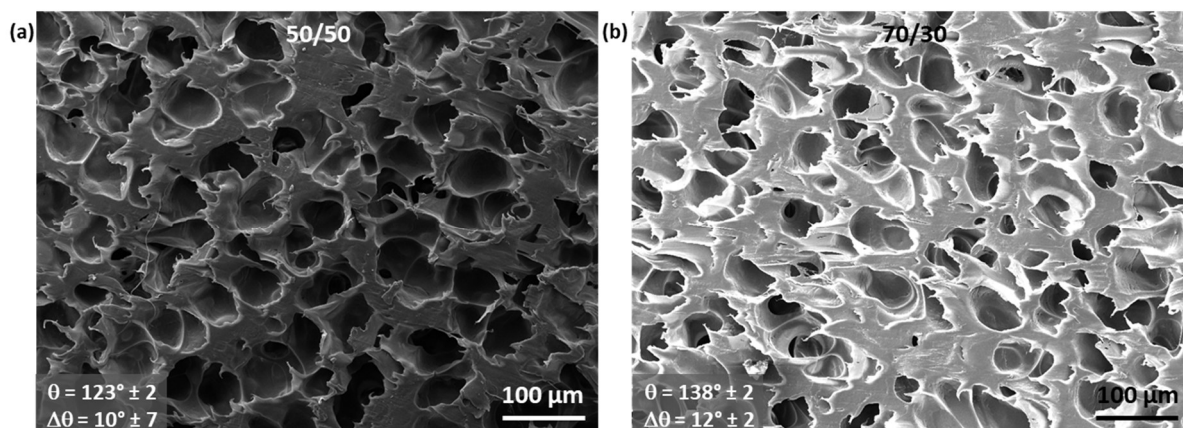


Figure 89 – Influence of the blend composition on the cells morphologies of (a) 50/50 and (b) 70/30 PP/HDPE (PPH4060 and 5502-R3) blend, after an exposure to Sc-CO₂ at 18MPa and 180°C for 5h followed by a cooling at 120°C, and a fast depressurization (flow control valve fully opened), observed by SEM.

PP and HDPE were used for an immiscible blend, in order to enhance the cells nucleation rate. For such blends, it appears that a dispersed HDPE in a PP matrix is more favorable than a co-continuous morphology. In fact, co-continuous interfaces generate larger cells and cells interspaces. However, as for PP/PS blends, none of the surfaces obtained after slicing a foamed blend were found to be superhydrophobic.

Table 25 – Water contact angle and hysteresis of foamed 50/50 and 70/30 PP/HDPE (PPH4060 and 5502-R3) immiscible blend, saturated with Sc-CO₂ at 18MPa and 180°C and foamed at 120°C, with a fast depressurization rate (fully opened flow control valve)

PP/HDPE (%wt)	θ_{adv} (°)	$\Delta\theta$ (°)
50/50	123±2	10±7
70/30	138±2	12±2

V.3. Conclusion

Foaming thermoplastics such as HDPE or PP using Sc-CO₂ is a powerful way of generating porous morphologies, even if the resulting materials always have an unfoamed skin. Slicing foams with a razor blade allowed the access to their inner structure.

Process effects such as the foaming temperature or depressurization rate have been investigated, as well as the impact of nucleating agents such as talc or calcium carbonate. It appears that a decrease of the temperature and/or of the depressurization rate led to a limitation of the cells growth. Addition of nucleating agents led to an increase of the cells nucleation rate. When fillers are incorporated in polypropylene, the cells growth can also be limited due to a change in the crystallization kinetic.

When considering immiscible polymer blends, such as PP blended with PS or HDPE, an increase of the cell nucleation rate at the interface is expected. Peculiar morphologies due to different phases viscosities could also be obtained. However, even if smaller cells size were obtained for such blends, the dimensions of the resulting surface texture are still too large for superhydrophobicity.

The obtained foams always needed to be sliced to reveal their inner structure, *i.e.* to generate textured surfaces. Even if such a route of generating textured surfaces has been found to be effective for providing superhydrophobicity, it can hardly be turned into an industrial continuous process. In fact, the batch-based foaming on one part, and the required slicing on another part limit the obtention of large textured surfaces.

However, this study allowed to give guidelines on how to obtain cells as small as possible in thermoplastic foams. Such a preliminary study will be helpful in the next part of this chapter, *i.e.* a direct extrusion of a foam to get textured surfaces.

VI. Continuous foaming process (extrusion)

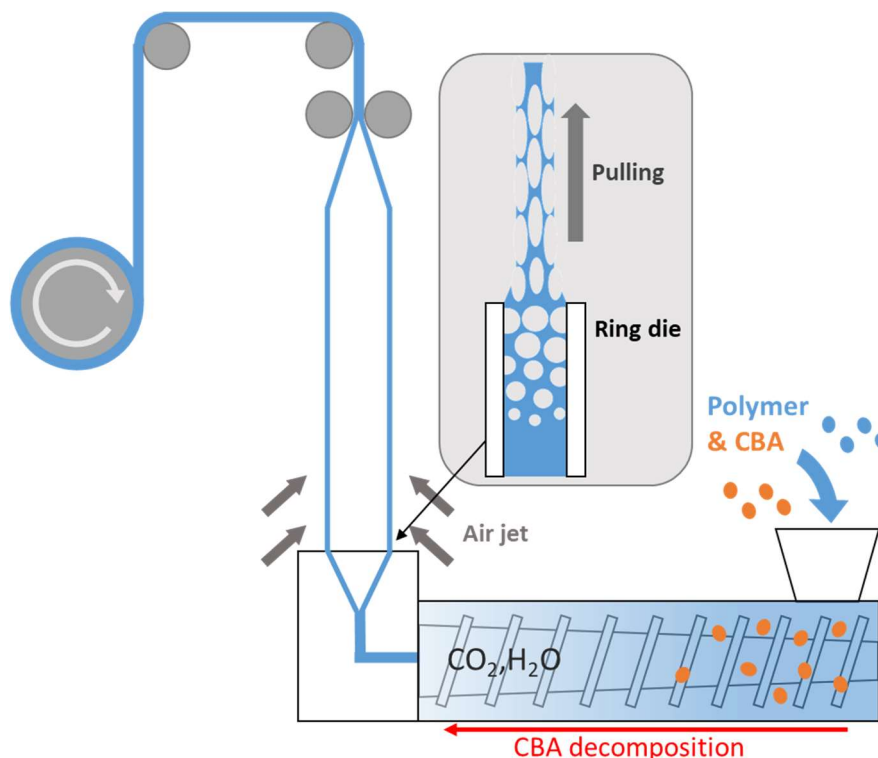


Figure 90 – Scheme of the texturing continuous foaming process route. Polymer and chemical blowing agents (CBA) are introduced in an extruder where CBA decompose into CO₂ and H₂O, and then extruded into a film (using a ring die).

VI.1. Blowing agents

To foam a thermoplastic by extrusion, two main kinds of blowing agents can be considered: “physical” and “chemical”.

Physical blowing agents are gaseous substances that are stable in the pressure and temperature range of the process, and that are introduced in the molten polymer at high pressure. The depressurization upon the extruder die produces a foam in a very analogous way as for batch-foamed samples using Sc-CO₂. Gases such as CO₂, N₂, air, or short alkanes (from propane to pentane) are commonly used for foaming thermoplastics such as polyethylene, polypropylene or polystyrene, or thermosets such as polyurethane.³⁰ In the past, chlorofluorocarbure (CFC) gases were also used as physical foaming agent, especially for insulation foams, but their use is now banned because of their large greenhouse effect. These physical blowing agents are powerful as their purity and concentration within the matrix can be easily tuned. Nevertheless, special setups are needed to make foams using physical blowing agent.

Chemical blowing agents (CBA) are usually solids that are mixed in the molten polymer, and that generate gases such as CO₂, H₂O or N₂ by decomposition or reaction at a given temperature. The gases are generated *in situ*, allowing the foaming of polymers without the need of any particular foaming equipment.

The most used CBA, which are compatible with food-contact applications, are citric acid (C₆H₈O₇), sodium hydrogen carbonate (NaHCO₃), and their combination. Citric acid generates CO₂ and H₂O, by decomposition into aconitic acid (C₆H₆O₆), which is decomposed into aconitic anhydride (C₆H₄O₅) and then into itaconic anhydride (C₅H₄O₃) (Figure 91a). Sodium hydrogen carbonate reaction leads to sodium carbonate, generating CO₂ and H₂O (Figure 91b). Citric acid can react with calcium carbonate to form a calcium citrate chelated salt (Ca₃(C₆H₅O₇)₂), generating CO₂ and H₂O (Figure 91c). Citric acid

can also react with sodium hydrogen carbonate, forming a sodium citrate salt ($\text{Na}_3\text{C}_6\text{H}_5\text{O}_7$) and generating CO_2 and H_2O (Figure 91d)³¹.

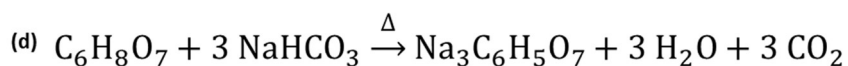
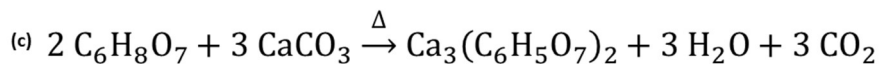
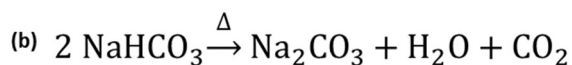
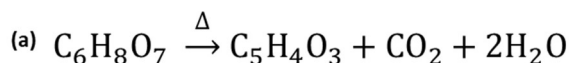


Figure 91 – Reaction mechanisms of some chemical blowing agents. (a) Citric acid thermal decomposition, (b) Sodium hydrogen carbonate thermal decomposition, (c) Citric acid reaction with calcium carbonate or (d) sodium hydrogen carbonate.

Figure 92 shows the weight loss measured by TGA of the four described CBA as solid powders. Table 26 reports the temperatures of start of decomposition, the expected weigh loss due to CO_2 and H_2O generation, and the measured weight loss at 250°C.

For the citric acid (CA) reaction with NaHCO_3 and CaCO_3 , the initial powders have been mixed and intimately grinded using a mortar, in order to maximize the final powder homogeneity. Citric acid alone starts to decompose at a temperature close to 170°C, whereas NaHCO_3 or CA mixed with either CaCO_3 or NaHCO_3 start to decompose at lower temperature (from 120°C for pure NaHCO_3 to 140°C for the NaHCO_3/CA mixture). However, it must be noted that for the NaHCO_3/CA mixture, a slight weight loss is observed from 100°C to 130°C, which can be due to NaHCO_3 decomposition.

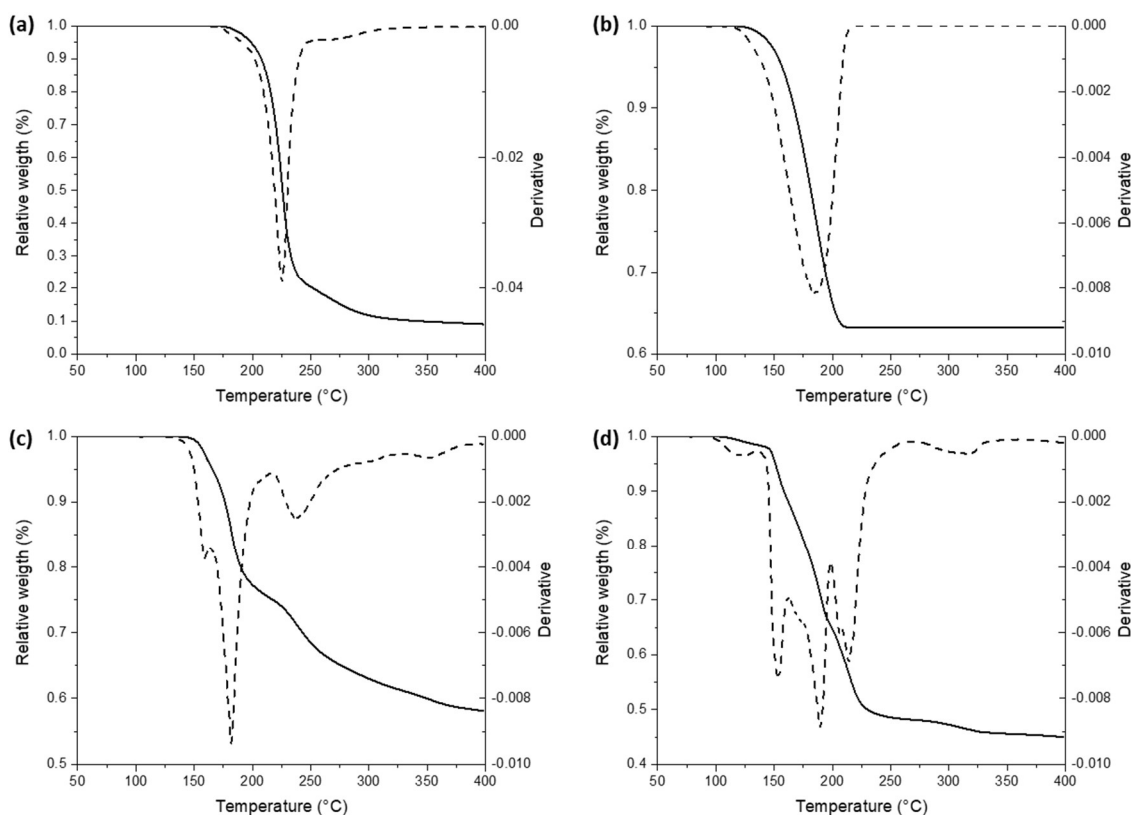


Figure 92 – Thermal degradation of chemical blowing agents. Relative weight loss (in solid lines) and derivative (in dashed lines) for (a) citric acid ($\text{C}_6\text{H}_8\text{O}_7$, CA), (b) sodium hydrogen carbonate (NaHCO_3), (c) CA + calcium carbonate in 2:3 molar proportions, and (d) CA + sodium hydrogen carbonate in 1:3 molar proportions. (Heating rate of $10\text{K}\cdot\text{min}^{-1}$, under nitrogen)

When comparing the expected and measured weight losses, it appears that the neat CA displays a very important weight loss, that could be attributed to itaconic anhydride evaporation. Sadik *et al.*³¹, who studied the decomposition of CA dispersed in a polymer matrix such as LDPE, reported a weight loss similar to the expected one. Itaconic anhydride could be stabilized by interactions with the polymer, avoiding its evaporation.

NaHCO₃ weight loss is equal to the expected one, *i.e.* corresponding to CO₂ and H₂O release, with stable sodium carbonate over the 210-400°C range.

CA reaction with CaCO₃ leads to a slightly higher weight loss than expected, probably because of CA decomposition in the mixture.

Concerning the CA reaction with NaHCO₃, a higher weight loss than expected is measured. This phenomenon could be due to CA and NaHCO₃ separate decomposition, and itaconic anhydride evaporation.

Table 26 – Chemical blowing agents thermal reaction characteristics

Compound	Start of decomposition (°C)	Theoretical weight loss (CO ₂ and H ₂ O release) (%)	Measured weight loss at 250°C (%)
Citric acid (CA)	170	42	80
NaHCO ₃	120	37	37
2 CA + 3 CaCO ₃	140	27	33
CA + 3 NaHCO ₃	140	41	51

As these CBA need to be used with a variety of polyolefins such as HDPE, the low temperature of start of decomposition of NaHCO₃ limit its use in the present study. On the opposite, citric acid has been successfully incorporated in HDPE (BM593 and 5502-R3) by mixing them at a maximum temperature of 160°C.

CaCO₃ was easily dispersed in HDPE at a higher temperature, thanks to its thermal stability. The CA and CaCO₃ mixture was only effective in the final foaming extrusion, so the low temperature of start of decomposition of such blend was not problematic. The advantage of the CA reaction with CaCO₃ in comparison to neat CA is that CaCO₃ and/or calcium citrate act as nucleating agents while generating gases, increasing the cells nucleation rate.

All masterbatches of HDPE, LDPE, or PP, containing CA, CaCO₃, NaHCO₃, talc, or even silica, were obtained by mixing them using a twin-screw micro-extruder (DSM Xplore MC15) or a twin-screw extruder (Leistritz ZSE18, with a L/D=60). The blends were extruded into a strand that was then pelletized for further use. The masterbatches preparation conditions are reported in Table 27.

Table 27 Compositions and processing conditions of HDPE and LDPE masterbatches with CBA and fillers.

Matrix	CBA	Content (%wt)	Blending setup	Temperature (°C)	Time (min)
HDPE (BM593)	Citric acid	20	DSM Xplore MC15	160	3
HDPE (BM593)	Calcium carbonate	20	DSM Xplore MC15	200	5
HDPE (BM593)	Talc (Luzenac A3)	10	DSM Xplore MC15	200	5
HDPE (BM593)	Silica (Aerosil®R812)	20	DSM Xplore MC15	200	5
HDPE (5502-R3)	Citric acid	30	Leistritz ZSE18	135	<2
HDPE (5502-R3)	Calcium carbonate	30	Leistritz ZSE18	160	<2
LDPE (FE8000)	Citric acid	30	DSM Xplore MC15	130	3
LDPE (FE8000)	NaHCO ₃	30	DSM Xplore MC15	130	3
LDPE (FE8000)	Calcium carbonate	30	DSM Xplore MC15	130	5

VI.2. Extrusion of polyethylene foams

VI.2.a. Influence of the CBA loading

Foams with a textured surface have been obtained by foaming HDPE (BM593) using citric acid and calcium carbonate in a blown-film extruder. Various amounts of CBA were used. The resulting films have open porosities, hindering their inflating, and were only uniaxially pulled.

The amount of CBA introduced in the blend is directly linked with the gas quantity that is generated during the extrusion process. As the gas concentration is known to strongly influence the final foam morphology, the influence of CBA content on the final film texture has been studied.

CA and CaCO_3 in equal proportions were used as CBA and nucleating agents in HDPE, for contents from 1 to 10%_{wt}. The extruder was heated at 180°C, 200°C, 220°C and 230°C from the hopper to the end in order to have the most complete CBA reaction during the extrusion (Figure 92). The blow-film die was heated at 180°C to promote a fast crystallization of HDPE, *i.e.* limiting the cells growth.

It was observed that the cells are already formed when going out of the ring die, as the depressurization is progressive from the inner part of the die to the air. The resulting films have a textured surface with open porosities without needing any post-treatment. The cell growth and the film stretching is found to be sufficient to obtain opened porosities. Such surface morphologies are in the opposite of the conventional closed-cells morphologies obtained after batch-foaming of polyolefins using Sc-CO_2 .

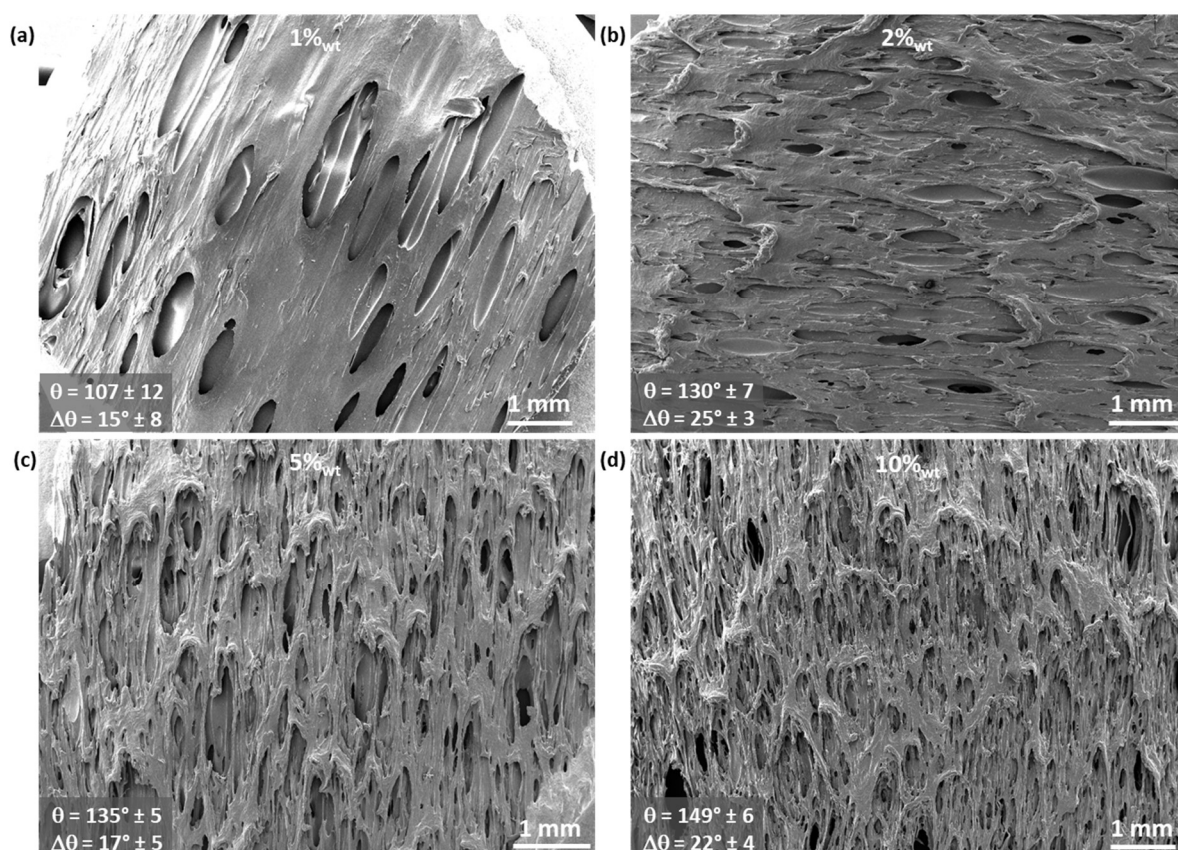


Figure 93 – SEM micrographs of HDPE (BM593) extruded foam with various amounts of CBA. HDPE was mixed at 230°C and extruded through a 180°C die with (a) 1%_{wt}, (b) 2%_{wt}, (c) 5%_{wt}, and (d) 10%_{wt} citric acid, and the same amount of calcium carbonate.

When only 1%_{wt} of CA and 1%_{wt} of CaCO_3 are introduced in HDPE, isolated elongated opened cells (from 0.5 to 2mm long and about 400 μm width) aligned in the direction of the film stretching, are

obtained (Figure 93a). Some cells are connected one to the other, but most of the parts of the film surface are smooth due to these very spaced cells. With such a small texture due to these rare and large voids, the surface is only hydrophobic (Table 28), with values close to unfoamed HDPE.

When the CA and CaCO₃ contents are increased up to 2%_{wt} each, opened cells deformed in the direction of the film stretching are still obtained. These are smaller, with a typical length of less than a millimeter and a width of about 150µm (Figure 93b). The voids density at the surface is also more important than with only 1%_{wt} of CBA, and some folds are also observed, due to some matter being concentrated at one of some large cells extremity. It could be noticed that a cells-in-cells structure is obtained, with larger ovoid cells being separated into tinier cells with a narrower shape. Even if such a surface is more textured than the first one, it is still not superhydrophobic (Table 28).

When further increasing the CA and CaCO₃ contents up to 5%_{wt} each, a similar effect as for 2%_{wt} loadings is observed. The voids density at the surface is higher, with cells of about the same dimensions as with 2%_{wt} CA and CaCO₃, *i.e.* less than a micrometer long and about 150µm width (Figure 93c). With a more textured surface and similar voids dimensions, the resulting surface is slightly more hydrophobic than the one obtained with 2%_{wt} of CBA (Table 28).

By increasing the CA and CaCO₃ content up to 10%_{wt}, the previously observed phenomenon is preserved: the cells are about the same size as before, but the voids density at the surface is larger, and the cells-to-cells morphology is also more important (Figure 93d). Smaller cells also appear from these cells-in-cells structures, but relatively large unfoamed parts and matter folds are still observable. Despite a more important texturing, the dimensions of this texture is still too important for a stable Cassie-Baxter's interface to be formed (Table 28).

It is supposed that if the texturing is furtherly increased, a water contact angle larger than 150° could be obtained. Nevertheless, the hysteresis will remain larger than 10° due to the too large dimensions of the surface texture with relatively large smooth areas leading to water pinning.

Table 28 – Water contact angle and hysteresis of HDPE (BM593) extruded foams containing from 1 to 10%_{wt} of citric acid, and the same amount of calcium carbonate as chemical blowing agents.

Citric acid and calcium carbonate contents (% _{wt})	θ_{adv} (°)	$\Delta\theta$ (°)
1	107±12	15±8
2	130±7	25±3
5	135±5	17±5
10	149±6	22±4

Slippery superhydrophobicity has not been reached from continuous foaming HDPE using citric acid and calcium carbonate. Sticky superhydrophobicity has almost been reached, and the influence of the amount of CBA on the surface texture has been clearly demonstrated. As expected, the more the CBA content is, the more the generated gas quantity is. With more gases, the cells nucleation rate is higher, leading to smaller cells with an increased density.

Moreover, the foaming of HDPE using the considered CBA led to textured films directly out of the extruder, without any post-treatments. The next step is to reduce the texture dimensions, in order to reach slippery superhydrophobicity using the same foaming approach.

VI.2.b. Influence of the CBA compound

To reduce the cell growth, a change in the nature of the CBA can be attempted, as they will release gases in various proportions at different temperatures. However, in order to be able to mix CBA such as NaHCO_3 , HDPE cannot be used as the matrix due to its processing temperature being higher than the NaHCO_3 temperature of decomposition. To avoid this problem, the investigation of the influence of the CBA nature on the final foam morphology was realized using LDPE (FE8000).

As a reference, a LDPE film foamed using 10%_{wt} (each) CA and CaCO_3 was extruded at 210°C with a die temperature of 160°. The resulting film looks like a less CBA-concentrated HDPE film. In fact, a low cells density and smaller folds in comparison to HDPE foamed with 10%_{wt} of CA and CaCO_3 are observed. However, the cells are smaller, with a length of about half a millimeter, and a width of about 100 μm . A cells-in-cells morphology is observed, and the cells seems to be less stretched than with HDPE (Figure 94a). Despite the reduced cells size, their lower surface density and the still too large texture scale did not lead to superhydrophobicity (Table 29).

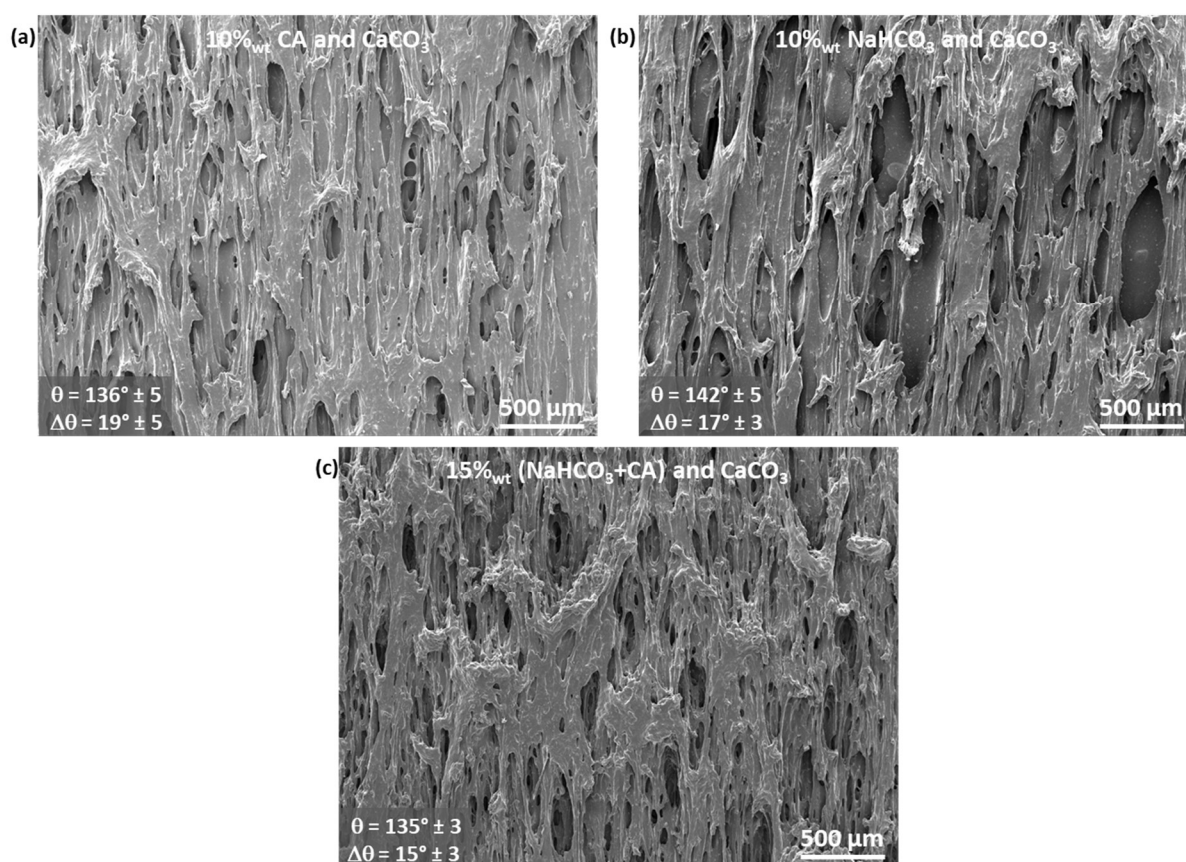


Figure 94 – SEM micrographs of LDPE (FE8000) extruded foams obtained from various chemical blowing agents. LDPE is mixed at 230°C and extruded through a 180°C die with (a) 10%_{wt} of citric acid and 10%_{wt} of calcium carbonate, (b) 10%_{wt} sodium hydrogen carbonate with 10%_{wt} calcium carbonate as filler, and (c) 15%_{wt} sodium hydrogen carbonate with citric acid in 3:1 molar proportion and 15%_{wt} calcium carbonate as filler.

As 10%_{wt} of neat NaHCO_3 is used as CBA in LDPE, with an additional 10%_{wt} of CaCO_3 as nucleating agent, the extrusion temperature is only of 180°C because of the lower decomposition temperature of NHCO_3 compared to citric acid. In such conditions, relatively large cells are generated with numerous large folds. Cells seem to be more stretched than in the previously considered surfaces. This phenomenon can be associated to the lower compounding temperature, *i.e.* a higher polymer viscosity (Figure 94b). The resulting textured surface is strongly hydrophobic (Table 29). Nevertheless, water droplets still got pinned on such a surface despite a large texturing and moderate dimensions.

For the last system, 15%_{wt} of CA and NaHCO₃, and 15%_{wt} of CaCO₃ were introduced in LDPE (CA and NaHCO₃ in 1:3 molar proportions). This blend was compounded at a 200°C, and extruded at a die temperature of 160°C. The resulting surface shows an important cells density, with a cells-in-cells morphology but also very large folds and unfoamed matter parts that create smoother area on the surface (Figure 94c). The cells dimensions are about 300µm long and from 50µm large, with some wider objects but also tinier voids. This surface structure is found to be too heterogeneous and has too much smooth areas for being superhydrophobic (Table 29).

Table 29 – Water contact angle and hysteresis of LDPE (FE8000) extruded foam containing citric acid, calcium hydrogen carbonate and calcium carbonate as chemical blowing agent and/or nucleating agents.

Matrix	Additives	θ_{adv} (°)	$\Delta\theta$ (°)
LDPE	10% _{wt} C ₆ H ₈ O ₇ + 10% _{wt} CaCO ₃	136±5	19±5
LDPE	10% _{wt} NaHCO ₃ + 10% _{wt} CaCO ₃	142±5	17±3
LDPE	15% _{wt} (NaHCO ₃ + C ₆ H ₈ O ₇ 1:3) + 15% _{wt} CaCO ₃	135±3	15±3

Although interesting surface morphologies could be obtained showing small cells (50µm width), superhydrophobicity cannot be reached with foamed LDPE films whatever the CBA used. Moreover, only neglectable changes in the resulting film wettability were observed for the different surfaces. The morphology changes could also be associated to the changes of the processing temperatures, which can be permitted by the use of CBA with lower decomposition temperatures. The impact of the gas nature was not been furtherly studied, as CBA generating gases such as N₂ or NH₃, like azodicarbonamide, are toxic.

VI.2.c. Influence of the nucleating agents

In order to get small cells with a large surface density of voids on a foamed film surface, nucleating agents could play a significant role. That is why CaCO₃ was added in the previous HDPE blends. However, the influence of the nature of these fillers needs to be investigated, as they might have different nucleating effects.

To investigate these effects, HDPE (BM593) blends containing 5%_{wt} of CA as a CBA and 5%_{wt} of talc (Luzenac A3) or hydrophobic silica (Aerosil® R812) were investigated. These surfaces were compared with a foamed HDPE film surface from 5%_{wt} of CA and CaCO₃ (large voids density on its surface, with cells of less than a millimeter and about 150µm width (Figure 93c)).

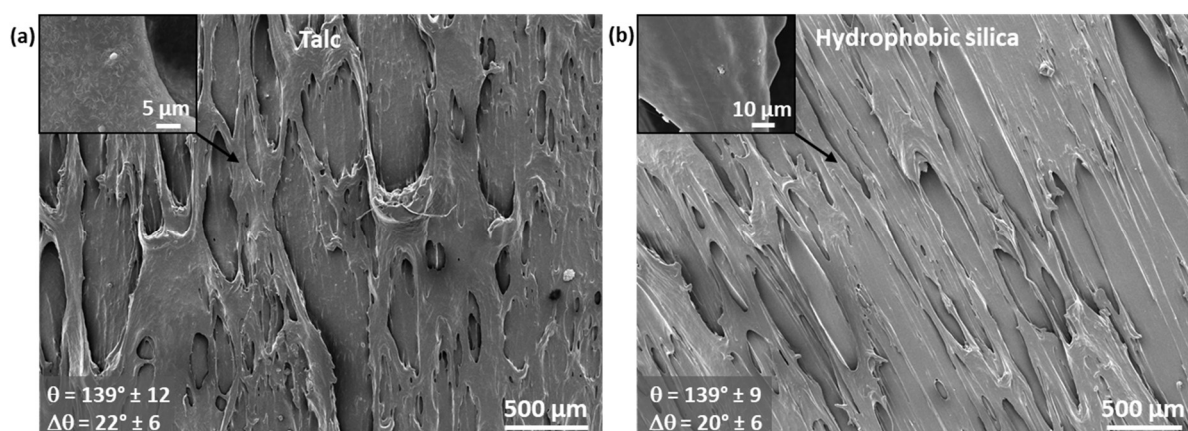


Figure 95 – SEM micrographs of HDPE (BM593) extruded foam with various fillers. HDPE was mixed at 230°C and extruded through a 180°C die with 5%_{wt} of citric acid and (a) 5%_{wt} of talc, or (b) 5%_{wt} of hydrophobic silica.

For both talc and silica, it must be noted that no particles could be observed on the surface, even if some objects could be observed (Figure 95). Such fillers have no effect on the texture of the foam surfaces.

Using talc, the cells surface density is relatively low, with ovoid cells and similar dimensions as blends containing CA and CaCO₃ in the same extent (Figure 95a).

For silica introduction, the cells appear to be more stretched, with lengths of more than a millimeter and about the same width as with talc or CaCO₃ (Figure 95b). The cells surface density seems to be lower when using silica as a nucleation agent than talc or CaCO₃. Such a behavior was expected with these nanoparticles in comparison to the 2D-inorganic objects such as talc particles, or with larger particles such as CaCO₃. Both of these surfaces have a marked (Table 30).

Table 30 – Water contact angle and hysteresis of HDPE (BM593) extruded foam containing 5%_{wt} of citric acid, and the same amount of talc or hydrophobic silica as nucleating agents.

Matrix	Filler content (% _{wt})	θ_{adv} (°)	$\Delta\theta$ (°)
HDPE	5% _{wt} talc (Luzenac A3)	139±12	22±6
HDPE	5% _{wt} silica (Aerosil® R-812)	139±9	20±6

The nature of the filler acting as a nucleating agent does not appear to have a remarkable influence on the resulting surface wettability. In fact, the filler does not stand at the surface, and does not participate in the surface texturing. If talc or CaCO₃ addition give more relevant surface morphologies for superhydrophobicity, the water wettability of all these surface remains very similar. Processing conditions might have a higher influence on the resulting surface texture. However, these process parameters cannot be tuned at will, for example due to the viscosity variations of the polymer.

VI.2.d. Extruding a HDPE foam with a high matrix viscosity

By changing the CBA or fillers nature, it was not possible to obtain a superhydrophobic surface by extrusion. Thus, a new way of limiting the cells growth would be the use of a highly viscous HDPE matrix, in order to freeze the film morphology out of the extruder die. For this purpose, a viscous HDPE (5502-R3) was extruded with citric acid and calcium carbonate in various proportions. The influence of the generated gas quantity or the nucleating agent content were also investigated. HDPE films were obtained from blends containing 20/10%_{wt}, 10/20%_{wt}, and 15/15%_{wt} of CA and CaCO₃ (Table 31).

The extrusion of foamed HDPE in highly viscous conditions led to string-based morphologies, with a uniaxial texturation of the film due to stretching. As suggested by the observation of these surfaces, in particular the one obtained with 15/15%_{wt} CA/CaCO₃ (Figure 96c), these strings come from the stretching of smaller cells created within the die. These cells are not able to grow because of the polymer freezing due to its crystallization, while ribbons are plastically deformed.

The resulting surfaces display a strong morphology isotropy in the direction of the film pulling, with relatively small asperities. The two first samples, with 10/20%_{wt} and 20/10%_{wt} of CA and CaCO₃, are strongly hydrophobic (Table 31). The third sample, obtained with 15/15%_{wt} of CA/CaCO₃ is sticky superhydrophobic (Table 31).

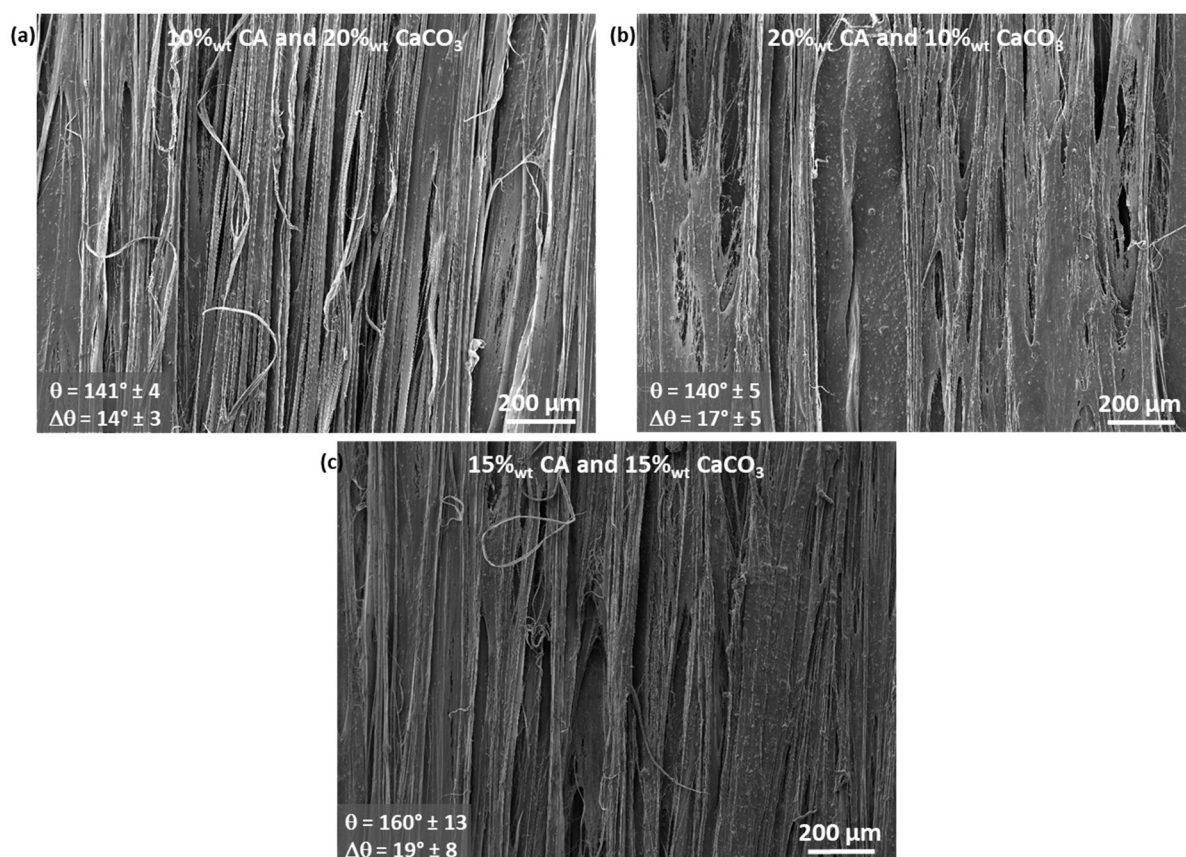


Figure 96 – SEM micrographs of HDPE (5502-R3) extruded in viscous conditions with various citric acid and calcium carbonate contents. HDPE is mixed at 230°C and extruded through a 160°C die with (a) 10%_{wt} of citric acid and 20%_{wt} of calcium carbonate, (b) 20%_{wt} of citric acid and 10%_{wt} of calcium carbonate, and (c) 15%_{wt} of citric acid and 15%_{wt} of calcium carbonate.

New morphologies were obtained using a high viscosity matrix processed in conditions involving a low temperature die, resulting in a fast cooling of the polymer. Slippery superhydrophobicity has not been reached, even if high water contact angle values were obtained. The dimensions of these morphologies are probably too large for superhydrophobicity (asperities of about 10μm). Moreover, the obtained textures are strongly isotropic. Thus, this isotropy could be partially responsible for the relatively high contact angle hysteresis. In fact, water droplets have to dewet along a smooth surface in the direction of the film elongation. As a consequence, the resulting adhesion is similar as the one of smooth HDPE.

Table 31 – Water contact angle and hysteresis of HDPE 5502-R3 extruded foam containing citric acid and calcium carbonate in various proportions.

Citric acid content (% _{wt})	Calcium carbonate content (% _{wt})	θ_{adv} (°)	$\Delta\theta$ (°)
10	20	141±4	14±3
20	10	140±5	17±5
15	15	160±13	19±8

VI.3. Conclusion

Foaming thermoplastics such as HDPE or LDPE in an extruder is a powerful process to obtain textured film surfaces. This foaming was conducted in a blow-film extruder apparatus, from the decomposition of given compounds, known as chemical blowing agents (CBA), into gases. These CBA were citric acid or sodium hydrogen carbonate, and their combination, as well as the combination of citric acid and calcium carbonate.

Nucleating agents were also used in these blends, such as the already mentioned calcium carbonate, but also talc or silica. Their role was to promote cell nucleation to enhance their density and to reduce their size.

The extruded film surfaces have an open-cells morphology, which is enhanced by the film stretching. Using such a process, various surface morphologies could be obtained: disperse ovoid voids, more textured surface with again ovoid voids with a cells-in-cells additional texture, parallel strings. The latter were obtained by stretching the cells close to the crystallization temperature of the polymer.

Despite the diversity of morphologies obtained, and even if a tuning of the asperities size and surface density can be achieved by controlling the blends formulation and process, slippery superhydrophobicity was not reached with this method. For further practical developments, the resulting films could not have been used as-it, as air was able to pass through because of the open porosities. A hermetic support-film is needed to turn such films into the desired shape. If true superhydrophobicity was not reached, this method is still an easy and inexpensive way to produce textured and porous surfaces for other applications.

VII. Chapter conclusion

In this chapter, various approaches have been investigated to produce textured slippery superhydrophobic surfaces. Based on an overview of potential and easily-handled processes that led to textured surfaces, some experiments have been set-upped. The considered approaches included texturing a thermoplastic film surface using fillers, making a porous HDPE film by removing the water-soluble PEO part from HDPE/PEO blends, foaming a polyolefin or an immiscible polyolefins blend using Sc-CO₂, or even extruding a foamed HDPE into a film. All these approaches have led to textured surfaces, but none of them is slippery superhydrophobic.

Adding fillers such as talc or silica nanoparticles to HDPE in the bulk, and then extruding the resulting blend into a film only led to poorly textured hydrophobic surfaces. Based on works done by Yüce *et al.*² or Fourmentin *et al.*⁴, for a surface textured using nanoparticles to be slippery superhydrophobic, the amount of particles might be larger than 50%_{wt}. Such filler contents have not been reached in the current study due to difficulties of processing such a viscous thermoplastic. Thus, this approach was abandoned.

Immiscible HDPE/PEO blends led to porous structures with various morphologies after PEO removal in water. It was found that the lower the HDPE content, the more hydrophobic the final surface. This phenomenon was expected as the PEO phase turns into an air after its removal. However, a film resulting from a low HDPE concentration has very poor cohesion, and is too brittle to be easily manipulated. Membranes with 46%_{vol} of HDPE were successfully prepared, and did not suffer from any handling issue.

Silica nanoparticles were introduced in these blends in order to stabilize the polymer phases and consequently to reduce their size. This effect was almost neglectable with 5%_{wt} of hydrophilic silica, but the nanoparticles that stood at the former HDPE/PEO interface added a nanotexture to the surface. With hydrophilic silica, the surface turned out to be superhydrophilic, with a complete absorption of water droplets. When using hydrophobic silica nanoparticles, the surface was found to be slightly hydrophobic, without any advantage from such a texturing in comparison to smooth HDPE.

Polytetrafluoroethylene microparticles were also used in such immiscible polymer blends, in order to texture the surface, in addition to its low surface energy. Whatever was the PTFE microparticles content (from 5 to 10%_{wt}) the particles were successfully located at the former HDPE/PEO interface, but the interparticle spacing was too large to get a superhydrophobic surface. This interparticle spacing is attributed to the HDPE phases elongation during the film pulling out of the extruder, as well as a potential removal of PTFE particles during the PEO dissolution. Thus, such an approach did not allow to reach superhydrophobicity neither. In addition, the use of PEO which requires a removal in a second-step process would be an issue for an industrial scale-up.

Foaming polyolefins such as HDPE, PP, PS, and their blends using Sc-CO₂ led to various closed-cells foams. All the obtained foams have a smooth skin on their outer surface, and its removal by slicing was always necessary to reveal a textured surface. The influence of the saturation pressure and time, foaming temperature, and depressurization flow rate were investigated. Materials-related effects such as the thermoplastic nature, the addition of nucleating agents, or the presence of interfaces in an immiscible polyolefins blend, were also investigated.

In order to get a superhydrophobic textured surface, the cells nucleation rate needed to be increased, and their growth limited. Highly viscous polymers containing nucleating agents such as talc or CaCO₃ are the best candidates. Concerning the process conditions, an exposure to a Sc-CO₂ pressure as high as possible is required. The foaming temperature might be as close as possible to the polymer crystallization temperature, as the crystallization will increase the matrix viscosity during the foaming, *i.e.* limiting the cells growth.

If some sticky superhydrophobic surfaces have been obtained from such an approach, none of them was found to be slippery superhydrophobic. It is believed that the texture scale remained too large for the water contact angle hysteresis to be below 10° . Moreover, the required slicing to reveal a textured surface, as well as the fact that it involved a batch-processing make this approach irrelevant for an industrial scale-up. Nevertheless, the observations made from this study have been useful for designing foam extrusion experiments.

The foam extrusion approach aimed to mimic the structures of the foams obtained using Sc-CO₂ in a more easy-to-industrialize process. Foams of HDPE or LDPE were obtained by generating CO₂ and H₂O directly in the extruder of a blown-film extrusion apparatus using various chemical blowing agents such as citric acid, sodium hydrogen carbonate, or their combination with calcium carbonate. Fillers were also used to increase the cells nucleation rate, as well as increasing the matrix viscosity. Various process conditions were investigated: extrusion temperature, rotating speed, die temperature, and pulling rate of the film. Textured surfaces were always obtained with this approach, without needing any post-treatments as the film was textured right at the end of the process. However, this texture remained at a too large scale for the films to be superhydrophobic, even if water contact angle values larger than 150° could be obtained. Attempts to reduce the size of the obtained surface texture until superhydrophobicity were not successful.

All these approaches, inspired by the literature dedicated to surface that are superhydrophobic or not, were not successful in turning a thermoplastic surface superhydrophobic by a simple texturing.

VIII. References

1. Manoudis, P. N. & Karapanagiotis, I. Modification of the wettability of polymer surfaces using nanoparticles. *Prog. Org. Coatings* **77**, 331–338 (2014).
2. Yüce, M. Y., Demirel, A. L. & Menzel, F. Tuning the surface hydrophobicity of polymer/nanoparticle composite films in the wenzel regime by composition. *Langmuir* **21**, 5073–5078 (2005).
3. Mark, J. *Polymer Data*. (Oxford University Press, Inc., 1999).
4. Fourmentin, A., Galy, J., Charlot, A. & Gérard, J.-F. Bioinspired silica-containing polyurethane-acrylate films: Towards superhydrophobicity with tunable water adhesion. *Polymer (Guildf)*. **155**, 1–12 (2018).
5. Chandra, A., Turng, L.-S., Gopalan, P., Rowell, R. M. & Gong, S. Study of utilizing thin polymer surface coating on the nanoparticles for melt compounding of polycarbonate/alumina nanocomposites and their optical properties. *Compos. Sci. Technol.* **68**, 768–776 (2008).
6. Parvinezadeh, M., Moradian, S., Rashidi, A. & Yazdanshenas, M. Surface characterization of polyethylene terephthalate/silica nanocomposites. *Appl. Surf. Sci.* **256**, 2792–2802 (2010).
7. Trifkovic, M., Hedegaard, A., Huston, K., Sheikhzadeh, M. & MacOsko, C. W. Porous films via PE/PEO cocontinuous blends. *Macromolecules* **45**, 6036–6044 (2012).
8. Zhang, M., Dou, M., Wang, M. & Yu, Y. Study on the solubility parameter of supercritical carbon dioxide system by molecular dynamics simulation. *J. Mol. Liq.* **248**, 322–329 (2017).
9. Goel, S. K. & Beckman, E. J. Generation of microcellular polymeric foams using supercritical carbon dioxide. I: Effect of pressure and temperature on nucleation. *Polym. Eng. Sci.* **34**, 1137–1147 (1994).
10. Reignier, J., Gendron, R. & Champagne, M. F. Autoclave Foaming of Poly(ϵ -Caprolactone) Using Carbon Dioxide: Impact of Crystallization on Cell Structure. *J. Cell. Plast.* **43**, 459–489 (2007).
11. Krause, B., Diekmann, K., van der Vegt, N. F. A. & Wessling, M. Open Nanoporous Morphologies from Polymeric Blends by Carbon Dioxide Foaming. *Macromolecules* **35**, 1738–1745 (2002).
12. Liao, X. & Nawaby, A. V. Solvent Free Generation of Open and Skinless Foam in Poly(L-lactic acid)/Poly(D,L-lactic acid) Blends Using Carbon Dioxide. *Ind. Eng. Chem. Res.* **51**, 6722–6730 (2012).
13. Areerat, S., Funami, E., Hayata, Y., Nakagawa, D. & Ohshima, M. Measurement and prediction of diffusion coefficients of supercritical CO₂ in molten polymers. *Polym. Eng. Sci.* **44**, 1915–1924 (2004).
14. Huang, H.-X. & Xu, H.-F. Preparation of microcellular polypropylene/polystyrene blend foams with tunable cell structure. *Polym. Adv. Technol.* **22**, 822–829 (2011).
15. Rachtanapun, P., Selke, S. E. M. & Matuana, L. M. Relationship between cell morphology and impact strength of microcellular foamed high-density polyethylene/polypropylene blends. *Polym. Eng. Sci.* **44**, 1551–1560 (2004).
16. McKeen, L. W. Production of Films, Containers, and Membranes. in *Permeability Properties of Plastics and Elastomers* 41–60 (Elsevier, 2017). doi:10.1016/B978-0-323-50859-9.00003-8
17. Wu, S. Calculation of interfacial tension in polymer systems. *J. Polym. Sci. Part C Polym. Symp.* **34**, 19–30 (2007).

18. Fenouillot, F., Cassagnau, P. & Majesté, J.-C. Uneven distribution of nanoparticles in immiscible fluids: Morphology development in polymer blends. *Polymer (Guildf)*. **50**, 1333–1350 (2009).
19. Elias, L., Fenouillot, F., Majesté, J.-C., Martin, G. & Cassagnau, P. Migration of nanosilica particles in polymer blends. *J. Polym. Sci. Part B Polym. Phys.* **46**, 1976–1983 (2008).
20. Huang, S., Bai, L., Trifkovic, M., Cheng, X. & Macosko, C. W. Controlling the morphology of immiscible cocontinuous polymer blends via silica nanoparticles jammed at the interface. *Macromolecules* **49**, 3911–3918 (2016).
21. Trifkovic, M., Hedegaard, A. T., Sheikhzadeh, M., Huang, S. & Macosko, C. W. Stabilization of PE/PEO Cocontinuous Blends by Interfacial Nanoclays. *Macromolecules* **48**, 4631–4644 (2015).
22. Reignier, J., Gendron, R. & Champagne, M. F. Extrusion Foaming of Poly(Lactic acid) Blown with CO₂: Toward 100% Green Material. *Cell. Polym.* **26**, 83–115 (2007).
23. Reignier, J., Tatibouët, J. & Gendron, R. Batch foaming of poly(ϵ -lactone) using carbon dioxide: Impact of crystallization on cell nucleation as probed by ultrasonic measurements. *Polymer (Guildf)*. **47**, 5012–5024 (2006).
24. Liu, S., Eijkelenkamp, R., Duvigneau, J. & Vancso, G. J. Silica-Assisted Nucleation of Polymer Foam Cells with Nanoscopic Dimensions: Impact of Particle Size, Line Tension, and Surface Functionality. *ACS Appl. Mater. Interfaces* **9**, 37929–37940 (2017).
25. Rachtanapun, P., Selke, S. E. M. & Matuana, L. M. Microcellular foam of polymer blends of HDPE/PP and their composites with wood fiber. *J. Appl. Polym. Sci.* **88**, 2842–2850 (2003).
26. Zimmermann, M. V., da Silva, M. P., Zattera, A. J. & Santana, R. M. Poly(lactic acid) foams reinforced with cellulose micro and nanofibers and foamed by chemical blowing agents. *J. Cell. Plast.* **54**, 577–596 (2018).
27. Miller, D. & Kumar, V. Fabrication of microcellular hdpe foams in a Sub-Critical CO₂ process. *Cell. Polym.* **28**, 25–40 (2009).
28. Omonov, T. S., Harrats, C., Moldenaers, P. & Groeninckx, G. Phase continuity detection and phase inversion phenomena in immiscible polypropylene/polystyrene blends with different viscosity ratios. *Polymer (Guildf)*. **48**, 5917–5927 (2007).
29. Yang, F., Pan, L., Du, H. Z., Ma, Z. & Li, Y. S. Effect of Olefin-based Compatibilizers on the Formation of Cocontinuous Structure in Immiscible HDPE/iPP Blends. *Chinese J. Polym. Sci. (English Ed)*. **38**, 1248–1257 (2020).
30. Spalding, M. A. & Chatterjee, A. M. *Handbook of Industrial Polyethylene Technology. Handbook of Industrial Polyethylene Technology* (2016). doi:10.1002/9781119159797
31. Sadik, T., Pillon, C., Carrot, C. & Reglero Ruiz, J.-A. Dsc studies on the decomposition of chemical blowing agents based on citric acid and sodium bicarbonate. *Thermochim. Acta* **659**, 74–81 (2018).

CHAPTER 4 – THERMOPLASTIC TEXTURING BY SOLVENT- INDUCED REORGANIZATION

Thermoplastic texturing by solvent induced reorganization

I.	Texturing a polymer by a solvent exposure	135
I.1.	Texturing HDPE surfaces with xylene	135
I.1.a.	Immersing HDPE in hot xylene.....	135
I.1.b.	Multiple baths immersion of HDPE in xylene	136
I.1.c.	Final process for texturing HDPE surfaces	138
I.2.	Applying the developed process to various polyethylene grades and polypropylene.....	139
I.2.a.	Influence of HDPE grade	139
I.2.b.	Impact of the polymer nature: texturing PP	140
I.2.c.	Influence of the presence of fillers in HDPE	142
I.3.	Resulting wettability.....	143
I.3.a.	Wettability predictions	143
I.3.b.	Water wettability	145
I.3.c.	Textured surface wetting by low surface tension liquids	146
I.4.	Conclusion	148
II.	Use of less-toxic solvents for surface texturing	149
II.1.	Solvents selection.....	149
II.2.	Processing HDPE and resulting surface textures	150
II.2.a.	Dipentene	150
II.2.b.	α -pinene	151
II.2.c.	Decane	151
II.2.d.	Paraffin wax.....	152
II.2.e.	Olive oil.....	153
II.2.f.	Summary of the texturing conditions and resulting wettability	155
II.3.	Application to PP and resulting surface textures	156
II.3.a.	Dipentene	156
II.3.b.	α -pinene	157
II.3.c.	Decane	158
II.3.d.	Olive oil.....	159
II.3.e.	Summary of the texturing conditions and resulting wettability.....	159
II.4.	Towards simplification for scale-up	161
II.4.a.	One-bath texturing of HDPE films	161
II.4.a.i.	Dipentene.....	161
II.4.a.ii.	α -pinene	162
II.4.a.iii.	Decane	163
II.4.a.iv.	Summary of the texturing conditions and resulting wettability	163
II.4.b.	One-bath texturing of PP films	164
II.4.b.i.	Dipentene.....	164
II.4.b.ii.	α -pinene	165
II.4.b.iii.	Decane	166
II.4.b.iv.	Summary of the texturing conditions and resulting wettability	166
II.4.c.	Continuous texturing proof-of-concept.....	167
II.4.c.i.	Continuous texturing of HDPE films.....	168
II.4.c.ii.	Polypropylene film continuous texturing.....	168
II.5.	Conclusion	170
III.	Understanding the texturing mechanisms	171
III.1.	Texturing from crystallization/precipitation	171
III.1.a.	Expected mechanisms	171
III.1.b.	Investigating the solvent-assisted crystallization of HDPE and PP	173
III.1.c.	Investigating the crystallization-induced precipitation	175
III.2.	Influence of solvent nature and temperature.....	178
III.2.a.	Crystallization temperature and surface morphology.....	178
III.2.b.	Polymer/solvent solubility considerations	179
III.3.	Conclusion	181

IV. Chapter conclusion	182
V. References	184

As discussed in the first chapter, there are several examples in the literature of superhydrophobic surfaces obtained from polymers in solution¹⁻⁹, or from exposing a polymer surface to a solvent, in particular polycarbonate with acetone¹⁰⁻¹³. Even if HDPE and PP are known to dissolve in only few solvents, it has been highlighted that a xylene exposure could induce a texturing favorable to superhydrophobicity. By combining solvent-casting and solvent-exposure processes described in the literature, an efficient texturing process of complex HDPE or PP objects has been obtained.

In the present chapter, the development of such a process will be described, as well as the resulting surface morphologies. To continue, further developments of this process will be discussed, by taking into account the process hazards and overpassing the productivity limits of batch-processing. Finally, texturing mechanisms will be proposed to understand the processing/surface properties relationships.

I. Texturing a polymer by a solvent exposure

I.1. Texturing HDPE surfaces with xylene

Brown and Bhushan¹⁰ or Cui *et al.*¹¹ have developed a process to texture polycarbonate leading to superhydrophobicity after an acetone immersion. Otherwise, Erbil¹ produced superhydrophobic textured surfaces using polypropylene from a xylene solution. Based on these results, a method consisting of an immersion of polyethylene in xylene is investigated. Polyethylene being a widely used hydrophobic thermoplastic, its texturing from a simple solvent exposure could lead to superhydrophobicity.

I.1.a. Immersing HDPE in hot xylene

For high density polyethylene (HDPE), benzene or its derivatives, such as toluene or xylene, are commonly used as solvents at high temperature. Thanks to a relatively high boiling point (close to 140°C, versus 110°C for toluene, and 80°C for benzene)¹⁴ and a reduced toxicity in comparison with toluene and benzene, xylene has been selected for this study.

A HDPE (HD6081) 2mm-thick film was dipped in xylene at 100°C for 90 seconds, showing a melting/swelling of the polymer surface. The film was then dried at room temperature for 2h, and then dried under vacuum at 40°C for 1h. Upon drying, the HDPE surface became whitish, revealing the appearance of low-size heterogeneities that scatters visible light. Surprisingly, a relatively smooth surface was obtained (Figure 97a). However, the underlying surface was found to be textured by a stacking of micrometric features (Figure 97b).

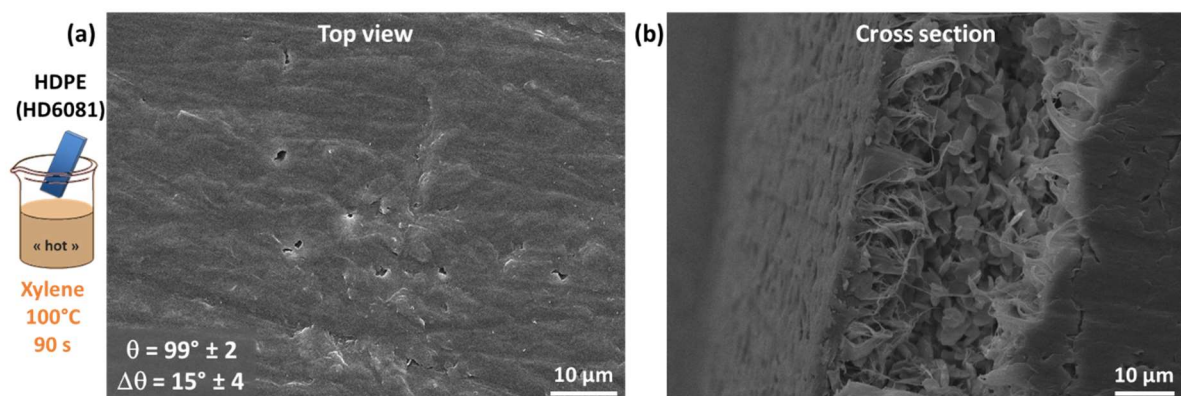


Figure 97 – SEM micrographs of a HDPE (HD6081) immersed in xylene at 100°C for 90s. (a) Relatively smooth surface, and (b) stack of micrometric features under a smooth skin revealed by slicing. Water contact angle and hysteresis values of the surface are inserted in the lower left corner.

Due to the high volatility of xylene, especially at 100°C, its fast evaporation results in a quenched smooth skin at the surface. When in a xylene solution, the crystallization of HDPE takes place around 80°C instead of 115°C (Figure 98). Thus, a fast solvent withdraw is equivalent to a 35°C quenching for the crystallization. Moreover, the fast cooling in, coupled to the endothermic evaporation of the solvent, favorize such a surface quenching. On the opposite, the under-skin polymer layer is “protected” from such a quenching, and has more time to crystallize. This longer crystallization time results in the observed under-skin texturing.

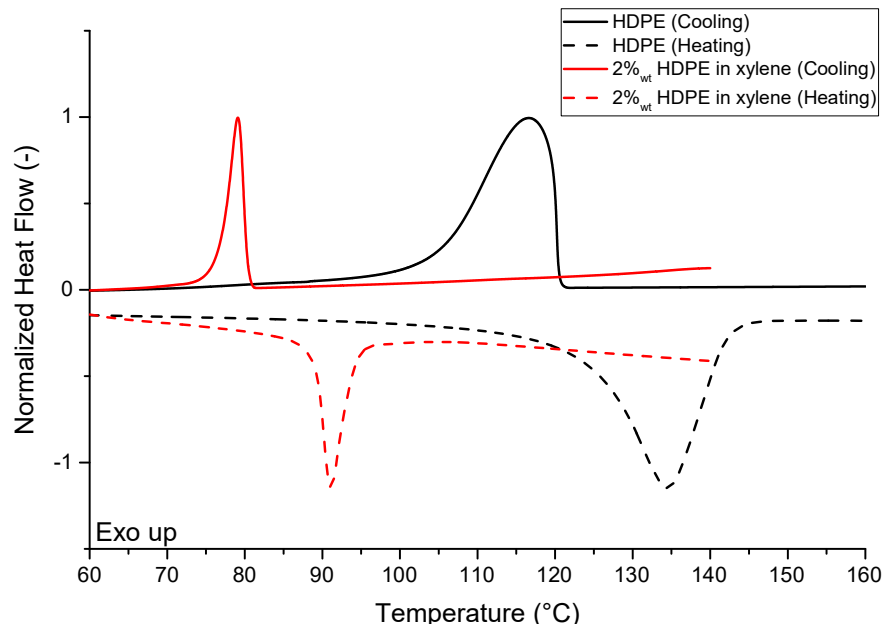


Figure 98 – DSC traces of neat HDPE (BM593) in black and HDPE in a xylene solution (2%_{wt}) in red, showing crystallization during cooling (solid lines) and melting during heating (dashed lines). (Heating and cooling rate are 10K.min⁻¹)

1.1.b. Multiple baths immersion of HDPE in xylene

To avoid the smooth skin formation, *i.e.* to obtain a surface texture similar to the one under the skin, the quenching of the extreme surface has to be eliminated. To do so, after the first immersion in hot xylene, the film was transferred to a second xylene bath to slowly cool down and crystallize without solvent evaporation. To reduce the swelling time, the temperature of the first bath was increased up to 130°C. In such conditions, the swelling of the polymer only took several seconds. Two process parameters were varied in order to optimize the process: 1/ the immersion time in the first bath, of 5 or 10s (higher immersion time led to a complete swelling of the film which lose its integrity), and 2/ the second bath temperature, 60 or 80°C, *i.e.* close or below the crystallization temperature of HDPE-in-xylene solution (Figure 99). This experiment was also conducted on a HDPE matrix with a lower crystallinity rate and higher viscosity (5502-R3), leading to similar results.

For all the films, the immersion in a second “cold” bath of xylene after the first exposure prevented the formation of a skinned surface. The temperature of the second bath seems to lead to a better texturing at the micrometric scale (left column). This observation is in good agreement with the hypothesis of a skin formation due to a quenching of the extreme surface. In fact, a higher temperature of the second bath offers more time to the polymer to crystallize, as the solvent does not evaporate. A lower temperature, such as 60°C, pushes the polymer to crystallize faster, as the polymer/solvent solution is then in a supercooled configuration. In addition, immersion of a swollen film in a xylene bath at room temperature resulted in a skinned surface. At such temperatures, xylene is no longer a solvent of polyethylene.

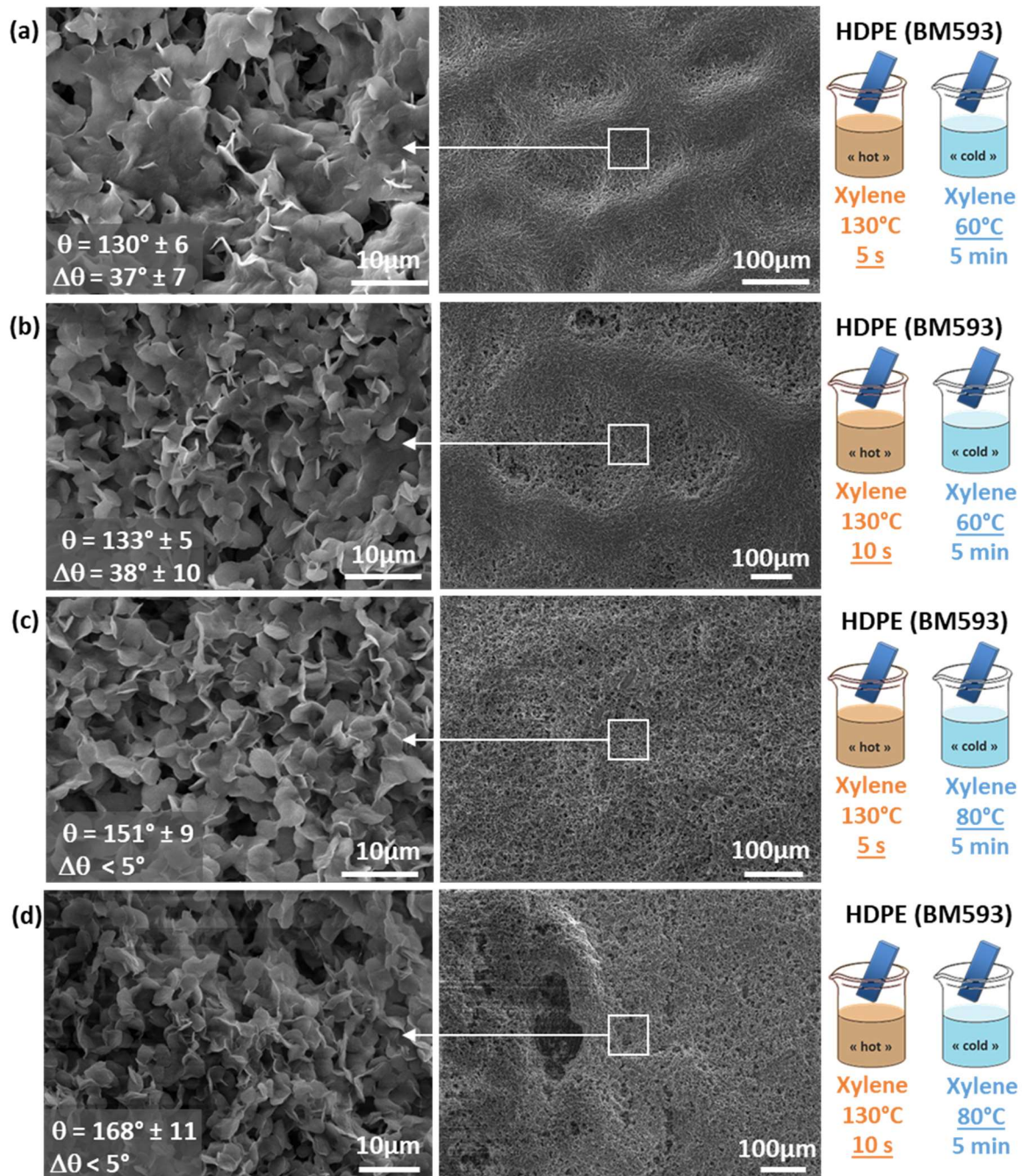


Figure 99 – Surfaces as obtained after immersion of HDPE (BM593) in xylene at 130°C for (a,c) 5s and (b,d) 10s, directly followed by an immersion in xylene at (a,b) 60°C and (c,d) 80°C for 5 minutes (SEM micrographs).

Erbil¹ observed the opposite phenomenon with the drying temperature of a diluted solution of PP in xylene. A lower temperature led to a lower solvent evaporation rate, an increased nucleation rate, and a more textured surface.

The immersion time of 5 or 10 seconds in the first “hot” bath does not seem to have a major influence on the microtexture, but leads to a macro-textured surface based on porosities or “hills and valleys” morphologies of hundreds of micrometers. This phenomenon might be due to a thicker swollen region of the film for longer exposure time. It must be noted that the thickness of the recrystallized surface does not seem to have an influence on the extreme surface morphology at micrometer scale.

I.1.c. Final process for texturing HDPE surfaces

According to the first results, a process has been developed for treating shaped polyethylene objects (Figure 100) such as tensile test specimens, beakers, or films. The process can be decomposed in three steps:

- 1- HDPE is exposed to a solvent by immersing it in a xylene bath at 130°C for 5s. This bath is called the “hot” bath. The 5 seconds duration is sufficient for swelling a sufficient thickness without altering the specimen shape.
- 2- After these 5s, the specimen is immediately immersed in a bath of xylene at 80°C for 5min. This bath is called the “cold” bath, which allows the polymer to re-organize without quenching the extreme surface. In this bath, the solvent slowly quits the polymer volume due to a loss of solvency power with a decreasing temperature. The 5min immersion time is found to be sufficient to robustly obtain textured surfaces. Nevertheless, this time has not been optimized. In fact, it might be reduced as the re-organization phenomenon is believed to happen in less than 5min.
- 3- The specimen is removed from the “cold” bath and dried at room temperature, leading to a surface whitening. Then, traces of solvent are removed by a drying at 60°C for one hour under vacuum. The HDPE surface is homogeneously textured, and the specimen has conserved its original shape.

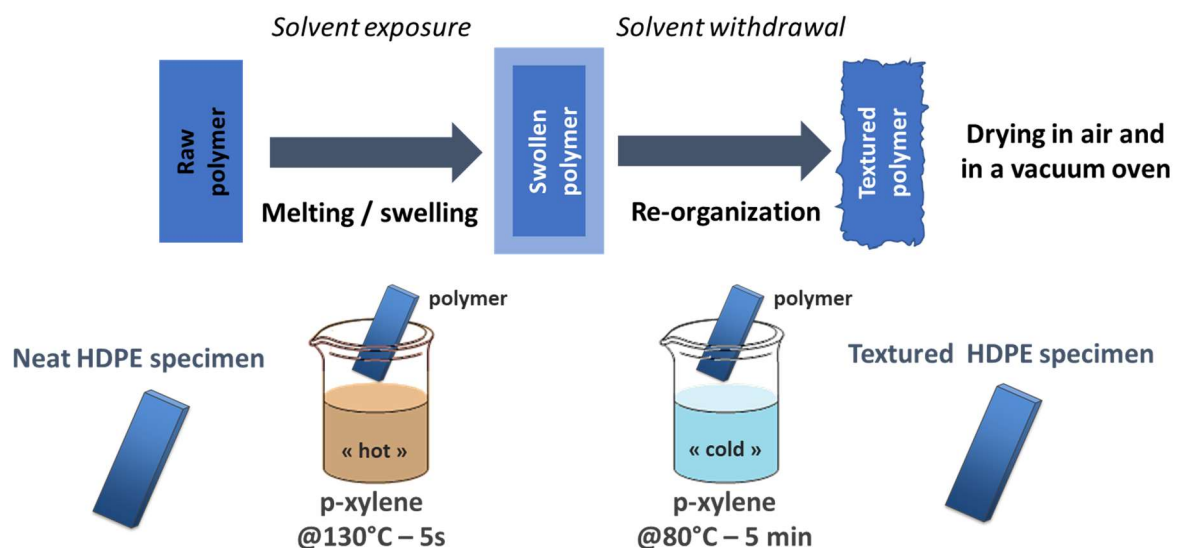


Figure 100 – Scheme of the process of texturing of polyethylene specimens through re-organization using p-xylene.

I.2. Applying the developed process to various polyethylene grades and polypropylene

I.2.a. Influence of HDPE grade

In order to ensure the reproducibility of this optimized process, as well as identifying its limits, various HDPE grades with different viscosities, polydispersities or crystallinity rates, were textured following this same process (BM593, 5502-R3, HD6081 and M6040).

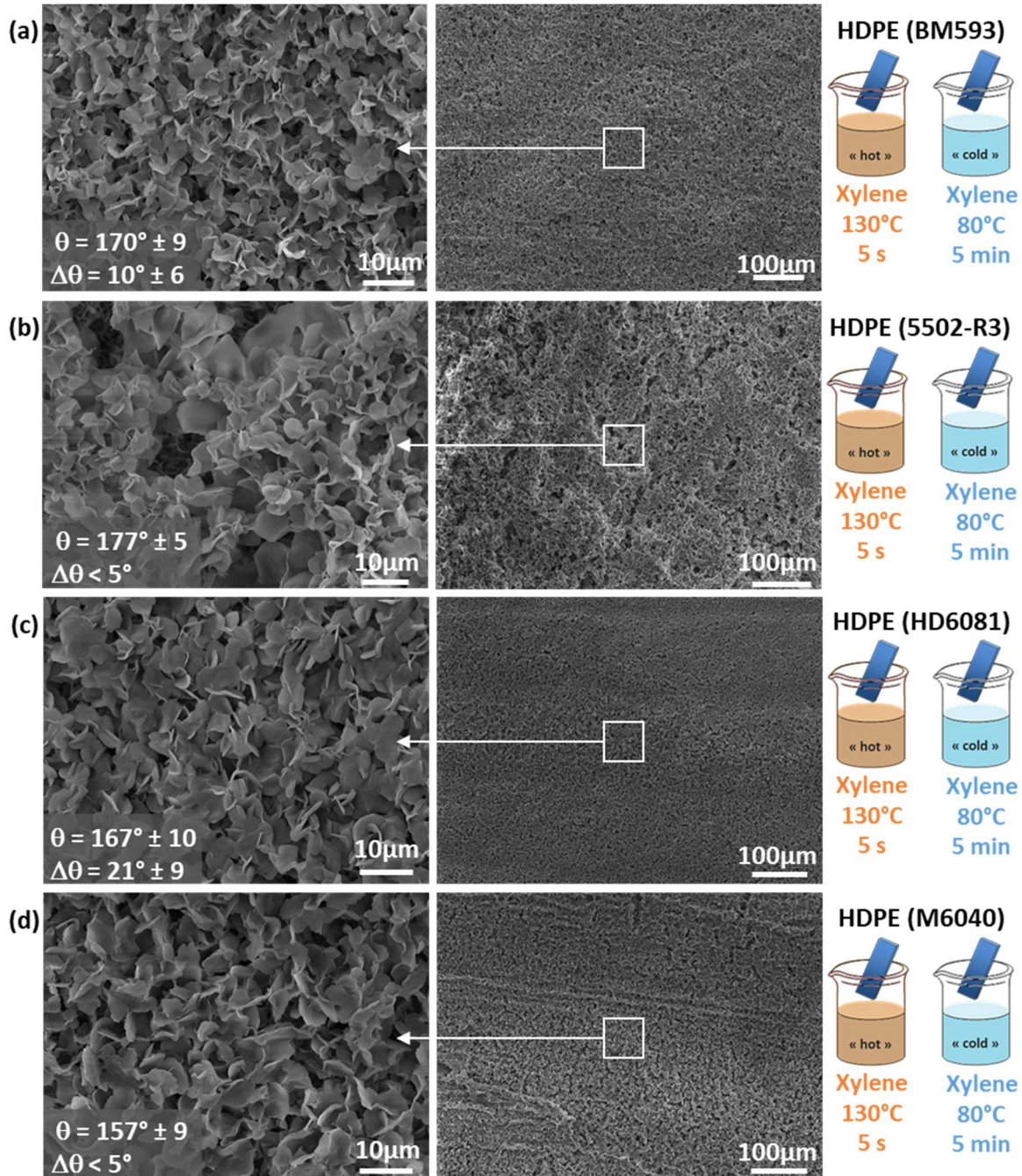


Figure 101 – SEM micrographs of textured films of various HDPE grades obtained by immersion in xylene. Grades are (a) BM593, (b) 5502-R3, (c) HD6081, and (d) M6040.

Figure 101 shows the resulting surface textures for these four HDPE grades, observed by SEM. The first column pictures show similar asperities shape for all grades, *i.e.* flakes of a thickness of less than a micrometer, with few micrometers large, randomly oriented. However, the overall flakes orientation seems to differ from one grade to another. If these texture variations are observed in the overall

samples surface with a good homogeneity, they were retrospectively found to be more process-dependent than grade-dependent. In fact, variations of temperature in the xylene baths, poorly regulated because of oil bath heating, can result in such differences.

From this experience it was thus considered that grades do not influence the resulting surface texture after exposition to the same process. A specific attention must however be kept on the process conditions, especially the solvent temperature.

1.2.b. Impact of the polymer nature: texturing PP

Based on the texturing process optimized for HDPE, PP surfaces were textured following the same procedure. The influence of the nature and/or the temperature of the second bath were investigated: After immersion in xylene at 130°C for 5s, the films were “immersed” in air, acetone, or xylene at 20, 80 or 100°C.

In a similar way as for HDPE, xylene-exposed PP surfaces show a partially smooth skin when not immersed in an 80°C xylene bath. However, compared to HDPE, this smooth skin appears shredded, with spherical stacked asperities. When PP was directly dried in air (Figure 102a) or immersed in acetone at room temperature (Figure 102b), asperities are almost perfectly spherical, and relatively large (from a few to tenth micrometers). These asperities were smaller for films immersed in xylene, at 20°C (Figure 102c) or 80°C (Figure 102d). When the film was immersed in xylene at 100°C (Figure 102e), a neglectable microscale texture could be observed, with a low texturing at a scale of tenth micrometers based on spherical grooves and folds. This second bath temperature appears to be too high to lead to an effective texturing of the surface.

It must be noted that for the surface resulting from the HDPE optimized process, asperities are thinner (a few micrometers large) and less-spherical. They are not randomly stacked, but seem arranged following bead-like chains. Besides the absence of a smooth skin on the surface, the larger scale texturing reveals irregular grooves of about a hundred micrometers.

The texturing process developed for HDPE appears to apply for PP as well. PP is less sensible to a skin formation in a single-bath process than HDPE. The smooth skin obtained with a single solvent immersion is shredded, showing the underlying texture. Moreover, PP displays textures with smaller asperities, from a bead-like stacking, and larger grooves of a few tenth micrometers. The same process conditions are needed for HDPE and PP to obtain a homogeneous texture, with asperities shape differences depending on the nature of the polymer. The PP texture is very similar to the one obtained by Erbil¹ from a diluted solution of PP in xylene, suggesting a common formation mechanism.

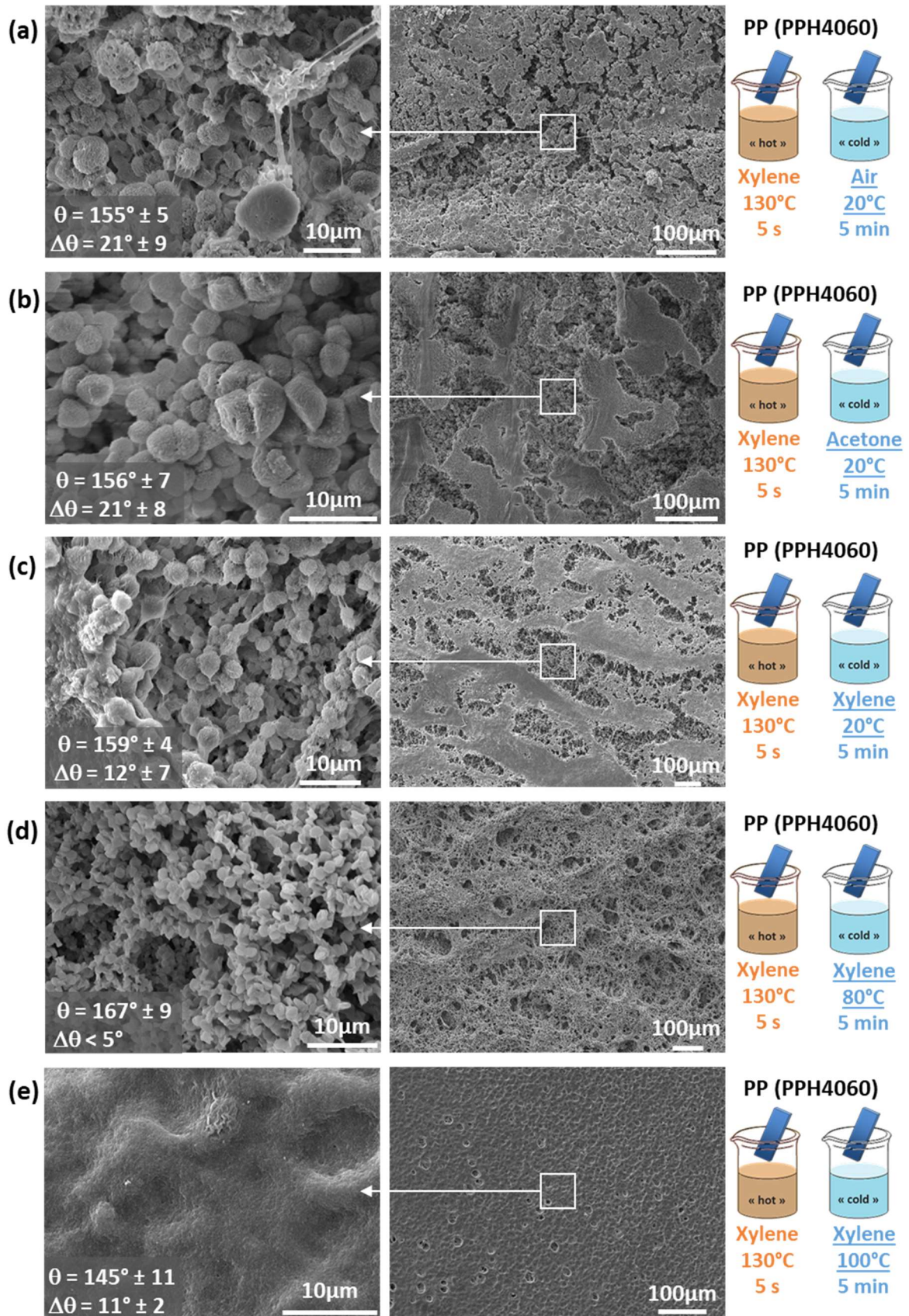


Figure 102 – SEM micrographs of PP (PPH4060) surfaces, textured by immersion in xylene for 5s at 130°C, followed by an “immersion” (a) in air at 20°C, (b) in acetone at 20°C, (c) in xylene at 20°C, (d) in xylene at 80°C, and (e) in xylene at 100°C, for 5 minutes.

I.2.c. Influence of the presence of fillers in HDPE

Because the mechanism responsible for such texturing is supposed to be based on crystallization and precipitation, as suggested by Erbil¹ and Hejazi *et al.*², the influence of the addition of fillers as nucleating agents in HDPE and PP has been investigated. Talc has been dispersed in HDPE (BM593) or PP (PPH4060) (from 2 to 5%_{vol} content), as well as calcium carbonate (3.8%_{vol}, *i.e.* 10%_{wt}). The specimens used for texturing were both massive (tensile test specimens) for HDPE filled with talc, and 300 μ m films for PP with talc and HDPE with calcium carbonate. Each specimen was immersed in xylene at 130°C for 5s, and transferred into a xylene bath at 80°C for 5 minutes.

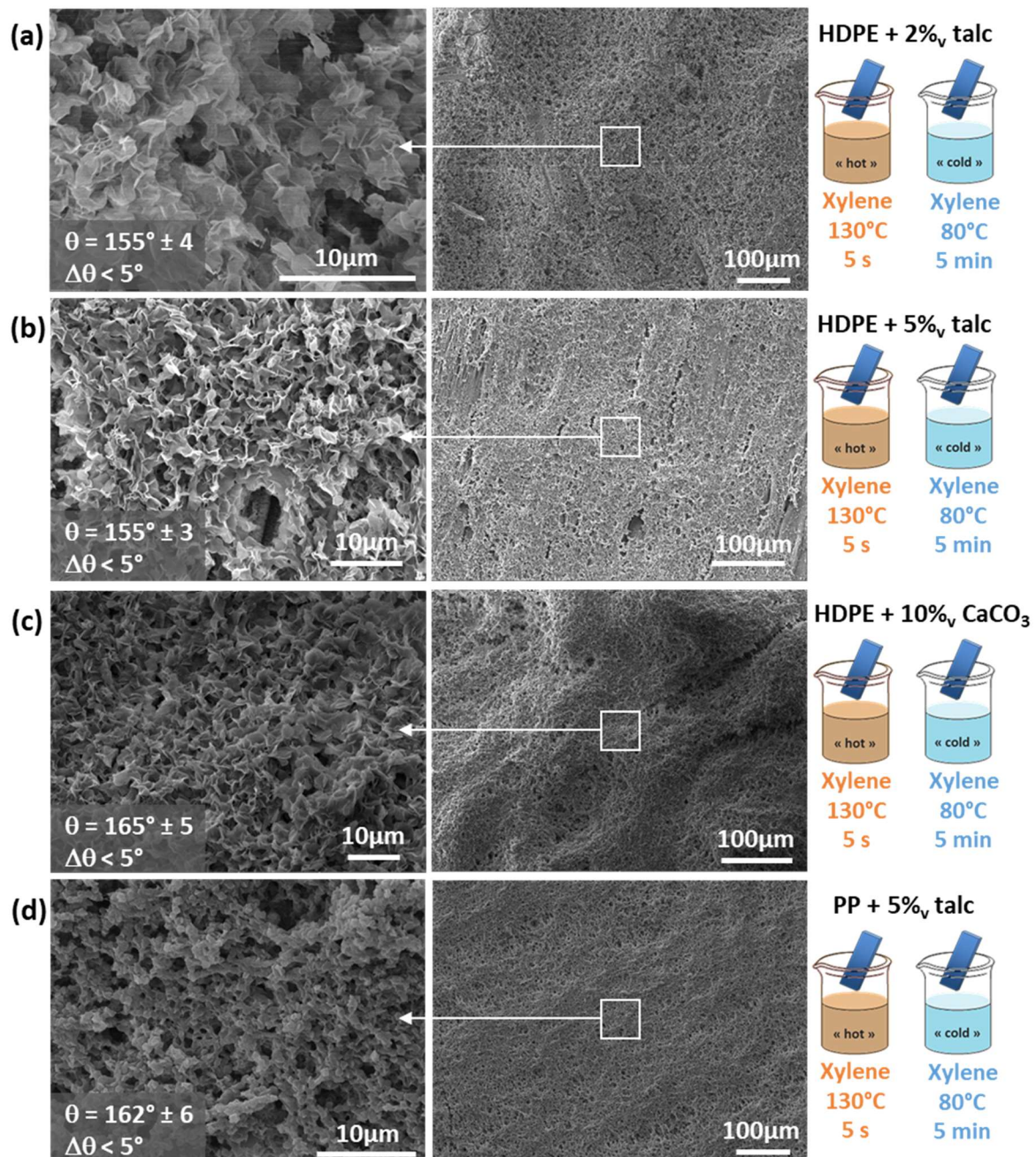


Figure 103 – SEM micrographs of textured HDPE (BM593) and PP (PPH4060) filled by talc or calcium carbonate, after immersion in xylene for 5s at 130°C and 80°C for 5 minutes: (a) BM593 + 2%_{vol} talc, (b) HDPE + 5%_{vol} talc, (c) HDPE + 3.8%_{vol} (10%_{wt}) calcium carbonate, and (d) PP + 5%_{vol} talc.

Based on the comparison between neat (Figure 99c and Figure 101a) and filled HDPE (Figure 103a-c), as well as the comparison between neat (Figure 102d) and filled (Figure 103d) PP, no influence of fillers on the asperities shape for HDPE and PP was found in the studied conditions. The filler nature has no visible effect on the resulting textures, as well as the filler content. Even if a crystallization and precipitation mechanism for texturing is suspected, the obtained texture did not followed the mechanism described by Hejazi *et al.*², as similar asperities shapes are observed with or without fillers.

I.3. Resulting wettability

I.3.a. Wettability predictions

Three of the seventeen samples textured through an immersion in xylene have been selected for their particular morphologies, in order to predict their wettability based on the Cassie-Baxter's interface stability model. The first is HDPE with a low texturing obtained after a colder second bath (#7 in Table 32, Figure 104a). The second one is HDPE with a high texturing, obtained using the optimized process (#5 in Table 32, Figure 104b). The third sample is a PP textured using the optimized process (#15 in Table 32, Figure 104c). These surface morphologies have been previously qualitatively described, but would they be suitable for stable superhydrophobicity?

Table 32 – Summary of the process conditions applied to various materials for their texturing using an immersion in xylene.

#	Material	Process conditions		Reference
		First bath	Second bath	
1	HDPE (HD6081)	Xylene 100°C 90s	None	Figure 97
2		Xylene 130°C 5s	Xylene 80°C 5min	Figure 101c
3	HDPE (5502-R3)	Xylene 130°C 5s	Xylene 80°C 5min	Figure 101b
4	HDPE (M6040)	Xylene 130°C 5s	Xylene 80°C 5min	Figure 101d
5	HDPE (BM593)	Xylene 130°C 5s	Xylene 60°C 5min	Figure 99a
6		Xylene 130°C 10s	Xylene 60°C 5min	Figure 99b
7		Xylene 130°C 5s	Xylene 80°C 5min	Figure 99c
7bis				Figure 101a
8		Xylene 130°C 10s	Xylene 80°C 5min	Figure 99d
9	HDPE (BM593) + 2% _{vol} talc	Xylene 130°C 5s	Xylene 80°C 5min	Figure 103a
10	HDPE (BM593) + 5% _{vol} talc	Xylene 130°C 5s	Xylene 80°C 5min	Figure 103b
11	HDPE (BM593) + 3.8% _{vol} calcium carbonate	Xylene 130°C 5s	Xylene 80°C 5min	Figure 103c
12	PP (PPH4060)	Xylene 130°C 5s	Air 20°C 5min	Figure 102a
13		Xylene 130°C 5s	Acetone 20°C 5min	Figure 102b
14		Xylene 130°C 5s	Xylene 20°C 5min	Figure 102c
15		Xylene 130°C 5s	Xylene 80°C 5min	Figure 102d
16		Xylene 130°C 5s	Xylene 100°C 5min	Figure 102e
17	PP (PPH4060) + 5% _{vol} talc	Xylene 130°C 5s	Xylene 80°C 5min	Figure 103d

For these three textures, morphologies parameters required for the model developed in the second chapter, were measured using image analysis (ImageJ software). Asperities thickness and spacing distance (a and D) were obtained by averaging more than 40 measurements, in order to be the most representative as possible (Figure 104d).

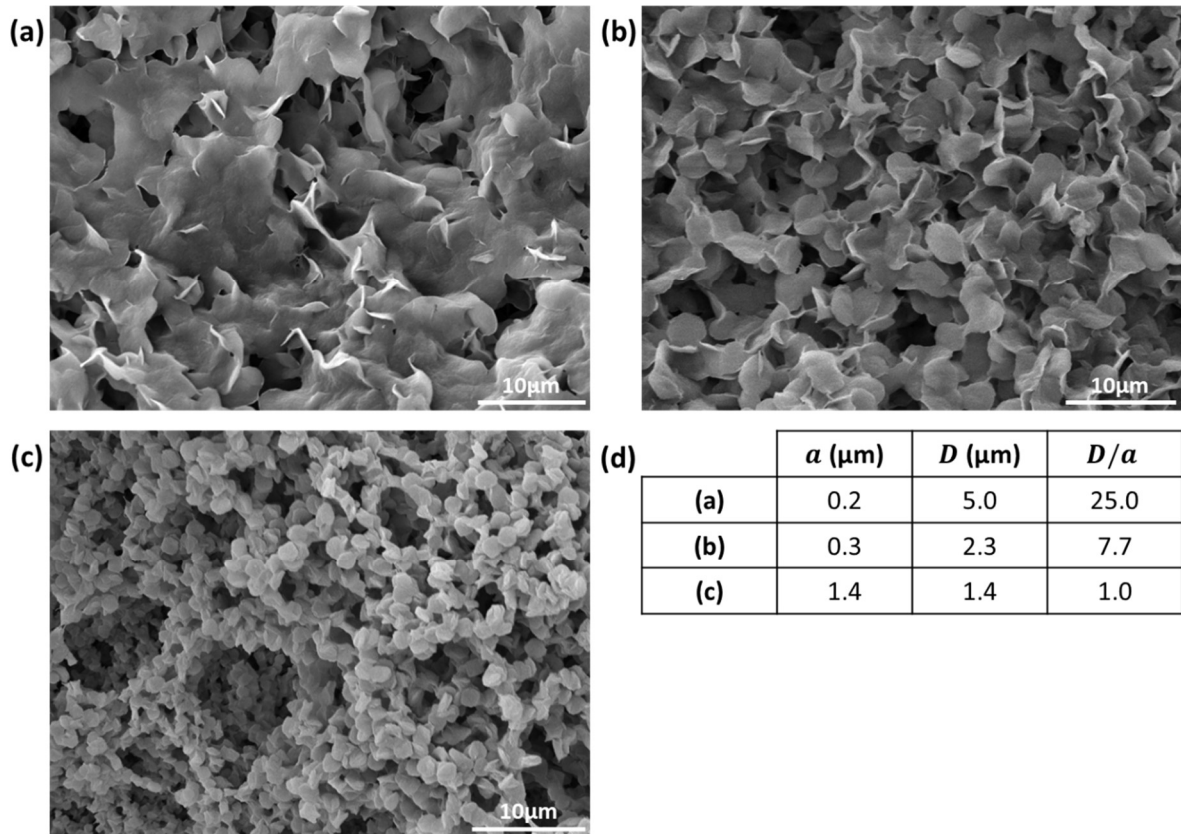


Figure 104 – SEM micrographs of morphologies used for Cassie-Baxter's interface stability model predictions: (a) HDPE (BM563) post-treated with a 60°C xylene bath, (b) HDPE (BM593) texturing using the optimized process, (c) PP (PPH4060) textured using the optimized process, and (d) resulting measured asperities width a , spacing distance D and D/a ratio, obtained using the ImageJ software.

The morphologies obtained from HDPE show similar asperities size, corresponding approximately to the flakes thickness, *i.e.* about 200nm for HDPE with a 60°C cold bath, and 300nm for HDPE with a 80°C cold bath. The difference between these surfaces is the spacing distance of each asperities. For the first one, flakes are continuously linked one from another, leading to large flat parts on the surface. The resulting average spacing distance is close to 5 μm , with larger spacing distances in some zones. By contrast, the second HDPE surface shows well-separated flakes, randomly packed, resulting in an average spacing distance corresponding to the flake width of about 2.3 μm .

For the textured PP surface, asperities are well-defined, with an average width of 1.4 μm . Because of their relatively random stacking, their spacing distance is almost the same as their size (1.4 μm). It must be noted for this sample that higher spacing distance exists at a tenth micrometers scale, which could contribute to increase the air fraction at the interface, without affecting the interface stability.

These three morphologies have a D/a ratio of 25.0, 7.7, and 1.0, respectively. Thus, the model predicts a superhydrophobic behavior for all of them, with a decreasing contact angle but increasing stability from (a) to (c). However, the PP surface could benefit of a multiscale texture to compensate the low air fraction at the smaller scale, resulting in a high contact angle. Moreover, the first HDPE surface has a very low asperities height in comparison to their spacing distance. This could lead to a break of the interface stability, which is already weak with such a large D/a ratio. In fact, the asperities height for HDPE surfaces correspond to the flakes width, and to the asperities size for PP. For surfaces (b) and (c) $H = D$, whereas $H \sim \frac{D}{2}$ for (a), asking questions about the model validity in such conditions.

The application of the Cassie-Baxter's interface stability model to the obtained surfaces is not easy, because of their poorly defined asperities, in comparison to well-defined pillars for example. However,

the study of such morphologies using the model predicts a stable superhydrophobicity for HDPE and PP textured by solvent exposure. A stability advantage for the PP surface is also predictable due to its lower D/a ratio. The PP surface larger texture could counterbalance its low air fraction at the interface, which contribute to an increased water contact angle.

If the model demonstrated its validity on more or less regular surfaces, its predictions on the obtained textured surfaces have now to face experimental results.

I.3.b. Water wettability

The water contact angles of these three considered textured surfaces are respectively 130° , 151° and 167° (Table 33 #5, 7 and 15 respectively), which can be compared to neat HDPE (91°) and PP (113°). The contact angle hysteresis the first surface is 37° , against 8° for neat HDPE. The hysteresis of the second and third samples are beyond 5° and hardly measurable, with the water droplet easily rolling on the surface.

The previously studied surfaces textured under various conditions, as well as their water wettability are summarized in Table 33. These results highlighted that slight process changes lead to minor changes in the surfaces morphologies, but larger effect on the wetting behavior. However, textured PP does not seem to suffer from such process sensitivity. This phenomenon is supposed to be associated to the intrinsically more superhydrophobicity-favorable texture obtained with PP.

Table 33 – Water contact angles and hysteresis of textured surfaces.

#	Material	Process conditions		Wettability	
		First bath	Second bath	θ ($^\circ$)	$\Delta\theta$ ($^\circ$)
1	HDPE (HD6081)	Xylene 100°C 90s	None	1	HDPE (HD6081)
2		Xylene 130°C 5s	Xylene 80°C 5min	167 ± 10	21 ± 9
3	HDPE (5502-R3)	Xylene 130°C 5s	Xylene 80°C 5min	177 ± 5	< 5
4	HDPE (M6040)	Xylene 130°C 5s	Xylene 80°C 5min	157 ± 9	< 5
5	HDPE (BM593)	Xylene 130°C 5s	Xylene 60°C 5min	130 ± 6	37 ± 7
6		Xylene 130°C 10s	Xylene 60°C 5min	133 ± 5	38 ± 10
7		Xylene 130°C 5s	Xylene 80°C 5min	151 ± 9	< 5
7b		Xylene 130°C 5s	Xylene 80°C 5min	170 ± 9	10 ± 6
8		Xylene 130°C 10s	Xylene 80°C 5min	168 ± 11	< 5
9	HDPE (BM593) + 2% _v talc	Xylene 130°C 5s	Xylene 80°C 5min	155 ± 4	< 5
10	HDPE (BM593) + 5% _v talc	Xylene 130°C 5s	Xylene 80°C 5min	155 ± 3	< 5
11	HDPE (BM593) + 3.8% _v calcium carbonate	Xylene 130°C 5s	Xylene 80°C 5min	165 ± 5	< 5
12	PP (PPH4060)	Xylene 130°C 5s	Air 20°C 5min	155 ± 5	21 ± 9
13		Xylene 130°C 5s	Acetone 20°C 5min	156 ± 7	21 ± 8
14		Xylene 130°C 5s	Xylene 20°C 5min	159 ± 4	12 ± 7
15		Xylene 130°C 5s	Xylene 80°C 5min	167 ± 9	< 5
16		Xylene 130°C 5s	Xylene 100°C 5min	145 ± 11	11 ± 2
17	PP (PPH4060) + 5% _v talc	Xylene 130°C 5s	Xylene 80°C 5min	162 ± 6	< 5

I.3.c. Textured surface wetting by low surface tension liquids

If water wettability is an interesting surface characteristic, repelling lower surface tension liquids might also be of interest for an anti-fouling application. Diiodomethane is commonly used as a low surface tension probe for surface wettability characterization (surface tension of 50.88mN/m at 20°C¹⁵, with a strong dispersive surface tension contribution).

On untextured HDPE and PP, diiodomethane have a “philic” behavior, with a contact angle lower than 90°. For HDPE or PP textured using the optimized process, a hybrid Wenzel’s and Cassie-Baxter’s wetting regime is observed (Table 34).

Table 34 – Diiodomethane contact angle and hysteresis for neat and textured HDPE and PP

#	Material	Process conditions		CH ₂ I ₂ wettability	
		First bath	Second bath	θ (°)	$\Delta\theta$ (°)
-	HDPE (BM593)	Neat		46 ± 1	-
7		Xylene 130°C 5s	Xylene 80°C 5min	113 ± 7	49 ± 2
-	PP (PPH4060)	Neat		60 ± 5	-
15		Xylene 130°C 5s	Xylene 80°C 5min	124 ± 6	41 ± 9

Even if textured HDPE and PP lead to different diiodomethane contact angles and hysteresis, their comparison does not permit to distinguish their ability to maintain a stable Cassie-Baxter’s interface. In order to define which surface displays the stronger superhydrophobicity and further, water-ethanol solutions were used as probes. These solutions have lower surface tensions with a strong non-dispersive part. Ethanol has a surface tension of 22.0mN/m at 20°C¹⁴, and solutions of ethanol diluted in water have intermediate surface tensions, depending on the concentration¹⁶. Thus, solutions of ethanol at a concentration of 5, 10, 20, 30, 40 and 50%_{w/v} in water were prepared. Their surface tensions were measured using a Wilhelmy balance with a platinum plate. Figure 105 presents the measured surface tension for these solutions (red), which are in good agreement with the results obtained by Vazquez *et al.*¹⁶ for similar solutions (black). Differences between measured results and the ones obtained by Vazquez *et al.* could be explained by temperature differences and/or liquids purities.

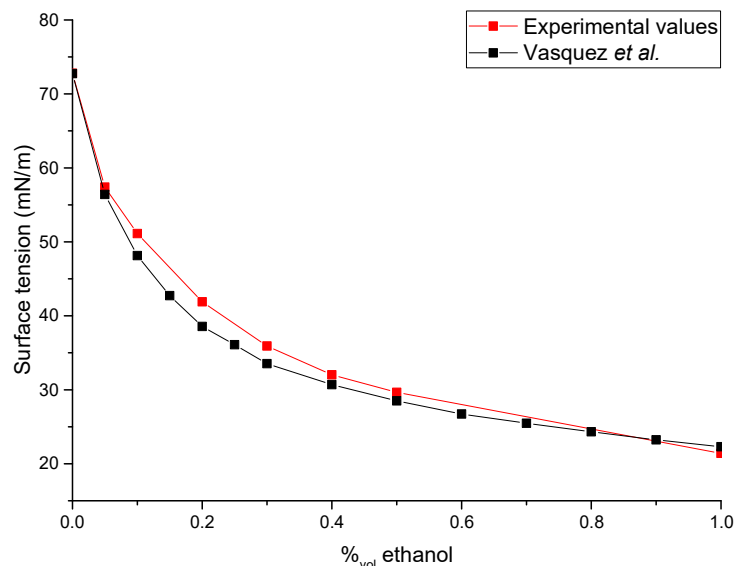


Figure 105 – Surface tension of ethanol in water solutions depending on the ethanol weight fraction. Blue circles are measured surface tension of prepared solutions from 95% pure ethanol and deionized water, and orange triangles are results from Vazquez *et al.*¹⁶.

These solutions were used as liquid probes for untreated and textured HDPE and PP surfaces. Only the four first solutions were finally used as probes as their surface tension values were sufficiently different to evidence different wetting behaviors for textured HDPE and PP, *i.e.* distinguish the more pronounced superhydrophobic surface.

The contact angle and contact angle hysteresis of these probe solutions are plotted versus surface tension for neat and textured HDPE and PP in Figure 106. It can be seen that raw HDPE and PP contact angles values (black and red squares) decrease with decreasing liquid surface tension.

As PP is more hydrophobic than HDPE, the decrease of the contact angle with surface tension is slower than with HDPE. It must be noted that for pure water, contact angles do not strictly correspond to Young's contact angle for water and HDPE or PP. This difference is due to the slight roughness of the considered film surfaces due to their preparation. These films were considered as references, even if they are not perfectly smooth. If neat PP have larger contact angle with probe solutions than HDPE, its hysteresis is also lower, except for pure water.

For textured polymer surfaces, the contact angle does not vary from 72.8mN/m to 51mN/m, and is similar for both polymers. Contact angle hysteresis of textured HDPE and PP varies with the surface tension of liquid probes. Both textured HDPE and PP have a hysteresis lower than 5° for pure water. Only textured PP keeps this neglectable hysteresis with liquids having a surface tension higher than 51mN/m. At the same time, textured HDPE suffers from an increase of its contact angle hysteresis: liquids with a surface tensions of 51mN/m or less get pinned to the surface.

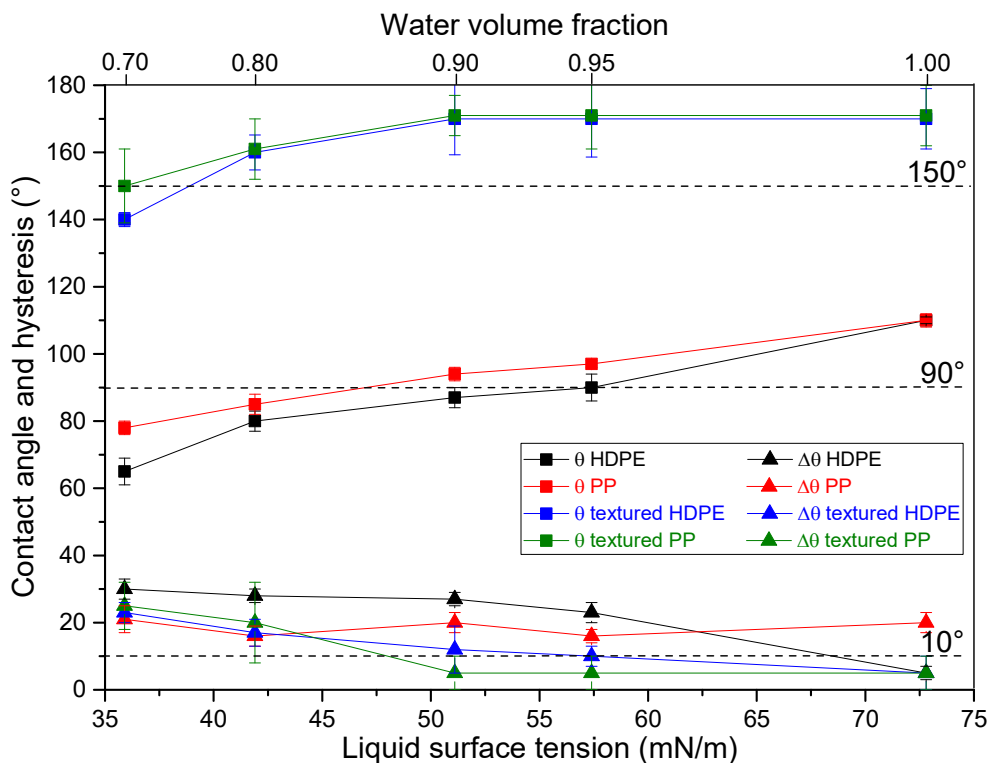


Figure 106 – Contact angle and hysteresis for untreated and textured HDPE (BM593) and PP (PPH4060) surfaces with water/ethanol solutions. Squares are contact angle values, and triangles are hysteresis values. Black, red, blue and green refer to HDPE, PP, textured HDPE, and textured PP, respectively.

From these observations, it seems that textured PP offers a higher Cassie-Baxter's interface stability upon decreasing surface tension than textured HDPE. In fact, it keeps a slippery behavior with liquids with a surface tension larger than 51mN/m (57mN/m for HDPE). However, it must be highlighted that the corresponding contact angle for an untreated surface is always higher for PP than for HDPE.

Hence, it is not established that PP has a morphology more favorable to superhydrophobicity than HDPE. The hypothesis of the asperities tilt angle to the surface being around 90° seems validated, as the Cassie-Baxter's interface starts to sag into a hybrid Wenzel/Cassie-Baxter's interface when the Young's contact angle is close to such a value ($\psi \sim \theta_Y$).

I.4. Conclusion

Using an optimized process based on solvent exposure, stable superhydrophobic textured HDPE and PP surfaces have been obtained. The resulting textured surfaces even keep their slippery behavior with low surface tension liquids, such as water-ethanol solutions. However, liquids with similar overall surface tension have been shown to have different behavior on a similar surface, depending on their dispersive and non-dispersive part. In fact, a droplet of a 10%_{wt} ethanol-water solution ($\gamma = 51\text{mN/m}$) slips on a textured PP surface, whereas a droplet of diiodomethane ($\gamma = 50.88\text{mN/m}$) gets pinned. As HDPE and PP surface energy mainly depend on their non-dispersive contribution, they will be less "phobic" with "non-dispersive liquids" than with "dispersive liquids". The Young's contact angle appears to be a better indication of the behavior of the textured surface. This process and the resulting surfaces are promising. Nevertheless, the xylene toxicity absolutely limits its use in industry, even if all solvent traces are removed at the final step. Thus, a more environmentally and industrially friendly process is required, which need to avoid volatile and toxic solvents.

II. Use of less-toxic solvents for surface texturing

II.1. Solvents selection

As previously discussed, few solvents are good candidates to solubilize HDPE, and these ones always require high temperatures. However, low-toxicity substances can be excellent alternatives to conventional solvents. For example, decahydronaphthalene can be replaced by vegetable oils for ultra-high molecular weight polyethylene (UHMWPE) gel-spinning for the production of high strength resistance fibers¹⁷. As the texturing process takes place at high temperature, alternative substances can be considered. Few solvents have been selected based on their solubility parameters, boiling temperature, toxicity and availability. The Hansen Solubility Parameters in Practice (HSPiP) software, from Hansen, Abbott and Yamamoto¹⁸, was used for such a selection. These solvents are listed in Table 35, from the lower to the higher HSP distance R_a , given by Eq. 1, reflecting the decreasing affinity of two substances. Health hazards codes are listed in the last column (

Table 36 gives the corresponding hazard statements).

$$R_a = \sqrt{4(\delta D_1 - \delta D_2)^2 + (\delta P_1 - \delta P_2)^2 + (\delta H_1 - \delta H_2)^2} \quad \text{Eq. 28}$$

Table 35 – A selection of alternative solvents for HDPE according to their solubility parameters, boiling point, and toxicity.

Substance	Hansen solubility parameters (MPa ^{1/2})				Boiling point (°C)	Health Hazards codes
	δ^D	δ^P	δ^H	R_a		
HDPE (reference)	16.9	0.8	2.8	0.0	-	-
Benzene	17.2	1	2	1.0	80	H304, H315, H319, H340, H350, H372
Xylene	17.8	1	3.1	1.8	140	H332, H312, H315
Dipentene (limonene)	17.2	1.8	4.3	1.9	176	H304, H315, H317
α -pinene	16.9	1.8	1.1	2.0	155	H302, H304, H315, H317
n-butylbenzene	17.4	0.1	1.1	2.1	183	H315, H319
Decahydronaphthalene	17.6	0	0	3.2	190	H304, H314, H318, H331, H332
Dodecane	16	0	0	3.4	215	H304
n-tetracosane (paraffin)	15.9	0.1	0.1	3.4	391	-
Decane	15.7	0	0	3.8	174	H304
Oleic acid (80% olive oil)	16	2.8	6.2	4.3	300	-

Table 36 – Hazard statements with their corresponding code for the selected solvents.

Code	Hazard Statement
H302	Harmful if swallowed
H304	May be fatal if swallowed and enters airways
H314	Causes severe skin burns and eye damage
H315	Causes skin irritation
H317	May cause an allergic skin reaction
H318	Causes serious eye damage
H319	Causes serious eye irritation
H331	Toxic if inhaled
H332	Harmful if inhaled
H340	May cause genetic defects
H350	May cause cancer
H372	Causes damage to organs through prolonged or repeated exposure

Benzene appears to be the best solvent for HDPE, but its high toxicity and low ebullition temperature limit its use in industry, as well as xylene. Dipentene, α -pinene, and linear alkanes such as decane and paraffin wax were considered as alternative solvents thanks to their low HSP distance, high boiling

points and reduced toxicity. Olive oil, composed of 80% of oleic acid and saturated and unsaturated other fatty acids, was also studied based on the Schaller *et al.*¹⁷ study on UHMWPE.

II.2. Processing HDPE and resulting surface textures

For each solvent, the process for texturing HDPE has been adapted due to the different solvency powers. In particular, the immersion time in the first bath has been increased for almost all solvents. In fact, the considered solvents are not as good as xylene for dissolving HDPE. Thus, an increase of the second bath temperature was also investigated, with an immersion at 100°C instead of 80°C. All surfaces were dried at room temperature for at least one hour, and finally dried under vacuum at 60°C overnight.

II.2.a. Dipentene

When dipentene was used instead of xylene, the immersion time was set to 10s against only 5s for xylene, based on the observation of the film creep. The other process parameters were not changed, *i.e.* an immersion temperature of 130°C for the hot bath and 80°C for the cold bath, in which the film was immersed for 5min. The resulting film has a textured surface, very similar to the ones obtained using xylene (Figure 107a), and leading to the same superhydrophobic behavior (Table 37).

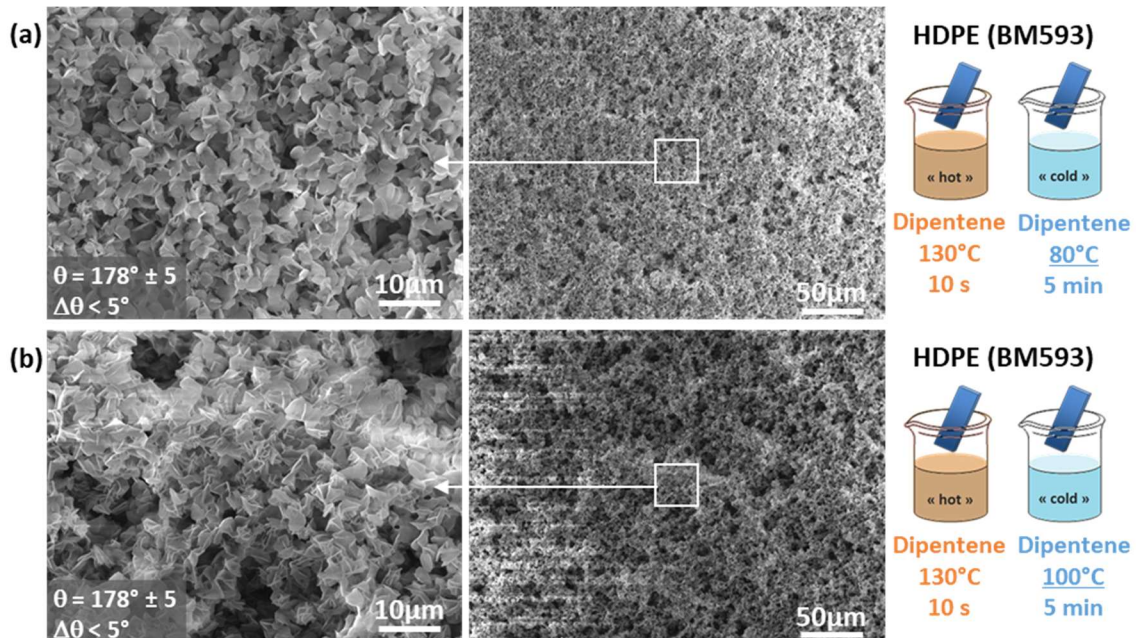


Figure 107 – SEM micrographs of HDPE (BM593) textured through dipentene exposure by a 10s immersion at 130°C, and 5min at (a) 80°C, or (b) 100°C.

With a second bath at 100°C, maintaining the first bath temperature and immersion time, the resulting surface was even more textured with desert-rose-like objects randomly stacked (Figure 107b). The flakes that were already observed are more imbricated. This results in a stronger texturing with a reduced spacing distance between flakes edges, which are far more abundant in this surface.

This second surface is also superhydrophobic, with no observable difference with the first one (Table 37). However, considering the increased flake edges, *i.e.* asperities crests, density leading to a reduced spacing distance, the model predicts a greater critical pressure for such a surface morphology.

For both surfaces, it must be noticed that an additional texture at a higher scale exists. In fact, porosities of less than a tenth micrometers are observed, which might help increasing the air fraction at the interface. As a consequence, the water contact angle for both surfaces increases, without affecting their stability upon pressure, as for xylene-textured surfaces.

II.2.b. α -pinene

Xylene was substituted by α -pinene, which is the solvent the most similar to xylene, with a relatively low boiling temperature and similar solvency power of HDPE. Nevertheless, the immersion time in the first bath had to be increased to 30s, based on the observation of the film transparency and creeping when immersed. The process parameters for the second bath were not changed, *i.e.* immersion in α -pinene at 80°C for 5 minutes.

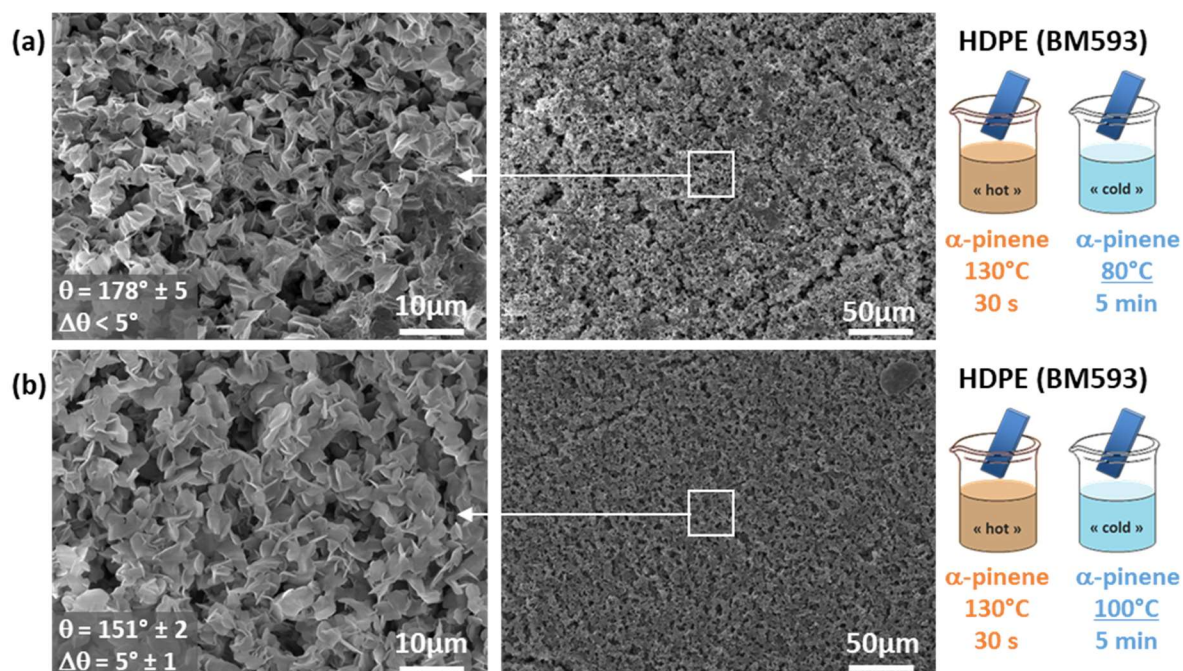


Figure 108 – SEM micrographs of HDPE (BM593) textured through α -pinene exposure by a 30s immersion at 130°C, and then 5min at (a) 80°C, or (b) 100°C.

Interestingly, the surface obtained with these process parameters is very similar to the one obtained with dipentene when the second bath temperature was increased up to 100°C. Desert-rose-like entangled flakes are observed, with a strong texturing and some cracks at a larger scale (Figure 108a). As for the surface textured using dipentene, this surface is superhydrophobic (Table 37). As this surface was only obtained when increasing the second bath temperature with dipentene, the question of the resulting morphology of a HDPE exposed to α -pinene with a hotter second bath is of interest.

Surprisingly, the surface obtained with a 100°C cold bath was similar to the one obtained with the 80°C second bath temperature using xylene or dipentene (Figure 108b). The solvent-assisted HDPE reorganization mechanism with α -pinene seems to be differently influenced by the second bath temperature than with dipentene. With a low texturing and without particular greater scale texture, this surface is still superhydrophobic, but with a relatively low water contact angle, barely higher than 150° (Table 37).

II.2.c. Decane

When decane was used in the texturing process, several adjustments from the xylene-optimized process were required. It appears that when the first bath was heated at 130°C, the swelling process took a very long time. Hence, the temperature of this first bath was increased up to 140°C, with an immersion time of 30s, the HDPE film becomes transparent and starts to creep. The second bath conditions were conserved, *i.e.* 5 minutes immersion in a decane bath at 80°C.

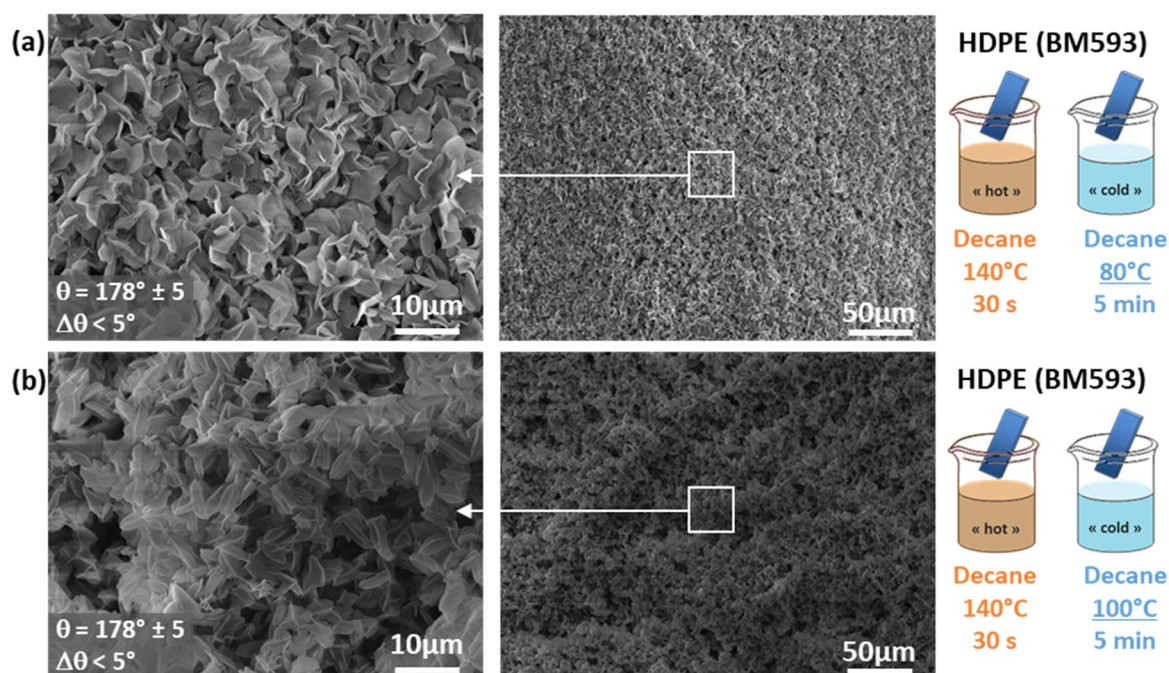


Figure 109 – SEM micrographs of HDPE (BM593) surfaces textured through decane exposure by a 30s immersion at 140°C, and then 5min at (a) 80°C, or (b) 100°C.

The surface resulting from this process is quite similar to the ones previously observed, *i.e.* stacked HDPE flakes. Compared to surfaces obtained after xylene, dipentene, or α -pinene exposure, the flakes seem to be less sharp. Nevertheless, their orientation perpendicular to the surface leads to a strong texturing, with similar spacing distances and edges density than previously described surfaces (Figure 109a). This textured surface is therefore superhydrophobic (Table 37).

As for dipentene, increasing the second bath temperature up to 100°C led to a change in the resulting surface morphology, with imbricated flakes and a hills and valleys larger scale texture (Figure 109b). The resulting surface is superhydrophobic (Table 37), and might have a greater stability upon pressure according to model. Thus, the texturing mechanism thus appears to be similarly influenced by the second bath temperature for dipentene and decane, whereas the temperature has the opposite effect when using α -pinene.

II.2.d. Paraffin wax

Despite its very high boiling temperature, and even high melting temperature (close to 60°C) n-paraffin wax has a theoretically similar solvency power than decane. As a consequence, the process for texturing HDPE should be very similar. That is why relatively high first bath temperatures (135°C and 140°C) were considered, with a 100°C second bath. The first bath immersion time was 5 minutes, as the films did not appear to be transparent or to creep with lower immersion times. When immersed in the second bath, the films turned whitish after a few seconds. As a thick n-paraffin wax layer was still on the surfaces, the films were cut in their length and one half was kept as it was, the other half being washed by immersing it in methylcyclohexane at room temperature overnight.

The rinsed surfaces present a greater texturing, with flakes-like asperities, that are however larger than the ones obtained with the other solvents. In particular, the 135°C treated film has very connected flakes, with asperities spacing distance of a tenth micrometers (Figure 110a). The 140°C treated sample have smaller asperities, but their general organization lead to relatively large smooth areas (Figure 110b). These surfaces are not slippery superhydrophobic, despite having water contact angles larger than 150° (Table 37).

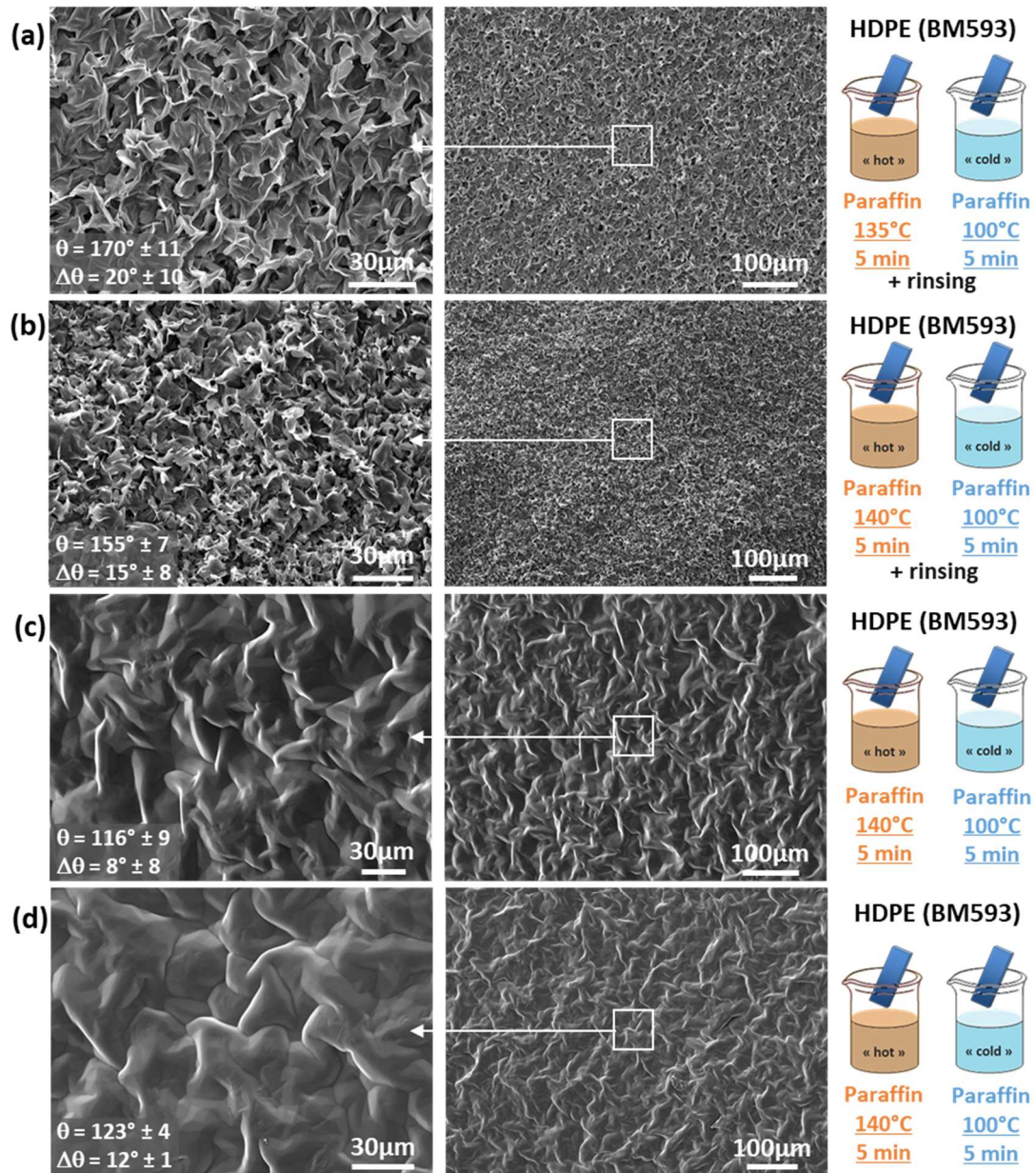


Figure 110 – SEM micrographs of HDPE (BM593) surfaces textured through *n*-paraffin exposure by a 5min immersion at (a, c) 135°C or (b, d) 140°C, and then 5min at 100°C. (a-b) were washed using methylcyclohexane upon drying, whereas (c-d) were kept as obtained after the second bath immersion, with a paraffin wax layer.

Non-washed (Figure 110c-d) surfaces display a *n*-paraffin wax layer on the surface that covers the texture. Non-washed surfaces display a large folded-like morphology, which only lead to hydrophobicity (Table 37).

II.2.e. Olive oil

When trying to substitute xylene by olive oil in the texturing process, several modifications were made. In fact, the conditions that worked with other solvents did not led to a significant texturing of HDPE with olive oil. In a first time, mimicking the “classic” process, the HDPE film was immersed in an olive oil bath at 140°C for 20s. At lower temperatures, it did not become transparent or even creep, but at 140°C and after only 20s, the sample started to creep and had a relatively good transparency. Then, the film was immersed in a second bath of olive oil at 105°C where it turned whitish quasi-instantly.

That is why the second bath immersion time was only 30s. After this treatment, the surface was washed by immersing it in acetone for at least one hour, and dried.

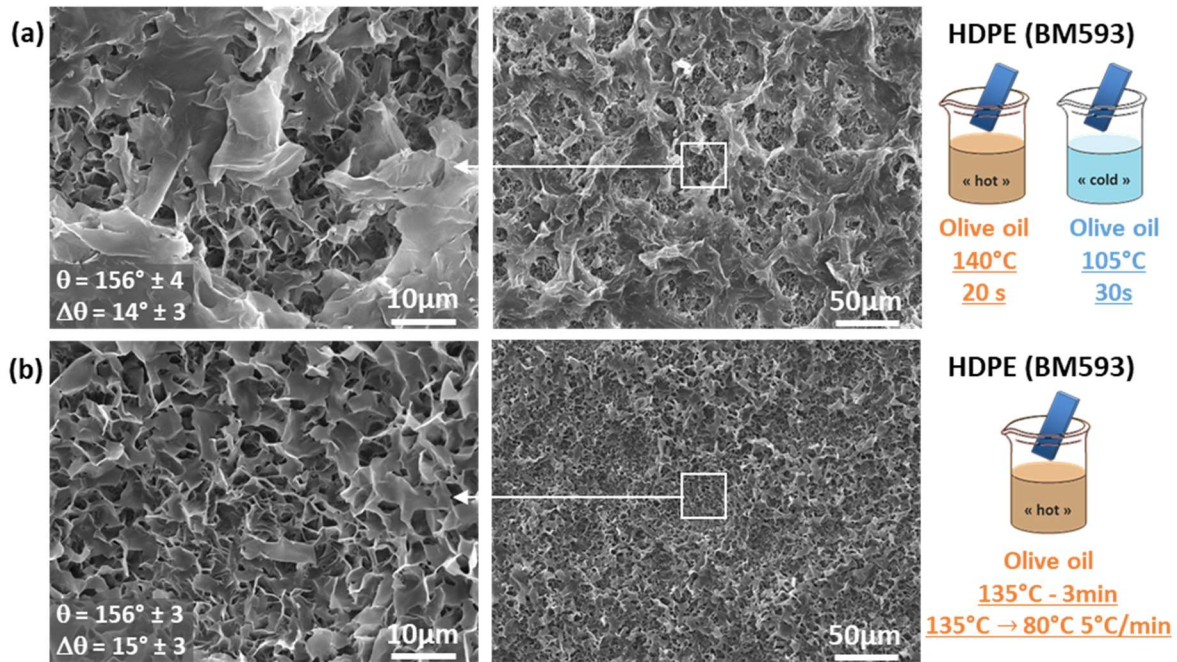


Figure 111 – SEM micrographs of HDPE (BM593) surfaces textured through olive oil exposure by a (a) 20s immersion at 140°C followed by a 30s immersion at 105°C, or (b) 5min immersion at 135°C followed by cooling at 5°C/min in the same bath.

The resulting surface is unusual, with well-connected HDPE flakes randomly oriented partially covered by a smooth film (Figure 111a), in a similar way PP when textured with a 20°C second bath (Figure 102b-c). The smooth skin that partially covers the surface dramatically reduces the fraction of air at the interface, with large smooth areas. As a consequence, a hybrid Wenzel's and Cassie-Baxter's wetting behavior is obtained (Table 37). Unfortunately, a greater second bath temperature did not result in a disappearance of this partially smooth skin, leading to slippery superhydrophobicity.

As the smooth skin formation was attributed to a swelled surface quench, another texturing process was proposed for olive oil and HDPE, based on the very poor solvency power of olive oil on HDPE. In this new process, a HDPE film was immersed in an olive oil bath at 135°C for 5 minutes. In such conditions, the film slowly became transparent. Then, the bath was cooled down ($5\text{K}\cdot\text{min}^{-1}$), without removing the film from the bath. During the olive oil bath cooling, the film turned whitish close to 120-115°C, but the cooling was pursued until the bath temperature reached 80°C.

The resulting surface has large HDPE flakes, mainly oriented in the plane of the surface with only a few edges pointed up. Moreover, at a larger scale, it appears that flakes do not have the same size everywhere on the surface: a crater-like larger scale organization, with smaller flakes in the craters floor, is observed (Figure 111b). The resulting surface is not slippery superhydrophobic, despite the absence of a smooth skin (Table 37). Water droplets get pinned on such a surface despite a contact angle larger than 150°.

No change in the baths temperature, immersion time, or cooling rate in a single-bath process led to a favorable to superhydrophobicity surface morphology.

II.2.f. Summary of the texturing conditions and resulting wettability

For solvents such as dipentene, α -pinene, and decane, the surfaces obtained with any of the two conditions of the adapted process leads to textured surfaces with a morphology similar to the one using xylene. Moreover, all these surfaces are found to be slippery superhydrophobic.

For dipentene and decane, a higher second bath temperature leads to desert rose-like flakes leading to an increased density of asperities and reduced spacing distance. Such surface morphologies are expected to offer a higher interface stability upon pressure, according to the Cassie-Baxter's interface stability model. For HDPE or PP textured using xylene, such high temperature for the second bath were not considered as xylene is still a too good solvent at this temperature.

For α -pinene exposed sample, the opposite effect is observed. Desert rose-like asperities are generated with an 80°C second bath, and classical flakes at 100°C. The understanding of such differences will be the objective of the last part of this chapter.

Table 37- Water contact angle and hysteresis of textured HDPE (BM593) surfaces exposed to various solvents.

Material	Process conditions		Wettability	
	First bath	Second bath	θ (°)	$\Delta\theta$ (°)
HDPE (BM593)	Dipentene 130°C 10s	Dipentene 80°C 5min	178 ± 5	< 5
	Dipentene 130°C 10s	Dipentene 100°C 5min	178 ± 5	< 5
	α -pinene 130°C 30s	α -pinene 80°C 5min	178 ± 5	< 5
	α -pinene 130°C 30s	α -pinene 100°C 5min	151 ± 2	5 ± 1
	Decane 140°C 30s	Decane 80°C 5min	178 ± 5	< 5
	Decane 140°C 30s	Decane 100°C 5min	178 ± 5	< 5
	Paraffin 135°C 5min	Paraffin 100°C 5min + rinsing	170 ± 11	20 ± 10
	Paraffin 140°C 5min	Paraffin 100°C 5min +rinsing	155 ± 7	15 ± 8
	Paraffin 135°C 5min	Paraffin 100°C 5min	116 ± 9	8 ± 8
	Paraffin 140°C 5min	Paraffin 100°C 5min	123 ± 4	12 ± 1
	Olive oil 140°C 20s	Olive oil 105°C 30s	156 ± 4	14 ± 3
		Olive oil 135°C 3min 135°C \rightarrow 80°C 5°C/min	156 ± 3	15 ± 3

For n-paraffin and olive oil, larger morphologies were obtained based on poorly separated flakes, leading to a reduced asperities density and larger spacing distance. N-paraffin exposed samples have water contact angles larger than 150°, but water droplets still get pinned on their surface. In addition, solid paraffin wax needs to be washed from the surface to reveal such a texture.

Olive oil exposed surfaces also display a water contact angle larger than 150°, but are not slippery superhydrophobic. It must be noted that the sample cooled in the olive oil bath resulted in the most homogeneously textured surface. On the opposite, the double-baths treated surface has the smaller asperities under a smooth skin.

It must also be noted that the low volatility of the substituting solvents promotes their use in an industrial context, but are at the same time more difficult to eliminate by evaporation. In fact, if solvent traces remain on the surface, its surface tension might change. As a consequence, superhydrophobicity, which is a combination of surface tension and texturing, could be lost.

For process HDPE superhydrophobic textured surfaces, dipentene, α -pinene and decane are the best alternative solvents. In particular, dipentene is the best choice because of its low toxicity, lowest required exposure time, and good surface morphology generation. Moreover, dipentene is a low-price substance that can be easily biobased.

II.3. Application to PP and resulting surface textures

As the texturing process using xylene, optimized for HDPE, has been found to be successfully applicable to PP, xylene substitution has also been studied with PP. The same solvents were considered, even if PP has different solubility parameters (Table 38). Because of the difficulties encountered with n-paraffin wax with HDPE, this substance has not been considered with PP. As previously reported for HDPE texturing process, some parameters variations of immersion time and temperatures were required for PP texturing.

Table 38 – Comparison of alternative solvents for PP and HDPE according to their solubility parameters and HSP distance.

Substance	Hansen solubility parameters (MPa ^{1/2})			HSP distance (Ra, MPa ^{1/2})	
	δ^D	δ^P	δ^H	With HDPE	With PP
HDPE	16.9	0.8	2.8	0.0	3.0
PP	18.0	0.0	1.0	3.0	0.0
Xylene	17.8	1	3.1	1.8	2.4
Dipentene (limonene)	17.2	1.8	4.3	1.9	4.1
α -pinene	16.9	1.8	1.1	2.0	2.8
n-tetracosane (paraffin)	15.9	0.1	0.1	3.4	4.3
Decane	15.7	0	0	3.8	4.7
Oleic acid (80% olive oil)	16	2.8	6.2	4.3	7.1

II.3.a. Dipentene

PP texturing with dipentene was conducted as for HDPE, *i.e.* an immersion in a 130°C dipentene bath for 10s, followed by an immersion in a dipentene “cold” bath at 80°C or 100°C.

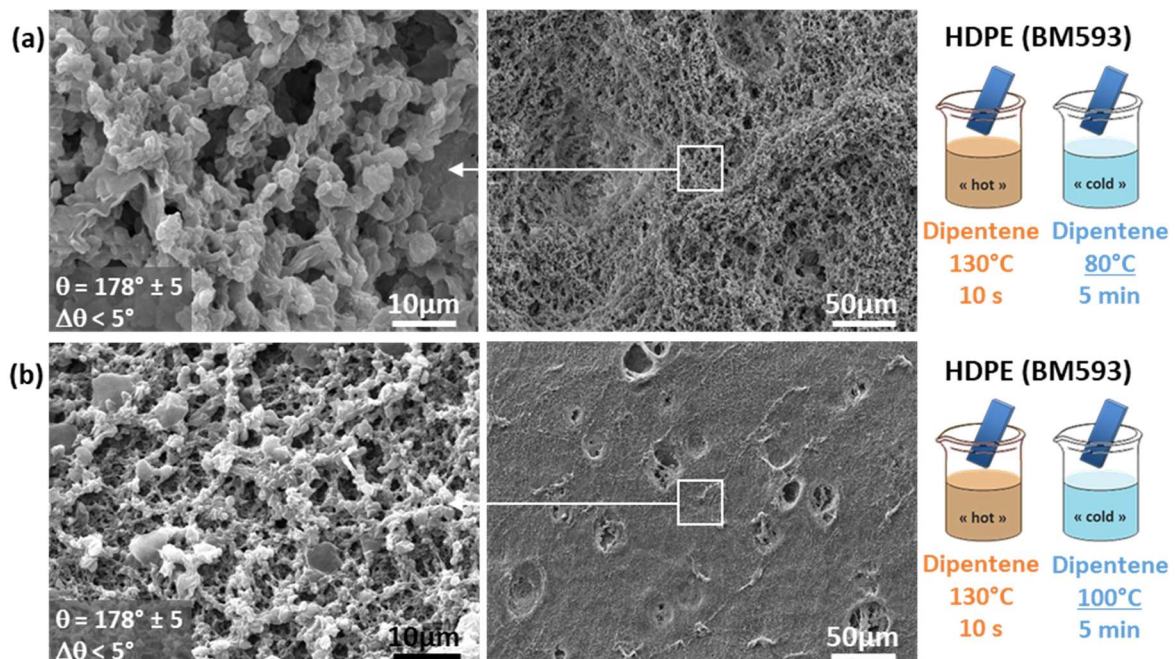


Figure 112 – SEM micrographs of PP (PPH4060) surfaces textured through dipentene exposure by a 10s immersion at 130°C, and then 5min at (a) 80°C, or (b) 100°C.

With the coldest second bath, the resulting surface displays spherical asperities with a bead-like organization, resulting in a multiple scale texturing as for xylene texturing (Figure 112a). However,

asperities appear to have a larger texturing in comparison with the ones obtained with xylene. Still, this textured surface is superhydrophobic (Table 39).

With the 100°C second bath, the resulting surface displays tinier asperities (about 1µm), less separated one from another (Figure 112b). Despite its relatively low large-scale texturing, with only a few large porosities of a few tenth micrometers, this surface is superhydrophobic (Table 39). The smaller asperities size of this second surface is believed to provide it a stronger interface pressure resistance.

II.3.b. α -pinene

When α -pinene was used as the texturing solvent, only 5s at 130°C were required for the PP film to become transparent and to creep, as for xylene. Then, the swelled surface was immersed in a second α -pinene bath at 80°C or 100°C.

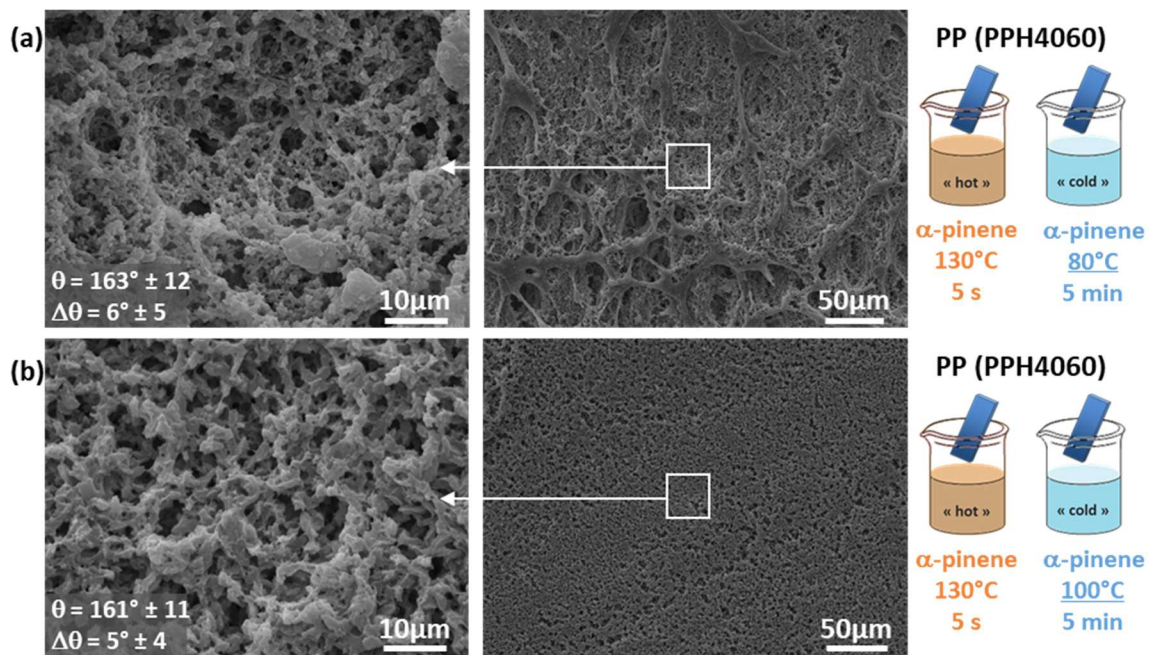


Figure 113 – SEM micrographs of PP (PPH4060) surfaces textured through α -pinene exposure by a 5s immersion at 130°C, and then 5min at (a) 80°C, or (b) 100°C.

The first sample, obtained with the coldest second bath, shows tiny bead-like asperities, as for PP textured using dipentene with a 100°C second bath (Figure 113a). However, it displays some smooth areas that might be responsible for occasional water droplets pinning. Despite this pinning phenomenon, this surface is superhydrophobic (Table 39).

The second sample, obtained with the 100°C second α -pinene bath, show larger asperities than the first one. These asperities are again bead-like objects, more or less randomly stacked. This surface is remarkably homogeneous at a larger scale (Figure 113b). Despite its larger asperities, the lack of smooth areas gives to this surface a superhydrophobic behavior (Table 39). Like for HDPE, the second bath temperature seems to have an opposite effect on the surface morphology depending on the solvent.

II.3.c. Decane

When using decane as the texturing solvent, the PP film swelling was revealed by its transparency and creeping after only 5s at 130°C. This behavior is opposed to the HDPE process in which the temperature had to be risen up to 140°C. The swollen film was then immersed in a second decane bath at 80°C or 100°C for 5 minutes.

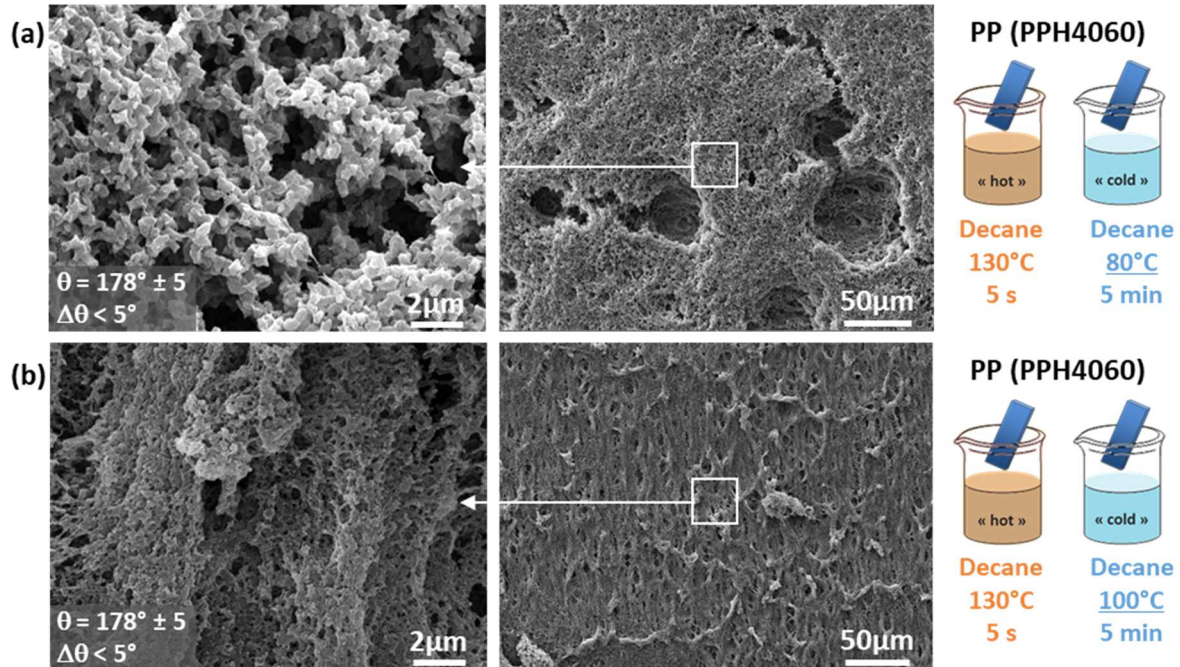


Figure 114 – SEM micrographs of PP (PPH4060) surfaces textured through decane exposure by a 5s immersion at 130°C, and then 5min at (a) 80°C, or (b) 100°C.

The film resulting from the 80°C second bath process displays bead-like asperities with a multiscale texture. Nevertheless, these asperities are very tiny, with an average width of less than 1 μm (Figure 114a). This micro-scale texture is completed by porosities of a few micrometers located between bead packs. A large-scale texture, due to erratically dispersed porosities of a few tenth micrometers, can also be observed. Such textured surface is superhydrophobic (Table 39).

The second surface resulting from the 100°C α -pinene second bath, seems to have a membrane-like morphology with nano-porosities due to very densely packed bead-like asperities. In addition, a larger scale texture due to regular fold-like hills and valleys of a tenth micrometers can also be observed (Figure 114b). This surface, despite its apparent low air fraction at the interface, is slippery superhydrophobic (Table 39). Thanks to its nanotexture, from its tiny porosities, this surface is believed to be very stable upon pressure, according to the Cassie-Baxter's interface stability model predictions.

II.3.d. Olive oil

As for HDPE, texturing PP using olive oil as a solvent required important modifications of the process conditions. Both the immersion time and bath temperature had to be increased in order to be able to get a film transparency, revealing its swelling.

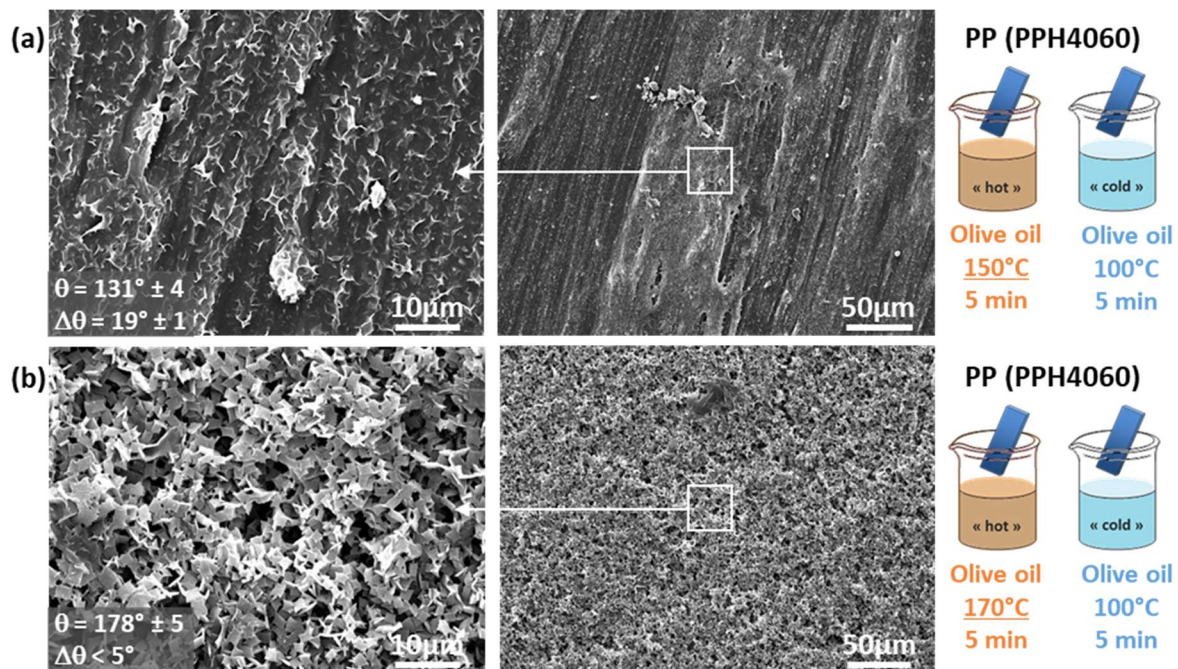


Figure 115 – SEM pictures of PP(PPH4060) textured through olive oil exposure by a 5min immersion at (a) 150°C, or (b) 170°C, and then 5min at 100°C.

A poorly textured PP surface has been obtained after immersing a PP film in olive oil at 150°C for 5 minutes, and then at 100°C for 5 minutes (Figure 115a). This poorly textured surface is only hydrophobic (Table 39).

However, when the first bath temperature was increased up to 170°C for 5 minutes, *i.e.* very close to the PP melting temperature, followed by a 5 minutes immersion in 100°C olive oil, a strongly textured surface is obtained. This surface is composed of squared flakes randomly stacked on the surface, with an average size from 1 to 2 μ m and a thickness of less than 100nm. This surface is pretty similar to the ones obtained with HDPE with good solvents. Nevertheless, its asperities have an almost perfectly squared shape compared to HDPE (Figure 115b). Such a textured surface with a low asperities size and reduced spacing distance is superhydrophobic (Table 39).

II.3.e. Summary of the texturing conditions and resulting wettability

PP have been successfully textured using low toxicity solvents such as dipentene, α -pinene, and decane. Despite a theoretically low solubility of PP with these solvents, PP was effectively textured at relatively low temperatures and with low immersion times. An increase of the second bath temperature from 80 to 100°C resulted in changes of the surfaces morphology. Formation of smaller asperities was observed at higher temperature for dipentene and decane, and the opposite with α -pinene.

All these surfaces were found to be slippery superhydrophobic, even if α -pinene textured samples showed some occasional water droplet pinning. Even olive oil textured PP with an adapted process,

i.e. increased temperature and immersion time, allowed the generation of superhydrophobic surfaces using a totally non-toxic, biobased and inexpensive solvent.

Table 39 – Water contact angle and hysteresis of textured PP (PPH4060) surfaces exposed to various solvents.

Material	Process conditions		Wettability	
	First bath	Second bath	θ (°)	$\Delta\theta$ (°)
PP (PPH4060)	Dipentene 130°C 10s	Dipentene 80°C 5min	178 ± 5	< 5
	Dipentene 130°C 10s	Dipentene 100°C 5min	178 ± 5	< 5
	α -pinene 130°C 5s	α -pinene 80°C 5min	163 ± 12	6 ± 5
	α -pinene 130°C 5s	α -pinene 100°C 5min	161 ± 11	5 ± 4
	Decane 130°C 5s	Decane 80°C 5min	178 ± 5	< 5
	Decane 130°C 5s	Decane 100°C 5min	178 ± 5	< 5
	Olive oil 150°C 5min	Olive oil 100°C 5min	131 ± 4	19 ± 1
	Olive oil 170°C 5min	Olive oil 100°C 5min	178 ± 5	< 5

The solvent nature seems to play a key role in the surface morphology when texturing PP. With the same process, sizes and even shapes differences were observed between dipentene and decane for example. Managing these changes could be a powerful tool to increase a superhydrophobic surface stability upon pressure. Reduced asperities size, as obtained with decane with a high second bath temperature is required. For PP solvent-textured surfaces, the second bath temperature seems to also have an effect on the large-scale texture, with more homogeneous surfaces at high temperature.

Such effects were not observed on HDPE solvent-textured surfaces, whose large-scale texture is almost neglectable compared to PP. Based on the Cassie-Baxter's interface stability model, PP textured surfaces using decane or olive oil as solvents might have a very stable superhydrophobicity upon pressure, thanks to their small texturing scale.

The use of low-volatility solvents is interesting from a toxicity point of view. Nevertheless, their elimination by evaporation is more difficult than for xylene. As a consequence, efficient drying process steps are required, *i.e.* increased drying time, reduced pressure, or higher temperature. When using olive oil as the texturing solvent, a rinsing is always required. Moreover, if the developed texturing process now involve only low-toxicity substances, it remains a batch process that is not very compatible with an industrial scale-up. Thus, there is a need to simply this process by reducing the number and conditions of steps, or turning it to a continuous process.

II.4. Towards simplification for scale-up

II.4.a. One-bath texturing of HDPE films

In order to simplify the texturing process, a single-immersion route has been investigated. Due to the use of alternative solvents with a low volatility, it is supposed that the untextured skin formation of HDPE with xylene can be avoided. Single-bath texturing was investigated on HDPE (BM593) films with dipentene, α -pinene, and decane (Figure 116).

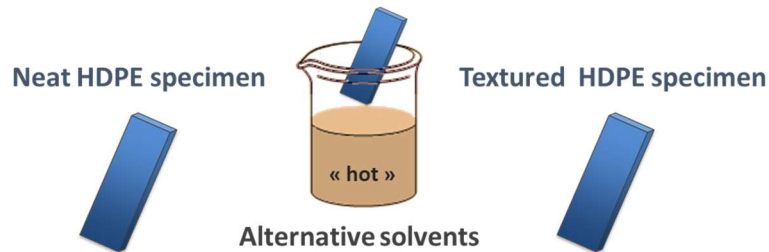


Figure 116 – Scheme of the single-immersion solvent texturing process.

II.4.a.i. Dipentene

When using dipentene, the solvent exposure was identical as for the double-immersion process, *i.e.* dipping the film for 10s in a 130°C bath. After one hour of drying at room temperature, the film became whitish, suggesting a successful texturing process.

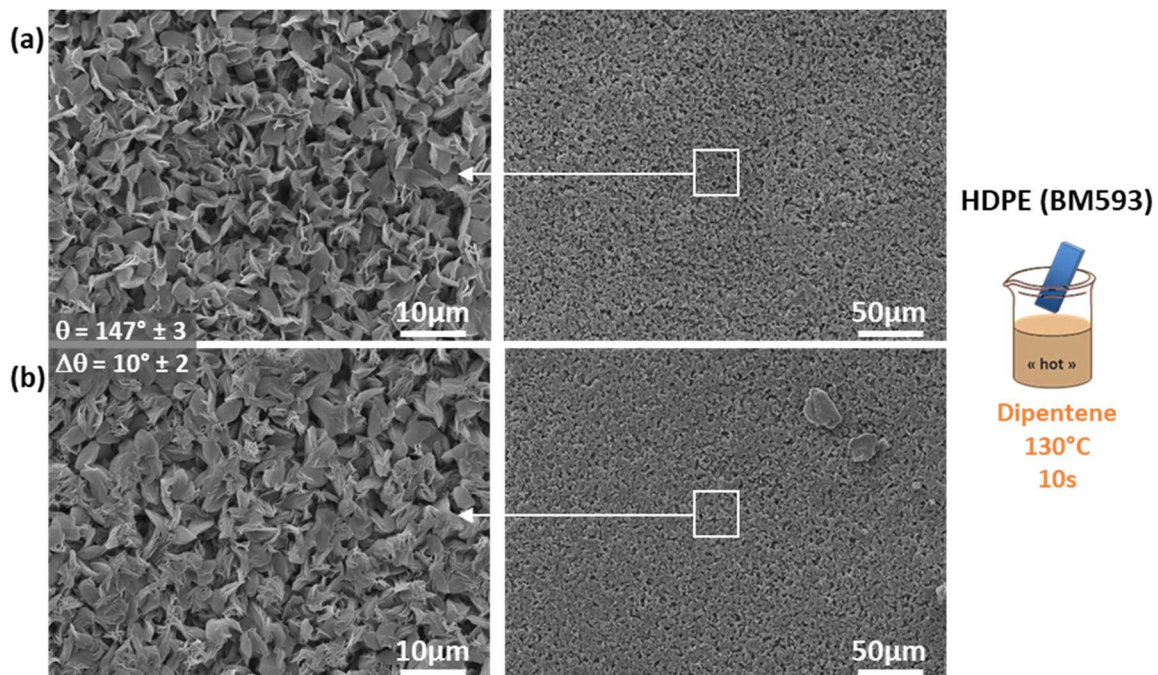


Figure 117 – SEM micrographs of HDPE (BM593) surfaces textured through dipentene exposure of 10s at 130°C with a single immersion followed by a drying in air. (a) and (b) are different parts of the same 5mm large sample.

The surface morphology of the resulting film is similar to the one observed with the complete process involving a double solvent bath. Nevertheless, the polymer flakes appear thicker (Figure 117a). The microscale texture of the surface appears to be very homogeneous, with no observable larger scale texture. However, at the scale of the sample (5mm large square), morphologies disparities are found, with some less-defined and thicker flakes, which could induce a reduced air fraction at the interface (Figure 117b). None of these morphologies seems to be predominant, and no differences gradient was

observed. The main hypothesis is that these variations come from local differences in conditions of solvent evaporation, due to aerobic differences which control solvent evaporation kinetic.

Despite a similar surface morphology, this surface was not shown to be strictly superhydrophobic (Table 40). Water droplets on this surface have difficulties to freely roll. This might be due to the less-favorable morphologies depicted in Figure 117b which offers a low air fraction at its surface.

11.4.a.ii. α -pinene

When α -pinene is used as the texturing solvent in a single immersion process, only a short immersion time seems necessary for the HDPE (BM593) film to turn transparent. After an immersion of only 1s in an α -pinene bath at 130°C, followed by a drying in air at room temperature, the sample turned whitish.

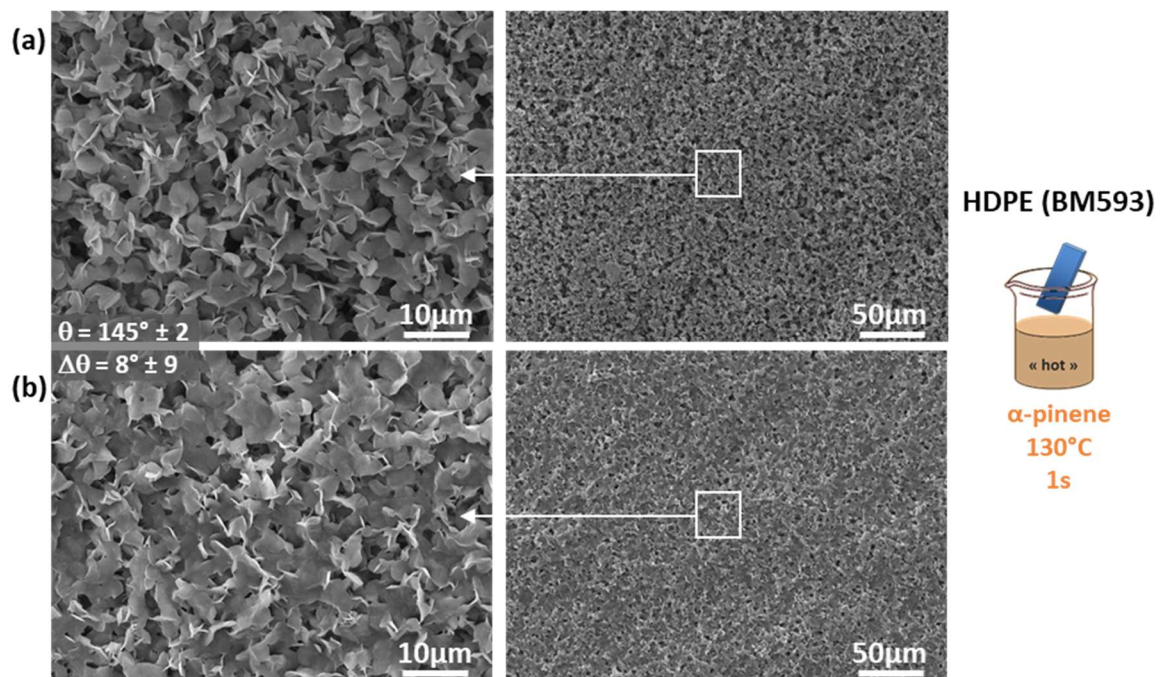


Figure 118 – SEM micrographs of HDPE (BM593) surface textured through α -pinene exposure of 1s at 130°C with a single immersion followed by a drying in air. (a) and (b) are different parts of the same 5mm large square sample.

As for HDPE textured using dipentene in a single bath process, the 5mm large square sample was found to have a heterogeneous surface morphology, despite a homogeneous morphology at a local scale. Again, morphologies changes were not found to follow a particular gradient. This fact reinforces the hypothesis of variation in the solvent evaporation kinetics.

All morphologies are very similar to the ones obtained for HDPE textured using a solvent with a double bath process. The first morphology consists in thin flakes randomly stacked at the surface, forming a superhydrophobicity-favorable texture, with a neglectable larger scale texture (Figure 118a). The second observed morphology evokes HDPE textured with a double-baths process with a cold second bath, *i.e.* poorly-separated flakes globally parallel to the surface (Figure 118b).

The resulting wettability is similar to the one of HDPE textured using dipentene, with a water contact angle below 150° (Table 40). Water droplets get pinned on some points of the surface, and freely roll on other points. This might be due to the heterogeneous surface morphology, with a superhydrophobicity-unfavorable texture affecting the overall surface wettability.

II.4.a.iii. Decane

For texturing HDPE (BM593) film using decane, the same solvent exposure conditions as for the double-bathes process was considered, *i.e.* an immersion in a decane bath at 140°C for 30s. After several minutes in air, the sample slowly turned whitish, revealing a very slow evaporation of decane.

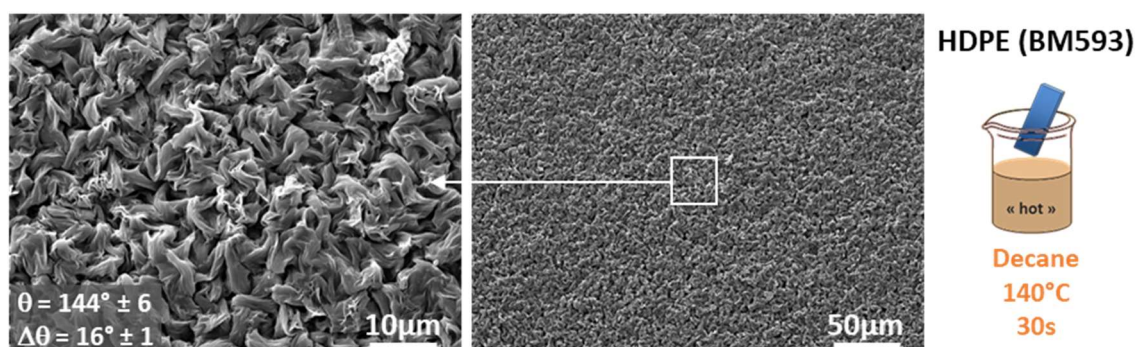


Figure 119 – SEM micrographs of HDPE (BM593) surface textured through decane exposure of 30s at 140°C with a single immersion followed by a drying in air.

After such a single bath process, the surface was found to be homogeneous at the scale of the sample. The resulting unexpected morphology is based on intricated folded objects with numerous circumvolutions and no apparent organization (Figure 119). It is difficult to describe asperities top and grooves of such a surface morphology. Nevertheless, the asperities width is larger than the ones of the previous samples, with a reduced spacing distance. Such a surface is hydrophobic with a water contact angle slightly below 150° (Table 40). Despite such an unexpected morphology, the wettability of this surface is not worse than the one of samples textured using dipentene or α -pinene. In fact, the latter have heterogeneous morphologies, whereas decane-exposed HDPE has a homogeneous morphology that is less favorable to superhydrophobicity.

II.4.a.iv. Summary of the texturing conditions and resulting wettability

When HDPE is textured using alternative solvents such as dipentene, α -pinene or decane in a single-bath process, morphologies similar to the ones obtained with the double-bath process were obtained. However, slight morphological changes were observed that avoided the surface to be superhydrophobic. Moreover, some surface morphology heterogeneities were observed, in particular on surfaces textured using dipentene and α -pinene, which could lead to water droplets pinning.

Table 40 – Water contact angle and hysteresis of textured HDPE surfaces exposed to various solvents in a single-bath process

Material	One-bath process conditions	Wettability	
		θ (°)	$\Delta\theta$ (°)
HDPE (BM593)	Dipentene 130°C 10s	147 ± 3	10 ± 2
	α -pinene 130°C 1s	145 ± 2	8 ± 9
	Decane 140°C 30s	144 ± 6	16 ± 1

Still, the obtained surfaces are almost superhydrophobic, and could probably be turned slippery superhydrophobic with some process adjustments (immersion time, temperature, drying temperature). Moreover, single-bath texturing processes open the way to on-line texturing of film surfaces.

II.4.b. One-bath texturing of PP films

The texturing of PP films with alternative solvents using a single-bath process was done in similar conditions as for the double-baths process. As PP is soluble in these solvents at 110°C, a solvent exposure at such a temperature was also investigated in order to decrease the solvent evaporation rate and consequently change the surface morphology.

II.4.b.i. Dipentene

When dipentene was used as the texturing solvent at 130°C, an immersion of 5s, as for the double-baths process, was sufficient for the film to turn transparent and to start creeping. After this immersion, the film was dried in air at room temperature for at least one hour. During the room temperature drying no whitening was observed after 10 minutes. The film finally turned transparent after drying it completely under vacuum at 60°C overnight.

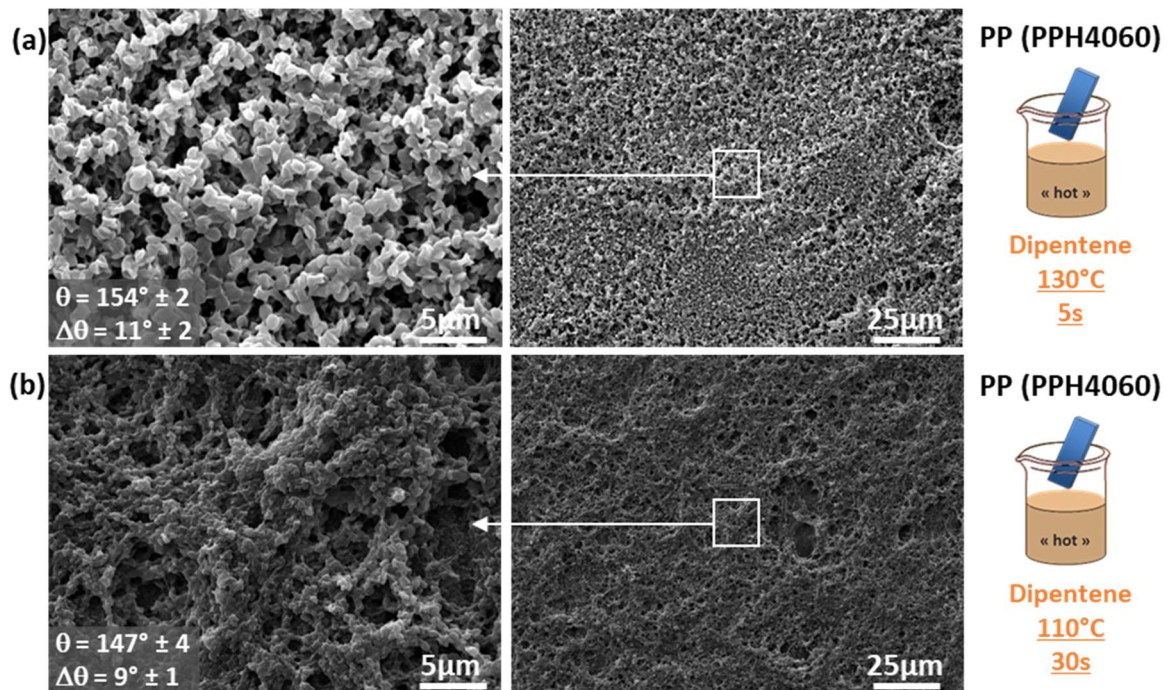


Figure 120 – SEM micrographs of PP (PPH4060) surface textured by a dipentene exposure with a single immersion followed by a drying in air. Conditions are: (a) 5s in dipentene at 130°C, (b) 30s in dipentene at 110°C.

The resulting surface morphology is very similar to the one observed on surfaces obtained with the double-bathes process, based on randomly packed more-or-less spherical asperities. However, an asperities size change is observed at a larger scale, without the usual hills and valleys texture (Figure 120a). This surface is slightly superhydrophobic (Table 41). Water droplets roll on the surface but can occasionally be pinned on some points. This wetting behavior can be attributed to the reduced air fraction at the interface due to the absence of the larger scale texture. Moreover, an unfavorable-to-superhydrophobicity surface morphology could locally be dominant due to large scale heterogeneities.

When the dipentene bath was cooled at 110°C, an immersion of 30s was necessary for the film to turn transparent. Again, no whitening was observed even after 10 minutes drying in air. The completely dried film kept a little transparency, probably because of a reduced textured thickness able to scatter the light. The resulting surface displays tinier asperities poorly dependent ones from others combined with a larger scale texture, consisting in a few micrometer large pores (Figure 120b).

This surface is supposed to be more favorable to superhydrophobicity due to its smaller asperities. Nevertheless, the reduced air fraction at the interface due to the asperities lower independency keep the surface from slippery superhydrophobicity (Table 41).

11.4.b.ii. α -pinene

When trying to texture a PP (PPH4060) film with the single-bath process using α -pinene, the same conditions as with dipentene were used, *i.e.* an immersion at 130°C for 5s or at 110°C for 30s. With the first conditions, the film quickly turned transparent and crept. During the drying in air, a strong whitening was observed after several minutes. The film turned out to be totally white after a full drying under vacuum at 60°C overnight.

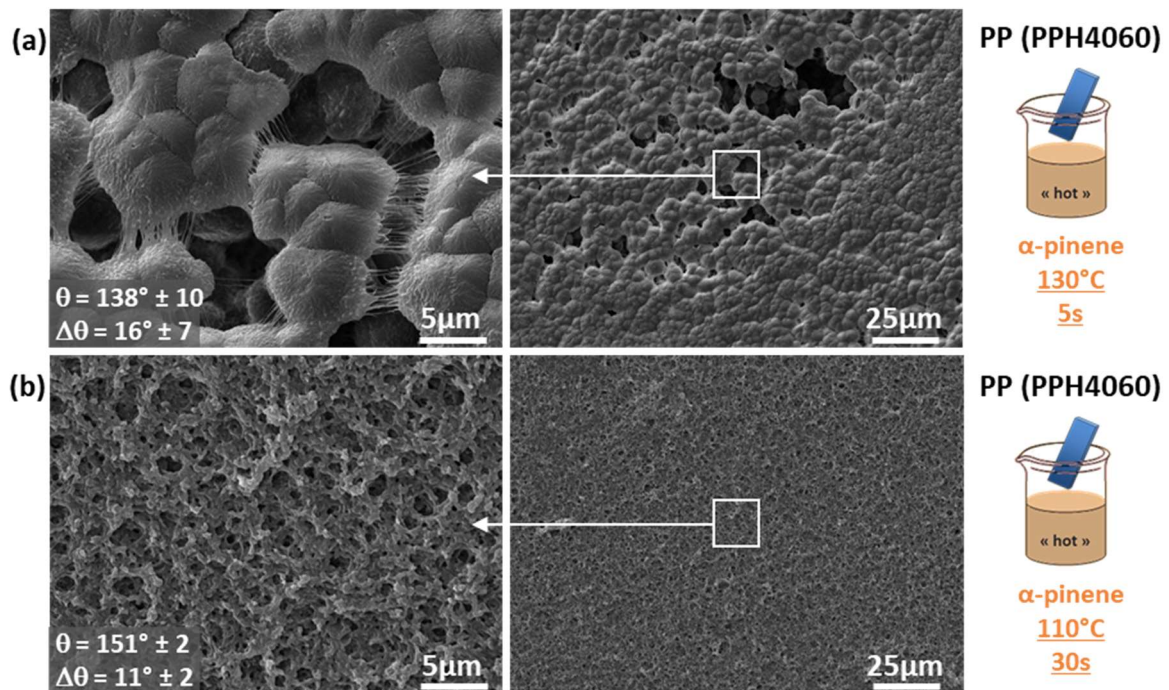


Figure 121 – SEM micrographs of PP (PPH4060) surfaces textured by a α -pinene exposure with a single immersion followed by a drying in air. Conditions are: (a) 5s in α -pinene at 130°C, (b) 30s in α -pinene at 110°C.

The resulting surface is similar to the one observed when xylene-swelled PP surfaces were directly dried in air. Very large spherulitic-like asperities, close ones from the others, with a very limited air fraction and a very large asperities angle to the surface are observed (Figure 121a). As predicted by the Cassie-Baxter's interface stability model guidelines, such a surface morphology does not allow superhydrophobicity (Table 41). However, spherulitic-like objects not linked ones from others are locally displays, offering an interesting surface morphology for superhydrophobicity due to reentrant angles.

When the α -pinene bath was cooled at 110°C, a 30s immersion time was required for the PP film to become transparent and to creep. After this immersion, the film was dried in air at room temperature and started to turn white in some local zones after 10 minutes. Even after a complete drying under vacuum at 60°C, the film remained mainly transparent. Such a phenomenon might be due to a very low textured thickness, leading to a limited visible light scattering. With this lower temperature process, a more common surface morphology was generated, with randomly packed spherical asperities of less than one micrometer (Figure 121b). This surface is not slippery superhydrophobic, despite a water contact angle larger than 150° (Table 41). Such a behavior can be associated to a low air fraction at the interface due to asperities being too close.

II.4.b.iii. Decane

For using decane as the texturing solvent in a single-bath process, some immersion time tuning had to be made. At 130°C, the PP film was dipped in decane for 10s for the film to turn transparent and to creep. After this solvent exposure, the film was dried in air at room temperature, and a whitening was only observable after almost one hour.

The resulting surface morphology consists in randomly packed nearly squared asperities with a relatively large air fraction. The surface also displays important differences of asperities size at a scale of a tenth micrometers (Figure 122a). These fluctuations are again attributed to local changes in the solvent evaporation kinetics. Despite these fluctuations, that could lead to poorer wettability properties with less-favorable morphologies, the surface is found to be superhydrophobic (Table 41).

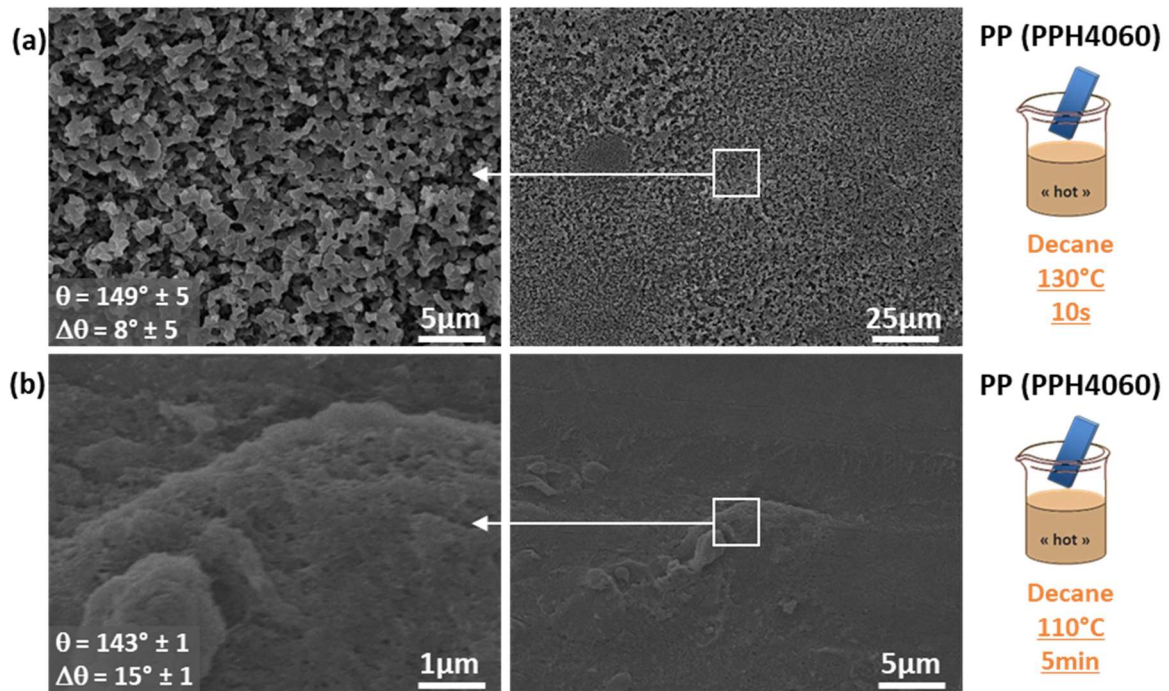


Figure 122 – SEM micrographs of PP (PPH4060) surfaces textured by a decane exposure with a single immersion followed by a drying in air. Conditions are: (a) 10s in decane at 130°C, (b) 5min in decane at 110°C.

When cooling the decane bath down to 110°C, a long exposure time of 5 minutes was required for the PP film to become transparent and start to creep. No whitening was observable after one hour in air. When the surface was completely dried under vacuum at 60°C overnight, it was still almost as transparent as a neat PP film.

From the observation of the resulting surface morphology, the transparency can be attributed to the very low degree of texturing reached. The surface displays tiny pores of less than a few tenths nanometers large and a neglectable larger scale texture (Figure 122b). Thanks to these nanoscale porosities, the film is not completely smooth and displays a water contact angle slightly lower than 150° (Table 41). If the nanoscale porosities density could be increased, such a surface would be slippery superhydrophobic.

II.4.b.iv. Summary of the texturing conditions and resulting wettability

Texturing PP with a solvent exposure in a single-bath process is possible, but leads to morphologies that seem to be less favorable to superhydrophobicity than the double-baths process. The main difference observed between surfaces obtained from single and double-baths processes is a large-scale homogeneity, with surfaces obtained through a single-bath process being more heterogeneous.

This may be due to local difference of the solvent evaporation kinetics. As for the double-baths process, texturing PP using α -pinene leads to morphologies oppositely influenced by the temperature as for other solvents, *i.e.* a lower solvent temperature leads to tinier asperities. This phenomenon is not explained yet and will be discussed in the last part of this chapter.

Table 41 – Water contact angle and hysteresis of textured PP (PPH4060) surfaces exposed to various solvents in a single-bath process

Material	One-bath process conditions	Wettability	
		Water contact angle	Hysteresis
PP (PPH4060)	Dipentene 130°C 5s	154° ± 2	11° ± 2
	Dipentene 110°C 30s	147° ± 4	9° ± 1
	α -pinene 130°C 5s	138° ± 10	16° ± 7
	α -pinene 110°C 30s	151° ± 2	11° ± 2
	Decane 130°C 10s	149° ± 5	8° ± 5
	Decane 110°C 5min	143° ± 1	15° ± 1

Even if the PP surfaces texturing using a single-bath process are not strictly superhydrophobic, most of the surfaces have interesting textures. With large water contact angle values and low hysteresis, these surfaces are close to superhydrophobicity. The single-bath process investigation opens the way for a continuous process with a single solvent bath and a reduced immersion time.

II.4.c. Continuous texturing proof-of-concept

For the continuous texturing proof-of-concept, dipentene has been considered as it is one of the best solvents for both HDPE and PP, thus requiring a limited immersion time to be effective. For this continuous process, a film was rolled around a 1cm diameter tube turning at 40rpm. Such conditions lead to a film speed close to 125cm/min, across a dipentene bath at 130°C. The scheme of the process is depicted in Figure 123a, and the experimental setup is pictured in Figure 123b. The film goes through the hot dipentene bath during nearly one second, before being rolled around itself a few seconds later. Samples were taken from the film prior to rolling (neat film) or in the roll (rolled film), in order to investigate a potential collapse of the texture.

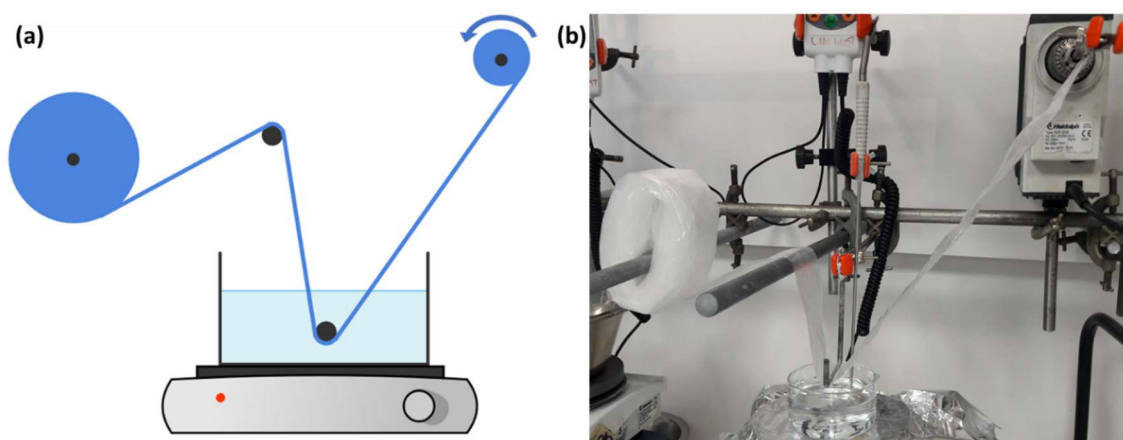


Figure 123 – (a) Scheme and (b) experimental setup of a continuous texturing process of HDPE and PP films through dipentene exposure.

II.4.c.i. Continuous texturing of HDPE films

At first, HDPE (BM593) was textured following the described process, with a film going through a 130°C dipentene bath for 1s. Both the neat and the rolled film surfaces display the usual surface morphology of HDPE films textured using dipentene (Figure 124). More interestingly, the surface homogeneity is found to be better with this continuous process than for the one-bath batch process. This might be due to a lower amount of swelled thickness due to the limited immersion time, or to more homogeneous evaporation kinetics. The rolled film, even if being covered with solvent, is also well textured, indicating that the texturing happened quickly after solvent exposure, during the film travel time from the solution to the roll, *i.e.* in less than 5 seconds.

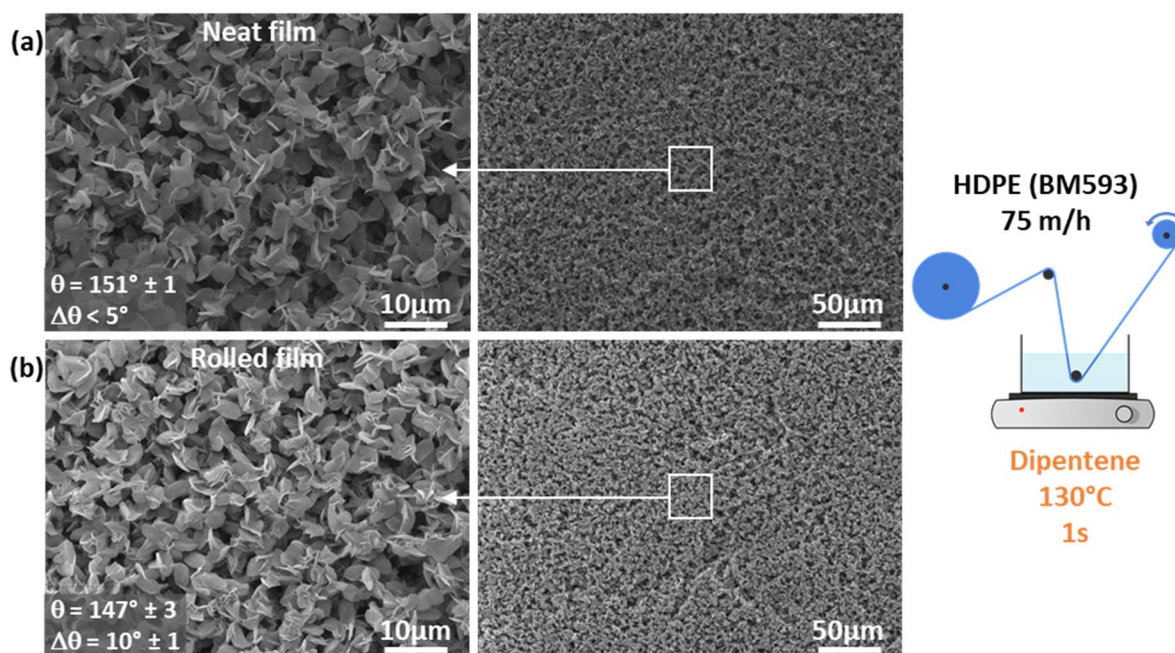


Figure 124 – SEM micrographs of HDPE (BM593) textured by a dipentene exposure in a continuous process: BM593 films gone through a 130°C dipentene bath, where it stayed less than 1s, followed by a drying in air. (a) is the neat film and (b) is the rolled film.

The two surfaces have very similar textures. The rolled film surface has some crushed flakes, probably because of the pressure exerted on the film surface texture by other layers. These two surfaces, despite their similarities, have a slight wettability behavior difference. The neat film is superhydrophobic, whereas the rolled film has a water contact angle slightly lower than 150° (Table 42). This non-superhydrophobic behavior might be due, as early mentioned, to a slight deformation of the flakes due to compression. Control the compression induced by rolling could help overpass this issue.

II.4.c.ii. Polypropylene film continuous texturing

Polypropylene was also textured using this continuous process, with an immersion in dipentene at 130°C for less than one second. As for HDPE, neat textured film and rolled film surfaces were investigated.

Figure 125 shows the resulting surfaces, depicting two areas for the rolled film: apparently undamaged area and a visibly compressed area. The first surface, corresponding to the textured film before rolling, has the usual PP morphology, *i.e.* tiny bead-like asperities of about 1 μm large (Figure 125a). The rolled film displays a relatively different surface morphology based on larger asperities (Figure 125b).

These differences could be explained by a slower texturing mechanism for PP than for HDPE with dipentene. For PP, the texturing might need a time longer than the 5s between the solvent exposure and the film rolling. With the continuous process, the solvent evaporation rate and the film cooling is

modified, leading to the observed changes of the surface morphology. On the visibly damaged area of the rolled, asperities are smaller, but long smooth strings are present at the surface, generating smooth areas (Figure 125c). These smooth strings could be generated by the contact between the swollen polymer and another film layer.

As for HDPE, this issue could be avoided with a pressure-controlled rolling. Moreover, a longer cooling/drying zone between the solvent bath and the roll could promote the neat film surface morphology. The neat sample is found to be superhydrophobic. On the opposite, water droplets get pinned on the rolled surfaces, probably on the collapsed areas (Table 42).

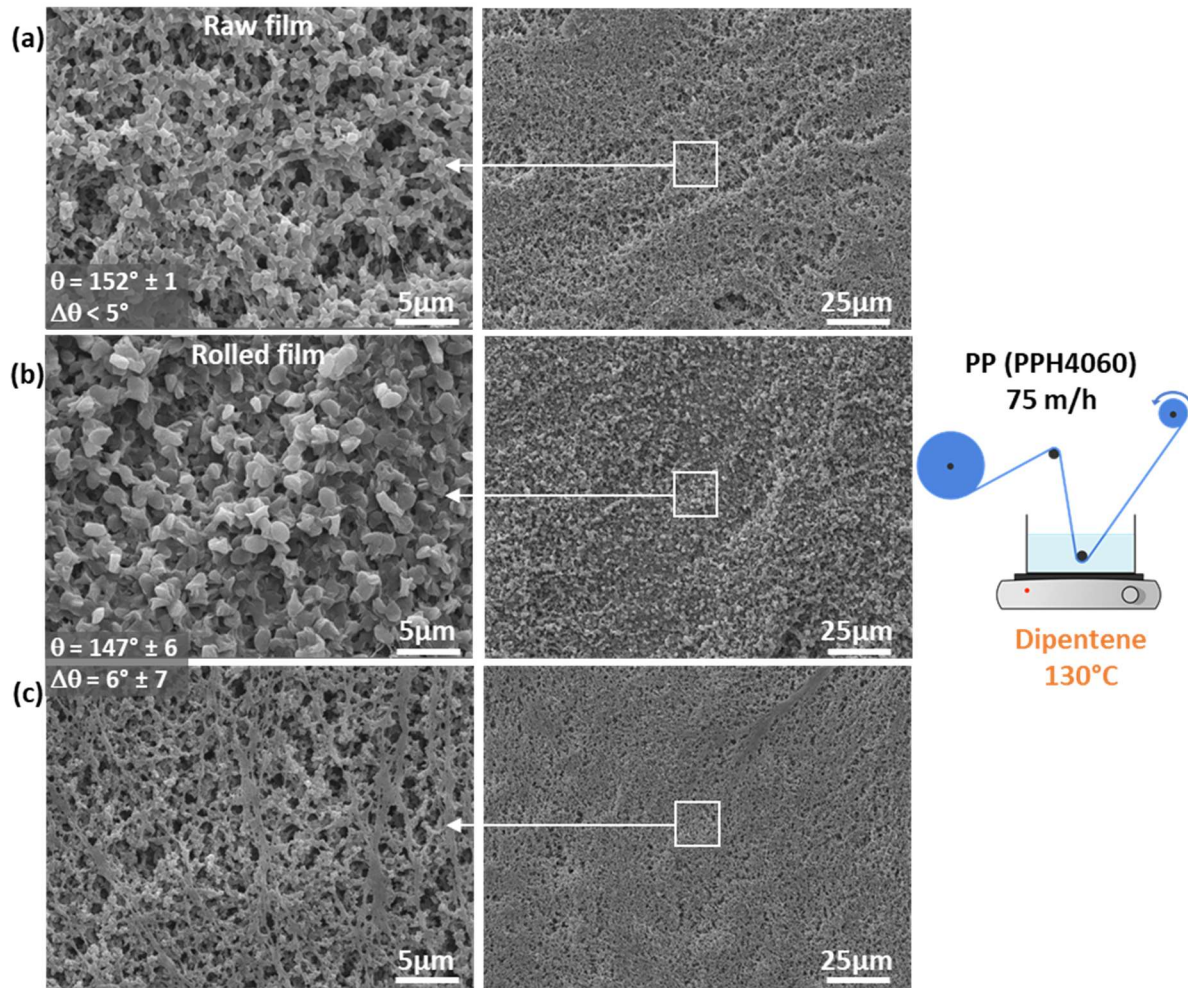


Figure 125 – SEM micrographs of PP (PPH4060) surfaces textured by a dipentene exposure in a continuous process: films gone through a 130°C dipentene bath, where it stayed less than 1s, followed by a drying in air. (a) is the raw film, (b) is the undamaged rolled film and (c) is a visibly crushed area of the rolled film.

Table 42 – Water contact angle and hysteresis of textured HDPE and PP surfaces exposed to various dipentene in a continuous process with a single bath. Highlighted cells are texturing conditions effectively leading to slippery superhydrophobicity.

Material	One-bath process conditions	Wettability	
		θ (°)	$\Delta\theta$ (°)
HDPE (BM593)	Dipentene 130°C 75m/h – Neat film	151 ± 1	< 5
	Dipentene 130°C 75m/h – Crushed film	147 ± 3	10 ± 1
PP (PPH4060)	Dipentene 130°C 75m/h – Neat film	151 ± 1	< 5
	Dipentene 130°C 75m/h – Crushed film	147 ± 2	6 ± 7

II.5. Conclusion

As the texturing process takes place at relatively high temperatures, xylene was found to be relatively easily substituted by less toxic solvents such as dipentene, α -pinene, decane, n-paraffin, or even olive oil. With these solvents, the original process was adapted to generate HDPE and PP surface morphologies favorable to superhydrophobicity. Even olive oil was found to be effective, upon some conditions, to efficiently texture PP to superhydrophobicity.

However, in order to simplify the process for an industrial scale-up, and thanks to the reduced volatility of the considered alternatives solvents, a one-bath process has been developed with the most effective solvents (dipentene, α -pinene, and decane).

The resulting surface morphologies are similar to the ones obtained with the double-baths process, but strict superhydrophobicity was only rarely reached. In fact, heterogeneous morphologies at a few hundred of micrometers scale were obtained.

Still, such a single-bath process development has led to a proof-of-concept of a continuous film texturing allowing superhydrophobicity, using dipentene with HDPE and PP. The remaining issues concern the surface damaging during the rolling of the film, but could be fixed using a rolling system with lower pressure applied on each film layer by the others.

III. Understanding the texturing mechanisms

III.1. Texturing from crystallization/precipitation

III.1.a. Expected mechanisms

As previously mentioned, Hejazi *et al.*² obtained superhydrophobic surfaces by precipitating polypropylene from a *p*-xylene solution, with or without zinc oxide nanoparticles. Based on the resulting surfaces and the understanding of the precipitation mechanism of these polymer/solvent solutions, they proposed two texturing mechanisms based on phase separation and precipitation (Figure 126). They investigated diluted solutions of polymer in solvent with only 1.8%_wt of PP in *p*-xylene, and with or without 1.1%_wt of ZnO nanoparticles.

They supposed that when decreasing the temperature, a phase separation occurred in the solution, with the formation of a polymer-rich and a polymer-poor phases. When ZnO nanoparticles are in the solution, they might act as nuclei in a nucleation and growth precipitation mechanism, leading to PP spheres in the polymer-rich phase (Figure 126a). The reduced size of the obtained PP spheres (about 1 μ m) is attributed to a very high nucleation rate because of ZnO nanoparticles. In addition, a relatively low mobility of the PP chains due to a high molecular weight could limit the spheres growth.

Without ZnO nanoparticles, the precipitation is believed to come from a spinodal decomposition, with a co-continuous organization (Figure 126b). Then, in the polymer-poor phase, polymer chains would concentrate, forming nanospheres that are deposited on the surface during the solvent evaporation. The authors claimed that such mechanisms could also be observed with others semicrystalline polymer using a similar process.

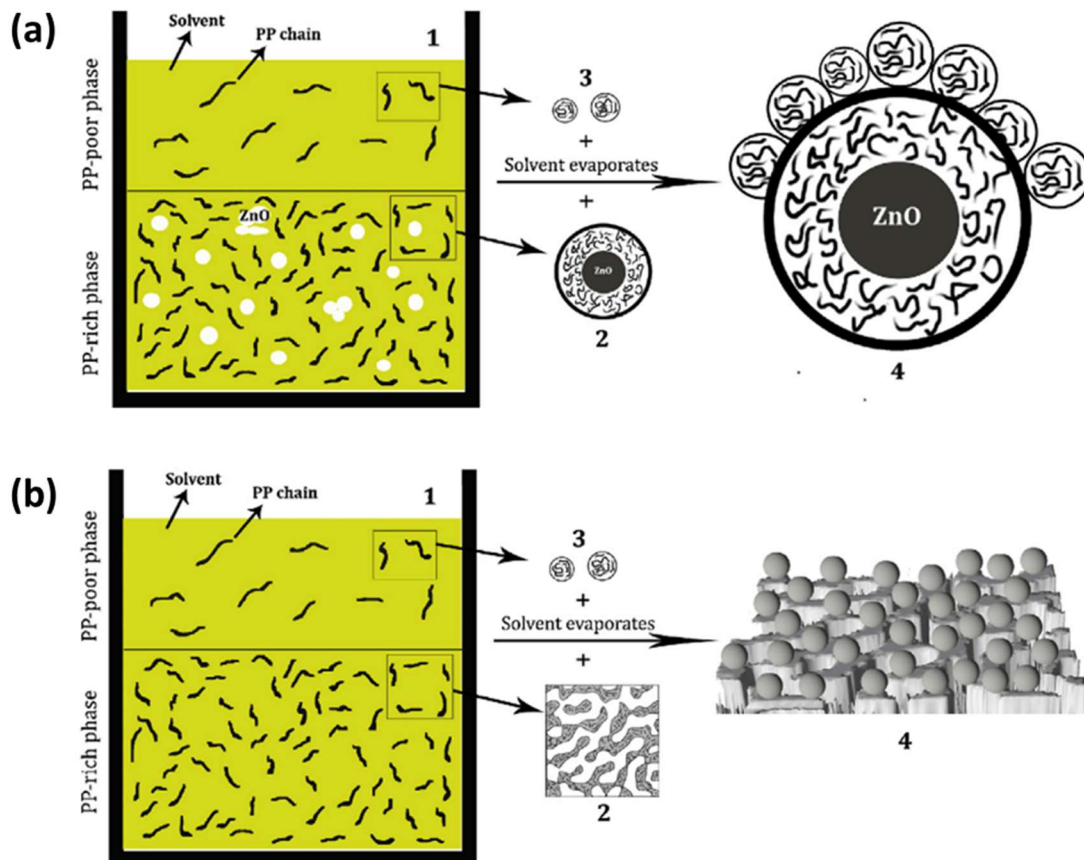


Figure 126 – Texturing mechanism from a solution of polypropylene proposed by Hejazi *et al.*². Copyright 2014 Elsevier.

The phase diagrams of polyethylene and polypropylene with *m*-xylene obtained by Mizerovskii *et al.*^{19,20} (Figure 127) show different lines and regions, corresponding to different equilibria. The region I corresponds to a homogeneous polymer/solvent solution, with the particularity of being solvent-in-polymer for temperatures above the BC line, and polymer-in-solvent above the AB line. However, above the AB line, due to the dissolving kinetic of the polymer in the solvent, a two-phase system can exist with a solvent-in-polymer phase with excess solvent aside. After a given time, the polymer is solubilized by the solvent, and a single phase is obtained. The region II characterizes a semicrystalline polymer whose amorphous regions are swollen by the solvent. The system is homogeneous at macro-scale, and heterogeneous at micro-scale with stable crystalline parts. The III region corresponds to a two-phase polymer/solvent system. When comparing these phase diagrams to the temperatures involved in the texturing process developed in the present chapter, the following system transformations can be supposed:

- 1- During the solvent exposure, *i.e.* dipping the polymer in solvent at 130°C (403K), the polymer is swollen by the solvent, and the system is above the BC line. It is supposed that the polymer concentration in the swollen area is larger than the concentration of the B point, because of the very limited exposure time. The solvent cannot penetrate in the polymer above this critical solubility value in such a short time. At the same time, the polymer concentration cannot be larger than the concentration needed to melt at this precise temperature. Thus, for HDPE the polymer weight fraction is from 25 to 80% at that time, whereas for PP it is from 20 to 40%, approximatively.
- 2- Then, the sample is immersed in a colder solvent bath (80°C, 353K). At this temperature, the solvent is no longer miscible in the polymer and precipitation occurs. The higher the temperature of this second bath, the more probable the system moves in the II regions of the phase diagrams. In such conditions, amorphous regions of the polymer are kept swollen, which offers more time to the polymer to reorganize, preventing its “quenching”.

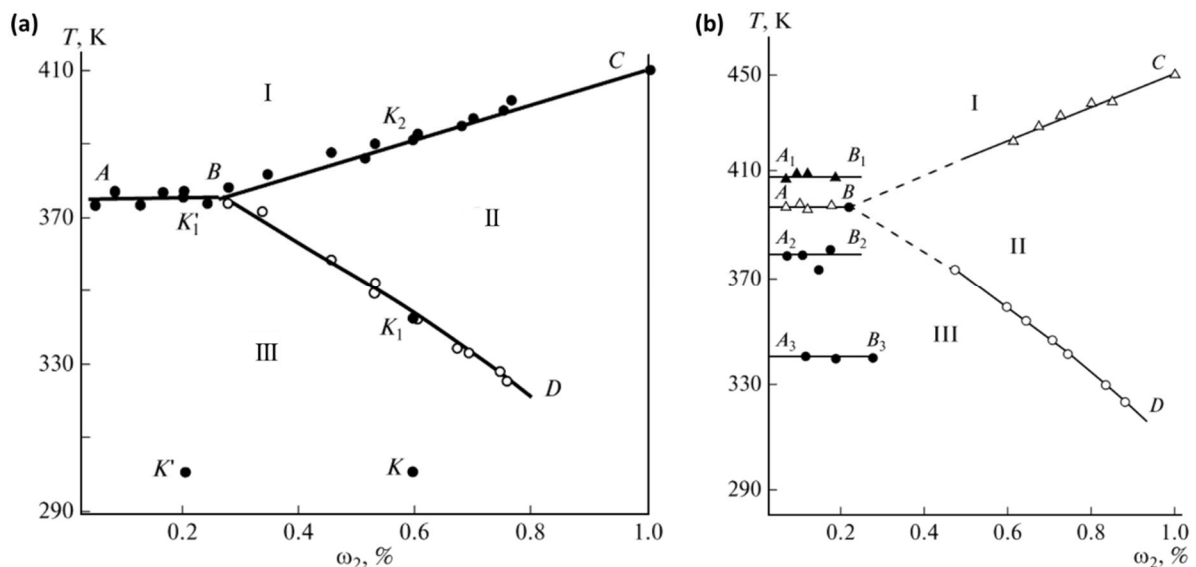


Figure 127 – Phase diagrams of (a) high density polyethylene and (b) isotactic polypropylene with *m*-xylene (the polymer weight fraction in abscissa). The I, II and III phases correspond to a homogeneous polymer/solvent solution, a semicrystalline polymer with solvent-swelled amorphous regions, and a two-phase amorphous system, respectively. Reprinted from Mizerovskii *et al.*^{19,20}. Copyright 2015 and 2013 Pleiades Publishing Ltd.

However, this simple observation of the phase diagrams cannot give an indication on the phase separation mechanism: spinodal decomposition or nucleation and growth, as well as how the crystallization impacts the final structure? Does the crystallization generates or freezes a growing morphology?

III.1.b. Investigating the solvent-assisted crystallization of HDPE and PP

In order to distinguish the role of the polymer crystallization on the texturing mechanism, HDPE and PP thin films have been exposed to xylene at high temperature before being cooled at $5\text{K}\cdot\text{min}^{-1}$ under polarized light microscopy. This experiment does not mean to exactly mimic the texturing process as a low volume of solvent is used and a fast evaporation due to the temperature occurs (Figure 128).

For HDPE (BM593, Figure 128a), the film is turned fully amorphous when adding one droplet of xylene at 130°C . After cooling the sample ($5\text{K}\cdot\text{min}^{-1}$), while xylene evaporated concomitantly, the film crystallinity seems to be increased, with a higher transmitted light intensity. Moreover, larger crystalline objects with larger aspect ratios are observed. Their sizes from 1 to 3 micrometers correspond to the size of the flakes observed with xylene-textured HDPE. When repeating the same experiment with PP (PPH4060, Figure 128b), spherulites are melted when a xylene droplet was deposited on the film at 130°C . After solvent evaporation while the film was cooled ($5\text{K}\cdot\text{min}^{-1}$), very small crystalline objects are generated. They have a very limited aspect ratio, and a size close to one micrometer is measured.

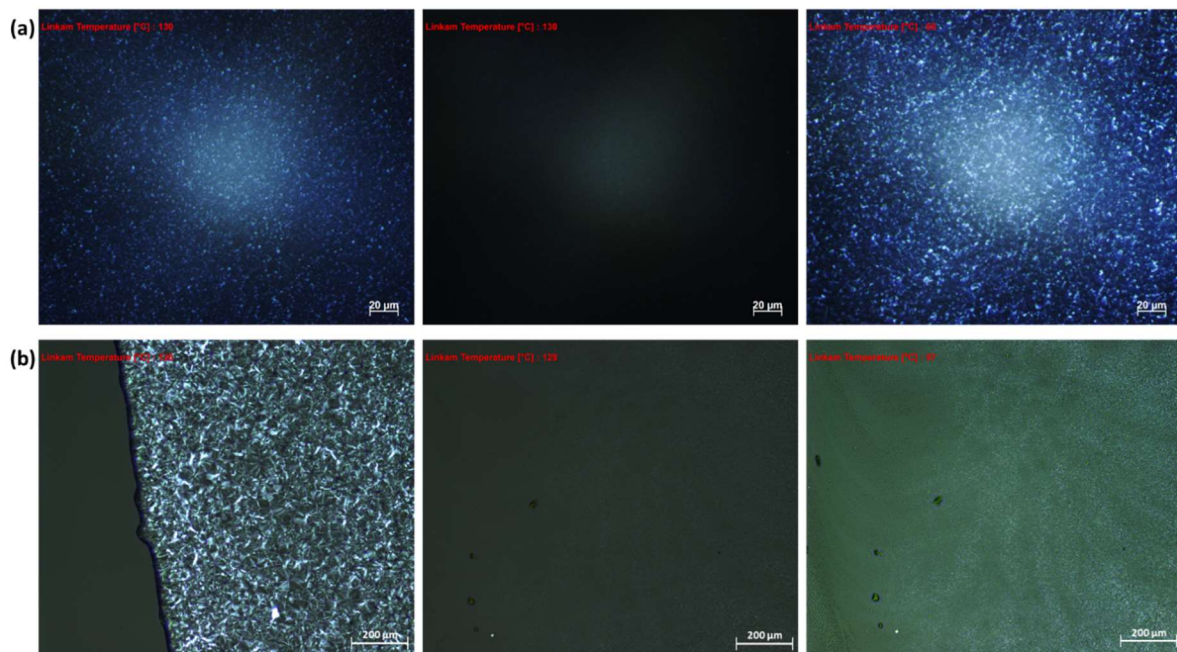


Figure 128 – Optical micrographs under polarized light of (a) HDPE (BM593), and (b) iPP (PPH4060) films exposed to xylene at 130°C . The first picture is the neat film at 130°C , the second picture the film after the addition of a xylene drop, and the third picture the resulting film after solvent evaporation and cooling at $5\text{K}\cdot\text{min}^{-1}$.

These changes of crystallinity are highlighted in Figure 129 showing HDPE and PP thin films exposed to xylene at 130°C at the droplet boundaries. Non-modified film and solvent-exposed parts are showed side-to-side for direct comparison. Observing Figure 129a makes clear that the addition of a solvent such as xylene increases the crystallinity of this HDPE thin film. These changes induce an increased transmitted light intensity for the solvent-exposed parts. Moreover, larger crystalline objects are found in the xylene-exposed part of HDPE.

Figure 129b illustrates the crystallinity changes for xylene-exposed PP, with the well-defined spherulites being replaced by micrometer-scale crystalline objects. It should also be noted that a size gradient of these crystalline objects is observable near the droplet boundary. Smaller objects are found far from the boundary, and a quasi-amorphous crown is evidenced at the extreme boundary of the exposed region.

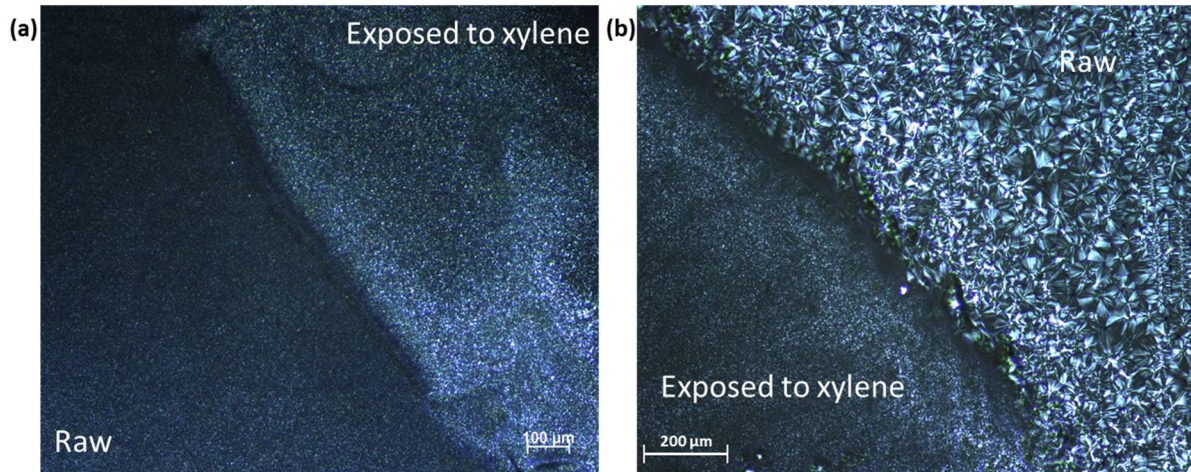


Figure 129 – Optical micrographs under polarized light of (a) HDPE (BM593) and (b) iPP (PPH4060) exposed to xylene at 130°C and then cooled at 5K.min⁻¹. Focus on the deposited solvent droplet boundary: (a) droplet was deposited on the upper right corner, and for (b) the droplet was deposited on the lower left corner.

Based on these polarized light observations, it seems that the asperities obtained with both HDPE and PP after exposing them to a solvent such as xylene could be associated to crystalline objects, according to their sizes and shapes. However, it is unclear that these crystalline objects constitute the asperities, or are just part of the asperities.

This question can be enlightened by comparing the obtained structures with some HDPE or PP crystals obtained from solutions in the literature. For example, Miao *et al.*²¹ obtained lamellar crystals by growing HDPE crystals (Figure 130a) from a xylene solution on Ultra High Molecular Weight Polyethylene (UHMWPE). These crystals were a bit smaller than the flakes observed when texturing HDPE through a xylene exposure, but their morphology is very similar. The major difference is that the crystals obtained by the authors epitaxially grown following a “shish-kebab” morphology. Such an observation is an argument that HDPE crystals grown from a solution can have such lamellar/flake morphology.

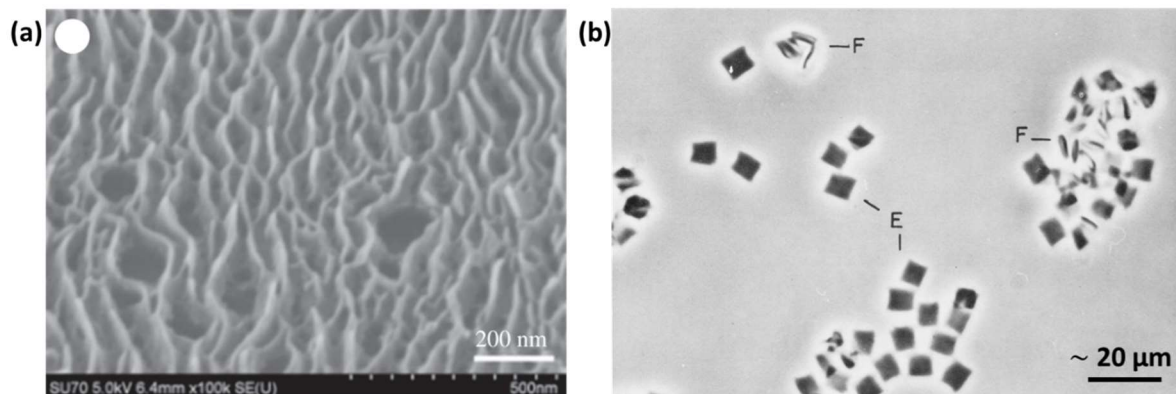


Figure 130 – Examples of HDPE and PP crystallized from a diluted solution found in the literature: (a) HDPE crystals grown on a UHMWPE fiber from a solution in xylene at 90°C, from Miao *et al.*²¹, (b) PP crystals obtained from a crystallization in amyl acetate at a concentration of 0.75% at 114°C, from Khoury²². In the later, the scalebar is approximate because of its absence in the original publication: it is here estimated based on the asperities size as indicated by the author. Copyright 2018 The Royal Society, and 1966 National Bureau of Standards, respectively.

Even if numerous texturing process using PP in solution led to morphologies very similar to the ones obtained using the presented process¹⁻³, very few authors tried to distinguish the precipitation and crystallization mechanisms for texturing. In such studies, relationships between solution temperature and resulting morphology are based on solvent evaporation rate rather than on crystallization kinetic considerations. However, PP crystals grown from a diluted amyl acetate solution at 114°C were

obtained by Khoury²² in 1966. As shown in Figure 130b, these crystals have a squared shape and a very limited size (about 5 to 7 μm large and 1 μm thick). Such crystals are similar to the ones obtained when exposing PP to olive oil at 170°C. Even if they differ from the ones obtained using others solvents, the order of magnitude of their size corresponds, making relevant the crystalline origin hypothesis for the asperities in textured PP. But still, one cannot exclude the possibility for PP asperities to be formed by a precipitation mechanism, due to spinodal decomposition. The decomposition could then be frozen by the polymer loss of mobility due to solvent removal and/or crystallization, leading to small polymer domains that are not able to coalesce.

If the role of the crystallization in PP texturing cannot be surely established, the observed flake morphology of the HDPE objects obtained after an exposure to solvents such as xylene is relevant with a crystallization hypothesis, as similar lamellar HDPE crystals have been observed by Miao *et al.*²¹. Moreover, such morphology is unlikely to be obtained from precipitation following a spinodal decomposition mechanism because of its relatively high aspect ratio. The most believable hypothesis for HDPE texturing is thus that the crystallization induces the precipitation. Concerning PP, no particular hypothesis takes the advantage over another.

III.1.c. Investigating the crystallization-induced precipitation

As the most robust hypotheses for HDPE texturing mechanism is the crystallization-induced precipitation, or phase separation by nucleation and growth, a diluted solution of HDPE (BM593) in xylene (2%_{wt}) has been prepared. Then, the homogeneous solution has then been casted on glass slides, after cooling it at 120°C, 90°C, and 20°C, corresponding approximately to the melting temperature, crystallization temperature of the neat HDPE, and to the room temperature, respectively (Figure 131).

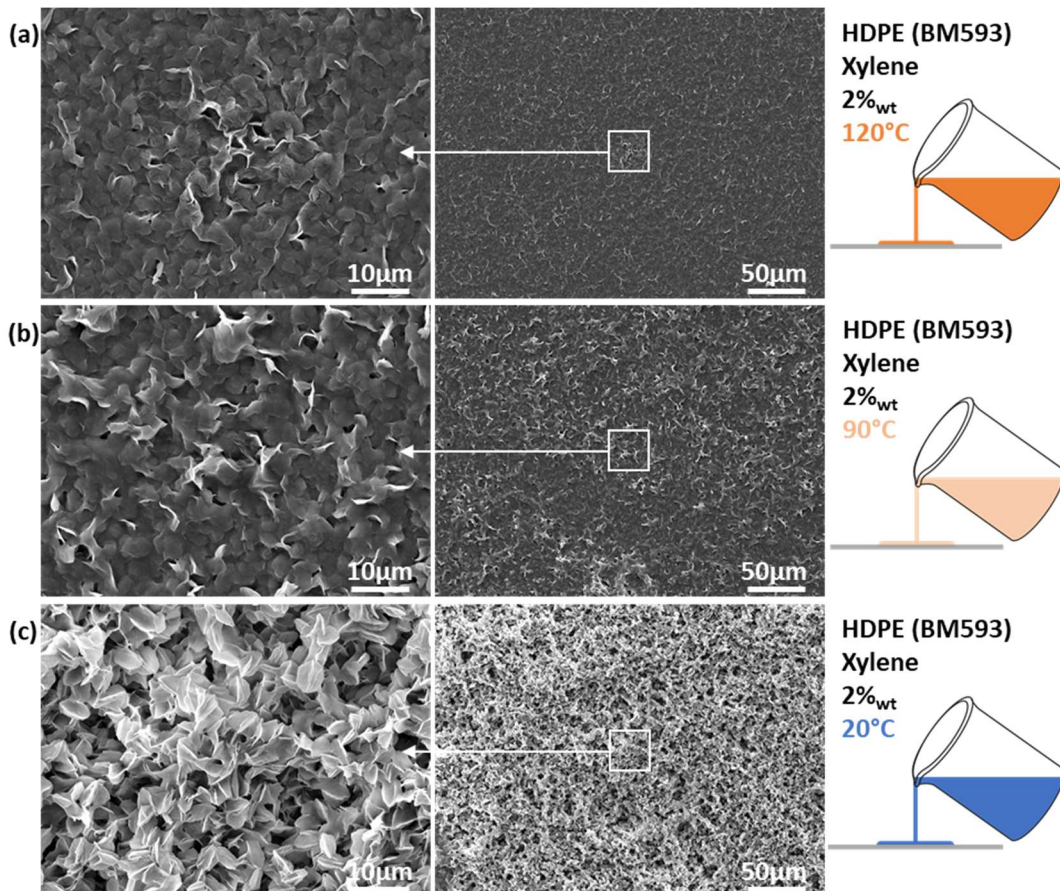


Figure 131 – SEM micrographs of HDPE (BM593) deposited on a glass substrate from a 2%_{wt} solution in xylene, deposited at (a) 120°C, (b) 90°C, and (c) 20°C.

The objective of such an experiment was to link the casting temperature to the resulting morphology in order to investigate the morphology generation mechanisms. In fact, the morphology could be obtained either during the solvent evaporation or during the solution cooling. The temperature and the solvent evaporation rate could not be totally distinguished. Still, experiments using less-volatile solvents such as dipentene, α -pinene or decane led to similar results.

When the solution of HDPE in xylene was casted at high temperature (120°C or 90°C, Figure 131a-b), flakes with a mainly smooth morphology is generated. Such a morphology is similar to the ones from the single-bath process using xylene. Thus, it could be stated that at such temperatures, the polymer is still amorphous and crystallizes quickly when casted, leading to a poorly textured surface.

However, when the solution was cooled at room temperature before casting, it turned whitish and the resulting surface was very similar to the ones obtained using the optimized texturing process. In such conditions, flakes are randomly stacked on the surface, resulting in an important texturing (Figure 131c). It is supposed that during the solution cooling, HDPE lamellar crystals grow from the solution, resulting in a suspension that concentrate on the surface after solvent evaporation, leading to a random stacking of the crystals. This hypothesis can be backed by observing the flakes extreme surface thanks to a low-acceleration voltage SEM. Such observation did not reveal any significant texture on the flakes surface (Figure 132a), which is in agreement with a single-step crystallization from solution hypothesis.

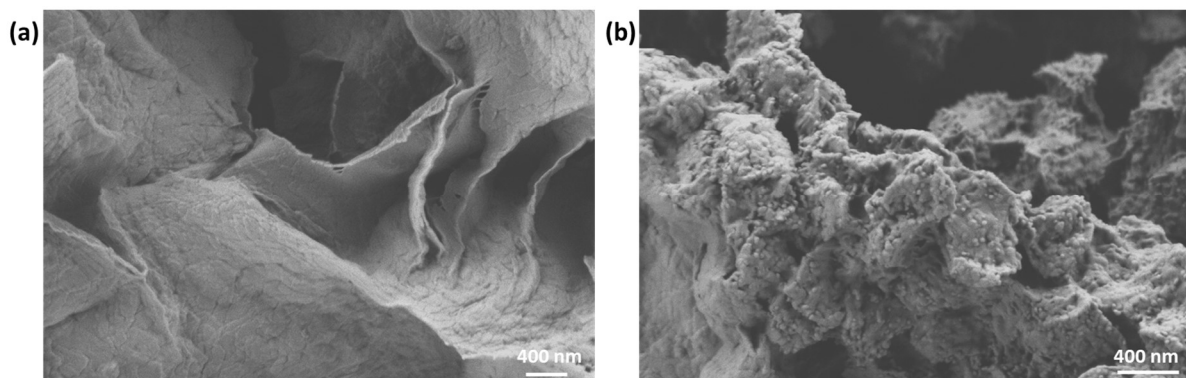


Figure 132 – Low acceleration voltage SEM micrographs of (a) HDPE (BM593) or (b) PP (PPH4060) surface asperities after a xylene texturing following the optimized process.

The same experience has been done with a 2%_{wt} xylene solution of PP (PPH4060). The resulting solution was then casted on glass slides at 120°C, 90°C, and 20°C, to investigate the influence of the thermal treatment of a diluted PP on the resulting surface morphology.

When the solution was casted at 120°C, a surface with very large string-like asperities and pores is generated (Figure 133a). Such a morphology is supposed to result from a polymer precipitation by spinodal decomposition, with large solvent domains leading to the observable porosities, and smaller polymer domains coalescing to finally form ribbon-like regions. Some nucleation and growth could still exist, as revealed by the presence of some spherulitic-like objects of a tenth micrometers. This spinodal decomposition could have been promoted by a fast cooling of the system. Such a method leads to a crystallization kinetic too slow to compete with the spinodal decomposition mechanism.

When the solution was cooled down to 90°C before casting, *i.e.* close to the crystallization temperature, a usual “PP textured by solvent” morphology was generated (Figure 133b). Such a morphology could result from a combination of precipitation by spinodal decomposition and nucleation and growth: first, the polymer and the solvent start to phase-separate in small domains, and in the polymer-rich domains a nucleation and growth of crystals occurs. This would lead to a limitation of the coalescence of the domains, keeping the solvent-rich domains as porosities. An

additional texturing could result from the growing of spherical crystals at the interface between polymer-rich and polymer-poor domains.

When the solution was cooled down to room temperature prior to casting, the solution turned whitish and then very large spherulitic-like objects are observed on the substrate, with a sub microscale texture on the surface of some objects (Figure 133c). Such a morphology is supposed to result of a nucleation and growth mechanism with a reduced competition of spinodal decomposition. During the cooling of the solution, some PP nuclei are formed, and then the polymer chains slowly crystallize from these nuclei as spherulites, as in bulk crystallization. These spherulites are suspended in the solution, and finally concentrate on the surface during the solvent is evaporation (as observed with HDPE casted at room temperature).

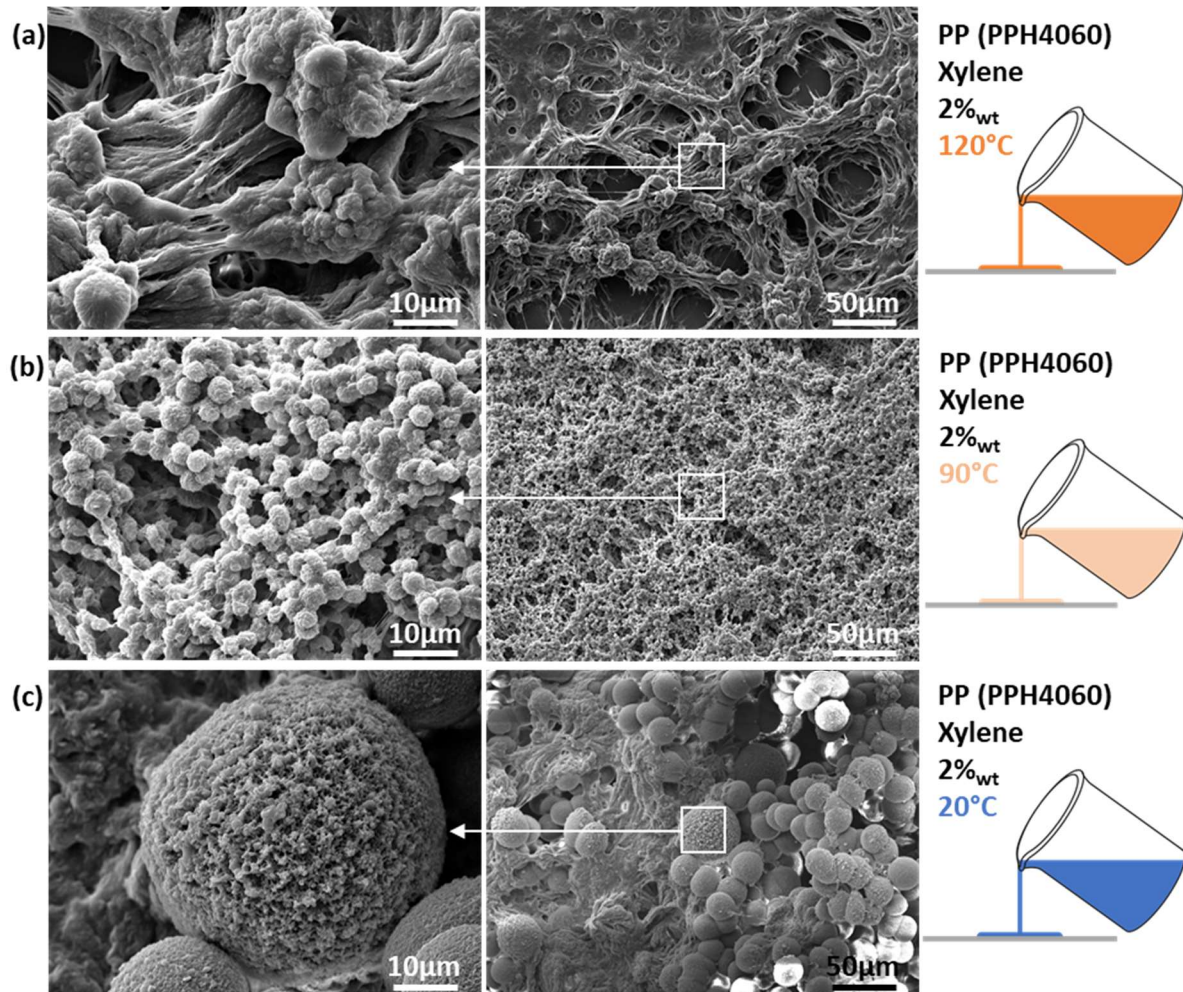


Figure 133 – SEM micrographs of PP (PPH4060) deposited on a glass substrate from a 2%wt solution in xylene, deposited at (a) 120°C, (b) 90°C, and (c) 20°C.

From these experiments, it appears that HDPE and PP texturing from solution can be induced by a crystallization-induced precipitation, or a nucleation and growth mechanism. The crystallization-induced precipitation mechanism seems to be responsible of the superhydrophobicity of solvent-textured HDPE.

However, a crystallization-induced precipitation of PP leads to a morphology far from the ones obtained with the optimized solvent-texturing process. For PP, it seems that a hybrid mechanism of spinodal decomposition and crystallization is at work. It is supposed that a polymer-rich phase is formed during precipitation, that acts as nuclei for a nucleation and growth mechanism from the polymer-poor phase. This hypothesis is reinforced by the observation of the extreme surface of

superhydrophobic PP asperities using a low-acceleration voltage SEM: Each asperity is found to be very textured and constituted of tinier spheres that had started to coalesce, backing a frozen spinodal decomposition hypothesis.

For HDPE and PP, temperature seems to play a major role on the resulting surface morphology, which requires a better understanding. In addition, the influence of the solvent nature and its miscibility with the polymer might be investigated.

III.2. Influence of solvent nature and temperature

III.2.a. Crystallization temperature and surface morphology

As highlighted by casting diluted solution of HDPE and PP on glass slides at different temperatures, or by processing surfaces with various second bath temperatures, the temperature seems to have a major influence on the generated surface morphology. The effect of a too low second bath temperature when texturing HDPE or PP using xylene has been attributed to a quenching of the polymer. This phenomenon is caused by a fast solvent evaporation, leading to an increase of the crystallization temperature of the polymer. However, the effect of an increase of the second bath temperature has still to be discussed in relation to the proposed texturing mechanism. An increase of the second bath temperature has been followed by a change in the HDPE crystals shape when using dipentene or decane. Nevertheless, such an observation was not possible with xylene, as it was found to be still partially miscible with HDPE at that temperature.

To overcome miscibility issues, dimethylsulfoxide (DMSO) has been added to the xylene second bath at a concentration of 20%_{wt}, in order to increase the solubility parameter of the solution, *i.e.* leading to a lower miscibility with HDPE. With such a second bath solution, it was possible to increase the temperature up to 100°C. The surface resulting from the exposure of a HDPE (BM593) film to such a process is very similar to the ones obtained using dipentene or decane with a 100°C second bath (Figure 134)

Based on these observations, it seems that when the temperature of the second bath is increased up to 100°C instead of 80°C, the HDPE crystals are intricated. Such a surface morphology results from a slower crystallization due to the higher temperature without solvent evaporation. In such conditions, the system could self-assemble into more complex shapes. However, the opposite observation was made with α -pinene, where more complex crystals shapes were observed with a 80°C second bath. This particularity needs and understanding by comparing the miscibility of HDPE with α -pinene and with the other solvents.

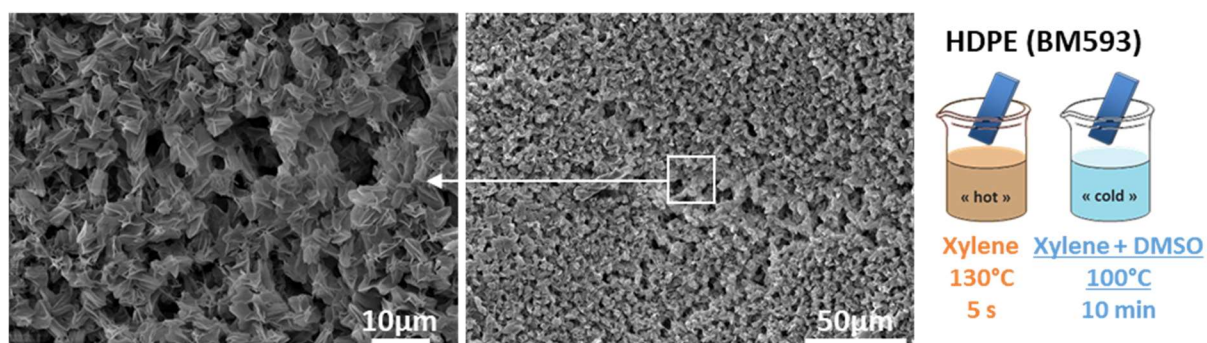


Figure 134 – SEM micrographs of a HDPE (BM593) surface exposed to xylene at 130°C for 5s, followed by an immersion in a xylene/DMSO solution (4:1) at 100°C for 5min.

For PP textured by solvent-exposure, similar observations could be made when using dipentene or decane. For such solvents, the higher the temperature of the second bath is, the smaller the asperities

are. Considering the proposed spinodal decomposition/nucleation and growth hybrid mechanism, one can explain that a faster crystallization occurs at higher temperature, resulting in a freezing of the phase-separated system. The remaining nucleation-and-growth mechanism is less extensive, resulting in less spherical and smaller objects. As for HDPE, the opposite impact of the second bath temperature on the structure when using α -pinene still need an understanding.

III.2.b. Polymer/solvent solubility considerations

Solvents such as xylene, dipentene, and decane lead to similar results with HDPE and PP, and other solvents such as α -pinene or even olive oil lead to very different results. Differences of miscibility with HDPE and PP need to be investigated.

To study the solubility of these solvents with HDPE and PP, their Hansen solubility parameters have been compared, as well as their evolution with temperature. All data concerning the Hansen solubility parameters have been obtained from the HSPiP software database, and solvents solubility parameters evolution with temperature have been calculated using Eq. 29, Eq. 30, and Eq. 31, considering a thermal expansion ratio (α) of xylene, dipentene, α -pinene, decane, and oleic acid as being 9.82, 8.80, 9.00, 10.20, and $6.90 \cdot 10^{-4} \text{K}^{-1}$ respectively¹⁴.

$$\delta^D(T) = \delta^D \times (1 - \Delta T \times \alpha \times 1.25) \quad \text{Eq. 29}$$

$$\delta^P(T) = \delta^P \times \left(1 - \Delta T \times \frac{\alpha}{2}\right) \quad \text{Eq. 30}$$

$$\delta^H(T) = \delta^H \times \left(1 - \Delta T \times \left(0.00122 + \frac{\alpha}{2}\right)\right) \quad \text{Eq. 31}$$

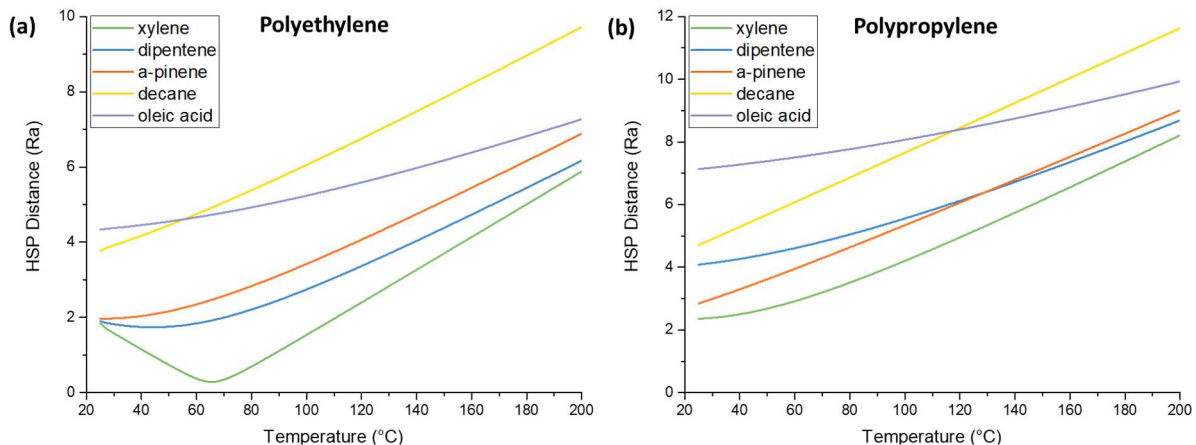


Figure 135 – HSP Distance (Ra) for (a) polyethylene and (b) polypropylene with solvents such as xylene, dipentene, α -pinene, decane and oleic acid with temperature.

According to these equations, the HSP of the solvents decrease with the temperature, whereas the HSP of the polymers are considered constant. To take into account the miscibility of these solvents with HDPE and PP, the HSP distance Ra is calculated for each polymer/solvent combination from 25 to 150°C (Figure 135).

The most interesting fact when plotting such data is the PE/xylene HSP distance decreasing with temperature until about 60°C, and then increasing for higher temperatures. For HDPE/dipentene, a similar behavior is observed but only limited to a decrease until 50°C approximatively. For all others polymer/solvent combinations, the HSP distance always increases with the temperature. Moreover, oleic acid is found to be a better solvent than decane for both PE and PP at high temperature, while

the experience showed the opposite trend. The comparison of these parameters cannot explain the observed surface morphology differences with the solvent nature or temperature.

Another way of approaching the interactions of solvents with HDPE and PP is the study of the melting point and crystallization temperature changes with solvent/polymer fraction. To do so, polymer/solvent mixtures of various weight contents (80/20, 60/40, 40/60, and 20/80) have been prepared and analyzed by DSC. The melting and crystallization temperatures have been measured for all polymer/solvent mixtures for HDPE (BM593) and PP (PPH4060) as polymers and xylene, dipentene, α -pinene, decane, and olive oil as solvents (Figure 136).

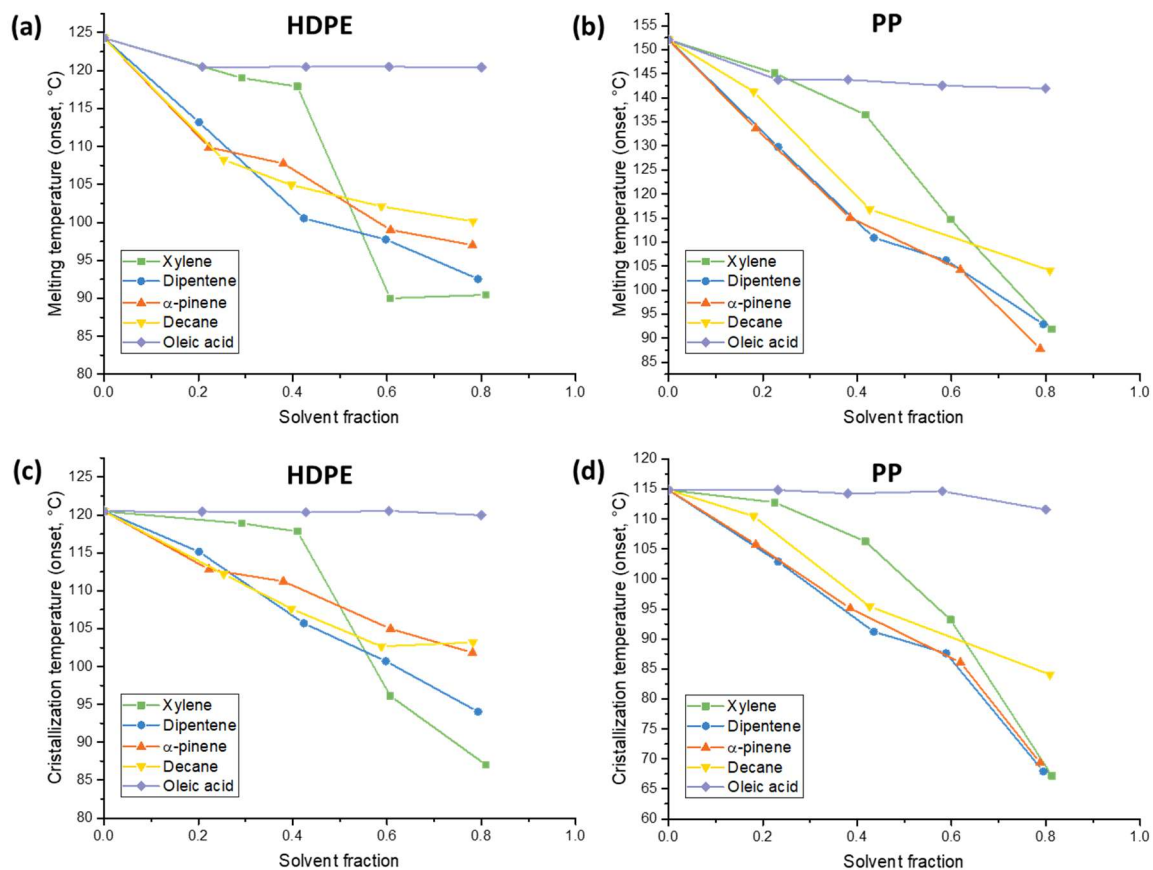


Figure 136 – Changes of (a-b) melting and (c-d) crystallization temperatures of (a-c) HDPE (BM593) and (b-d) PP (PPH4060) with the solvent fraction. Solvents are xylene, dipentene, α -pinene, decane and olive oil (DSC measurements at $10\text{K}\cdot\text{min}^{-1}$)

For the four “good solvents” of HDPE and PP, *i.e.* xylene, dipentene, α -pinene and decane, both melting and crystallization temperatures evolve similarly.

When olive oil is blended with HDPE, the melting temperature is slightly decreased by 4°C and does not change with an increased oil content. This decrease might not be significant, and the crystallization temperature does not change with the oil content.

When blended with PP, olive oil leads to a decrease of the melting temperature of about 10°C with $20\%_{\text{wt}}$ of oil, but additional amount of solvent was not found to further decrease the melting temperature. No significant change was observed concerning the crystallization temperature of PP with olive oil.

It can be assumed that olive oil has a very reduced miscibility in HDPE or PP, *i.e.* reaching the polymer saturation at solvent fraction well below $20\%_{\text{wt}}$. Olive oil miscibility in PP might be higher than in HDPE, leading to a higher melting temperature decrease at saturation. Solubilization of HDPE or PP by olive oil could then be theoretically possible but would take a long time, as also observed by Mizerovskii *et*

al.^{19,20}. Such a phenomenon could explain why HDPE and PP texturation was possible with olive oil, even if the expected surface morphologies are not generated. With olive oil, long exposition time were required as the polymer has to be partially solubilized in order to recrystallize from a solution state.

III.3. Conclusion

Based on texturing mechanism proposed by Hejazi et al.² and phase diagrams of HDPE and PP with xylene, texturing mechanisms for HDPE and PP have been proposed. Hypotheses have been confronted to experiments such as casting a diluted solution of HDPE or PP at various temperatures. The proposed texturing mechanisms can be described as follows:

- For HDPE, the polymer is swollen during the solvent exposure. When the system is cooled (in a second bath or in air for low-volatility solvents), the polyethylene chains crystallize from the more and more concentrated solution. It results in flakes that randomly pack on the surface.
- For PP, the polymer is swollen during the solvent exposure. When decreasing the solution temperature, the polymer and the solvent separate following a spinodal decomposition mechanism. The coalescence of the polymer phases is frozen by crystallization, leading to spherical asperities which are bead-like organized, with larger porosities from former solvent phases.

The influence of the process temperature on the resulting morphology has also be studied. It is believed than an increase of the temperature for the second bath led to a speed-off of the crystallization kinetics, resulting in intricated crystalline structures for HDPE, and tinier polymer phases for PP, due to a shorter coalescence time.

The nature of the solvent, as long as it is miscible within the polymer in large proportions, has not be found to have a major effect on the texturing mechanisms. Observed surface morphologies differences seems to be associated to volatility differences.

The analysis of the solvents Hansen solubility parameters and their evolution with temperature was not found to be relevant for explaining the texturing mechanisms or predicting the conditions needed to reach a given surface morphology.

The study of the dependence of the melting and crystallization temperatures with the solvent fraction was found to be a good indicator of a solvent suitability for the developed texturing process.

IV. Chapter conclusion

A promising texturing process from solvent exposure has been developed based on previous works on polymer-in-solvent solutions casting or polymer-immersed-in-solvent processes. This process involves two major steps: 1/ a solvent exposure from dipping a polymer film or complex shape objects in the hot solvent, followed by 2/ a solvent withdraw from dipping the swollen polymer in a colder solvent bath. This process has been found to be effective to produce superhydrophobic surfaces from HDPE and PP, with no significant influence of the polymer viscosity or molecular weight. The resulting surfaces were found to be superhydrophobic, and are even able to repel polar liquids with a surface tension down to 51mN/m.

Such a process, involving a volatile and toxic solvent such as xylene has been successfully transferred to less-volatile and low-toxicity solvents such as dipentene, α -pinene, or decane. Thanks to these alternative solvents having a low volatility, it was even possible to simplify the process by avoiding a second immersion step at a lower temperature. This single-step surface processing opens the way of a continuous texturing of HDPE or PP films, by exposing their surface to a solvent in a heated bath for less than 1s. The proof-of-concept of such on-line texturing process has been obtained using dipentene heated at 130°C for both HDPE and PP.

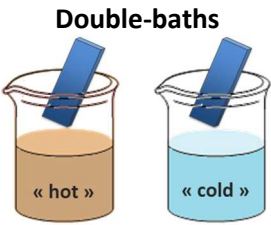
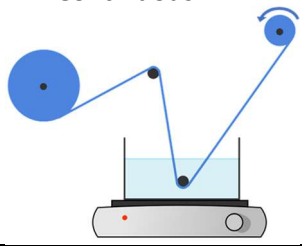
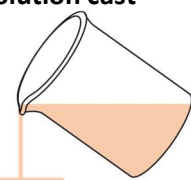
Based on the resulting surface morphologies and with relevant related experiments, various mechanisms have been proposed to explain HDPE and PP texturing. It was found that the origin of the asperities was different depending on the polymer used, but that the nature of the solvent had no impact on the mechanisms themselves. Nevertheless, changes in evaporation kinetics between the solvents can lead to various surface morphologies, *i.e.* smaller asperities or even porosities.

For HDPE, it is believed that during the solvent exposure, a polymer-in-solution phase is obtained, and that polyethylene chains crystallize from this solution when the system is cooled. The resulting HDPE flakes then concentrate on the surface resulting in a randomly stacked textured surface.

For PP, it is believed that the polymer is swollen by the solvent during the first immersion, and that the polymer and the solvent phase-separate following a spinodal decomposition mechanism upon cooling. Then, the coalescence of the polymer domains is frozen by crystallization. Crystallization of polypropylene chains in the solvent-rich phase could result in an additional texturing of the polymer domains.

In conclusion, an effective way of producing superhydrophobic surfaces from complex HDPE or PP objects has been developed using low-toxicity solvent. This process could be easily industrialized for the on-line production of superhydrophobic films, or for the batch production of superhydrophobic complex shape objects. Hypothesis concerning the texturing mechanisms have been made and confronted with experiments, and permit a better control of the texturing process thanks to the process/property relationships understanding.

Table 43 – Summary of the best texturing conditions for HDPE and PP for stable superhydrophobicity of their surface depending on the texturing process and solvent used.

Texturing process	Material	Solvent	Texturing conditions
Double-baths 	HDPE	Xylene	130°C 5s 80°C 5min
		Dipentene	130°C 10s 100°C 30s
		α -pinene	130°C 30s 80°C 5min
		Decane	140°C 30s 100°C 5min
	PP	Xylene	130°C 5s 80°C 5min
		Dipentene	130°C 10s 100°C 5min
		α -pinene	130°C 5s 100°C 5min
		Decane	130°C 5s 100°C 5min
		Olive oil	170°C 5min 100°C 5min
	Continuous film 	HDPE	Dipentene
PP		Dipentene	130°C <2s
Solution cast 	HDPE	Xylene, dipentene, α -pinene, decane	Casting at 20°C
	PP	Xylene, dipentene, α -pinene, decane	Casting at 90°C

V. References

1. Erbil, H., Demirel, A. L., Avci, Y. & Mert, O. Transformation of a Simple Plastic into a Superhydrophobic Surface. *Science (80-.)*. **299**, 1377–1380 (2003).
2. Hejazi, I. *et al.* Role of nanoparticles in phase separation and final morphology of superhydrophobic polypropylene/zinc oxide nanocomposite surfaces. *Appl. Surf. Sci.* **293**, 116–123 (2014).
3. Brown, P. S. & Bhushan, B. Liquid-impregnated porous polypropylene surfaces for liquid repellency. *J. Colloid Interface Sci.* **487**, 437–443 (2017).
4. Rioboo, R. *et al.* Superhydrophobic Surfaces from Various Polypropylenes. *Langmuir* **24**, 9508–9514 (2008).
5. Cheng, Y. *et al.* Facile preparation of high density polyethylene superhydrophobic/superoleophilic coatings on glass, copper and polyurethane sponge for self-cleaning, corrosion resistance and efficient oil/water separation. *J. Colloid Interface Sci.* **525**, 76–85 (2018).
6. Lu, X., Zhang, C. & Han, Y. Low-Density Polyethylene Superhydrophobic Surface by Control of Its Crystallization Behavior. *Macromol. Rapid Commun.* **25**, 1606–1610 (2004).
7. Sousa, C. *et al.* Superhydrophobic poly(L-lactic acid) surface as potential bacterial colonization substrate. *AMB Express* **1**, 34 (2011).
8. Bai, W. *et al.* Petal-effect superhydrophobic surface self-assembled from poly(p-phenylene)s. *Eur. Polym. J.* **101**, 12–17 (2018).
9. Zhao, N. *et al.* Fabrication of biomimetic superhydrophobic coating with a micro-nano-binary structure. *Macromol. Rapid Commun.* **26**, 1075–1080 (2005).
10. Brown, P. S. & Bhushan, B. Durable, superoleophobic polymer–nanoparticle composite surfaces with re-entrant geometry via solvent-induced phase transformation. *Sci. Rep.* **6**, 21048 (2016).
11. Cui, Y., Paxson, A. T., Smyth, K. M. & Varanasi, K. K. Hierarchical polymeric textures via solvent-induced phase transformation: A single-step production of large-area superhydrophobic surfaces. *Colloids Surfaces A Physicochem. Eng. Asp.* **394**, 8–13 (2012).
12. Krishnan, K. *et al.* Method to modify surface of an article and the article obtained therefrom. *Pat. N° US 20070009709A1* (2017).
13. Zhao, N. *et al.* A lotus-leaf-like superhydrophobic surface prepared by solvent-induced crystallization. *ChemPhysChem* **7**, 824–827 (2006).
14. Wypych, A. & Wypych, G. *Databook of Solvents*. (Elsevier, 2015). doi:10.1016/C2013-0-13245-X
15. Körösi, G. & Kováts, E. S. Density and Surface Tension of 83 Organic Liquids. *J. Chem. Eng. Data* **26**, 323–332 (1981).
16. Vazquez, G., Alvarez, E. & Navaza, J. M. Surface Tension of Alcohol + Water from 20 to 50 °C. *J. Chem. Eng. Data* **40**, 611–614 (1995).
17. Schaller, R., Feldman, K., Smith, P. & Tervoort, T. A. High-Performance Polyethylene Fibers ‘al Dente’: Improved Gel-Spinning of Ultrahigh Molecular Weight Polyethylene Using Vegetable Oils. *Macromolecules* **48**, 8877–8884 (2015).
18. Abbott, S., Hansen, C. M. & Yamamoto, H. *Hansen solubility parameters in practice complete*

with eBook , software and data. (2013).

19. Mizerovskii, L. N., Lebedeva, T. N. & Pochivalov, K. V. The phase diagram of the high-density polyethylene-m-xylene system. *Polym. Sci. Ser. A* **57**, 257–260 (2015).
20. Mizerovskii, L. N., Pochivalov, K. V. & Vyalova, A. N. State diagrams of partially crystalline polymer-good solvent systems: The isotactic polypropylene-m-xylene system. *Polym. Sci. - Ser. A* **55**, 295–301 (2013).
21. Miao, W. *et al.* High-density polyethylene crystals with double melting peaks induced by ultra-high-molecular-weight polyethylene fibre. *R. Soc. Open Sci.* **5**, 180394 (2018).
22. Khoury, F. The spherulitic crystallization of isotactic polypropylene from solution: On the evolution of monoclinic spherulites from dendritic chain-folded crystal precursors. *J. Res. Natl. Bur. Stand. Sect. A Phys. Chem.* **70A**, 29 (1966).

GENERAL CONCLUSION AND PERSPECTIVES

In this thesis manuscript, superhydrophobicity has been studied through multiple angles: after reviewing the most common routes for designing a superhydrophobic surface, an understanding of the texturing mechanisms has been carried, through a simple modeling of a Cassie-Baxter's interface. Then, based on the guidelines obtained by applying the developed model to theoretical surfaces, easy ways of obtaining such surface textures with thermoplastics have been prospected, and the results were confronted with the developed model. Finally, a texturing process through a solvent-exposure of thermoplastics leading to a precipitation and texturation mechanism had been developed, described and explained.

Based on the current knowledge concerning superhydrophobicity, built on works described in the literature and the model developed in this work, making a surface superhydrophobic requires:

- Intrinsic hydrophobicity, even if this criterion can be overpassed with
- re-entrant asperities,
- tiny asperities (1 μ m or less, the lower the better), and
- spaced by at least their own size or the double.

The described surface is an ideal that should be considered as a guideline, as it is possible for a rough surface to be superhydrophobic without matching all these conditions. Rough surfaces of HDPE, LDPE and PP were obtained using multiple approaches.

The first explored approach was the addition of nanoparticles in HDPE as texturing fillers in the bulk, and then extruding the formed blend as a film. If rough surfaces were obtained, they were far from being rough enough for superhydrophobicity. This approach was thus quickly abandoned for immiscible polymer blends. HDPE and poly(ethylene oxide) (PEO) were mixed together in almost equivolometric conditions to promote co-continuity. Such blends were extruded into films and PEO was removed by dissolution in water. The resulting rough HDPE surface had a reinforced hydrophobicity, but without reaching superhydrophobicity. Addition of silica nanoparticles in the blend as compatibilizer did not led to a significant phase size reduction, but these nanoparticles allowed a nano-texturation of the final surface, by being localized at the former HDPE/PEO interface. With hydrophilic silica, the resulting porous film was superhydrophilic, leading to a complete absorption of water droplets. Using silica nanoparticles with hydrophobic groups on their surface, known as hydrophobic but with a water contact angle still lower than 90°, permitted the obtention of hydrophilic surfaces. Polytetrafluoroethylene (PTFE) microparticles were introduced into a HDPE/PEO blend, and were found to be at the HDPE surface after PEO removal in a similar way as with silica. Despite their texturing effect and their high intrinsic hydrophobicity, such surface was not superhydrophobic, probably because of the too important space between these particles, mainly due to phases elongation during the film pulling after its extrusion.

Foaming of HDPE and PP was pursued using supercritical CO₂ in a batch process in order to generate porous superhydrophobic surfaces. It was found that in order to reduce the cells size while keeping an important cells density, the foaming should be made at high pressure, close to 20MPa (the maximum of the foaming apparatus), at a temperature close to the polymer's crystallization temperature and with nucleating agents such as talc or calcium carbonate. However, only closed cells were obtained by foaming thermoplastics with SC-CO₂, and all samples had a smooth and dense skin. The studied textures were thus always sliced samples that revealed the foam inner structure. Samples with water contact angle larger than 150° were obtained, but the water droplet always got pinned on these surfaces, resulting in contact angle hysteresis values larger than 10°, thus not satisfying the two conditions for making the surface superhydrophobic.

The foaming of HDPE and LDPE was also conducted *in situ* in a blown-film extruder, using chemical blowing agents (CBA) and nucleating agents such as citric acid and calcium carbonate. The CBA reacted in the extruder heated at more than 200°C, generating gases such as CO₂ and H₂O, and the resulting mix was extruded through a ring die at a temperature from 180°C to 160°C and pulled uniaxially. Rough

surfaces were obtained right out of the extruder, without requiring any post-treatment. Open porosities were observed on these samples, with a “cells-in-cells” morphology and some matter folds at one extremity of the larger porosities. Even if rougher surfaces with smaller voids were obtained while increasing the CBA content, and if isotropic surfaces with small HDPE strings were produced by decreasing the die temperature, none of these surfaces was superhydrophobic. Some surfaces had a water contact angle larger than 150° , but again water droplets always got pinned on some smooth areas of such surfaces. No way of reducing the size of this roughness of about a decade was found, and slippery superhydrophobicity could not have been reached.

However, a simple process has been successful for producing rough superhydrophobic surfaces from HDPE or PP. This process uses a hot solvent bath to swell the surface of a polymer already in its final shape, becoming rough by a precipitation and crystallization mechanism. The final rough surfaces are superhydrophobic, and even repel polar liquids with surface tension close to 50mN/m . The first developed process used xylene as a solvent, with two steps for an efficient texturing: an immersion in a hot bath at 130°C for a few seconds, followed by an immersion in a colder bath at 80°C for a few minutes. During the second bath immersion, the polymer/solvent miscibility was poor enough to promote the phase separation and the polymer crystallization. For HDPE, it was found that the crystallization of polyethylene chains into micrometric flakes induced a precipitation, whereas for polypropylene, a phase separation by spinodal decomposition was frozen by the polymer crystallization, resulting in bead-like asperities. As this process involved a toxic solvent in a batch reactor, less toxic substances that could act as solvents at high temperature were studied. High boiling temperature liquids such as dipentene, α -decane or decane successfully replaced xylene in an almost identical process, only changing the immersion time. With these less-volatile solvents, the second bath had even been made unnecessary, opening the way of in-line texturing of HDPE or PP film. A proof of concept of such in-line texturing has been obtained with HDPE and dipentene, and the use of such process in a pilot or industrial scale could be considered.

As perspectives for this project, the size reduction of the roughness obtained by foaming thermoplastics during their extrusion might be of greater interest. By changing the nature of the used polymer resins, and varying the process with more flexibility upon the depressurization rate and temperatures of extrusion, smaller porosities could lead to superhydrophobicity without any post-treatment. However, such modifications would make more difficult the transfer of the process to the industry, by being less universal. Once a proof of concept would be obtained, work could be done on the optimization of the process. On the other hand, transferring the solvent-based texturing process into extrusion would be of interest, removing the need of a solvent bath and making the process suitable for all thermoplastic transformation methods. Adding the identified low-toxicity solvent within the polymer bulk and extruding the resulting blend under given conditions could lead to mimic the in-lab process at a larger scale, and allow the transfer to an industrial scale. In general, as clear guidelines on how a surface roughness should be for making it superhydrophobic have been established, all processes even out of the surface science field could be considered for producing such surfaces.

It has also been demonstrated that if it is relatively simple to make a surface superhydrophobic, it is quite difficult to do it with simplicity.

ANNEXES

I. Tables of Figures

I.1. Figures

Figure 1 – Global plastic production per year from 1950 to 2015, in megatons, based on data from Geyer et al. ²	3
Figure 2 – Shares of total polymer resin production depending on their use, with a detail of the polymer resins nature used in the packaging industry in 2015, based on data from Geyer et al. ²	4
Figure 3 – The « Lotus effect »: the superhydrophobicity of the lotus leaves, (a) illustrated by a photography, (b) with the corresponding surface roughness observed by SEM. (b) is reprinted from ³ , Copyright 1997 Springer.....	4
Figure 4 – Number of publications per year on the topic “superhydrophobicity”, based on Web of Science database analysis realized on December 2020.	5
Figure 5 – Surface energy and surface tension of liquids. (a) Molecular origin of surface energy: schematic representation of atoms or molecules in the bulk and at the surface and their interactions with neighbors. (b) Soap bubble and string trick: (i) equilibrated water and soap solution films separated by a string, and (ii) rupture of equilibrium by removing of a film: the remaining film minimizes its surface by pulling on the string.	8
Figure 6 – Various wetting regimes of a solid by a liquid. As water at the liquid, solids with those wetting are denoted as (a) hydrophilic, (b) hydrophobic, (c) superhydrophilic, (d) superhydrophobic.....	10
Figure 7 – Schematic representation of a liquid drop rolling on an inclined solid “phobic” surface....	11
Figure 8 – Wenzel’s state wetting of a liquid on a textured solid: (a) schematic representation of a “phobic” textured surface fully wetted by a liquid and (b) computed Wenzel’s contact angle depending on intrinsic Young contact angle and roughness. (c) water droplet pinned on a Rosa Bairage and (d) corresponding surface texture observed by SEM. (c) and (d) are reprinted from ⁸ , Copyright 2010 American Chemical Society	12
Figure 9 – Cassie-Baxter’s partial wetting of a rough solid: (a) schematic representation of a “phobic” rough surface holding a liquid drop on top of its asperities and (b) computed Cassie-Baxter’s contact angle depending on intrinsic Young’s contact angle and gas (air) fraction at the interface. (c) water droplet on a lotus leaf and (d) corresponding surface texture observed by SEM. (d) is reprinted from ¹¹ , Copyright 1997 Springer Nature.....	13
Figure 10 – Schematic representation of a Cassie-Baxter’s and Wenzel’s mixed interface	15
Figure 11 – Air plastron decay with pressure monitored by laser beam diffraction. (a) Scheme of the experimental set, (b) Corresponding interfaces upon pressure based on diffracted light analysis. Reprinted from ³³ , Copyright 2010 American Chemical Society	16
Figure 12 – Water/air meniscus shape under pressure monitored by laser beam diffraction. (a) Scheme of experimental set, (b) cross-view of the superhydrophobic sample (hydrophobized textured silicon wafer) and (c) plot of results: meniscus curvature κ and local contact angle α with the applied hydrostatic pressure (Ph) and the corresponding Laplace pressure (ΔPL). Reprinted from ³⁴ , Copyright 2010 The Royal Society of Chemistry	17
Figure 13 – Air plastron decay over time with different hydrostatic pressure monitored by relative reflectivity. (a) Sample surface observed by SEM, (b) plastron reflectivity decay over time for various immersion depth and thus hydrostatic pressure, (c) scheme of plastron decay mechanism, and (d) summary of plastron lifetime with immersion depth. Reprinted from ³⁵ , Copyright 2010 American Physical Society	18
Figure 14 – Wool textile turned superhydrophobic by polysiloxane accumulation. (a) Water droplet on untreated superhydrophilic and (b) treated superhydrophobic wool textile. (c) SEM observation of the untreated and (d) treated fibers. Reprinted from ³⁷ , Copyright 2008 Springer-Nature	19
Figure 15 – Polyester textile turned superomniphobic until hexadecane, using a fluorinated alkyl silane. (a) Complete absorption of a red-colored hexadecane droplet and a green-colored water droplet by an untreated polyester textile, and (b) complete repellence of hexadecane and water by the treated superomniphobic polyester textile. (c) SEM observation of the fibers of untreated and (d) treated	

textile, showing no roughness differences. Reprinted from ³⁸ , Copyright 2011 The Royal Society of Chemistry	20
Figure 16 – Superhydrophobic polyurethane foam. (a) Water repelling polyurethane foam (b) SEM observation of untreated and (c) PTFE NP treated foam. Reprinted from ¹⁸ , Copyright 2012 American Chemical Society.....	20
Figure 17 – Hydrophobized silicon surfaces patterned using a dicing machine. (a) Anisotropic surface with 49µm large and 160µm deep grooves separated by 96µm, (b) quasi-isotropic surface with squared pillar of 96µm large and 160µm height separated by 49µm, and (c) resulting wetting behavior with a water droplet seated on top of pillars. Reprinted from ⁴⁰ , Copyright 2002 American Chemical Society	21
Figure 18 – Textured polymer surfaces obtained by micro and nano imprinting. (a) Scheme of the imprinting process: a polymer substrate is hot-pressed ($T > T_g$) using a hard microrough mold, and then cold-pressed ($T < T_g$) by a hard nanorough mold. (b) Resulting surfaces with various angle variations between the first and second mold: A, B and C are obtained by a micro/nano imprinting, whereas D and E are obtained by a micro/micro imprinting. Reprinted from Zhang and Low ⁴¹ , Copyright 2007 American Chemical Society.	22
Figure 19 – Superhydrophobic patterned silicon surfaces. (a) Smooth sidewalls pillars, (b) wavy sidewalls pillars and (c) nail-like pillars, all obtained using photolithography, and of 3µm large, 7µm height and 3µm spaced. Reprinted from ⁴² , Copyright 2011 American Chemical Society.....	22
Figure 20 – Hierarchically textured superhydrophobic surface. (a) Molded epoxy resin surfaces with micropillars and (b) nanotexture made of hexatriacontane epitaxial crystals. Reprinted from ⁸ , Copyright 2010 American Chemical Society	23
Figure 21 – Ginkgo leaf superhydrophobicity. (a) A natural Ginkgo leaf and (b) its PDMS negative replicated surface. (c) SEM observation of the natural Ginkgo leaf and (d) its negative replica. Reprinted from ⁴⁴ , Copyright 2014 Trans Tech Publications.....	24
Figure 22 – Superhydrophobic silicon surface obtained using laser etching. (a) SEM observations of microtexture made of 5µm deep and 4µm large grooves and (b) nanotexture made of oxidized silicon sputtered chippings. Reprinted from ⁴⁵ , Copyright 2005 American Chemical Society	24
Figure 23 – PTFE coated textured alumina surface obtained from chemical etching and anodization followed by hydrophobization using an alkylsilane and PTFE. (a) SEM observation of the hierarchical roughness and (b) resulting superhydrophobicity of the treated aluminum. Reprinted from ⁴⁶ , Copyright 2010 American Chemical Society	25
Figure 24 – Superhydrophobic metal oxide surfaces. (a) SEM observation of ZnO pillar-like texture, (b) CuO flower-like texture and (c) CuO in the presence of zinc flower-like texture, obtained from hydrothermal reaction or chemical oxidation of smooth zinc, copper, and brass surfaces, hydrophobized using a fluorinated acid. Reprinted from ¹⁹ , Copyright 2020 American Chemical Society.	26
Figure 25 – Needle-like brucite-type cobalt oxide obtained by crystallization from solution, hydrophobized using lauric acid. (a) SEM observation from top and (b) and from side. (c) Resulting superhydrophobicity. Reprinted from ⁴⁷ , Copyright 2005 American Chemical Society.....	26
Figure 26 – Superhydrophobic silver coated surface. SEM observations of silver deposited on a copper substrate from a silver nitrate solution with (a) and without (b) benzoic acid. Reprinted from ⁴⁸ , Copyright 2010 Elsevier.....	27
Figure 27 – Superhydrophobic honeycomb-like surface from polyelectrolyte multilayers. (a) Honeycomb-like micro-texturing is obtained by acidic treatment of poly(allylamine hydrochloride)/poly(acrylic acid) multilayers assembly, and (b) nanotexturing is obtained by silica nanoparticles deposition from a solution, followed by hydrophobization using fluorinated silane, and resulting superhydrophobicity. Reprinted from ⁴⁹ , Copyright 2004 American Chemical Society.....	27
Figure 28 – Zinc oxide coated superhydrophobic surfaces. (a) ZnO/PDMS blend sprayed on an aluminum substrate, (b) Hydrophobic ZnO particles deposited on a PDMS substrate from solution. Reprinted from (a) ⁵⁰ and (b) ⁵¹ Copyright 2011 Elsevier and 2010 American Chemical Society, respectively.	28

- Figure 29 – Superhydrophobic poly(urethane-acrylate) resin textured using silica with tunable water adhesion. (a) AFM imaging of a Cassie-Baxter’s superhydrophobic surface roughness with 60%_w silica content, (b) Evolution of water contact angle hysteresis with silica content in the coating, linking roughness and surface wetting regime. Reprinted from ⁵², Copyright 2018 Elsevier..... 29
- Figure 30 – Superhydrophobic silica coated surfaces. (a) Spin-coated and (b) doctor blade coated silica in a polystyrene matrix, (c) Spin-coated and (d) doctor blade coated fluorinated silica nanoparticles in an epoxy resin matrix. Reprinted from ⁵³, Copyright 2016 Elsevier..... 29
- Figure 31 – Superomniphobic surface from a fluorinated silica coating. (a) SEM observation of the obtained superomniphobic surface and (b) resulting wettability with 5 μ L droplets of (i) water, (ii) diiodomethane, (iii) decahydronaphthalene, (iv) soybean oil, (v) diesel fuel, (vi) xylene. Reprinted from ⁵⁴, Copyright 2008 Wiley..... 30
- Figure 32 – Armored superhydrophobic surface consisting of a side-to-side pyramids silicon structure, obtained by photolithography, with voids filled by a superhydrophobic material: fluorinated silica nanoparticles. (a) Scheme of the armored surface viewed from the side, before and after abrasion, and (b) are SEM pictures of the obtained surface before abrasion, showing the armor silicon frame and the fluorinated nanoparticles. Reprinted from⁵⁵, Copyright 2020 Springer Nature 30
- Figure 33 – Superhydrophobic surfaces from hydrophobized mulberry-like particles. (a) Bare silica nanoparticles on CaCO₃ microparticles, (b) silica nanoparticles on CaCO₃ microparticles mixed with PDMS and sprayed on a glass slide, and corresponding water CA. (c) Silica-on-silica multiple scales particle mixed with crosslinked silanized polyacrylate and sprayed on a steel plate, and corresponding water CA. Reprinted from (a, b) ⁵⁶ and(c) ⁵⁷, respectively, Copyright 2009 and 2017 Elsevier..... 31
- Figure 34 – Superhydrophobic surfaces from carbon nanotubes. (a) Randomly stacked CNT sprayed from a solution of CNT, OPV and chloroform, and resulting (b) self-cleaning and (c) water-repelling properties. (d) Poly(phenylene sulfide) sprayed coating, with silicon rubber particles and carbon nanotubes, and resulting wetting behavior. Reprinted from (a, b, c) ⁵⁸ and (d) ⁵⁹, Copyright 2008 Wiley and 2017 Elsevier, respectively. 32
- Figure 35 – Superhydrophobic surfaces using “floating” particles. (a) Fluorinated diatomaceous earth particles bound by polyurethane: particles migrate to the surface during drying of the coating. (b) Fluorinated wax crystals with silica nanoparticles “floating” at its surface: nanoparticles are expelled from the wax during crystallization. Reprinted from ⁶⁰ and ⁶¹, Copyright 2016 Wiley and 2012 American Chemical Society, respectively. 33
- Figure 36 – Superhydrophobic organosilica sol-gel foams. (a) Foam slice with nanofeatures obtained from quick phase separation and (b) foam slice with microfeatures obtained from a slow phase separation. Reprinted from ⁶², Copyright 2003 American Chemical Society. 34
- Figure 37 – Superhydrophobic coating from crystallization/precipitation of polypropylene. (a) Small PP particles obtained from precipitation and crystallization from a xylene/MEK solution, (b) Larger PP particles obtained from crystallization from a pure xylene solution. Reprinted from ⁶³, Copyright 2003 American Association for the Advancement of Science 35
- Figure 38 – Superhydrophobic PP surfaces obtained by precipitation from a xylene solution. (a) Superhydrophobic surface with a multiscale texture obtained using ZnO as a nucleating agent, and (b) proposed formation mechanism. (c) Non-superhydrophobic surface with a one-scale texture obtained from a pure xylene solution, and (d) proposed formation mechanism. Reprinted from ⁶⁵, Copyright 2014 Elsevier 36
- Figure 39 – Superhydrophobic polycarbonate surfaces. Precipitation from a DMF solution in air with (a) 0%, (b) 50% and (c) 75% relative humidity. (d) Precipitation from an acetone solution immersed in methanol. Reprinted from (a), (b), (c)⁶⁶ and (d)⁶⁷, Copyright 2005 and 2006 Wiley..... 37
- Figure 40 – Superhydrophobic PC surfaces from acetone solution. (a) PC surface roughness with immersion time in an acetone solution, and (b) corresponding water contact angle and sliding angle. (c) Superoleophobic PC surface with re-entrant asperities. Reprinted from (a), (b) ²⁸ and (c) ¹⁴, Copyright 2012 Elsevier and 2016 Springer-Nature, respectively. 38
- Figure 41 – Superhydrophobic and superoleophilic sponge. (a) Untreated kitchen sponge structure. (b) Kitchen sponge covered with HDPE deposited from a xylene/ethanol solution, preserving the sponge

structure and adding a microstructure combined with hydrophobization, and corresponding water CA. Reprinted from ¹⁷ , Copyright 2018 Elsevier.....	39
Figure 42 – Superhydrophobic PMMA/FPU textured surface. (a) Textured pure PMMA surface, exhibiting a Wenzel’s wetting behavior, and (b) textured PMMA/FPU surface with a Cassie-Baxter’s regime superhydrophobicity. Reprinted from ⁶⁹ , Copyright 2004 Wiley	39
Figure 43 – Superhydrophobic textured surfaces from polymer precipitation. (a) Textured PLLA superhydrophobic surface from a PLLA/dioxane solution. (b) Textured hydrophobic PS surface from a PS/DMF solution casted in humid air. (c) Textured superhydrophobic surface from a PS-b-PDMS block copolymer casted from a DMF solution in humid air. Reprinted from (a) ⁷⁰ and (b,c) ⁷¹ , Copyright 2011 Springer and 2005 American Chemical Society, respectively.	40
Figure 44 – Superhydrophobic surfaces from epitaxial wax crystals. (a) Indian cress wax recrystallized on a glass slide, (b) n-hexatriacontane thermally deposited on glass slide and aged, (c) C ₃₆ H ₇₄ epitaxial wax crystals, (d) C ₄₄ H ₉₀ epitaxial wax crystals, (e) C ₃₆ H ₇₄ epitaxial wax crystals with C ₄₄ H ₉₀ epitaxial wax crystals grown on it. Reprinted from (a) ⁷⁴ , (b) ⁷⁵ and (c-e) ⁷⁶ , Copyright 2009 Elsevier, 2012 Wiley, and 2013 The Royal Society of Chemistry, respectively.....	41
Figure 45 – Superhydrophobic polymer surfaces from foams. (a) Superhydrophobic and superoleophilic PP foam with PTFE fibrils from foaming with SC-CO ₂ during and extrusion process, and (b) in a batch process. Reprinted from (a) ⁷⁷ and (b) ⁷⁸ , Copyright 2014 and 2019 American Chemical Society, respectively.	42
Figure 46 – Scale length impact on contact angle and hysteresis. (a) Rhombus pillars of 4x8 μm large and 40μm height, separated by a tenth micrometers, with (i) flat tops and (ii) nanorough tops; (b) Square pillars with increasing scale length from 2 to 40μm with a 30μm height and a constant solid area fraction of 0.16; (c) Hexagonal pillars with (i) constant length and distance kept equal with values from 4 to 128μm and (ii) constant height of 16μm, and (iii) resulting equilibrium (□), advancing (Δ), and receding (○) contact angles. (a), (b) and (c) are reprinted from ^{6,7} and ⁸ respectively, Copyright 2006, 2012 and 2014, American Chemical Society	55
Figure 47 – Study of a Cassie-Baxter’s interface stability with (a) monoscale and (b) hierarchical roughness, and (c-d) resulting interface free energy for mono- and multiple scale roughness, respectively. Reprinted from ¹⁵ , Copyright 2007 American Chemical Society.....	56
Figure 48 – Impact of multiscale roughness on the wetting properties. (a) Studied topographies, based on (a-c) sinusoidal curvature, (d-f) flat-top pillars, and (g-j) triadic Koch curve. (b) Resulting free energy of the system with liquid penetration depth for flat-top pillars, with 1, 2 or 3 roughness scales. (c) Calculated water contact angle with the number of roughness scales, for sinusoidal, flat-top pillars and triadic Koch curve topographies. Reprinted from ¹⁶ , Copyright 2012 American Chemical Society	57
Figure 49 – Re-entrant asperities and corresponding wetting properties. (a) Scheme of re-entrant asperities and corresponding calculation parameters: (A) fibers and (B-C) micro-hoodoos. (b) Doubly re-entrant nail-likes asperities with superomniphobicity, and (c) corresponding contact angle with various surface tension liquids. Reprinted from (a) ¹⁷ and (b-c) ²¹ , Copyright 2008 The National Academy of Science of the USA and 2014 American Association for the Advancement of Science, respectively.	59
Figure 50 – Schemes of the deformation of the liquid/air interface with pressure and stability rupture. (a) Bending of the liquid meniscus with increasing pressure, from a flat (solid line) solid/liquid interface with no applied pressure to a bended meniscus forming a local contact angle equal to Young contact angle at maximum applied pressure (pointed line), and intermediate bending with local contact angle lower than the Young contact angle value. (b) Sagging of the bended solid/liquid interface when the maximum pressure is overpassed ($P > P_{max}$): the initial Cassie-Baxter’s state turn into a Wenzel’s state over time, passing by hybrid wetting state. (c) Formation of a Wenzel’s interface for pressure values below the maximum calculated pressure for a system with a too low asperities height ($H < H_{min}$): the bending of the meniscus with increasing pressure leads to a wetting of the void floor at lower pressure and thus meniscus curvature than with a sufficient height. This last case is excluded from the current model.....	61

Figure 51 – Application of the proposed model to a regularly patterned surface based on polyethylene circular pillars: Changes of the interface stability (evaluated from the maximum pressure before transition from Cassie-Baxter’s to Wenzel’s state) and contact angle with pillar spacing D , and width a . Solid lines correspond to stability and dashed lines correspond to contact angle.....	62
Figure 52 – Evolution of the air surface S_{air} and triple line length l with spacing distance D and asperities width a for circular asperities following a squared pattern, as shown in the insert. Solid lines correspond to air surface and dashed lines correspond to triple line length.....	63
Figure 53 –Change of the interface stability and contact angle with spacing on asperity size ratio D/a for circular asperities from 1 to 1,000 μm . Solid lines correspond to stability, and dashed line correspond to contact angle (numerical application based on polyethylene and water). The insert shows the considered asperities shape.	64
Figure 54 – Application of the proposed model to patterned surfaces based on square section pillars. (a) Changes of the interface stability (evaluated from the maximum pressure before transition from Cassie-Baxter’s to Wenzel’s state) and contact angle with pillar spacing, D , for circular section pillars from 1 to 1,000 μm large. (b) Change of the interface stability and contact angle with spacing on asperity size ratio D/a for circular asperities from 1 to 1,000 μm . (c) Calculated maximum D/a ratio allowing interface stability for a given maximum pressure P_{max} with a given vertical surface tension contribution (from θY and ψ) and asperity width a (d) Asperity shape and parameters used for application of the model	65
Figure 55 – Application of the proposed to model patterned surfaces based on cross section pillars. (a) Changes of the interface stability (evaluated from the maximum pressure before transition from Cassie-Baxter’s to Wenzel’s state) and contact angle with pillar spacing, D , for circular section pillars from 1 to 1,000 μm large. (b) Change of the interface stability and contact angle with spacing on asperity size ratio D/a for circular asperities from 1 to 1,000 μm . (c) Calculated maximum D/a ratio allowing interface stability for a given maximum pressure P_{max} with a given vertical surface tension contribution (from θY and ψ) and asperity width a (d) Asperity shape and parameters used for application of the model	66
Figure 56 – Application of the proposed model to patterned surfaces based on multiple-harms cross section pillars. (a) Changes of the interface stability (evaluated from the maximum pressure before transition from Cassie-Baxter’s to Wenzel’s state) and contact angle with pillar spacing, D , for circular section pillars from 1 to 1,000 μm large. (b) Change of the interface stability and contact angle with spacing on asperity size ratio D/a for circular asperities from 1 to 1,000 μm . (c) Calculated maximum D/a ratio allowing interface stability for a given maximum pressure P_{max} with a given vertical surface tension contribution (from θY and ψ) and asperity width a (d) Asperity shape and parameters used for application of the model.....	66
Figure 57 – Superhydrophobic surfaces reported in the literature. (a) Molded epoxy micropillars of 14 μm large and 30 μm height and spaced by (i) 23, (ii) 105, and (iii) 210 μm from Bhushan et.al. ²⁴ . (b) Epitaxial hexatriacontane wax on top of micropillars: (i) low and (ii) large wax content from Bhushan et.al. ²⁴ . (c) Epitaxial waxes crystals from n-paraffin of chain lengths of 36, 40, 44, and 50 carbon respectively (i-iv), from Pechook et.al. ¹³ . (d) Size, spacing distance, and height of the n-paraffin wax crystals and resulting contact angle reported for the surfaces represented in (c). (Reprinted respectively from ²⁴ and ¹³ , Copyright 2010 American Chemical Society and 2013 Royal Society of Chemistry.)	68
Figure 58 – Measuring the pressure effect on the interface stability. (a) (i) PDMS textured surface with cylindrical pillars, (ii) diffraction of light by the air plastron of the immersed surface experimental set scheme, and (iii) resulting measurements of diffracted intensity with applied pressure. (b) Fluorinated silicon textured surface with streaks (i) optical microscopy view and lattice cell representation, (ii) scheme of the experimental set for measuring the meniscus curvature, and (iii) resulting results: curvature and local contact angle variation with hydrostatic pressure and Laplace pressure corresponding to the curvature of the meniscus. Reprinted from ²⁷ and ²³ respectively, Copyright 2010 American Chemical Society and The Royal Society of Chemistry.	70

- Figure 59 – SEM micrographs of textured surfaces obtained by depositing nanoparticles on a substrate by (a,b,c) spray or (d) spin-coating. (a) Zinc oxide nanoparticles at 100g.L^{-1} in a PDMS-in-white-spirit solution, sprayed on a silicon wafer¹. (b) Silica nanoparticles at 20g.L^{-1} in a PMMA-in-toluene solution, sprayed on a silicon wafer¹. (c) SiO_2 nanoparticles at $40\%_{\text{wt}}$ in a polystyrene-in-chloroform solution, spin-coated on glass substrate². Reprinted from (a,b)¹, (c)², Copyright 2014 Elsevier and 2005 American Chemical Society, respectively. 79
- Figure 60 – SEM observations of textured surfaces obtained by hot-pressing polymer/particles nanocomposites. (a) Hot-pressed $2\%_{\text{wt}}$ Al_2O_3 in polycarbonate film⁵. (b) Hot-pressed $5\%_{\text{wt}}$ hydrophilic silica in poly(ethylene terephthalate) film⁶. Reprinted from ^{5,6}, Copyright 2008 and 2010 Elsevier. ... 80
- Figure 61 – SEM observations of sliced polyethylene or polyethylene-grafted-maleic anhydride/poly(ethylene oxide) immiscible polymer blends after PEO removal. (a), (b) correspond to various mixing conditions of PE-g-MA/PEO 50/50 blends, from the greater mixing time (a) to the lesser (b), whereas (c) is a PE/PEO 50/50 blend compounded with the same conditions than (a). Reprinted from ⁷, Copyright 2012 American Chemical Society..... 81
- Figure 62 – SEM observations of thermoplastics foam inner structures obtained using carbon dioxide. (a) PMMA foamed at 40°C after a 24h exposure of Sc-CO_2 at 34.47MPa .⁹ (b) Poly(ϵ -caprolactone) filled with $5\%_{\text{wt}}$ of talc foamed at 30°C after a CO_2 exposure of 3h at 6.41MPa and 70°C .¹⁰ (c) Polyimide and (d) polysulfone foamed in a glycerol bath at 170°C and 260°C respectively, after a CO_2 exposure at 5MPa and 25°C .¹¹ Reprinted from (a)⁹, (b)¹⁰, and (c,d)¹¹, Copyright 1994 Wiley, 2007 SAGE Publications, and 2002 American Chemical Society, respectively..... 82
- Figure 63 – SEM observation of foamed thermoplastics blends. (a) Poly(L-lactic acid)/poly(D,L-lactic acid) blend in 70/30 proportions foamed in water at 90°C , after a CO_2 exposure at 2.8MPa and 0°C for 24h.¹² (b) PP/PS 70/30 blend foamed at 179°C , after a Sc-CO_2 exposure at 19MPa and 179°C for 10h.¹⁴ (c) HDPE/PP blend in (i)50/50 and (ii) 30/70 proportions foamed in glycerin at 175°C , after a CO_2 exposure at 5.5MPa at room temperature for 24h.¹⁵ Reprinted from (a)¹², b(c)¹⁴ and (c)¹⁵, Copyright 2012 American Chemical Society, 2011 Wiley, and 2004 Society of Plastics Engineers, respectively. 83
- Figure 64 – DSM Xplore® MC15 micro-extruder 86
- Figure 65 – Scheme of the Sc-CO_2 batch foaming apparatus consisting of a 300cm^3 tank fed with CO_2 using a high-pressure pump and an electric heater. Pressure and temperature are computer-monitored. The foaming tank, from Parr, is designed to work at a maximum pressure of 20MPa and a maximum temperature of 350°C 87
- Figure 66 – Blown-film extruder apparatus. (a) Collin Tech-line® BL 50T blow film system with a Collin Tech-line® E20T extruder. (A) Hopper, (B) single-screw extruder for material melting and compression, (C) ring die of 30mm diameter and 1mm thick, with a film cooling by air flow, (D) rollers for film pinching and drawing., and (b) corresponding scheme, from ¹⁶. Copyright Elsevier 2017. 88
- Figure 67 – Measuring advancing and receding contact angle with the sessile drop technique. (a) Advancing and (b) receding contact angle measurement on advancing and receding triple lines due to liquid addition or removal from a drop (dynamic measurement, and simplified measurement technique for (c) advancing and (d) receding contact angle at equilibrium after drop deposition and liquid removal..... 89
- Figure 68 – Scheme of the texturing from fillers route. Polymer and fillers are introduced in a twin-screw extruder, and extruded into a film, leading to emerge particles during the film shrinking. 90
- Figure 69 – SEM observation of surfaces based on HDPE (BM593) filled with various amount of hydrophilic and hydrophobic silica. (a,b) HDPE filled with $6\%_{\text{vol}}$ ($11\%_{\text{wt}}$) of silica, and (c,d) $22\%_{\text{vol}}$ ($34\%_{\text{wt}}$) of silica. (a,c) HDPE with hydrophilic Wacker S13 silica, and (b,d) HDPE with hydrophobic Wacker H20 silica..... 91
- Figure 70 – Glass beads of about $30\mu\text{m}$ average diameter. (a) SEM micrograph of the microspheres before introduction in HDPE, and (b) corresponding size distribution from SEM image analysis using ImageJ..... 92
- Figure 71 – SEM micrographs of glass microspheres-filled HDPE films. (a) HDPE (BM593) filled with $23\%_{\text{vol}}$ glass microspheres, (b,c) $35\%_{\text{vol}}$ glass microspheres. (a) and (b) are compounded and extruded at 220°C , and (c) is compounded and extruded at 200°C 93

Figure 72 – SEM micrographs of a HDPE film surface containing 20% _{vol} PTFE microparticles at different magnifications.	94
Figure 73 – SEM observation of HDPE (BM593) films containing (a) 20% _{vol} , (b) 33% _{vol} , and (c) 50% _{vol} UHMWPE particles.	95
Figure 74 – Scheme of the texturing from immiscible polymer blends route. Polymers are introduced in a twin-screw extruder, and extruded into a film. The polymer B (PEO) is then removed by dissolution in water, revealing a porous polymer A (HDPE) surface textured film.	97
Figure 75 – SEM micrographs of PE/PEO immiscible blends surface after PEO removal for various PE/PEO volumetric proportions: (a) 36/64, (b) 46/54, and (c) 56/44.	98
Figure 76 – SEM micrographs of a HDPE/PEO immiscible blend based on 46% _{vol} HDPE (BM593) after PEO removal, containing 5% _{wt} hydrophilic silica (Aerosil® 200)	99
Figure 77 – SEM micrographs of HDPE/PEO immiscible blends surface with 46% _{vol} HDPE (BM593) after PEO removal, containing 5% _{wt} “hydrophobic” silicas: (a) HDK® H20, and (b) Aerosil® R812.	100
Figure 78 – SEM micrographs of HDPE/PEO immiscible blends surface based on 46% _{vol} HDPE (after PEO removal), and (a) 5% _{wt} ; (b) 10% _{wt} PTFE microparticles	101
Figure 79 – Scheme of the texturing from Sc-CO ₂ foaming route. Polymer are introduced in pressure barrel and swelled with Sc-CO ₂ , then foamed during the pressure release. The foamed polymer is sliced to reveal a textured surface.	104
Figure 80 – (a) Foaming process and (b) corresponding temperatures on a HDPE (BM593) DSC thermogram showing melting (dash line) and crystallization (solid line) peaks, and process temperatures (denoted on the crystallization exotherm) (Heating and cooling rates are 10K.min ⁻¹)	104
Figure 81 – Effect of foaming temperature on the cells size of HDPE (BM593). The polymer has been exposed to Sc-CO ₂ at 14MPa and 135°C for 1h, then cooled at (a) 117°C, (b) 115°C, (c) 114°C, and (d) 110°C for a pressure release at a 100% flow control valve opening. (e) Size distribution of the cells from samples foamed at 117°C, 115°C and 114°C, measured from SEM pictures using ImageJ.	105
Figure 82 – Large HDPE (BM593) sample foamed by Sc-CO ₂ at 110°C after an exposure at 14MPa and 135°C for 1h.....	106
Figure 83 – Influence of the depressurization flow rate on the cells size of HDPE (5502-R3). SEM micrographs of HDPE exposed to Sc-CO ₂ at 17MPa and 135°C for 5h and foamed at 115°C with a flow control valve opened at (a) 100%, (b) 50%, and (c) 25%. (d) Cells size distribution of the foamed HDPE as a function of the depressurization flow rate (from SEM pictures using the ImageJ software).....	107
Figure 84 – DSC thermograms of neat HDPE (BM593) and HDPE filled with 10% _{wt} of talc or calcium carbonate. (Heating and cooling rates are 10K.min ⁻¹)	109
Figure 85 – Influence of the presence of fillers in the cells size and size distribution of HDPE (BM593), after an exposure to Sc-CO ₂ at 17MPa and 140°C for 5h followed by a cooling at 115°C and pressure release at the lowest depressurization rate (flow control valve opened at 25%). SEM micrographs of (a) Neat HDPE, (b) HDPE containing 10% _{wt} CaCO ₃ , and (c) HDPE containing 10% _{wt} talc. (d) Size distribution of the cells (from SEM using ImageJ).....	109
Figure 86 – Influence of the presence of nucleating agents on the cells size and distribution of PP (PPH4060). SEM micrographs of (a) Neat PP and (b) PP containing 20% _{wt} talc. (c) Size distribution of the cells (from SEM using ImageJ). (d) DSC thermograms of neat PP and PP filled with talc (Heating and cooling rates are 10K.min ⁻¹).	111
Figure 87 – Influence of the foaming temperature on the cells size and distribution of a PP/PS (PPH4060/PS1070N) blend in 50/50 weight proportions, after an exposure to Sc-CO ₂ at 18MPa and 180°C for 5h followed by a cooling at (a) 120°C, (b) 150°C, and (c) 180°C, i.e. no cooling, and pressure release with the flow control valve fully opened, observed by SEM. (d) Size distribution of the cells (from SEM using ImageJ).	112
Figure 88 – Influence of the foaming temperature on the cells size and distribution of a PP/PS blend in 70/30 weight proportions, after an exposure to Sc-CO ₂ at 18MPa and 180°C for 5h followed by a cooling at (a) 120°C, (b) 150°C, and (c) 180°C, and pressure release with the flow control valve fully opened, observed by SEM.	114

Figure 89 – Influence of the blend composition on the cells morphologies of (a) 50/50 and (b) 70/30 PP/HDPE (PPH4060 and 5502-R3) blend, after an exposure to Sc-CO ₂ at 18MPa and 180°C for 5h followed by a cooling at 120°C, and a fast depressurization (flow control valve fully opened), observed by SEM.	115
Figure 90 – Scheme of the texturing continuous foaming process route. Polymer and chemical blowing agents (CBA) are introduced in an extruder where CBA decompose into CO ₂ and H ₂ O, and then extruded into a film (using a ring die).	117
Figure 91 – Reaction mechanisms of some chemical blowing agents. (a) Citric acid thermal decomposition, (b) Sodium hydrogen carbonate thermal decomposition, (c) Citric acid reaction with calcium carbonate or (d) sodium hydrogen carbonate.....	118
Figure 92 – Thermal degradation of chemical blowing agents. Relative weight loss (in solid lines) and derivative (in dashed lines) for (a) citric acid (C ₆ H ₈ O ₇ , CA), (b) sodium hydrogen carbonate (NaHCO ₃), (c) CA + calcium carbonate in 2:3 molar proportions, and (d) CA + sodium hydrogen carbonate in 1:3 molar proportions. (Heating rate of 10K.min ⁻¹ , under nitrogen)	118
Figure 93 – SEM micrographs of HDPE (BM593) extruded foam with various amounts of CBA. HDPE was mixed at 230°C and extruded through a 180°C die with (a) 1% _{wt} , (b) 2% _{wt} , (c) 5% _{wt} , and (d) 10% _{wt} citric acid, and the same amount of calcium carbonate.....	120
Figure 94 – SEM micrographs of LDPE (FE8000) extruded foams obtained from various chemical blowing agents. LDPE is mixed at 230°C and extruded through a 180°C die with (a) 10% _{wt} of citric acid and 10% _{wt} of calcium carbonate, (b) 10% _{wt} sodium hydrogen carbonate with 10% _{wt} calcium carbonate as filler, and (c) 15% _{wt} sodium hydrogen carbonate with citric acid in 3:1 molar proportion and 15% _{wt} calcium carbonate as filler.	122
Figure 95 – SEM micrographs of HDPE (BM593) extruded foam with various fillers. HDPE was mixed at 230°C and extruded through a 180°C die with 5% _{wt} of citric acid and (a) 5% _{wt} of talc, or(b) 5% _{wt} of hydrophobic silica.....	123
Figure 96 – SEM micrographs of HDPE (5502-R3) extruded in viscous conditions with various citric acid and calcium carbonate contents. HDPE is mixed at 230°C and extruded through a 160°C die with (a) 10% _{wt} of citric acid and 20% _{wt} of calcium carbonate, (b) 20% _{wt} of citric acid and 10% _{wt} of calcium carbonate, and (c) 15% _{wt} of citric acid and 15% _{wt} of calcium carbonate.	125
Figure 97 – SEM micrographs of a HDPE (HD6081) immersed in xylene at 100°C for 90s. (a) Relatively smooth surface, and (b) stack of micrometric features under a smooth skin revealed by slicing. Water contact angle and hysteresis values of the surface are inserted in the lower left corner.....	135
Figure 98 – DSC traces of neat HDPE (BM593) in black and HDPE in a xylene solution (2% _{wt}) in red, showing crystallization during cooling (solid lines) and melting during heating (dashed lines). (Heating and cooling rate are 10K.min ⁻¹)	136
Figure 99 – Surfaces as obtained after immersion of HDPE (BM593) in xylene at 130°C for (a,c) 5s and (b,d) 10s, directly followed by an immersion in xylene at (a,b) 60°C and (c,d) 80°C for 5 minutes (SEM micrographs).	137
Figure 100 – Scheme of the process of texturing of polyethylene specimens through re-organization using p-xylene.....	138
Figure 101 – SEM micrographs of textured films of various HDPE grades obtained by immersion in xylene. Grades are (a) BM593, (b) 5502-R3, (c) HD6081, and (d) M6040.....	139
Figure 102 – SEM micrographs of PP (PPH4060) surfaces, textured by immersion in xylene for 5s at 130°C, followed by an “immersion” (a) in air at 20°C, (b) in acetone at 20°C, (c) in xylene at 20°C, (d) in xylene at 80°C, and (e) in xylene at 100°C, for 5 minutes.	141
Figure 103 – SEM micrographs of textured HDPE (BM593) and PP (PPH4060) filled by talc or calcium carbonate, after immersion in xylene for 5s at 130°C and 80°C for 5 minutes: (a) BM593 + 2% _{vol} talc, (b) HDPE + 5% _{vol} talc, (c) HDPE + 3.8% _{vol} (10% _{wt}) calcium carbonate, and (d) PP + 5% _{vol} talc.	142
Figure 104 – SEM micrographs of morphologies used for Cassie-Baxter’s interface stability model predictions: (a) HDPE (BM563) post-treated with a 60°C xylene bath, (b) HDPE (BM593) texturing using the optimized process, (c) PP (PPH4060) textured using the optimized process, and (d) resulting	

measured asperities width a , spacing distance D and D/a ratio, obtained using the ImageJ software.	144
Figure 105 – Surface tension of ethanol in water solutions depending on the ethanol weight fraction. Blue circles are measured surface tension of prepared solutions from 95% pure ethanol and deionized water, and orange triangles are results from Vazquez et al. ¹⁶	146
Figure 106 – Contact angle and hysteresis for untreated and textured HDPE (BM593) and PP (PPH4060) surfaces with water/ethanol solutions. Squares are contact angle values, and triangles are hysteresis values. Black, red, blue and green refer to HDPE, PP, textured HDPE, and textured PP, respectively.	147
Figure 107 – SEM micrographs of HDPE (BM593) textured through dipentene exposure by a 10s immersion at 130°C, and 5min at (a) 80°C, or (b) 100°C.....	150
Figure 108 – SEM micrographs of HDPE (BM593) textured through α -pinene exposure by a 30s immersion at 130°C, and then 5min at (a) 80°C, or (b) 100°C.	151
Figure 109 – SEM micrographs of HDPE (BM593) surfaces textured through decane exposure by a 30s immersion at 140°C, and then 5min at (a) 80°C, or (b) 100°C.	152
Figure 110 – SEM micrographs of HDPE (BM593) surfaces textured through n-paraffin exposure by a 5min immersion at (a, c) 135°C or (b, d) 140°C, and then 5min at 100°C. (a-b) were washed using methylcyclohexane upon drying, whereas (c-d) were kept as obtained after the second bath immersion, with a paraffin wax layer.....	153
Figure 111 – SEM micrographs of HDPE (BM593) surfaces textured through olive oil exposure by a (a) 20s immersion at 140°C followed by a 30s immersion at 105°C, or (b) 5min immersion at 135°C followed by cooling at 5°C/min in the same bath.	154
Figure 112 – SEM micrographs of PP (PPH4060) surfaces textured through dipentene exposure by a 10s immersion at 130°C, and then 5min at (a) 80°C, or (b) 100°C.....	156
Figure 113 – SEM micrographs of PP (PPH4060) surfaces textured through α -pinene exposure by a 5s immersion at 130°C, and then 5min at (a) 80°C, or (b) 100°C.	157
Figure 114 – SEM micrographs of PP (PPH4060) surfaces textured through decane exposure by a 5s immersion at 130°C, and then 5min at (a) 80°C, or (b) 100°C.	158
Figure 115 – SEM pictures of PP(PPH4060) textured through olive oil exposure by a 5min immersion at (a) 150°C, or (b) 170°C, and then 5min at 100°C.....	159
Figure 116 – Scheme of the single-immersion solvent texturing process.	161
Figure 117 – SEM micrographs of HDPE (BM593) surfaces textured through dipentene exposure of 10s at 130°C with a single immersion followed by a drying in air. (a) and (b) are different parts of the same 5mm large sample.....	161
Figure 118 – SEM micrographs of HDPE (BM593) surface textured through α -pinene exposure of 1s at 130°C with a single immersion followed by a drying in air. (a) and (b) are different parts of the same 5mm large square sample.	162
Figure 119 – SEM micrographs of HDPE (BM593) surface textured through decane exposure of 30s at 140°C with a single immersion followed by a drying in air.	163
Figure 120 – SEM micrographs of PP (PPH4060) surface textured by a dipentene exposure with a single immersion followed by a drying in air. Conditions are: (a) 5s in dipentene at 130°C, (b) 30s in dipentene at 110°C.	164
Figure 121 – SEM micrographs of PP (PPH4060) surfaces textured by a α -pinene exposure with a single immersion followed by a drying in air. Conditions are: (a) 5s in α -pinene at 130°C, (b) 30s in α -pinene at 110°C.	165
Figure 122 – SEM micrographs of PP (PPH4060) surfaces textured by a decane exposure with a single immersion followed by a drying in air. Conditions are: (a) 10s in decane at 130°C, (b) 5min in decane at 110°C.	166
Figure 123 – (a) Scheme and (b) experimental setup of a continuous texturing process of HDPE and PP films through dipentene exposure.....	167

Figure 124 – SEM micrographs of HDPE (BM593) textured by a dipentene exposure in a continuous process: BM593 films gone through a 130°C dipentene bath, where it stayed less than 1s, followed by a drying in air. (a) is the neat film and (b) is the rolled film.	168
Figure 125 – SEM micrographs of PP (PPH4060) surfaces textured by a dipentene exposure in a continuous process: films gone through a 130°C dipentene bath, where it stayed less than 1s, followed by a drying in air. (a) is the raw film, (b) is the undamaged rolled film and (c) is a visibly crushed area of the rolled film.	169
Figure 126 – Texturing mechanism from a solution of polypropylene proposed by Hejazi et al. ² . Copyright 2014 Elsevier.	171
Figure 127 – Phase diagrams of (a) high density polyethylene and (b) isotactic polypropylene with m-xylene (the polymer weight fraction in abscissa). The I, II and III phases correspond to a homogeneous polymer/solvent solution, a semicrystalline polymer with solvent-swelled amorphous regions, and a two-phase amorphous system, respectively. Reprinted from Mizerovskii et al. ^{19,20} . Copyright 2015 and 2013 Pleiades Publishing Ltd.	172
Figure 128 – Optical micrographs under polarized light of (a) HDPE (BM593), and (b) iPP (PPH4060) films exposed to xylene at 130°C. The first picture is the neat film at 130°C, the second picture the film after the addition of a xylene drop, and the third picture the resulting film after solvent evaporation and cooling at 5K.min ⁻¹	173
Figure 129 – Optical micrographs under polarized light of (a) HDPE (BM593) and (b) iPP (PPH4060) exposed to xylene at 130°C and then cooled at 5K.min ⁻¹ . Focus on the deposited solvent droplet boundary: (a) droplet was deposited on the upper right corner, and for (b) the droplet was deposited on the lower left corner.	174
Figure 130 – Examples of HDPE and PP crystallized from a diluted solution found in the literature: (a) HDPE crystals grown on a UHMWPE fiber from a solution in xylene at 90°C, from Miao et al. ²¹ , (b) PP crystals obtained from a crystallization in amyl acetate at a concentration of 0.75% at 114°C, from Khoury ²² . In the later, the scalebar is approximate because of its absence in the original publication: it is here estimated based on the asperities size as indicated by the author. Copyright 2018 The Royal Society, and 1966 National Bureau of Standards, respectively.	174
Figure 131 – SEM micrographs of HDPE (BM593) deposited on a glass substrate from a 2% _{wt} solution in xylene, deposited at (a) 120°C, (b) 90°C, and (c) 20°C.	175
Figure 132 – Low acceleration voltage SEM micrographs of (a) HDPE (BM593) or (b) PP (PPH4060) surface asperities after a xylene texturing following the optimized process.	176
Figure 133 – SEM micrographs of PP (PPH4060) deposited on a glass substrate from a 2% _{wt} solution in xylene, deposited at (a) 120°C, (b) 90°C, and (c) 20°C.	177
Figure 134 – SEM micrographs of a HDPE (BM593) surface exposed to xylene at 130°C for 5s, followed by an immersion in a xylene/DMSO solution (4:1) at 100°C for 5min.	178
Figure 135 – HSP Distance (Ra) for (a) polyethylene and (b) polypropylene with solvents such as xylene, dipentene, α -pinene, decane and oleic acid with temperature.	179
Figure 136 – Changes of (a-b) melting and (c-d) crystallization temperatures of (a-c) HDPE (BM593) and (b-d) PP (PPH4060) with the solvent fraction. Solvents are xylene, dipentene, α -pinene, decane and olive oil (DSC measurements at 10K.min ⁻¹).	180

I.2. Tables

Table 1 – Summary of surface energy reduction approaches and resulting wettability	21
Table 2 – Summary of superhydrophobic processed surfaces.....	25
Table 3 – Summary of superhydrophobic isotropic textured surfaces after hydrophobization.....	27
Table 4 – Summary of superhydrophobic textured surfaces from hydrophobic particles	34
Table 5 – Summary of superhydrophobic surfaces from self-textured polymers	43
Table 6 – Summary of studied superhydrophobic surfaces, depending on their texturing and surface energy reduction ways.	45
Table 7 – Relevant size parameters of asperities having different shapes	61
Table 8 – Calculated maximum D/a ratio allowing interface stability for a given maximum pressure P_{max} with a given vertical surface tension contribution (from θY and ψ) and asperity width a for circular asperities following a square pattern. 20Pa correspond to the pressure exerted by a 2mm water drop on a surface due to its weight, and 1,000Pa correspond to a 10cm deep immersion of the surface in water.....	64
Table 9 – Polymer considered in this study.....	85
Table 10 – Silica particles considered in this study	85
Table 11 – Particles (organic or inorganic) considered in this study.....	86
Table 12 – Water contact angle and hysteresis of surfaces processed from HDPE filled with silica, depending on silica content and nature.....	91
Table 13 – Water contact angle and hysteresis of HDPE (BM593) filled with 13-45 μ m diameter glass microspheres depending on the particles loading and extrusion temperature.	94
Table 14 – Water contact angle and hysteresis of HDPE (BM593) film filled with PTFE particles.....	94
Table 15 – Water contact angle and hysteresis of HDPE (BM593) films filled with UHMWPE particles, depending on the particle loading.	96
Table 16 – Summary of PE/PEO blends realized, with their volume and weight proportions, and the presence of a compatibilizer.	97
Table 17 – Water contact angle and hysteresis of HDPE/PEO immiscible blends (after PEO removal) depending on the volume proportions.	99
Table 18 – Water contact angle and hysteresis for HDPE/PEO blends filled with hydrophobic silica nanoparticles (after PEO removal).	101
Table 19 – Water contact angle and hysteresis for HDPE/PEO immiscible blends filled with PTFE particles (after PEO removal).	102
Table 20 – Water contact angle and hysteresis of HDPE (BM593) foamed at different temperatures after a 1h exposure to Sc-CO ₂ at 14MPa and 135°C.	106
Table 21 – Water contact angle and hysteresis of HDPE (5502-R3) foamed at 115°C depending on the flow control valve opening, after an exposure to Sc-CO ₂ at 17MPa and 135°C for 5h.....	108
Table 22 – Water contact angle and hysteresis of foamed HDPE (BM593) containing fillers such as CaCO ₃ or talc, saturated with Sc-CO ₂ at 17MPa and 135°C and foamed at 115°C with a 25% opening of the flow control valve.....	110
Table 23 – Water contact angle and hysteresis of foamed PP (PPH4060) containing talc as a nucleating agent, saturated with Sc-CO ₂ at 17MPa and 155°C and foamed at 130°C with a fully opened flow control valve.	111
Table 24 – Water contact angle and hysteresis of foamed 50/50 and 70/30 PP/PS (PPH4060 and PS1070N) immiscible blend, saturated with Sc-CO ₂ at 18MPa and 180°C and foamed at 120°C, 150°C or 180°C, at the fastest depressurization rate (fully opened flow control valve).	114
Table 25 – Water contact angle and hysteresis of foamed 50/50 and 70/30 PP/HDPE (PPH4060 and 5502-R3) immiscible blend, saturated with Sc-CO ₂ at 18MPa and 180°C and foamed at 120°C, with a fast depressurization rate (fully opened flow control valve)	115
Table 26 – Chemical blowing agents thermal reaction characteristics.....	119
Table 27 Compositions and processing conditions of HDPE and LDPE masterbatches with CBA and fillers.	119

Table 28 – Water contact angle and hysteresis of HDPE (BM593) extruded foams containing from 1 to 10% _{wt} of citric acid, and the same amount of calcium carbonate as chemical blowing agents.	121
Table 29 – Water contact angle and hysteresis of LDPE (FE8000) extruded foam containing citric acid, calcium hydrogen carbonate and calcium carbonate as chemical blowing agent and/or nucleating agents.	123
Table 30 – Water contact angle and hysteresis of HDPE (BM593) extruded foam containing 5% _{wt} of citric acid, and the same amount of talc or hydrophobic silica as nucleating agents.....	124
Table 31 – Water contact angle and hysteresis of HDPE 5502-R3 extruded foam containing citric acid and calcium carbonate in various proportions.	125
Table 32 – Summary of the process conditions applied to various materials for their texturing using an immersion in xylene.	143
Table 33 – Water contact angles and hysteresis of textured surfaces.	145
Table 34 – Diiodomethane contact angle and hysteresis for neat and textured HDPE and PP.....	146
Table 35 – A selection of alternative solvents for HDPE according to their solubility parameters, boiling point, and toxicity.....	149
Table 36 – Hazard statements with their corresponding code for the selected solvents.	149
Table 37- Water contact angle and hysteresis of textured HDPE (BM593) surfaces exposed to various solvents.....	155
Table 38 – Comparison of alternative solvents for PP and HDPE according to their solubility parameters and HSP distance.	156
Table 39 – Water contact angle and hysteresis of textured PP (PPH4060) surfaces exposed to various solvents.....	160
Table 40 – Water contact angle and hysteresis of textured HDPE surfaces exposed to various solvents in a single-bath process.....	163
Table 41 – Water contact angle and hysteresis of textured PP (PPH4060) surfaces exposed to various solvents in a single-bath process.....	167
Table 42 – Water contact angle and hysteresis of textured HDPE and PP surfaces exposed to various dipentene in a continuous process with a single bath. Highlighted cells are texturing conditions effectively leading to slippery superhydrophobicity.....	169
Table 43 – Summary of the best texturing conditions for HDPE and PP for stable superhydrophobicity of their surface depending on the texturing process and solvent used.	183